Fall 2012

Purification of metals through filtration and electromagnetic separation

Lucas Nana Wiredu Damoah

Department: Materials Science and Engineering

PURIFICATION OF METALS THROUGH FILTRATION AND ELECTROMAGNETIC SEPARATION

by

LUCAS NANA WIREDU DAMOAH

A DISSERTATION

Presented to the Faculty of the Graduate School of the

MISSOURI UNIVERSITY OF SCIENCE AND TECHNOLOGY

In Partial Fulfillment of the Requirements for the Degree

DOCTOR OF PHILOSOPHY

in

MATERIALS SCIENCE AND ENGINEERING

2012

Approved by

Lifeng Zhang, Advisor

Kent D. Peaslee, Co-advisor

Von Richards

David Van Aken

David DeYoung

PUBLICATION DISSERTATION OPTION

This dissertation consists of five manuscripts prepared for publication peer reviewed journals and a peer reviewed conference proceeding. Pages 13-52 make a manuscript intended for publication in Solar Energy Materials and Solar Cells. The manuscript on pages 53-88 is also intended for publication in Solar Energy Materials and Solar Cells. Pages 89-109 is an extended version of one published in the TMS Proceedings on Light Metals 2012. Pages 110-156 have been published in Metallurgical and Materials transactions B but include two schematics for this dissertation. Pages 157-191 have been published in Acta Materialia.

ABSTRACT

The applicability of a high frequency electromagnetic field to the removal of nonmetallic inclusions from silicon and aluminum, and the mechanism of depth mode filtration during aluminum purification were investigated. Electromagnetic separation experiments at frequencies of 63 – 120 kHz and aluminum filtration experiments using both conventional Al_2O_3 filters and AlF_3 coated Al_2O_3 filters were carried out by flowing molten aluminum through, and partly solidified in the filter bed followed by analysis of the metal and filter material. Materials were characterized with an optical microscope and macroscope, scanning electron microscope (SEM/EDX), x-ray diffraction (XRD), electron probe microanalysis (EPMA) and glow discharge mass spectrometry (GDMS). 3D FLUENT CFD simulation was made in support of the filtration experiments. In the high frequency electromagnetic field work, the induced fluid flow significantly enhanced particle segregation either at the wall or at the bottom or deposition close to the top. The electromagnetic particle separation efficiency was significantly improved by higher coil current and longer separation time. Higher frequency also improved particle separation efficiency but was less significant than current or separation time. Filtration results showed that depth filtration of aluminum involves the contribution of three important mechanisms which are (1) collision and interception effect which involves particles transport from the melt and attachment to filter wall, (2) effect of inclusion bridges and (3) interfacial energy between collided inclusions.

ACKNOWLEDGEMENT

I am most thankful to God for the gift of life and His unfailing grace. I especially thank my wife, Ama for her sacrifices, prayer support and encouragement during the tough times. My children Melody and Daniel have been great source of joy and inspiration with their tireless labor in our home. I am grateful for their distractions too.

The research work of this dissertation has been sponsored by Department of Energy (Award No. DE-EE0000575), University of Missouri Research Board, the Material Research Center (MRC) and Intelligent Systems Center (ISC) at Missouri University of Science and Technology (Missouri S&T); I am grateful for their financial and logistical support.

I appreciate the invaluable advice and direction offered by my advisors Dr. Lifeng Zhang and Dr. Kent Peaslee and the guidance of my advisory committee members, Dr. Von L. Richards, Dr. David Van Aken, and Dr. David DeYoung.

I am very grateful for the support I received from the University of Science and Technology Beijing (USTB) in the provision of the free Al-SiC materials for my study, Dr Anping Dong for his help for setting up the initial silicon EM experiments, and thanks to Dr. Shufeng Yang for providing many free experimental crucibles for my research and his help in polishing some of my samples.

I thank my colleagues at the Green Process Metallurgy and Modeling laboratory, Dr. David G. Robertson**,** Dr. Simon N. Lekakh**,** Dr. William G. Fahrenholtz and Mingzhi Xu for their advice, suggestions and hands-on support. I will like to thank my numerous friends at the Department of Materials Science and Engineering and the Missouri University of Science and Technology at large who supported me with their pieces of advice, encouragements, smiles and prayers.

Finally, to all my teachers in the class room and those I have silently learnt from, I am grateful for your help. I promise to do the best possible to put to good use all the knowledge you have imparted to me.

TABLE OF CONTENTS

Page

PUBLICATION DISSERTATION OPTION iii
ABSTRACT iv
ACKNOWLEDGEMENT v
LIST OF ILLUSTRATIONS xi
LIST OF TABLES xix
1. INTRODUCTION 1
1.1. OVERVIEW 1
1.2. THEORETICAL CONCEPTS INVOLVED IN THE SEPARATION PROCESSES 2
1.2.1. Filtration 2
1.2.2. Electromagnetic Separation 2
1.3. SCOPE OF STUDY 3
1.4. INCLUSIONS IN SILICON 3
1.5. INCLUSIONS IN ALUMINUM 4
1.6. RESEARCH OBJECTIVES 6
1.7. METHODOLOGY 7
1.8. SUMMARY OF RESULTS 8
REFERENCES 10
PAPER
I. HIGH FREQUENCY ELECTROMAGNETIC PURIFICATION OF SILICON 13
Abstract 14
1. Introduction 14
2. Materials and Methods 16
2.1. Materials 16
2.2 Equipment and Experimental Set-up 19
2.3 Experimental procedure for Settling of Inclusions in Si(Al) – SiC Composite 20
2.4 Evaluation of Separation Efficiency, η 23
2.5 Modeling of Magnetic Field and Fluid Flow 26

2.5.1 Modeling of Magnetic Field 27
2.5.2 MHD Modeling with ANSYS FLUENT 27
3. Results and Discussion 30
3.1. Overall Separation 30
3.2. Separation Mechanisms and Fluid flow 37
3.2.1 Contributing forces 37
3.2.2 Fluid flow 39
3.3. Effect of Separation Time 42
3.4. Effect of Coil Current, I_{rms} 43
3.5. Effect of frequency 44
3.6. Separation in larger volume melt 47
4. Conclusions 49
References 50
II. SETTLING OF INCLUSIONS IN SILICON UNDER ELECTROMAGNETIC FIELD 53
Abstract 54
1. Introduction 54
2. Materials and Experimental Procedure 56
2.1. Top-cut SoG-Si scrap 56
2.2. Si(Al) – SiC Composite 57
2.3. Equipment and Experimental Set-up 57
2.4. Experimental Procedure for Particle Settling in Top-cut SoG-Si Scrap 58
2.5. Experimental Procedure for Settling of Inclusions in Si(Al) – SiC Composite 59
2.6. Modeling of Magnetic Field and Fluid Flow 61
2.6.1. Modeling of Magnetic Field 61
2.6.2. MHD Modeling with ANSYS FLUENT 62
3. Results and Discussion 64
3.1. Settling of Particles in Top-cut SoG Silicon 64

3.1.1. Status of Si_3N_4 particles in top-cut scrap after EM experiments 67
3.2. Settling of Particles in Si (Al) – SiC Composite Material 70
3.2.1. Quantification of settling results 71
3.2.2. Effect of Separation Time 73
3.2.3. Effect of Coil Current, I_{rms} and Frequency 74
3.3. Settling Mechanism 77
3.3.1. Magnetic Field 77
3.3.2. Forces acting on a particle 79
3.3.3. Induced fluid flow 80
3.3.4. Magnetization force due to magnetic field gradients 84
4. Conclusions 85
References 86
III. HIGH FREQUENCY ELECTROMAGNETIC SEPARATION OF INCLUSIONS FROM ALUMINUM 89
Abstract 90
Introduction 90
Materials and Experiments 91
Results and Discussions 95
Particle separation from experiments 95
Flow pattern and Separation Mechanism 100
Temperature and Viscosity Distribution 104
Summary 107
References 107
IV. REMOVAL OF INCLUSIONS FROM ALUMINUM THROUGH FILTRATION 110
I. INTRODUCTION 111
II. MATERIALS AND EXPERIMENTAL METHODS 113
III. INCLUSIONS IN ALUMINUM 119
IV. REMOVAL OF NONMETALLIC INCLUSIONS 123
A. Evaluation of inclusions removal 123

B. Filtration Mechanisms 131
1. Collision with walls and Interception Effect 132
2. Effect of Inclusion Bridges on Filtration 138
3. Interfacial Energy between Two Collided Inclusions 139
V. REMOVAL OF IMPURITY ELEMENTS 143
VI. NEW DESIGNS OF FILTRATION 146
A. Multi-pore filtration 148
B. Multi – stage filtration 150
C. Reverse filtration 150
VII. CONCLUSIONS 151
ACKNOWLEDGEMENTS 152
REFERENCES 153
V. ALF_3 REACTIVE AL_2O_3 FOAM FILTER FOR THE REMOVAL OF DISSOLVED IMPURITIES FROM MOLTEN ALUMINUM: PRELIMINARY RESULTS 157
Abstract 158
1. Introduction 158
2. Experiments 163
2.1. Trial Experiments 163
2.2. Reacting Al_2O_3 Filter with Anhydrous HF Gas 163
3. Results and Discussions 166
3.1. Comparison between Al2O3 Filters Coated with AlF3 Slurry and coating by Reacting with HF Gas 166
3.2. Evaluation of HF gas coating process 170
3.3. Theoretical analysis of [Ca] and [Mg] removal from molten Al 180
3.4. Experimental Results of molten aluminum purification with a coated filter 185
4. Summary 187
5. Future work 188
Acknowledgement 188
References 188

VITA 192

LIST OF ILLUSTRATIONS

Page

Figure 1.1. Typical composition and morphologies of nonmetallic inclusions in top-cut silicon..... 4

Figure 1.2. Typical inclusions commonly found in aluminum..... 6

PAPER I

Fig. 1. Microstructure of Si (Al) – 3 % SiC composite material made from metallurgical silicon and Al - 15 % SiC composite through the stir-solidification process. 17

Fig. 2. Typical microstructure of the aluminum dominant Al-Si eutectic structure of the material that precipitated on top of the solidified Si (Al) – SiC composite material during the stir – solidification process. 18

Fig. 3. Type and average size of inclusions in the Si – SiC composite material. 18

Fig. 4. Picture of the equipment showing the coil – power supply system..... 19

Fig. 5. Schematic of the experimental set-up for the electromagnetic separation of particles from silicon..... 20

Fig. 6. Heating rates recorded for the experiments. 23

Fig. 7. Sample sectioning and observed surface.. 24

Fig. 8. Vertical cross-section of an actual sample with an outline and equivalent shape, and dimensions of the sample architecture with a shaded region of inclusion. 25

Fig. 9. Example of separation efficiency – time plot. 26

Fig. 10. View of the skin-depth based mesh of the 3D geometry of solids within the coil..... 28

Fig. 11. 2D Mesh of the model solved in ANSYS Fluent. 29

Fig. 12. Typical optical macro- and micro-graphs of the quarter vertical cross-section of the EM separated sample. 31

Fig. 13. SEM micrographs of the top part of the samples in Fig. 12 after separation showing a thin topmost oxide layer of aluminum and silicon oxide and the transition from the particles in the top area to the clean area. 33

Fig. 14. Micrographs of the various locations capturing the distribution of particles at bottom (top), side wall (middle) and center (bottom) for separation at frequency of 65 kHz, coil current of 533 A and a time of 10 s. 34
Fig. 15. Typical EDX spectrum of the small size particles in the side and bottom wall layers. 35
Fig. 16. Magnetic field vectors within the experimental set-up and B contours within the crucible, sheath, susceptor and silicon 36
Fig. 17. The effect of gradient magnetic field and Reynolds number on the settling velocity of a 10 μm SiC particle in molten silicon..... 39
Fig. 18. Contours of velocity magnitude and streamlines of fluid flow as calculated by ANSYS FLUENT..... 40
Fig. 19. Comparison of faceted minimum, maximum and average fluid velocities for various parameters..... 41
Fig. 20. Quarter cross-sectional macrographs showing the effect of separation time at coil current I_{rms} = 278 A and frequency f = 65 kHz. 42
Fig. 21. Quarter cross-sectional macrographs showing the effect of separation time at coil current I_{rms} = 278 A and frequency f = 90 kHz 43
Fig. 22. Quarter cross-sectional macrographs comparing the effect of coil current..... 44
Fig. 23. The dependence of the separation efficiency on coil current and time at 65 kHz based on the corrected time for individual experiments..... 45
Fig. 24. Quarter cross-sectional macrographs showing the dependence of separation efficiency on frequency at 278 A and separation time of 45 s. 45
Fig. 25. The dependence of the separation efficiency on the frequency and separation time at a coil current of 278 A..... 46
Fig. 26. Recorded separation efficiencies plotted against coil current for various frequencies and particle concentrations. 47
Fig. 27. Optical macrographs of larger size samples separated at a frequency of 65 kHz, coil current of 350 A for respective separation times of 30 s 48
Fig. 28. Enlarged view of the matrix of the samples shown in Fig. 22 showing the clean and the particle containing matrix (top – right corner). 49

PAPER II

Fig. 1. Optical micrographs of inclusions in a top-cut SoG-Si scrap on the surface (left) and at a depth of 1mm beneath the top surface showing lumpy SiC and rod-like Si_3N_4 particles. 57

Fig. 2. Si (Al) – 3 % SiC composite material made from metallurgical silicon and Al - 37 % SiC composite through stir solidification. 58

Fig. 3. Scaled schematic of the experimental set-up used for the electromagnetic settling experiments. 58

Fig. 4. Particle size distribution of inclusions in the Si (Al) – 3% SiC composite material. 60

Fig. 5. View of the skin-depth based mesh of the 3D geometry of solids within the coil..... 62

Fig. 6. 2D Mesh of the model solved in ANSYS Fluent. 63

Fig. 7. Collection of optical micrographs showing the distribution of inclusions in a top-cut SoG-Si scrap melted at 1600^{o}C at a heating rate of 4 ^{o}C/min and held for two hours before cooling at 4 ^{o}C/min to room temperature in a high temperature furnace without EM field.. 65

Fig. 8. Terminal velocity of Si_3N_4 and SiC particles in silicon at 1600^{o}C. 66

Fig. 9. Optical micrographs of the bottom of the sample after the EM settling experiment Si-SD–1 showing that inclusions settled to the bottom of the crucible and were well distributed along the diameter.. 67

Fig. 10. Optical micrographs from top to bottom of the samples after the EM settling experiments Si-SD–1 and Si-SD–2 showing a cleaner inner silicon matrix and settled particles at the bottom of the samples.. 68

Fig. 11. Optical micrographs showing a continuous SiC phase generated as a result of the interaction between the graphite crucible and molten silicon at the walls of the crucible.. 69

Fig. 12. Part of the top and bottom views of the sample from experiment Si-SD–2 showing settled particles at the bottom, a continuous slag layer on top and a continuous SiC reaction layer at the graphite-molten silicon interface..... 69

Fig. 13. Distribution of particles across a vertical cross-section sample after gravity sedimentation at 1600 ^{o}C for 9 hours. 70
Fig. 14. Optical macro- and micro-graphs of a quarter vertical cross-sectional view of the sample from the settling experiments using 486 A coil current, at 65 kHz and separated for 50 s. 71
Fig. 15. Optical Macrographs of vertical cross-sections of samples showing the effect of time on the separation process for 10 s (left) and 30 s (right) as repective examples of 45 % and 60 % separation in graphite crucible at I_{rms} = 270 A and f= 65 kHz. 72
Fig. 16. Area fraction determination using particle analysis tool in image processing software *imageJ.* 72
Fig. 17. Dependence of the separation efficiency with time for experiments in graphite and alumina crucibles at 65 kHz. 73
Fig. 18. Distribution of particles (area percent) from top – bottom of the sample comparing separation at the different coil currents. 75
Fig. 19. Distribution of particles (area percent) from top – bottom of the sample comparing separation at the different frequencies. 75
Fig. 20. Macrographs of quarter vertical cross-section of Si (Al) -3 % SiC after settling for 50 s under EM of f = 65 kHz 76
Fig. 21. Optical macro- and micro-graphs of a quarter vertical cross-sectional view of the sample from the settling experiments using 397 A coil current, at 65 kHz and separated from 50 s. 76
Fig. 22. Macrographs of quarter vertical cross-section of Si (Al) -3 % SiC after settling for 50 s under EM of I_{rms} = 268 A. 77
Fig. 23. Magnetic field vectors within the set-up and B contours within the crucible, sheath, susceptor and silicon. 78
Fig. 24. Effect of temperature on the viscosity of silicon based on the results of Sato *et al.*[18]. 81
Fig. 25. Effect of Reynolds number on settling velocity of a 10 µm particle 81
Fig. 26. Velocity contours and streamlines of induced fluid flow in the crucible calculated by ANSYS FLUENT. 82

Fig 27. Comparison of faceted minimum, maximum and average velocities for various parameters. 84
Fig. 28. The effect of gradient magnetic field and Reynolds number on the settling velocity of a 10 μm SiC particle in molten silicon. 85

PAPER III

Figure 1. Microstructure of the as procured Al – SiC composite material showing clusters of particles of sizes ranging 1 – 30 μm acquired with SEM (top) and optical microscope (bottom). 92
Figure 2. Typical EDX results of the particle clusters in the composite sample. 93
Figure 3. Experimental set-up for EM separation of inclusions from aluminum with water cooling. 93
Figure 4. Accumulation of larger particles in the vicinity of the crucible wall where fluid viscosity is not high enough to trap them due to the high wall temperature observed from experiment Al-EM–1. 96
Figure 5. Thick accumulation of particles at the wall of the crucible (left) and a cleaner aluminum matrix close to the center of the crucible observed from Exp. Al-EM–2. 96
Figure 6. Complete view of the cross-section of the sample from Exp. Al-EM–2 showing a thick accumulation of particles at the wall of the crucible and a cleaner aluminum matrix close to the center of the crucible.. 97
Figure 7. Optical macrographs of a horizontal cross-section of the samples. 98
Figure 8. Scanned vertical cross-sectional image close to the center of the crucible from experiment Al-EM–3 (40mm SiO_2 crucible), which was water cooled on the bottom half showing a cleaner matrix and separated particle layer in the bottom half and well distributed particles in the matrix of aluminum in the upper half. 99
Figure 9. Optical micrographic view of part of the side wall along the vertical cross-section from experiment Al-EM–3 (40mm SiO_2 crucible), which was water cooled at the bottom half of the crucible showing a cleaner matrix and a separated particle layer where cooled and a well distributed particle in the matrix of aluminum in the upper half. 99

Figure 10. Particle distribution in the metal after experiment Al-EM–4 showing the path of fluid motion during the experiment 101
Figure 11. Particle distributions showing the fluid flow paths. 102
Figure 12. Magnetic field vectors and contours of magnetic field within aluminum for the experimental set-up. 103
Figure 13. Calculated fluid contours and streamlines for the experimental set-up 105
Figure 14. Temperature and viscosity distribution within the metal for various outside wall temperatures, T_o of Al_2O_3 crucible after a time of 10 s..... 106

PAPER IV

Fig. 1—Microstructure of HCl etched Al-Mg alloy revealing dissolves matrix and partly dissolved Fe-rich intermetallic phase after 100 seconds etching time.... 114
Fig. 2—Filtration crucible fitted with filter at the bottom and schematic filtration experimental set-up. 115
Fig. 3—30 ppi uncoated Al_2O_3 CFF (a) and AlF_3 slurry coated CFF (b)..... 116
Fig. 4—Pressure drop across filter, Δp and corresponding metallostatic height, h of various pore sizes of Al_2O_3 CFFs. 119
Fig. 5—2D and 3D inclusion morphologies. 121
Fig. 6—Morphologies of double oxides. 123
Fig.7—Contribution of filtration to inclusion removal from molten aluminum. 125
Fig. 8—Morphologies of Fe-rich intermetallic phases. 126
Fig. 9—Contribution of filtration to inclusion removal from molten aluminum. 127
Fig. 10—Al_4C_3 particles, resulting from Eq.[6], in aluminum matrix after slurry coated filtration of Alloy-1 (experiment E2). 128
Fig. 11—Al_2O_3 particles resulting from reoxidation of filtered aluminum during experiments. 129
Fig. 12—Evidence of inclusions trapped within filter windows. 130
Fig. 13—Inclusions with varying size distribution trapped within filter windows after filtration (experiment E1). 131
Fig. 14—Inclusion removal through interception effect during filtration. 133
Fig.15—Calculated fluid flow velocity (m/s). 135

Fig. 16—Distribution of inclusions within the filter from the top of filter (molten aluminum entry). 136
Fig. 17—Calculated inclusion removal fraction through 3-D fluid flow simulation. 137
Fig.18—Inclusion ("mushy zone") bridge within filter window showing inclusions trapped on to the bridge (experiment E3).. 138
Fig. 19—Fe-rich inclusion bridges collecting more inclusions during use (experiment E3). 139
Fig. 20—Schematic collision between two particles in liquid: r_1 is particle radius, R_2 is neck radius and h is distance between the two attaching particles. 140
Fig. 21—Energy between two 5 µm, and 10 µm collided particles. 142
Fig. 22—Time dependence of contact angle for pure aluminum on alumina at temperature 900 ^{o}C to 1250 ^{o}C. 143
Fig. 23—EPMA map of elements present within filter window with metal matrix in between (AlF_3 slurry coated filtration of alloy 2 – E3). 146
Fig. 24—Removal efficiency of [*Ca*] by coated filter plotted against residence time of molten aluminum in filter. 147
Fig. 25—Removal efficiency of [*Mg*] by coated filter plotted against residence time of molten aluminum for various pore sizes. 148
Fig. 26—Future filtration design concepts. 149

PAPER V

Fig.1. Schematic of AlF_3 CFF slip casting in a rectangular mold.. 162
Fig. 2. Schematic diagram of the experiment setup used for HF gas coating process.... 164
Fig. 3. Images of uncoated Al_2O_3 CFF (a) and AlF_3 slurry coated (b) and HF gas coated (c) CFF as taken with a scanner (30ppi). 166
Fig. 4. Comparison between (a) HF gas coated filter and (b) slurry coated filter in the distribution of fluoride in filter walls. 167
Fig. 5. Microstructure of various filters 169
Fig. 6. Compositions of various elements detected in the filters after the various experiments.. 169
Fig. 7. Dependence of fluoride yield in the filter on the HF gas pressure.. 170
Fig. 8. EPMA mapping of elements in uncoated filter. 171

Fig. 9. Mapping of elements in filter after coating experiment. 173
Fig. 10. XRD results of slurry aluminum fluoride coated alumina CFF. 176
Fig. 11. XRD spectra of AlF_3 coated filter by HF gas method in experiment. 177
Fig. 12. Elemental maps of HF coated filter from experiment 6. 179
Fig.13. Schematic of the concentration profile of [*M*] at the filter molten aluminum interface..... 181
Fig. 14. The effect of various parameters including filter pore size, mass transfer coefficient, and time on removal efficiency of a coated filter for dissolved [*Ca*] 184
Fig. 15. Filtration results after the use of AlF_3 slurry coated Al_2O_3 CFF. It shows solidified aluminum within the filter and reaction products between the AlF_3 coating and dissolved [Na] and [Mg]. 185
Fig. 16. EPMA maps of elements on granular bed filter after aluminum filtration..... 186

LIST OF TABLES

Page

Table 1.1. Typical Inclusions and their characteristics in aluminum and morphologies of nonmetallic inclusions in top-cut silicon. 5

PAPER I

Table 1 Experimental plan and actual separation parameters. 22

Table 2 Data of materials properties used in the calculations. 30

PAPER II

Table 1 Experimental scheme used for the EM sedimentation experiments 59

Table 2 Summary of the experimental plan used in this study. 60

Table 3 Data of materials properties used in the calculations. 64

Table 4 Comparison of densities of molten silicon and inclusions. 65

PAPER III

Table I Experimental materials and condition. 94

Table II Material properties for the crucible and aluminum. 106

PAPER IV

Table I. Experimental samples used in inclusions observation. 113

Table II. Filtration experiments parameters. 116

Table III. Data for various CFF pore sizes adopted from reference. 118

Table IV. Removal of inclusions by CFF from molten aluminum. 130

Table V. Interfacial properties in liquid aluminum – inclusion systems at 850 ^{o}C. 141

Table VI. Elemental composition before and after filtration GDMS (in ppm). 144

PAPER V

Table 1 Experimental conditions. 165

Table 2 Data for various CFF pore sizes adopted from Ref. [34] 183

1. INTRODUCTION

1.1. OVERVIEW

Both demand and high prices of high quality metals and alloys have motivated efforts at finding effective ways to refine and remove contaminants. Impurities in metals may be in the form of dissolved metals, gases, or inclusions which may be nonmetallic or intermetallic in nature. Inclusions have detrimental effects on both the service and processing properties of metals. For instance, the presence of microscopic inclusions, in the order of 10 – 50 μm in size in aluminum alloys can lead to reduced fluidity of the molten metal, poor surface finish, increased internal porosity, spots of high hardness which cause poor machinability, nucleation sites for fatigue cracks and a tendency to increase corrosion. Nonmetallic inclusions act as stress-raisers, and can cause premature failure of components. Moreover, the main limiting factor to effective degassing of molten aluminum is the interaction between inclusions and dissolved hydrogen [1]. In solar grade silicon (SoG-Si) the detrimental effect of metallic impurities is intensified by the presence of nonmetallic inclusions which act as segregation sites. For instance, in a study of SiC particles in ribbon grown silicon, it was concluded that the effect of SiC on the solar cell characteristics resulted in impurity accumulation.[2] The conversion efficiency of solar cells is limited by minority carrier recombination at dislocations and intra-granular defects such as impurities, small clusters of atoms, or precipitates [3]. Therefore effort at refining metals of such impurities should be of significant importance to manufacturers, consumers, researchers and other stake holders of these materials.

Several methods exist for the removal of impurities from aluminum and silicon. Methods such as flotation, sedimentation, centrifugal separation, filtration, and electromagnetic separation have been proposed [4-8] and some are being used in industry for the removal of nonmetallic inclusions from aluminum. For silicon, methods such as fractional melting, plasma refining, sedimentation and filtration are being employed. Filtration requires simple equipment and the least capital investment among the options. However, it is limited by its low efficiencies for the removal of inclusions smaller in size than 10 μm, and in the case of silicon, the filter material may contaminate the melt. Understanding the separation technologies is key to achieving higher efficiencies with

these processes and further improving the process. Therefore, there is a critical need to explore some of the methods for the purification of aluminum and silicon, and break new ground in the purification technology of these metals.

1.2. THEORETICAL CONCEPTS INVOLVED IN THE SEPARATION PROCESSES

1.2.1. Filtration. This separation process involves the removal of solid contaminants in liquids by flowing through a filter medium. In metals filtration, the removal mechanism is controlled by several mechanical and physical processes. Mechanical processes control the removal of particles with sizes larger than the filter pore size, as in sieving, or sieving of approaching large size particles by a particle layer on top of the filter in the process called cake filtration. However, the major mechanism of particle separation from metals through filtration is in the depth mode, where particles smaller in size than the filter pore size, are removed. In this mode, particle separation is controlled by many physical forces including gravity (leading to sedimentation and flotation), surface energy, collisions and interception, diffusion Brownian motion, inertia effects, and turbulent deposition.

1.2.2. Electromagnetic Separation. The principle of this separation technology is based on the difference in electrical conductivity between a dispersed phase and the dispersant. When an electromagnetic field is applied to an electrically conductive melt containing less- or non-electrically conductive particles, such as nonmetallic inclusions, a pressure gradient is generated by the electromagnetic (EM) field in the melt, which causes an inclusion in the melt to be influenced by the pressure gradient or volume force ("buoyancy") of the molten metal. In principle, the Lorenz force induced by the EM field will force the electrically conductive molten metal to move toward the center region and the non-metallic particles to be pushed to the boundary by the EM force acting on particles also known as EM Archimedes force [1]. The principle of EM separation of particles from liquids was first proposed by Kolin in 1953 [9], and by Leenov and Kolin in 1954 [10].

Associated with the alternating current magnetic field is the induction of fluid flow in the melt which makes important contributions to the separation process:

- Carrying particles to the side walls of the container to be trapped by the EM Archimedes force.
- Depositing particles at less convective regions of the system.
- Increased convection leading to enhanced settling rates

1.3. SCOPE OF STUDY

This study is focused on the removal of nonmetallic inclusions from aluminum through filtration and the separation of inclusions from both aluminum and silicon via the application of an electromagnetic field. These materials and methods were chosen for their strategic importance.

Due to aluminum's high strength to weight ratio, corrosion resistance, ease of formability and versatility in its application in the automobile, construction, communication, packaging and energy industries, aluminum alloys have seen significant increase in production. In addition, silicon has a wide variety of applications including use as an alloying element and deoxidizer (metallurgical grade), solar cells (solar grade silicon), and semiconductors (electronic grade silicon). The critical nature of these applications requires that clean and affordable materials are available for use. Thus more effort is required to develop technologies and improve existing ones through research for product quality improvement, production waste minimization and to enhance waste material recycling to assure sustainability. Due to the economic and environmental costs associated with the production of these materials, more efforts at recycling them in secondary processes are needed. However, the greatest impediment to successful recycling is the presence of contaminants. In the production of solar silicon, it is estimated that over 68% of the silicon feedstock that enters the production chain is lost during the different production stages in one form or another.[11] This is made up of approximately 30% lost to top-cut and shaping of ingot into block, 34% lost to wire sawing slurries and 4% loss as broken wafers, which is partly contaminated.

1.4. INCLUSIONS IN SILICON

Impurities in SoG-Si are metallic and nonmetallic in nature. Nonmetallic inclusions are mainly SiC and Si_3N_4 particles.[12] The detrimental effect of metallic impurities on the conversion efficiency of silicon PV cells is made worse by the presence

of nonmetallic inclusions as they act as sites for their segregation. Si_3N_4 particles are from the coating material at the inner surface of the silica crucible and from air absorption during the solidification process. SiC particles are mainly from the carbothermal reduction process during primary production [13] and graphite rich materials used during SoG-Si processing [14]. Figure 1.1 shows the typical composition of inclusions and their characteristic morphologies in silicon. SiC particles are lumpy with sizes ranging from a few micrometers to 500 μm, while Si_3N_4 particles are rod-like with diameter ranging 10 – 200 μm and up to several millimeters long. They may also appear in clusters of their characteristic morphologies.

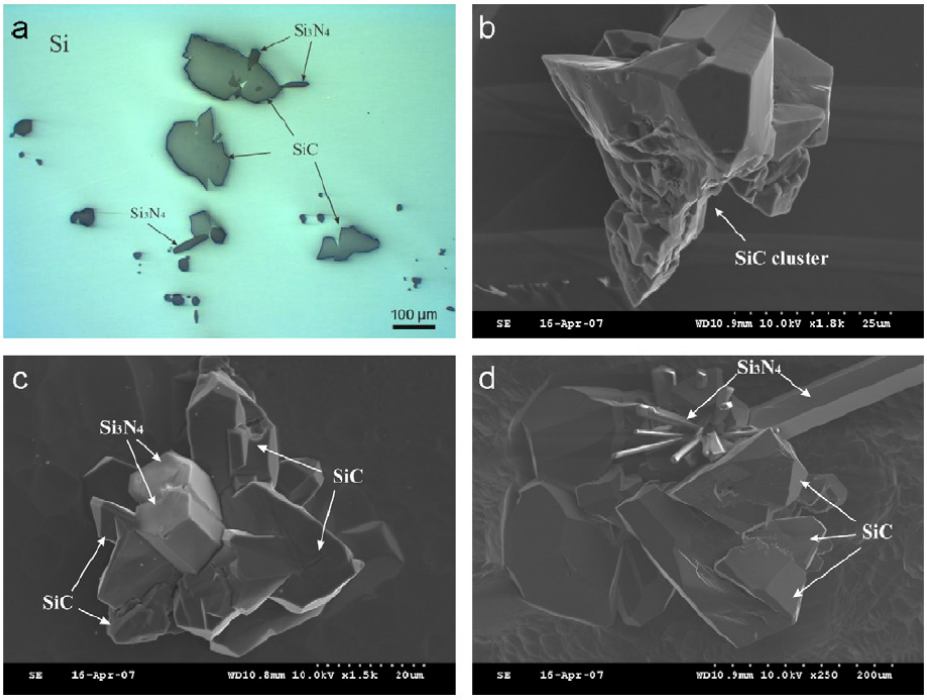

Figure 1.1. Typical composition and morphologies of nonmetallic inclusions in top-cut silicon. The SiC particles are lumpy and clustered while Si_3N_4 particles are rod-like. [15]

1.5. INCLUSIONS IN ALUMINUM

Nonmetallic inclusions have long been recognized as a problem to aluminum alloys. The literature [16] summarizes the detrimental effects of inclusions in aluminum. The size, shape, type, and distribution of nonmetallic inclusions in a finished metal

product are important parameters to aluminum foundry metallurgists [17]. Inclusions may be indigenous or exogenous. Indigenous inclusions exist primarily as alumina, MgO and spinel, which result from the oxidation of molten aluminum and aluminum containing magnesium melts. Another indigenous example is titanium diboride, which originates principally from grain refiners added to the melt prior to casting [18]. Exogenous inclusions include refractory particles, such as alumina, silica, silicon carbide, etc., which are picked up by the molten aluminum as a result of wear and erosion of the lining materials in the vessel used for melting and molten metal transfer. The observed particle size in molten aluminum varies between inclusion dispersoids of less than a micron in diameter to oxide skins of several millimeters (Table 1.1) [19-22], with a variety of morphologies reported in the literature [23-24] (see Figure 1.2).

Table 1.1. Typical Inclusions and their characteristics in aluminum and morphologies of nonmetallic inclusions in top-cut silicon. [19-22]

Inclusion Type	**Morphologies**	**Density (g/cm^3)**	**Dimensions (μm)**
Al_2O_3	Particles, films	3.97	0.2-30, 10-5000
MgO	Particles, films	3.58	0.1-5, 10-5000
Mg Al_2O_4	Particles, films	3.6	0.1-5, 10-5000
Salts chlorides, fluorides	Particles	1.98-2.16	0.1-5
Al_4C_3	Particles	2.36	0.5-25
AlN	Particles, films	3.26	10-50
TiB_2	Particles, agglomerates	4.5	1-30
AlB_2	Particles, agglomerates	3.19	0.1-3

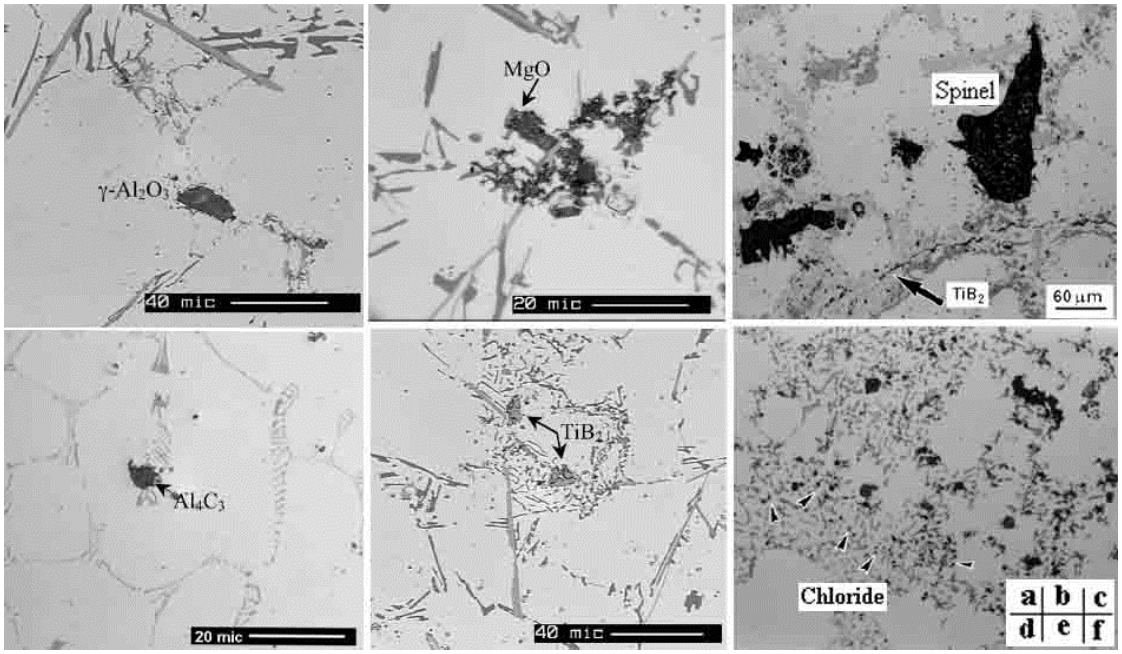

Figure 1.2. Typical inclusions commonly found in aluminum (a)γ-Al_2O_3 [24], (b)MgO [24], (c) $MgAl_2O_4$ [23], (d)Al_4C_3 [24], (e) TiB_2 [24], and (f) potential chloride particles [23]

1.6. RESEARCH OBJECTIVES

The objects of this study are to:

1). Investigate the mechanism of purification of aluminum through ceramic foam filtration in the depth mode.

2). Investigate the feasibility of coating an Al_2O_3 ceramic foam filter (CFF) with AlF_3 for the removal of dissolved impurity elements through filtration.

3). Explore the feasibility of the removal of inclusions from silicon using an electromagnetic field.

4). Investigate the use of a high frequency electromagnetic field for the removal of inclusions from aluminum.

1.7. METHODOLOGY

To achieve the stated objectives, three broad sets of experiments were designed: filtration of aluminum, coating of Al_2O_3 CFF with AlF_3 and electromagnetic separation of inclusions from aluminum and silicon.

- For the aluminum filtration research, an aluminum alloy containing nonmetallic inclusions was put in a graphite crucible fitted with a 30 ppi ceramic foam filter (CFF) and inductively heated. The molten metal flowed through the CFF and the filtrate was collected. Samples were taken from the metal before and after filtration and the filter bearing solidified metal, which were analyzed via optical microscopy, SEM/EDX, Electron Probe Microanalysis (EPMA) and Glow Discharge Mass Spectrometry (GDMS). Three dimensional, 3D FLUENT CFD modeling was undertaken to further understand the filtration process.
- To coat a conventional 30 ppi Al_2O_3 CFF with AlF_3, an experiment was designed based on a reaction between either NaF or CaF_2 and H_2SO_4 to generate anhydrous HF gas, which was fed in a nitrogen carrier gas to react with the filter in a quartz tube furnace. The effect of the HF gas pressure on the coating process was studied by varying the concentrations of the reactants involved in generating the HF gas. Effluent and excess HF gas from the coating reactant was channeled through a 5.3 L, 15 M NaOH solution to remove the HF before discharging to the atmosphere. Samples of the filter before and after coating were characterized using SEM/EDX, X-Ray Diffraction (XRD) and EPMA.
- The electromagnetic separation experiments focused on inclusion separation from aluminum and silicon. Aluminum – 15 wt% SiC particulate composite with an average particle size of 10 μm was used to study EM inclusion separation from aluminum. Silicon containing SiC particles was the material employed in the experiments to separate inclusions from silicon. An approach to settling nonmetallic inclusions in silicon under EM field was designed and studied. The metal, containing the particles to be separated was put in a crucible and inductively melted. The electromagnetic separation parameters were set after melting and the particles allowed to be influenced under the magnetic field for a time period. The electromagnetic field application is discontinued and the sample

allowed to cool down to room temperature. Samples from these experiments were analyzed with an optical microscope and SEM/EDX. Magnetic and 2D ANSYS Fluent CFD simulations were made to understand the separation process.

1.8. SUMMARY OF RESULTS

Detailed results from this research are included in subsequent chapters of this dissertation which is made up of five (5) manuscripts. The following is a summary of the results in the various manuscripts.

- Paper I (Chapter 2) reports on the study of high frequency separation of inclusions from silicon and indicates that strong fluid flow induced by the high frequency magnetic field is the main contributor to the removal of particles from this melt. Thus particles carried by the flow ended up either at the bottom due to enhanced gravity separation by the fluid flow and EM body force or at the wall due to the confining effect of skin depth on the EM Archimedes force or mainly at the top due to the effect of circulatory flow. The separation efficiency was enhanced by longer separation times. However, prolonged separation times could lead to overheating and a less viscous melt resulting from the associated joule effect of the EM field, which could reduce the contribution of viscous forces to the separation process. Increasing the coil current and the frequency increased significantly the separation efficiency due to stronger induced circulatory fluid flow and electromagnetic body force in the fluid. Particle separation of over 95 % was recorded. The results showed excellent separation even for particles smaller than 3 μm.
- Paper II (Chapter 3) reports on a study of particle settling in silicon under an AC EM field. The results showed that, unlike natural settling of inclusions by gravitational force which is a slow and unattractive process, settling under an EM field is fast and effective. The mechanisms by which particles settled are proposed as (1) enhanced convection due to EM induced fluid flow, leading to higher Reynold's numbers, particle collision and agglomeration, and thus enhanced gravity separation; and (2) the contribution of magnetization force due to the difference in magnetic susceptibility of the inclusions and the melt in the presence of local magnetic field gradient, although this effect is minimal because of a weak gradient

magnetic field. The results showed that the settling rate is much faster when the coil current and frequency are increased.

- Paper III (Chapter 4) summarized separation of inclusions from aluminum by an electromagnetic field. The study showed that without maintaining the temperature of the separator wall below the melting point of the metal to introduce high viscous forces near the wall, high frequency inclusions separation in aluminum is ineffective. This is due to the strong recirculatory fluid flow which carried the small particles within the flow eddies rather than separating. When this condition is satisfied, particle separation occurs as a result of the induced secondary fluid flow carrying these particles from the bulk of the melt to the vicinity of the wall where the EM Archimedes force is concentrated in the presence of strong viscous forces to trap the particles. Increasing coil current and the frequency of the field enhanced penetration of the induced fluid flow into the melt thus enhancing the separation process.
- Paper IV (Chapter 5) reported on filtration experiments using both AlF_3 slurry coated, and uncoated Al_2O_3 CFF. Filtration efficiency of up to 85% was recorded for the 30 ppi filter and the removal efficiency was reduced with higher flow rates. Two mechanisms contributing broadly to the removal of nonmetallic inclusions in the deep bed filtration mode were proposed: (1) collision with walls and interception effect; and (2) the formation of both intermetallic and nonmetallic inclusion bridges during filtration. CFD modeling of the process showed that most inclusions, especially those with larger sizes, were entrapped at the upper part of the filter while smaller inclusions dispersed well throughout the filter, which confirmed the experimental observation. Alkaline earth metal impurities were removed up to 86 % by the AlF_3 slurry coated filter. This is reported in paper 3.
- Paper V (Chapter 6) reports preliminary results of the coating experiments and showed that it is possible to coat Al_2O_3 filters with AlF_3 by reacting it with HF gas which is the product of the reaction between NaF or CaF_2 and H_2SO_4. The yield of AlF_3 in the filter had a linear dependence on the HF gas pressure. It increased with increasing HF gas pressure. The results showed that both NaF and CaF_2 could end up in the filter, an undesirable outcome.

REFERENCES

1. Sun, Bao-de, Wen-jiang Ding, Da Shu and Yao-he Zhou, *Purification technology of molten aluminium.* J. CENT. SOUTH UNIV. TECHNOL, 11(2) 2004, 134-141.

2. Rao, C. V. Hari, H. E. Bates and K. V. Ravi, *Electrical effects of SiC inclusions in EFG silicon ribbon solar cells.* J. Appl. Phys., 47 1976, 2614 -2619.

3. MoÈller, H. J., L. Long, M. Werner and D. Yang, *Oxygen and carbon precipitation in multicrystalline solar silicon.* Phys. Status Solidi A, 171 1999, 175-189.

4. Damoah, Lucas N. W. and Lifeng Zhang, *Removal of inclusions from aluminum through filtration.* Metallurgical and Materials Transactions B, 41B 2010, 886-907.

5. Makarov, Sergey, Reinhold Ludwig and Diran Apelian, *Electromagnetic Separation Techniques in Metal Casting. I. Conventional Methods.* IEEE TRANSACTIONS ON MAGNETICS, 36(4) 2000, 2015-2021.

6. Zhang, Lifeng, Arjan Ciftja and Lucas Damoah. *Removal of non-metallic inclusions from molten aluminum*. in *Proceedings of EMC*. 2007, 1413-1428.

7. Fernandes, M., J. C. Pires, N. Cheung and A. Garcia, *Investigation of the chemical composition of nonmetallic inclusions utilizing ternary phase diagrams.* Mater. Char., 49 2003, 437-443.

8. Zhou, M, D. Shu, K. Li, W. Zhang, B. Sun, J. Wang and H. Ni, *Performance improvement of industrial pure aluminum treated by stirring molten fluxes.* Mater. Sci. Eng. A, 347 2003, 280-290.

9. Kolin, A., *An electromagnetokinetic phenomenon involving migration of neutral particles.* Science, 117(2) 1953, 134-137.

10. Leenov, D. and A. Kolin, *Theory of electromagnetophoresis. I. Magnetohydrodynamic forces experienced by spherical and symmetrically oriented cylindrical particles.* J. Chem. Phys., 22(4) 1954, 683-688.

11. Sarti, Dominique and Roland Einhaus, *Silicon feedstock for the multi-crystalline photovoltaic industry.* Solar Energy Materials and Solar Cells, 72(1-4) 2002, 27-40.

12. Søiland, A.K., E.J. Øvrelid, T.A. Engh, O. Lohne, J.K. Tuset and Ø. Gjerstad, *SiC and Si_3N_4 inclusions in multicrystalline silicon ingots.* Materials Science in Semiconductor Processing, 7 2004, 39-43.

13. Zhang, Lifeng, Eivind Øvrelid, Samuel Senanu, Benjamin Agyei-Tuffour and Adegboyega Nathaniel Femi. *Nonmetallic Inclusions in Solar Cell Silicon: Focusing on Recycling of Scraps*. in *Rewas2008: 2008 Global Symposium on Recycling, Waste Treatment and Clean Technology*. 2008, TMS, Warrendale, PA, USA, CANCUN, MEXICO, 1011-1026.

14. Ceccaroli, Bruno and Otto Lohne, eds. *Solar Grade Silicon Feedstock*. Handbook of Photovoltaic Science and Engineering, ed. A. Luque and S. Hegedus. 2011, John Wiley & Sons, Ltd.

15. Zhang, Lifeng and Arjan Ciftja, *Recycling of solar cell silicon scraps through filtration, Part I: Experimental investigation.* Solar Energy Materials and Solar Cells, 92(11) 2008, 1450-1461.

16. Prebble, Jonathan, *Improving Performance in the Filtration Process.* Pyrotek Supplement, http://www.pyrotek.info/section.asp?id=105.

17. Fei, Ming, Reinhold Ludwig, Sumanth Shankar and Diran Apelian, *Electromagnetic detection and infrared visualizaiton techniques for non-metallic inclusions on molten aluminum.* Review of Quantitative Nondestructure Evaluation, 21 2002, 1719-171726.

18. Towsey, Nicholas, Wolfgang Schneider, Hans-Peter Krug, Angela Hardman and Neil J Keegan. *The Influence of Grain Refiners on the efficiency of Ceramic Foam Filters*. in *Light Metals*. 2001, 973-977.

19. Eckert, C.E., R.E. Miller, D. Apelian and R. Mutharasan. *Molten aluminum filtration: fundametals and models*. in *Light Metals*. 1984, 1281-1304.

20. Conti, C. and P. Netter, *Deep filtration of liquid metals: application of a simplified model based on the limiting trajectory method.* Sep. Technol., 2 1992, 46-56.

21. Gauckler, L. J., M. M. Waeber, C. Conti and M. Jacob-Duliere. *Industrial Application of Open Pore Ceramic Foam for Molten Metal Filtration*. in *Light Metals*. 1985, 1261-1283.

22. Yuan, Qingbo, Xinhua Liu, Yunbo Zhong and Zhongming Ren, *Experimental research on purification of molten aluminum through electromagnetic field.* Yunnan Metallurgy, 32,Supplementary 2003, 106-108.

23. Liu, L and F. H Samuel, *Assessment of melt cleanliness in A356.2 aluminium casting alloy using the porous disc filtration apparatus technique: Part I Inclusion measurements* Journal of Materials Science, 32 1997, 5907-5925.

24. Khalifa, W., F. H. Samuel and J. E. Gruzleski, *Nucleation of solid aluminum on inclusion particles injected into Al-Si-Fe alloys.* Metall. & Mater. Trans. A, 35A(10) 2004, 3233-3250.

I. HIGH FREQUENCY ELECTROMAGNETIC PURIFICATION OF SILICON

Lucas Nana Wiredu Damoah, Lifeng Zhang, Kent D. Peaslee

Department of Materials Science & Engineering
Missouri University of Science and Technology (Missouri S&T)
223 McNutt Hall, Rolla, MO 65409-0340, USA
Email: zhanglife@mst.edu

This manuscript has been prepared for submission to Solar Energy Materials and Solar Cells

Abstract

The effect of a high frequency electromagnetic field on the removal of nonmetallic inclusions from molten silicon was investigated. Inclusion separation efficiencies of up to 99 % were reached. The separation efficiency was independent of the particle concentration in the melt and increased significantly with increases in the frequency, separation time and coil current. Particles were separated from the silicon matrix and relocated to the top, bottom and side walls of the crucible due to the effect of three mechanisms, induced secondary fluid flow which carried particles from the bulk of the melt, electromagnetic Archimedes force which worked in the skin depth area to trap particles on the side wall and the magnetization force due to the magnetic field gradient, which promoted the settling of particles to the bottom of the crucible. Higher coil current enhanced the strength of the magnetic field which enhanced fluid flow while higher frequency also improved the fluid flow, and the effect of current was more pronounced leading to better particle separation.

1. Introduction

Recent global developments in the energy sector with a drive for the production of clean, reliable, and affordable energy have stirred a rapid growth in the production of photovoltaic (PV) cells [1]. This has led to growth in silicon based PV cells which control over 90 % of the PV market share [2] either as single-crystalline silicon, or multi-crystalline silicon (MC-Si), or amorphous silicon [3]. MC-Si produced by directional solidification of solar grade silicon melt dominates the silicon PV market.

During the directional solidification process, SiC and Si_3N_4 particles within the molten silicon are pushed by the solidification front to the top of the ingot which is the last to solidify. Therefore the top of the ingot is cut generating what is known as top-cut solar silicon scrap. The Si_3N_4 particles are mainly from the coating material on the inside surface of the silica crucible and from the air absorption during the solidification process. The SiC particles mainly stem from the carbon reduction process during the primary production of silicon [4]. For sustainability, the silicon in the top-cut silicon scrap must be recovered. Therefore methods for removing non-metallic particles, such as SiC and

Si_3N_4, from the silicon are important in order to recycle top-cut silicon scrap to a useful feedstock for silicon solar cells manufacturing.

Methods such as sedimentation, filtration, fractional melting, plasma refining and electromagnetic separation hold the potential to purify SoG-Si. Although the density of SiC and Si_3N_4 particles are higher than the silicon melt, the sedimentation process poses an industrial implementation challenge since the natural sedimentation requires long periods of time [5-6]. Fishman [5-6] reported that during the sedimentation process, natural convection generates a recirculating flow pattern transporting particles to the top and directional solidification pushes the particles into the solidifying liquid at the top.. However, these complications might be reduced by performing the sedimentation process in a different furnace than directional solidification. Furthermore, it is also well known that the settling velocity of particles is enhanced in convective melts, except for excessive flow velocities that may result in back diffusion of already settled particles [7]. Any method that could enhance the particle sedimentation velocity will be advantageous. Filtration using ceramic foam filters to remove SiC and Si_3N_4 inclusions has been investigated by Zhang *et al* [4, 8] with reported filtration efficiencies of over 97% for inclusions >10 μm in size. However, the filtration process also poses certain industrial implementation questions regarding the design of a continuous process, and selection of filter materials that will prevent contamination of the molten silicon. Zhang *et al* [8] showed that the filtration process was effective at removing most of the large inclusions but was less effective at removing inclusions smaller than 10 μm which are still very detrimental to the properties of silicon solar cells.

Electromagnetic (EM) removal of nonmetallic particles from silicon has yet to be well explored although it has been studied for inclusion removal from other metals such as aluminum and steel since Kolin in 1953 [9], and later by Leenov and Kolin in 1954 [10] proposed the principle. It can introduce magnetic pressure in the melt which has the potential to remove inclusions of all size ranges and could also induce fluid flow that may help to remove particles by settling. Others have applied a gradient magnetic field to the melt to induce magnetization forces that may cause inclusions to rise or settle in the melt [11-14]. Electromagnetic separation uses the difference in the electrical conductivity between the inclusions and the melt and thus, when a uniform EM field is applied to a

molten metal, the metal is compressed by the EM force (Lorentz force) and a pressure gradient is generated in the metal. The non-conductive particles or less conductive particles are forced to move in the opposite direction of EM force, thereby getting separated from the melt [15-16]. Some feasibility studies on the use of a high frequency alternating current (AC) electromagnetic field to remove suspended particles from silicon has been studied and reported by the authors [17-19]. The current study investigates the subject further and discusses new results on the effect of processing parameters such as time, coil current, and frequency on the removal of inclusions from silicon under a high frequency AC electromagnetic field. Inclusion separation mechanisms under the AC magnetic field are also presented.

2. Materials and Methods

2.1. Materials

Following successful trials of this current method of particle separation from silicon with top-cut solar silicon scrap material, and another with a mixture of silicon and SiC particles of difference volume fractions, a new Si – SiC composite material with uniform particle dispersion was desire for parametric investigation. The results of the trial experiments have been published in two international conferences. Top-cut SoG-Si scrap has particles concentrated on one of the sides and a mixture of solid silicon and SiC particles did not assure uniform particle dispersion. This material was prepared by a stir-solidification method in which metallurgical grade silicon and Al – 15 % SiC composite material were melted at 1500 ^{o}C and continuously stirred until it solidified under argon gas. The stir-solidification process was undertaken through the following steps:

- Approximately 80 wt% of metallurgical grade silicon and 20 wt% Al–15 % SiC composite material were melted at 1500^{o}C in a fused silica crucible in an induction furnace in an argon gas atmosphere.
- After melting, the furnace was turn off and the molten material was stirred continuously with a mullite rod until it solidified
- The solidified material was allowed to furnace cool to room temperature in the argon gas atmosphere.

- The resulting material was removed from the furnace and sectioned into appropriate sizes to be used in the subsequent particle separation experiments.

Typical microstructures of the materials are shown in Fig. 1 to summarize the Si - SiC composite making process. During cooling after the stir-solicitation process, some of the aluminum (approximately 10 wt%) precipitated in the eutectic composition with the silicon to the top of the material (see microstructure in Fig. 2). This region contained no particles, making the stir-solidification process a good method to produce eutectic Al-Si alloys from metallurgical grade silicon and waste Al-SiC composites, if it ever becomes necessary. The particle-free eutectic composition was separated from the composite materials by removing with the hand or breaking with a hammer where necessary.

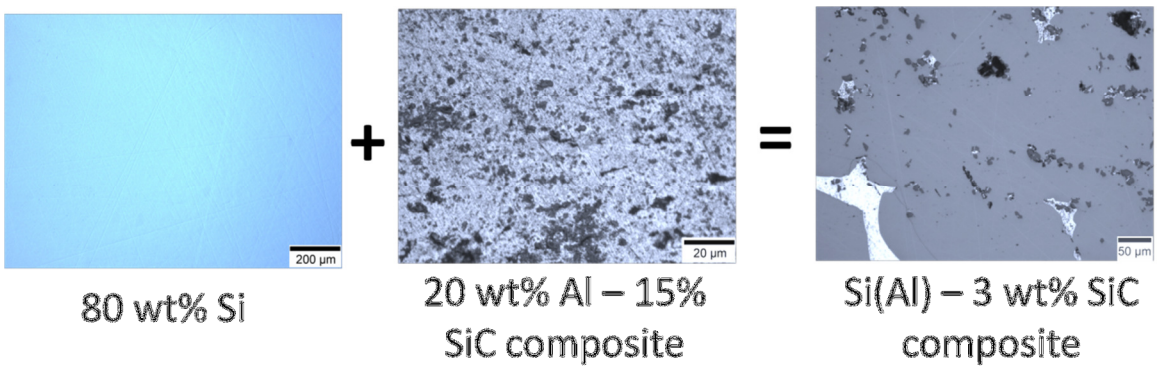

Fig. 1. Microstructure of Si (Al) – 3 % SiC composite material made from metallurgical silicon and Al - 15 % SiC composite through the stir-solidification process.

The type and size of inclusions in the Si – SiC composite material were determined using an SEM with automated feature analysis capability (ASPEX) as shown in Fig. 3. The mean sizes shown are for particles larger than 3 µm. There, were however, a large number of particles smaller than 3 µm which when included in the distribution resulted in an overall average particle size of 5±5 µm with an average area fraction of 11±5% particles. The SiO_2 could have resulted from surface oxidation of SiC particles, as the typical EDX composition showed traces of carbon.

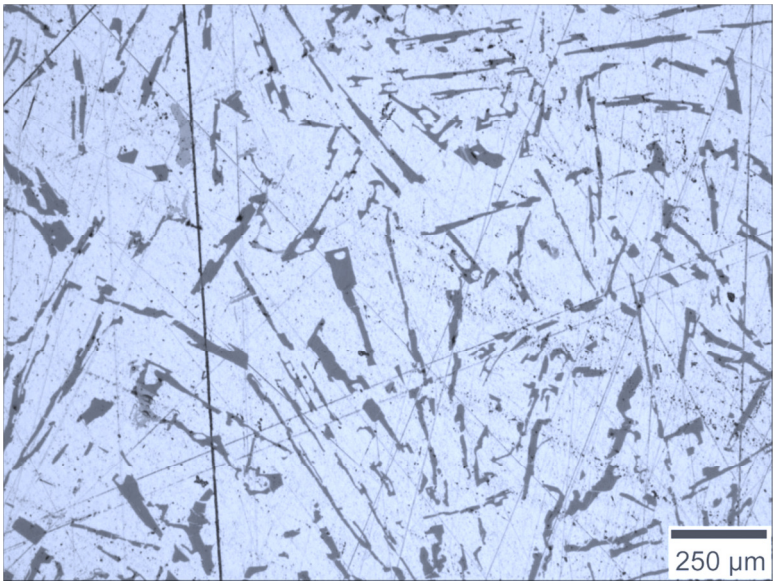

Fig. 2. Typical microstructure of the aluminum dominant Al-Si eutectic structure of the material that precipitated on top of the solidified Si (Al) – SiC composite material during the stir – solidification process.

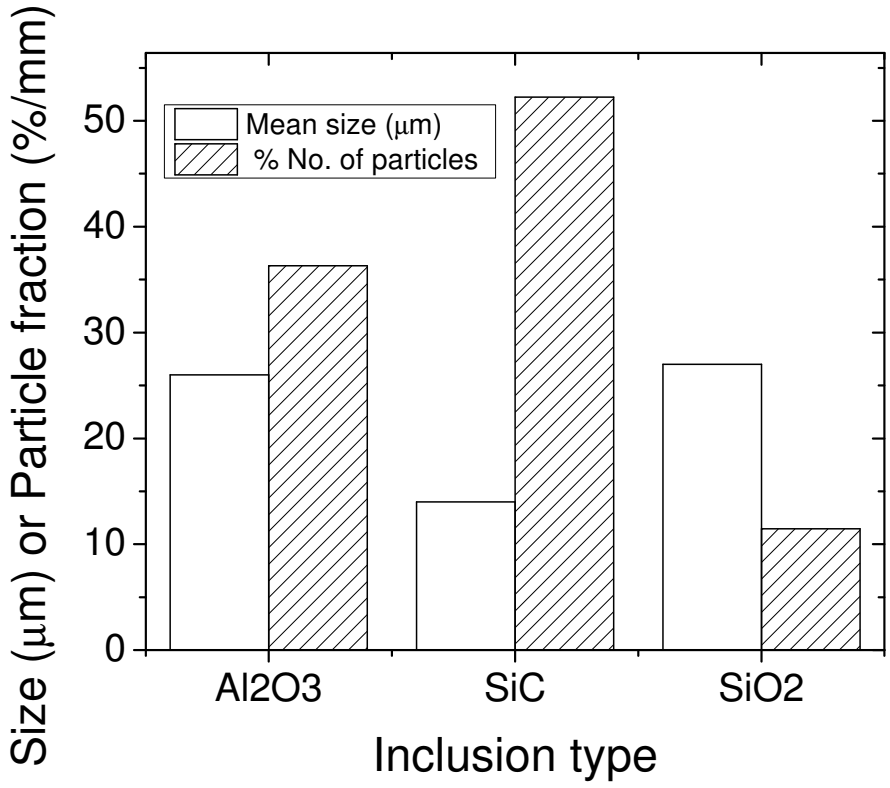

Fig. 3. Type and average size of inclusions in the Si – SiC composite material.

2.2. Equipment and Experimental Set-up

The experimental equipment is made of a water cooled copper induction coil of 7 turns, 196 mm high and 150 mm inner diameter. The copper tubing has a 14 mm by 14 mm square cross-section and 12 mm adjacent turn spacing. The coil was powered by a 100 kW generator with a capacitor bank and the capability to change frequency within the range 50-200 kHz by changing the capacitance within the circuit. The power supply is also equipped with a LCD touch screen panel where power input can be made and the current, voltage, frequency and power information were recorded during the experiment. The set-up included a graphite susceptor and a crucible. Figure 4 shows a picture of the experimental equipment and Figure 5 shows the schematics of the experimental set-up.

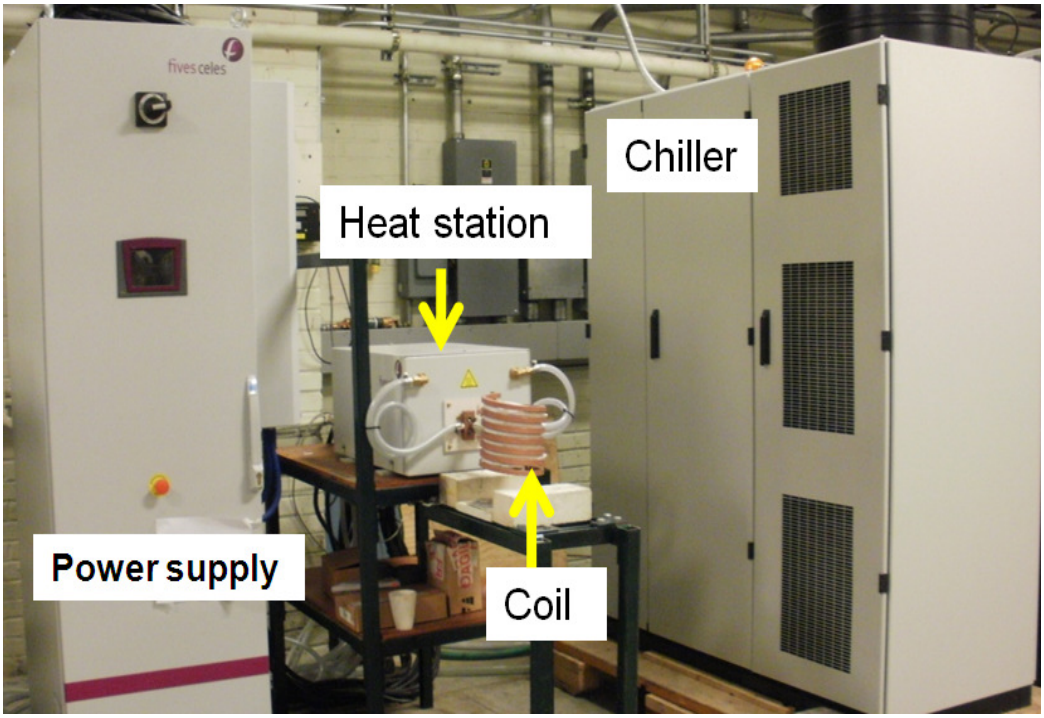

Fig. 4. Picture of the equipment showing the coil – power supply system.

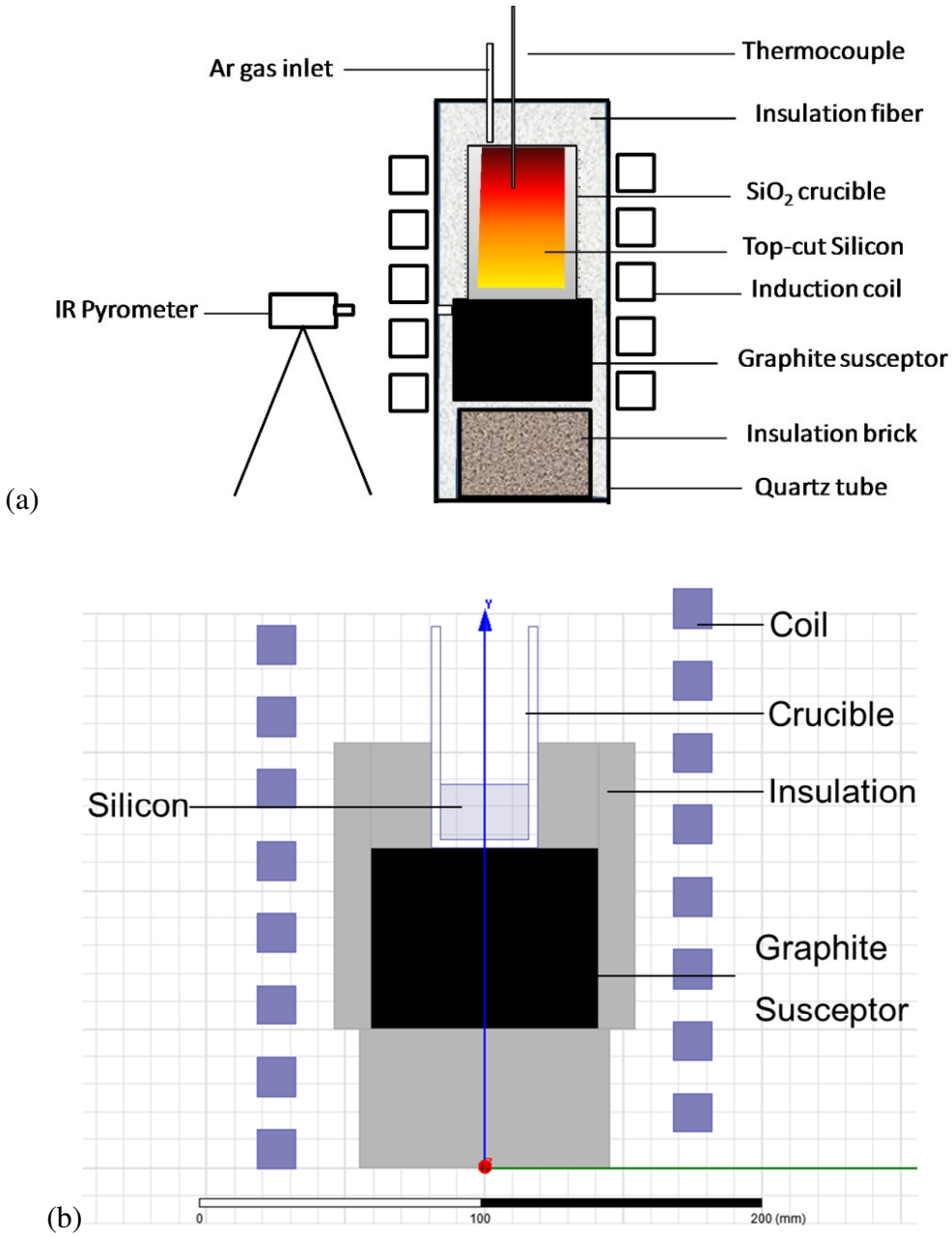

Fig. 5. Schematic of the experimental set-up for the electromagnetic separation of particles from silicon (a) complete set-up and (b) scaled schematic of relevant components.

2.3. Experimental procedure for Settling of Inclusions in Si(Al) – SiC Composite

The Si(Al) – SiC composite material prepared by the stir-solidification process was cut into pieces of approximately 54 g mean size for this study. Table 1 summarizes the experimental plan used in this study. The experiment followed three main steps:

- *Melting*: The composite material was placed in the crucible set in place within the coil. The power supply was turned and the sample monitored until melting. The melting duration was predetermined in a series of trials as 16 minutes at a coil current of 230A before particle separation. So all samples were melted under the same coil current for 16 minutes before separation. The heating process followed the rate described in Fig. 6. The temperature was measured by means of a calibrated infrared pyrometer which was positioned 1 m away from the coil. After the melting time elapsed, the power supply was turned off.
- *Particle separation*: The separation conditions of frequency and coil current were set immediately after turning of the power supply following sample melting. The power supply was turn back on and the duration of separation recorded with a stop watch. When the desired separation time was attained the power supply was switched off.
- *Still air cooling*: after particle separation, the sample was cooled to ambient temperature in still air.

The cooled sample was then sectioned vertically to form four quarter sections as illustrated in Fig. 7. A quarter vertical cross-sectional sample was polished for each experiment and analyzed by means of optical macro- and micro-scopes and SEM/EDX.

The effect of the quantity of material under purification of the separation process was investigated by separating 120 g of material made of approximately 96 g of metallurgical grade silicon and 24 g of Al – 15% SiC composite in an *in situ* dispersion process. These experiments are named CB 1 – 3 in Table 1. In these experiments silicon was first melted at 230 A and 65 kHz following the procedure described above. The power supply is turned off after melting and then a piece of Al – 15 % SiC composite material with a known weight was put into the molten silicon. The molten silicon was mechanically stirred continuously with alumina rod for the aluminum composite material to dissolve and disperse in the molten silicon at a temperature of approximately 1500 ^{o}C. Separation was done at coil current of 350 A for 30 s, 60 s, and 90 s separation durations. After the experiments, samples were sectioned vertically and observed for the distribution of particles by means of an optical macroscopy.

Table 1 Experimental plan and actual separation parameters.

Exp. #	Material Si(Al)-SiC (g)	Capacitance, C (#) and μF	Parameters				Separation Time (s)	Coil current, (A) $I_{rms} = 2\pi fCV$
			I, A	V, V	f, kHz	P, kWt		
C10-1	56.0468	(4) 2.64	17.6	262	64	4.3	10	278
C10-2	53.6120	(4) 2.64	21.5	312	64	6.0	10	331
C10-3	64.1534	(4) 2.64	31.5	499	65	13.6	10	538
C10-4	59.2054	(4) 2.64	42.4	502	65.5	18.4	10	545
C25-1	53.4226	(4) 2.64	17.5	264	64	4.35	25	280
C25-2	56.1613	(4) 2.64	22	308	64.5	6.15	25	330
C25-3	58.7110	(4) 2.64	32	492	64	13.6	25	522
C25-4	59.2617	(4) 2.64	44.3	502	65.5	19.0	25	545
C45-1	56.3080	(4) 2.64	17.7	261.5	64	4.35	45	278
C45-2	55.6334	(4) 2.64	22.3	305	65	6.2	45	329
C45-3	55.8530	(4) 2.64	35.9	454	65	14.2	45	490
C45-4	59.5975	(4) 2.64	41	502	65.5	18.1	45	545
C60 -1	56.0378	(4) 2.64	19	259	65	4.5	60	279
C90 -1	54.6405	(4) 2.64	20	260	64.5	4.5	90	278
C120-1	58.9530	(4) 2.64	18.2	260	64	4.4	120	276
C45-1/4	59.4218	(4) 2.64	17	253	64	4.1	45	269
D10-1	43.9048	(3) 1.98	16.2	301	74	4.6	10	277
D25-1	56.2552	(3) 1.98	16.6	300	74	4.7	25	276
D45-1	59.3491	(3) 1.98	16.8	298	74	4.7	45	274

Table 1 Experimental plan and actual separation parameters (cont.)

E10-1	41.5848	(2) 1.32	15.6	371	89	5.5	10	274
E25-1	42.6131	(2) 1.32	16	370	89	5.5	25	273
E45-1	44.4584	(2) 1.32	16.4	374	90	5.6	45	279
CB1	120	(4) 2.64	20	325	65	5.9	90	350
CB2	120	(4) 2.64	19.8	326	64	5.9	30	346
CB3	120	(4) 2.64	20	318	64	5.9	30	338

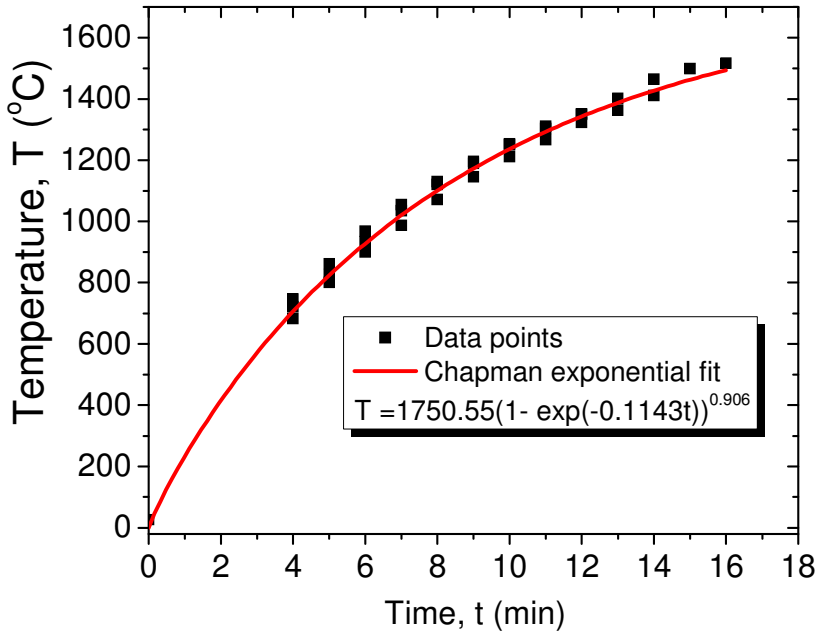

Fig. 6. Heating rates recorded for the experiments.

2.4. Evaluation of Separation Efficiency, η

The particle removal efficiency for a melt with an initial particle concentration C_o and a final concentration C can be defined as follows:

$$\eta = \frac{C_o - C}{C_o} \times 100\% = \left(1 - \frac{C}{C_o}\right) \times 100\% \quad (1)$$

Takahashi and Taniguchi [20] presented a mass balance of inclusions within the melt which could be adopted and modified as:

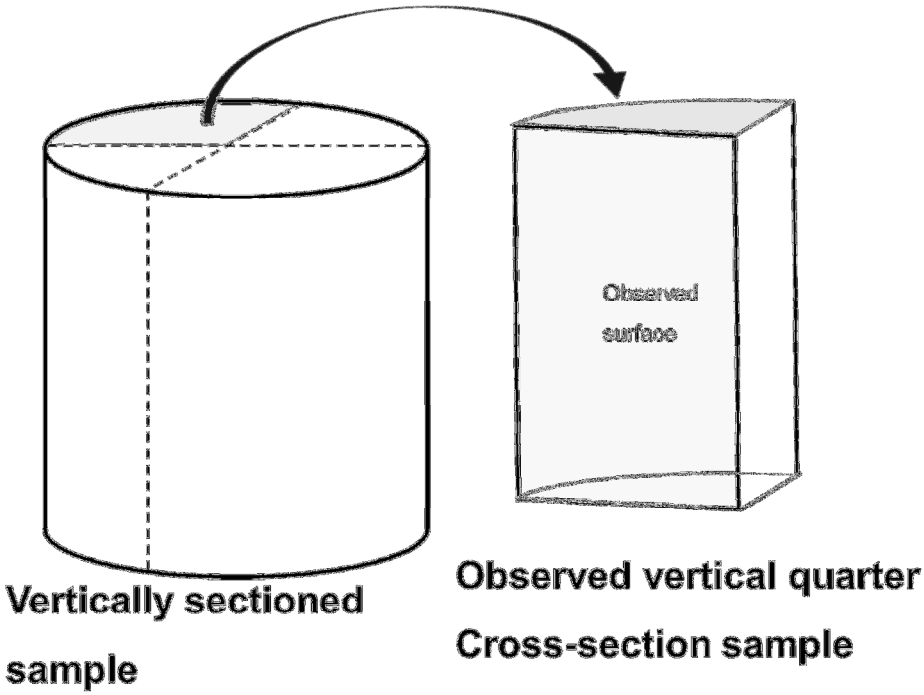

Fig. 7. Sample sectioning and observed surface. Sample is aligned with gravity direction from top to bottom.

$$-V\frac{dC}{dt}=\left(A_W u_W + A_B\left(u_B+u_t\right)+A_T u_T\right)C = aC \tag{2}$$

where V is volume of melt, A and u are the surface area of separator and particle velocity respectively and *"a"* is a certain constant. The subscripts W, B, t and T representing respectively the side wall, bottom, terminal, and top. Equation (2) could be solved with the initial condition $C = C_o$ when $t = 0$ s and substituted into Eq.(1) as follows.

$$\ln(C)-\ln(C_o)=-\frac{a}{V}t=-\lambda t \tag{3}$$

$$\frac{C}{C_o}=e^{(-\lambda t)} \tag{4}$$

$$\eta=\left(1-e^{(-\lambda t)}\right)\times 100\% \tag{5}$$

where λ is a constant for the separation process that relates the magnetic field and flow parameters. Equation (5) indicates an exponential dependence of the separation on time and other parameters such as volume of melt and particle velocity which depend on the magnetic field strength, current density and frequency.

The separation efficiency for the experiments was measured as the ratio of the volume of effective separation regions to the total volume of the sample. The effective separation regions were taken as the region where the matrix is clean with no inclusions in addition to the separated regions with particles at the side and bottom of the sample. This is based on the assumption that particles have accumulated at the side and bottom walls due to the confinement or restrictions imposed by the walls. Figure 8 shows an example of an optical macrograph of the quarter vertical cross-section of a separated sample and the outline of equivalent shape of the sample architecture in which the area of the sample occupied by inclusions is shaded.

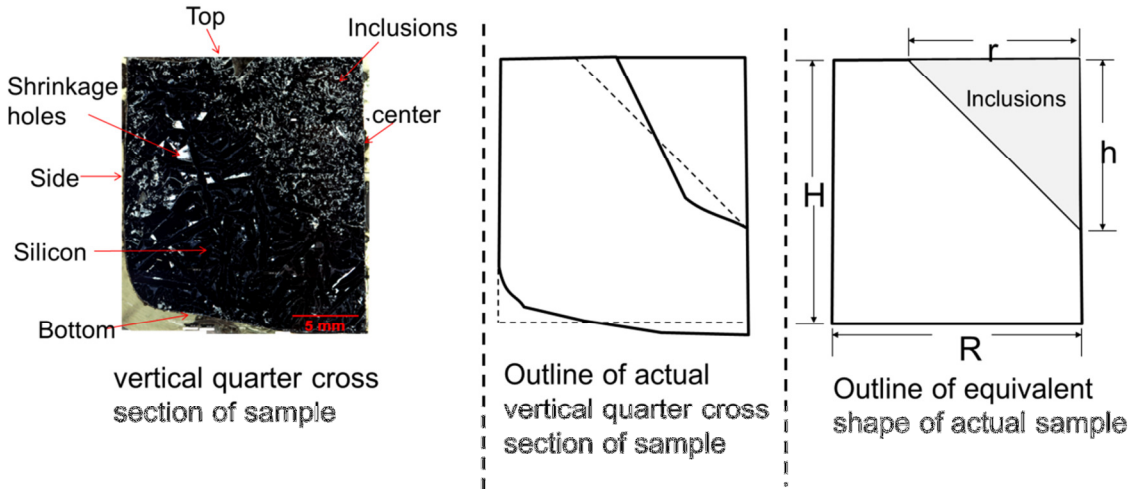

Fig. 8. Vertical cross-section of an actual sample with an outline and equivalent shape, and dimensions of the sample architecture with a shaded region of inclusion.

It must be noted that the experimental sample taken is based on the assumption of 3D symmetry. In 3D, the equivalent outline of the sample is a quarter cross-section of a cylinder and the region of inclusions represents a cone. The separation efficiency (η), which is volume fraction of the clean region, was defined as the ratio of the difference

between the volumes of the equivalent cylinder and cone to the volume of the equivalent cylinder, expressed quantitatively as:

$$\eta = \frac{\left(\pi R^2 H\right) - \left(\pi r^2 h / 3\right)}{\left(\pi R^2 H\right)} = 1 - \frac{h}{3H}\left(\frac{r}{R}\right)^2 \tag{6}$$

According to Eq.(5) the separation efficiency has exponential dependence of time with a pre-exponential parameter of unity. However, when the separation efficiency – time plot from the experiment was fitted with the model, a non-unity pre-exponential parameter was recorded as showed for example in Fig. 9(a). This means that before the separation process was timed some particles had already separated. Therefore, the actual separation time had to be determined by means of the fitted equation and then a corrected plot made as shown in Fig. 9(b). The adjustment corresponded to an average pre-separation time t_o of 90±10 s for the experiments.

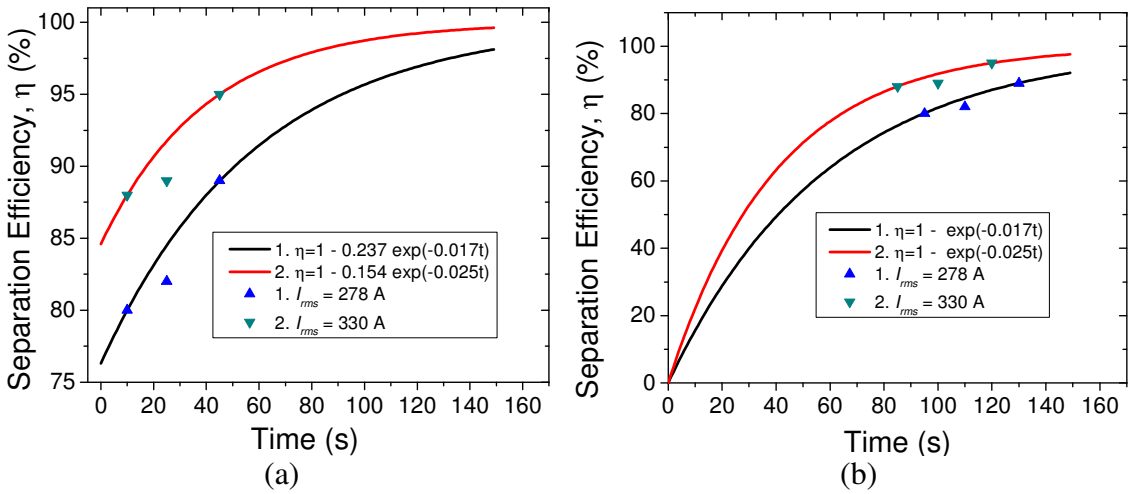

Fig. 9. Example of separation efficiency – time plot (a) based on experimental duration and (b) based on corrected time taken into account pre-separation during the melting process.

2.5. Modeling of Magnetic Field and Fluid Flow

To understand the particle separation mechanism, magnetic field and fluid flow simulations were undertaken. The magnetic field in the experimental set-up was modeled in the finite element magnetic field simulation software ANSOFT Maxwell, and the

MagnetoHydroDynamics (MHD) was calculated via ANSYS FLUENT utilizing the magnetic field data from the ANSOFT Maxwell calculations.

2.5.1. Modeling of Magnetic Field

A 3D model of the experimental set-up was created to scale in ANSOFT Maxwell and the eddy current solver was used to simulate the electromagnetic field which is described by Maxwell's equations (Eq. (7)):

$$\begin{cases} \nabla \cdot B = 0 \\ \nabla \times E = -\dfrac{\partial B}{\partial t} \\ \nabla \cdot D = q \\ \nabla \times H = j + \dfrac{\partial j}{\partial t} \end{cases} \tag{7}$$

where B (Tesla) and E (V/m) are the magnetic and electric fields respectively, and H and D are the induction fields for the magnetic and electric fields respectively. q (C/m^3) is the electric charge density, and j (A/m^2) is the electric current density vector. The skin-depth based approach was adopted to mesh the model shown in Fig. 10 and the insulation boundary condition was employed in the calculation. This boundary condition assumes there is a perfectly insulating sheet between electrical conductors and that current cannot cross it, and the magnetic field is tangential to the boundary.

2.5.2. MHD Modeling with ANSYS FLUENT

A 2D model of the experimental case was created and meshed in ANSYS Gambit for a 32 mm in diameter by 20 mm high cylindrical crucible. The mesh was made of 2560 quadrilaterateral cells of 0.5 mm × 0.5 mm and 2665 nodes. Figure 11 shows the structure of the mesh.

Ohm's law and Maxwell's equations present the coupling between the electromagnetic and fluid velocity field. Equation (8) defines Ohm's law for an electrically conductive molten metal with a velocity field U.

$$j = \sigma\left(E + U \times B\right) \tag{8}$$

The magnetic induction equation can be derived from Eqs. (7) and (8) for a conductive medium as:

$$\frac{\partial b}{\partial t}+(U\cdot\nabla)b=\frac{1}{\mu\sigma}\nabla^2 b+((B_o+b)\cdot\nabla)U-(U\cdot\nabla)B_o \tag{9}$$

where B_o and b are the externally imposed and induced magnetic fields, respectively, and μ and σ are the magnetic permeability and electrical conductivity of the molten metal respectively. And the current density based on Ampere's law is given by:

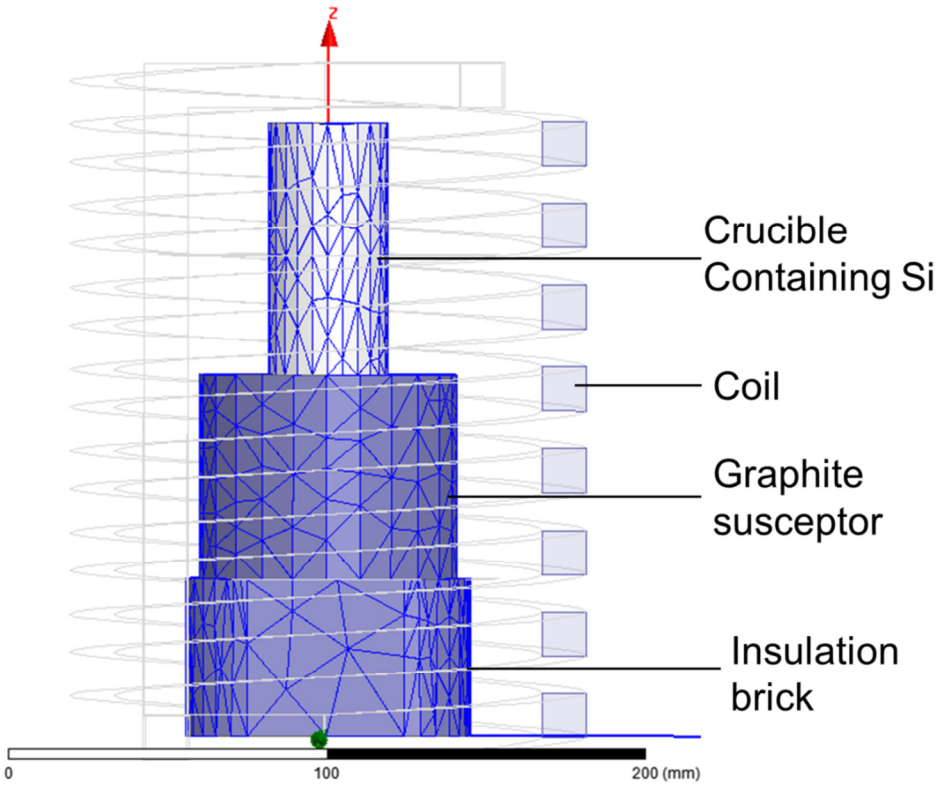

Fig. 10. View of the skin-depth based mesh of the 3D geometry of solids within the coil.

$$j=\frac{1}{\mu}\nabla\times(B_o+b) \tag{10}$$

The boundary condition for the induced field was set as electrically insulating which means $j = 0$ and the tangential components of the magnetic field are zero.

2D transient turbulent fluid flow and heat transfer for the model was calculated by solving the continuity equation, two Navier-Stokes momentum equations, the two equations for turbulent energy and its dissipation rate and the general energy equation. Due to the effect of the electromagnetic fields, additional source terms are introduced to

the fluid momentum equation (i.e. Lorentz force (N/m^3) given by Eq.(11)) and energy equation (i.e. Joule heating rate (W/m^3)) given by Eq. (12).

$$F = j \times B \tag{11}$$

$$Q = \frac{1}{\sigma} j \cdot j \tag{12}$$

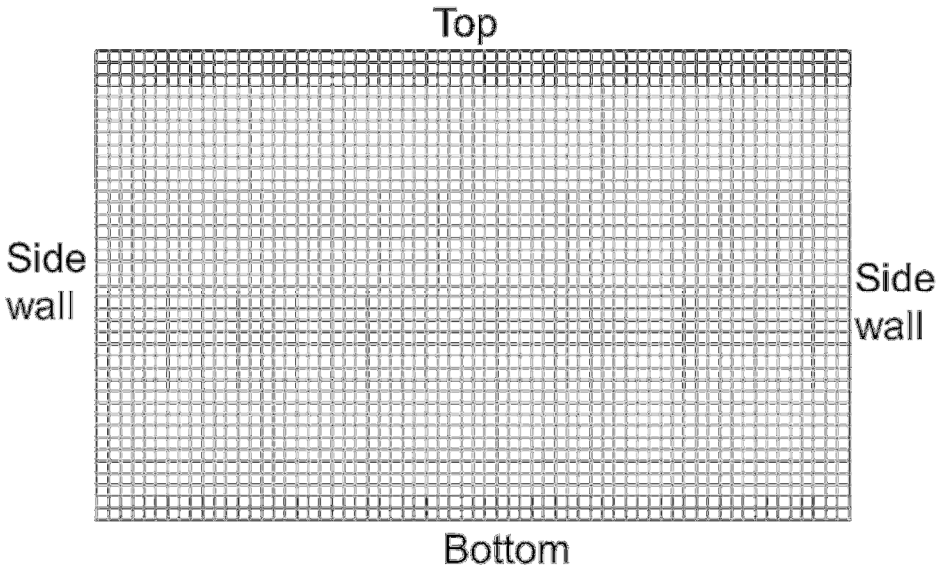

Fig. 11. 2D Mesh of the model solved in ANSYS Fluent.

The no-slip and stationary wall boundary conditions were employed for the momentum equations. The temperature boundary conditions used are 1823.15 K for the side wall, 1973.15 K for the bottom wall and a backflow temperature of 1773.15 K same as the temperature of molten silicon. The wall thickness was 0.003 m for both the side and bottom walls. Table 2 presents data for materials properties used in the calculations. For the initial conditions, the velocity and turbulent parameters were all set to zero. The solution was obtained by iterating at a time step-size of 1.0×10^{-5} s to cater for the possible high frequency errors.

Table 2 Data of materials properties used in the calculations.

Property	Silicon	SiO_2 crucible	Graphite
Density, ρ (kg/m^3)	2570	2210	/
Viscosity, η (kg/m-s)	0.000543	/	/
Thermal conductivity, k (W/m-K)	58	2.01	/
Specific heat capacity, C_p (j/kg-K)	900	733	/
Electrical conductivity, σ (S/m)	1400000	0	1200000
Magnetic permeability, μ (H/m)	1.26×10^{-6}	1.26×10^{-6}	1.26×10^{-6}

3. Results and Discussion

3.1. Overall Separation

For a complete view of the quarter vertical cross-sectional sample taken for the various experiments to understand the separation process, combined optical macrographs were made. In general, particles accumulate at the side wall, bottom wall and close to the center at the top of the sample. The particles that were moved to the central part at the top, then started settling through the central region of the sample toward the bottom. The optical macrograph shown in Fig. 12 indicates the separation of particles from portions of the sample close to the wall and the bottom, leaving a cleaner matrix at these regions.

The microstructures of the various regions in the macrograph are also shown in the figure. The dark phase is the primary silicon phase, the gray phases within the primary silicon is the aluminum dominant Al – Si eutectic phase and the bright spots are the nonmetallic particles. Many areas of porosity can be observed in the sample as a result of solidification shrinkage. Between the liquidus and solidus temperatures of the system, the primary silicon (~92 wt% Si) solidified first and contained the Al-Si liquid at the grain boundaries which was forced to the top due to pressure from grain growth leaving voids within the grains. Comparing the micrographs of the side wall to the bottom wall, a thinner layer of particles was observed at the side wall than at the bottom of the crucible. The particles observed within the central part of the sample were dispersed and clustered. These particles appeared to have been acted upon by a certain

downward pressure causing what seems like particle settling with difference velocities from the top close to the central part and also close to the bottom. Figure 13 shows SEM micrographs of the top part of the sample. A thin layer of particles can be observed at the top beneath the epoxy mounting material (dark layer). This particle was determined by EDX to contain mainly Al, O, and Si. This layer is attributed to the atmospheric oxidation of the melt.

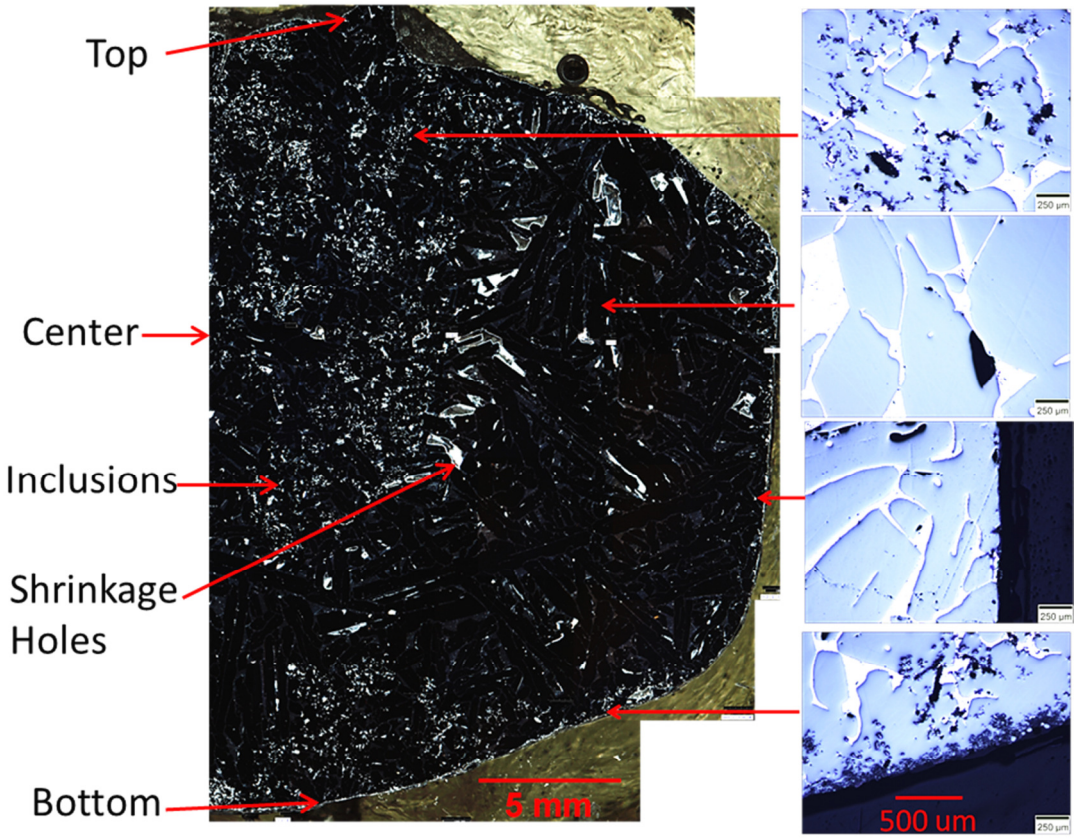

Fig. 12. Typical optical macro- and micro-graphs of the quarter vertical cross-section of the EM separated sample.

Figure 14 shows the distribution of particles in the bottom, side wall and center of the crucible. In general the central part of the sample was clean and particles were not detected. On the other hand, thick and dense particle layers were observed near the side wall and the bottom of the samples. An interesting observation is the size and locations of the trapped particles in the layers at the side wall and the bottom of the samples. It can be

seen that larger particles were trapped closest to the walls while fine particles accumulated and deposited on the large particles. This confirms the idea that large particles are easier to separate than smaller particles. Smaller particles are easily carried by the motion of the fluid and therefore have longer residence time within the fluid flow before being separated. A typical EDX area spectrum of these small particles is shown in Fig. 15, which shows that the major elements are Si, Al and O. This indicates that some of the original particles might have been oxidized during the experiments. The original sample did not contain Al_2O_3 particles smaller than 5 μm, unlike the SiC particles which had over 50 % smaller than 3 μm.

The observation of the texture of the particle layer at the bottom and side walls (see Figs. 12 and 14) suggests the presence of strong downward and side forces confined to a certain distance from the bottom and side of the crucible respectively. The particle layer at the bottom was dense and appeared cemented. A similar observation was made for the particle layer at the side wall, but it was much thinner than the bottom.

The downward force is attributed to the contribution of the EM induced flow in the molten silicon coupled with gravity and magnetization forces. Magnetization forces result due to the difference in magnetic susceptibility between the phases in a domain with a non-uniform distribution of magnetic field. These forces increased the particle settling rate and therefore causes particles being carried by the flow eddies to have a net downward motion. Due to uneven distribution of fluid velocity throughout the sample (as will be shown in the next section), particles that appear to be settling in the center also settle at different rates. Particles closer to the bottom have higher settling velocities dues to the stronger flow in these regions.

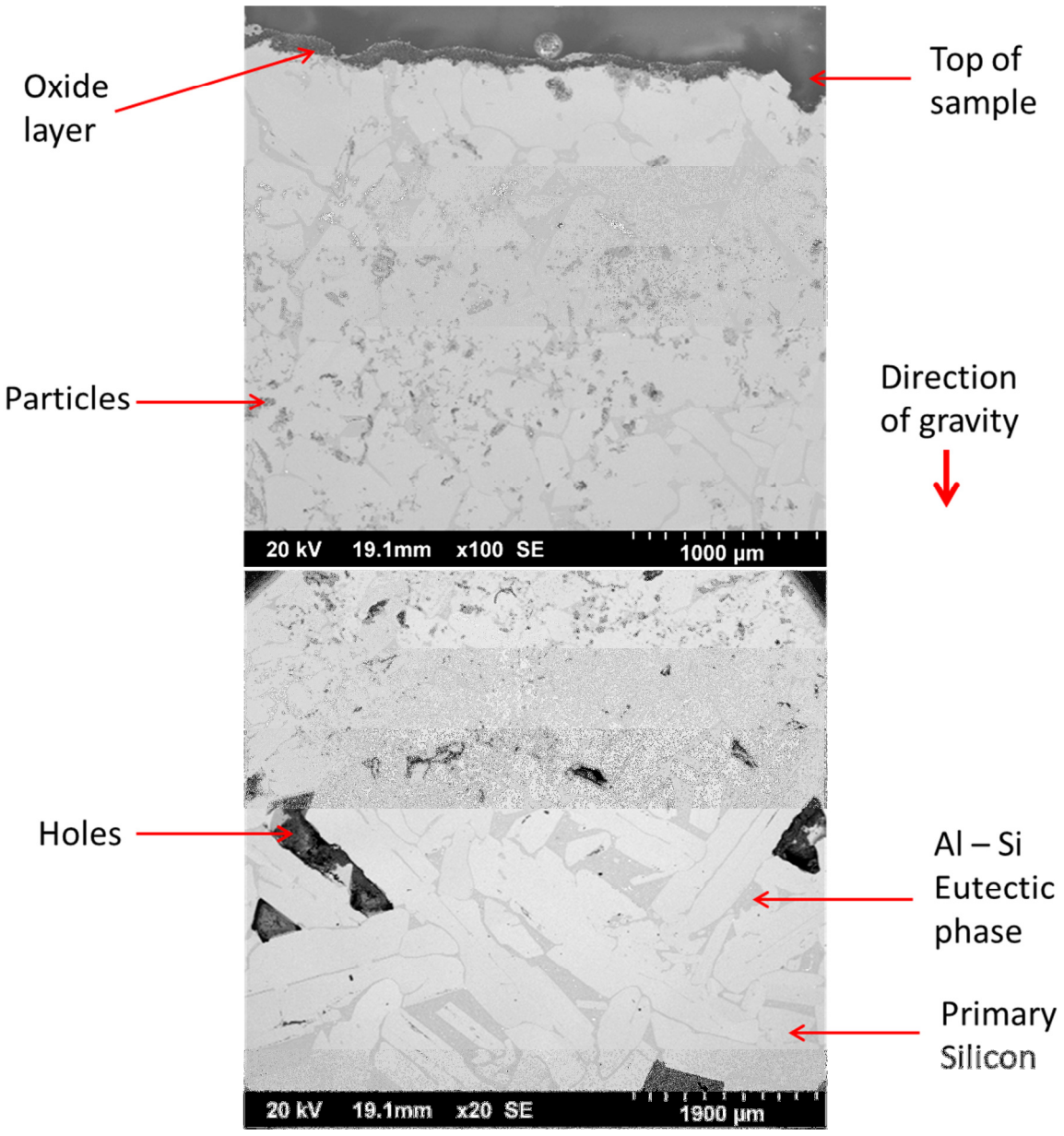

Fig. 13. SEM micrographs of the top part of the samples in Fig. 12 after separation showing a thin topmost oxide layer of aluminum and silicon oxide and the transition from the particles in the top area to the clean area. Many areas of porosity are also observed.

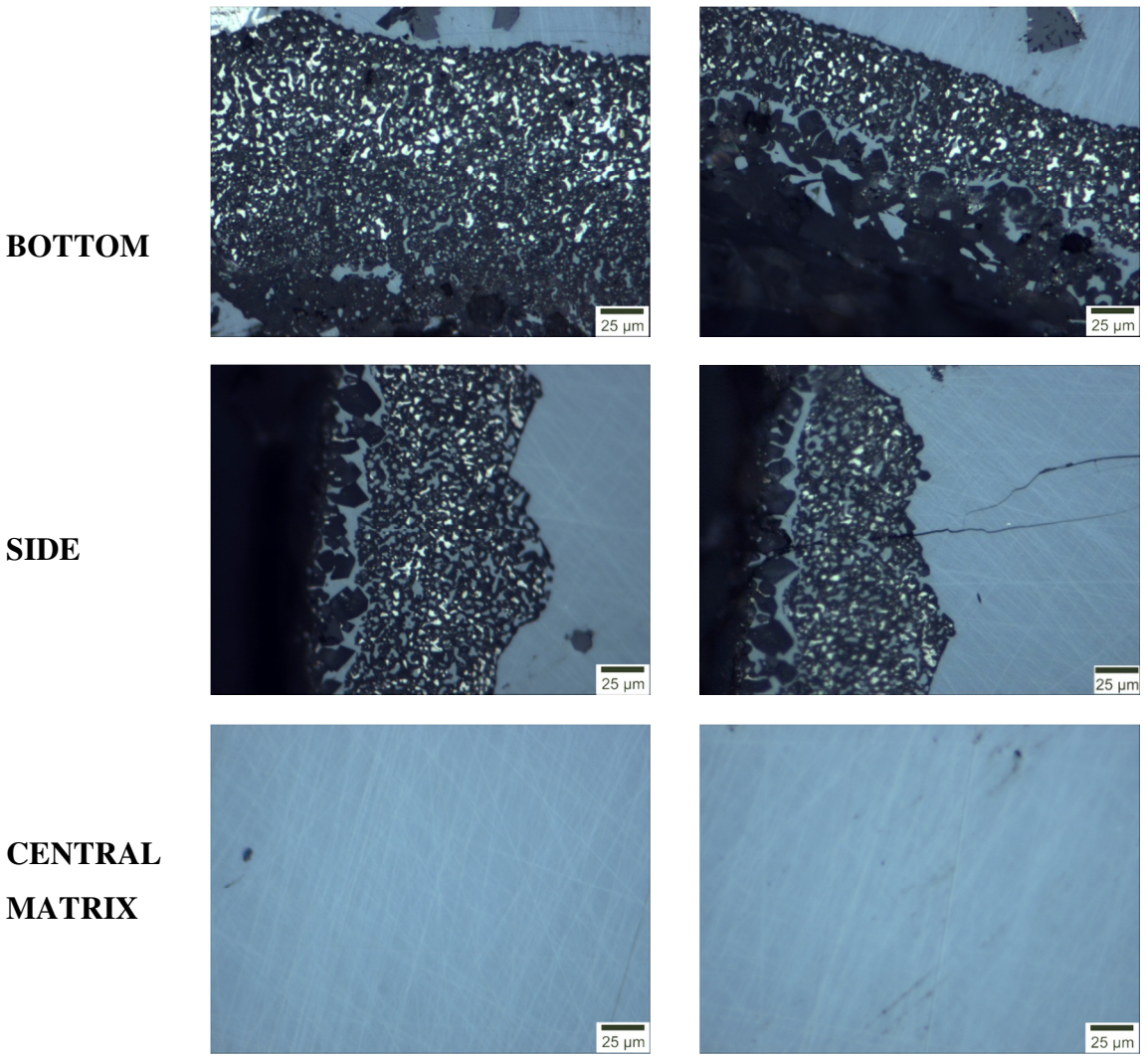

Fig. 14. Micrographs of the various locations capturing the distribution of particles at bottom (top), side wall (middle) and center (bottom) for separation at frequency of 65 kHz, coil current of 533 A and a time of 10 s.

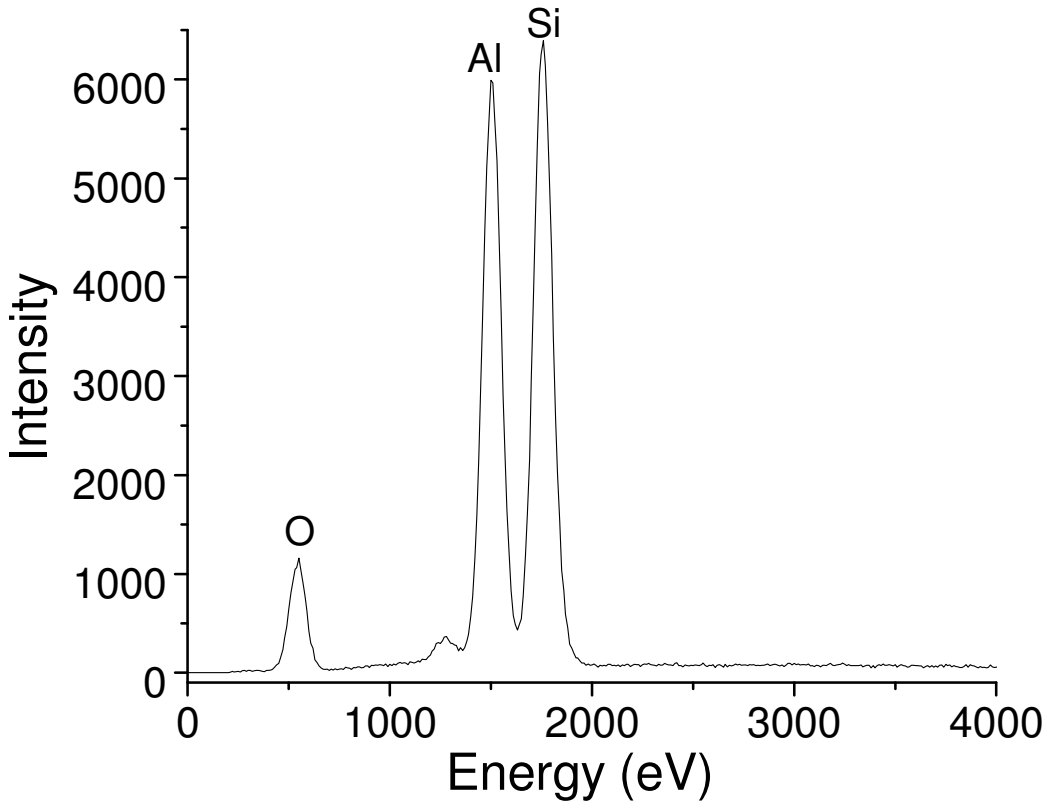

Fig. 15. Typical EDX spectrum of the small size particles in the side and bottom wall layers.

The magnetic field distribution vectors within the experimental set-up and contours within the molten silicon for various currents and frequencies calculated via the ANSOFT Maxwell simulations are showed in Fig. 16. The strength of the magnetic field increases strongly with increased current and slightly with increased frequency. Within the molten silicon, the magnetic field is concentrated within a layer close to the side wall and diffuses until it reaches a minimum value at the center. The high intensity of the magnetic field near the surface of the molten silicon is due to the limiting effect of skin depth at high frequencies. The skin depth (δ) which depends on the electrical conductivity (σ) of the molten metal, and the frequency is defined as:

$$\delta = \frac{1}{\sqrt{\pi \mu \sigma f}} \tag{13}$$

where μ is the magnetic permeability of the conductor.

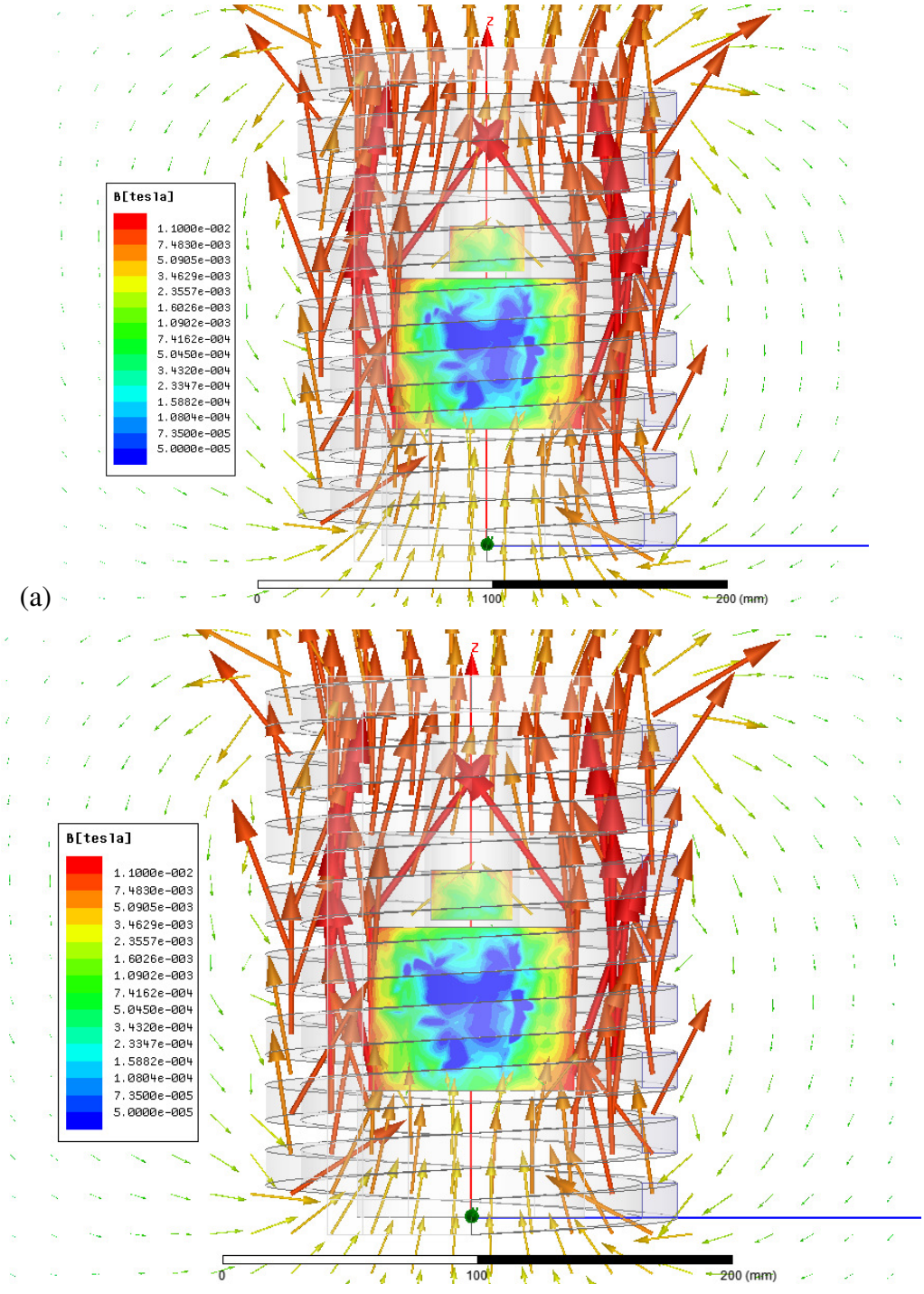

Fig. 16. Magnetic field vectors within the experimental set-up and B contours within the crucible, sheath, susceptor and silicon for (a) 280 A, 65 kHz, (b) 280 A, 90 kHz and (c) 535 A, 65 kHz.

(c)

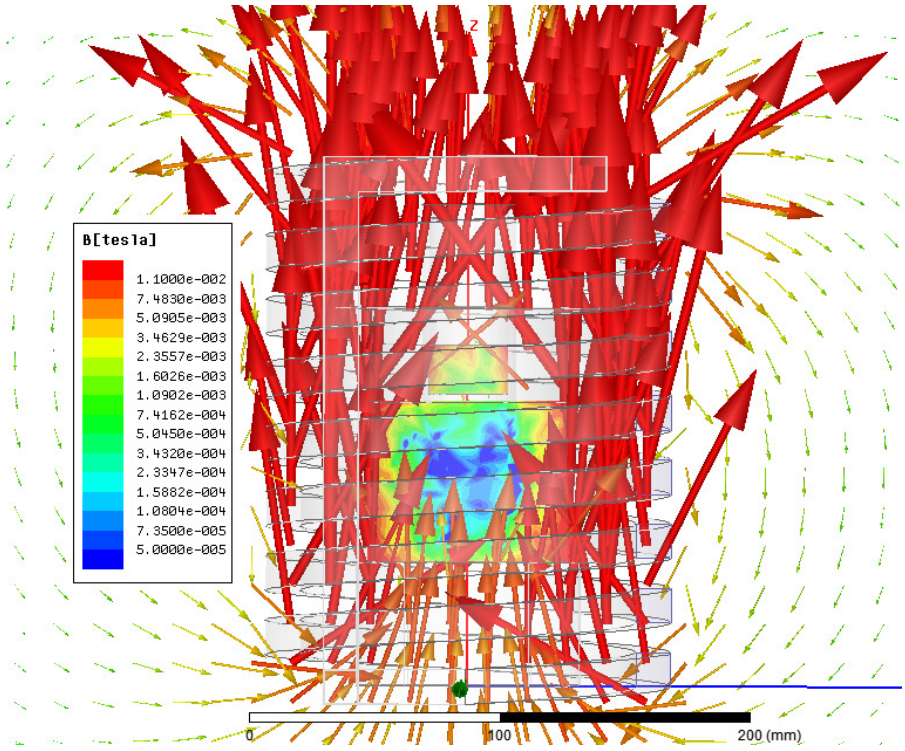

Fig. 16. Magnetic field vectors within the experimental set-up and B contours within the crucible, sheath, susceptor and silicon for (a) 280 A, 65 kHz, (b) 280 A, 90 kHz and (c) 535 A, 65 kHz. (cont.)

Therefore the electromagnetic force acting on the particles is most effective in the vicinity of the side wall. The EM induced circulatory flow carries particles throughout the fluid and when these particles are in the vicinity of the walls where settling and EM forces are effective they are trapped. The remaining particles are carried with the flow and deposited at favorable sites where the fluid flow is weak.

3.2. Separation Mechanisms and Fluid flow

3.2.1. Contributing forces

From the foregoing discussion three important phenomena contributed to the separation process, namely:

- electromagnetic Archimedes force (EM particle force)
- effect of fluid flow
- effect of magnetization force.

The electromagnetic Archimedes force is the force which acts on the nonconductive particles in a direction opposite to the Lorentz force. It is 3/4 of the magnitude of the Lorentz force and is concentrated within the skin depth of the alternating magnetic field. The settling force had contributions, to a greater extent, from the induced fluid flow and to a lesser extent from the magnetization force. Many researchers in diverse fields have studied the effect of flow on the settling behavior of particles in fluids and have concluded that particles settle faster in more convective fluids [21-23]. One proposed mechanism for this result is that particles interact with the underlying turbulence and concentrate preferentially in certain flow regions, leading to particle clustering and increases in characteristic size [23] leading to an enhanced settling. Another possible reason is a decreased fluid viscosity leading to lowering of the resistant forces in the molten metal, thereby enhancing particle settling velocity. This can be expressed mathematically by combining gravity, drag and magnetization forces to describe the particle settling velocity as Eq.(14).

$$\begin{cases} v_p = \sqrt{\dfrac{4d_p}{3C_D\rho_m}\left[\left(\rho_p-\rho_m\right)g+\left(\chi_m-\chi_p\right)\dfrac{1}{\mu_o}B\dfrac{\partial B}{\partial z}\right]}; \\ C_D \approx \dfrac{24}{\mathrm{Re}}\left(1+0.15\,\mathrm{Re}^{0.687}\right) \end{cases} \tag{14}$$

where d_p is particle diameter, BdB/dz is magnetic field gradient, ρ and χ are respectively density and magnetic susceptibility and the subscripts m and p present metal and particle respectively. Figure 17 shows the effect of Reynolds number and gradient magnetic field on the settling velocity of 10 μm SiC particles in molten silicon at 1500 ^{o}C. As is evident, increasing flow velocity has the potential to enhance the settling velocity of particles greatly. It is important to emphasize at this point that if the convective forces are too strong, particles may be carried in the flow instead of settling and already settled particles may be eroded. This effect could also lead to the agglomeration of small particles into larger ones, which in turn could enhance their settling rates.

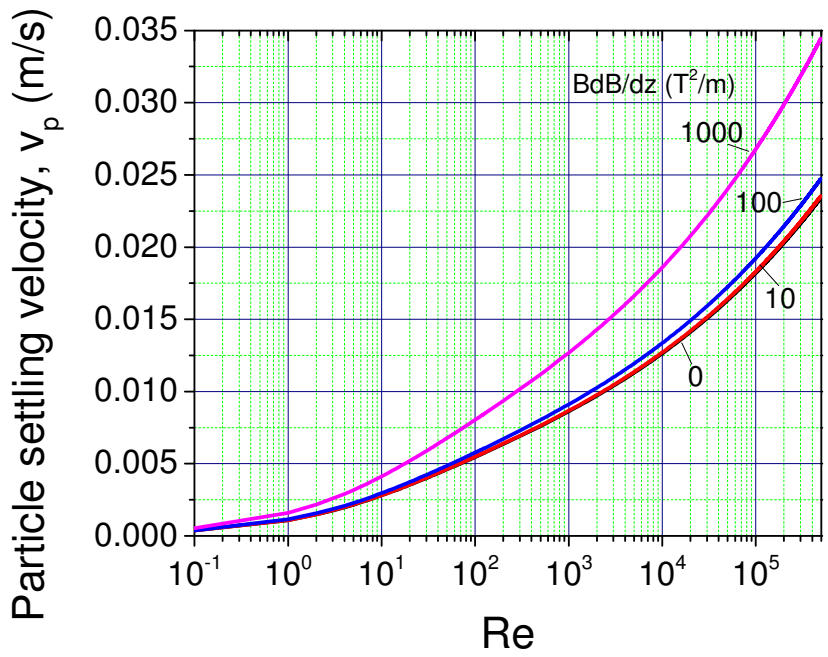

Fig. 17. The effect of gradient magnetic field and Reynolds number on the settling velocity of a 10 µm SiC particle in molten silicon

3.2.2. Fluid flow

When the electromagnetic field is applied to the molten metal, the magnetic field (*B*) and current density (*J*) fields combine to create the electromagnetic force known as the Lorentz force (given by *JB*) at orthogonal angles to each other. Strong flow is induced as a result of Lorentz force acting on the molten silicon. Figure 18 shows the flow pattern in the molten silicon calculated by ANSYS Fluent for various currents and frequencies of a vertical plane through the center of the crucible. The streamlines show that fluid flow develops mainly from the top and bottom and drives the molten silicon in a circulatory flow pattern. The strongest flow is recorded near the bottom of the molten metal and part of the side walls. The asymmetry in the fluid flow simulation is the result of the unstructured mesh used in calculating the magnetic field. Figure 19 presents numbers for the velocity statistics for various parameters. Comparisons between various parameters indicate that the fluid velocity is enhanced by increasing both the frequency and current of the magnetic field. However, higher current has a stronger effect on the velocity than higher frequency.

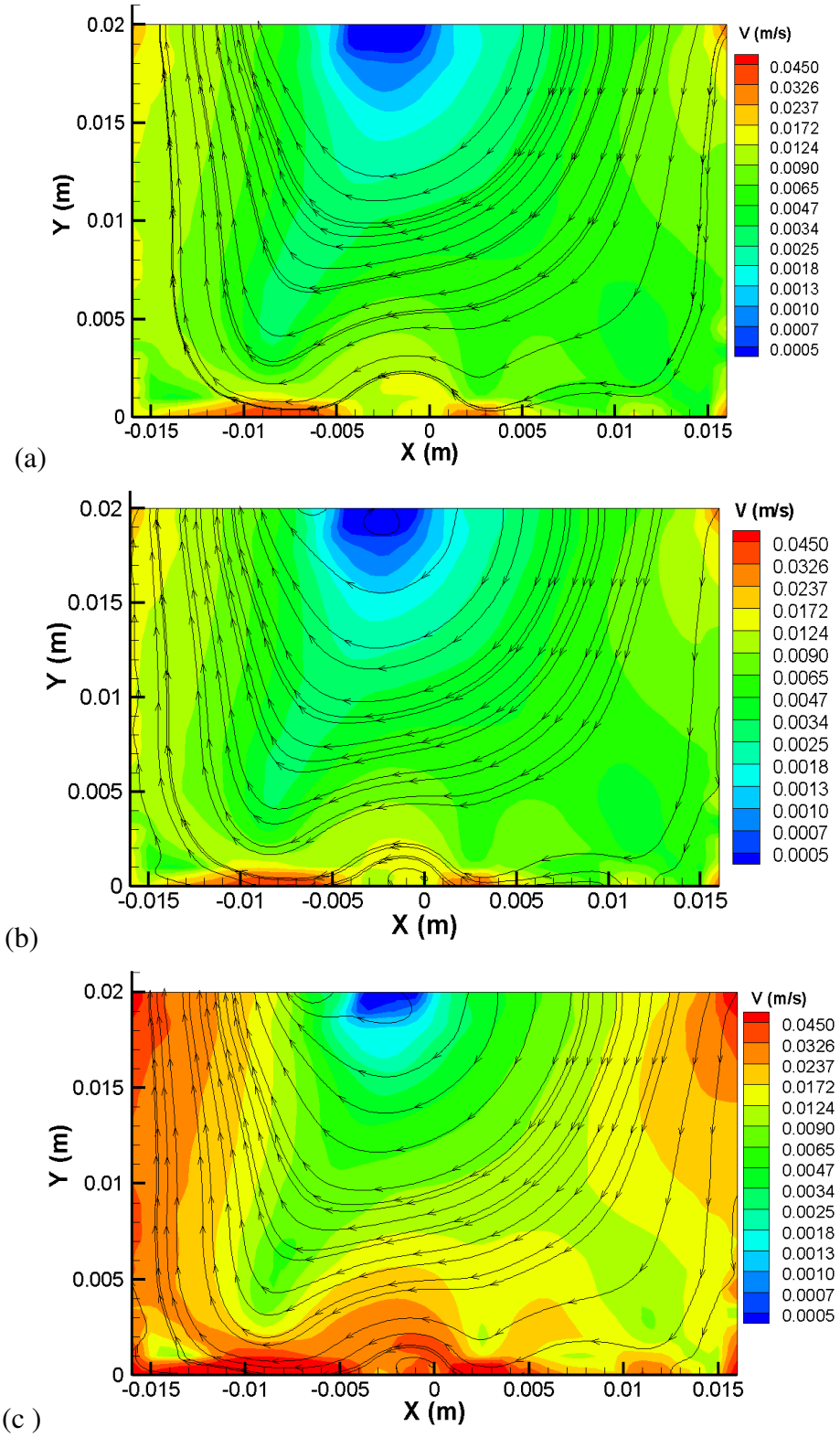

Fig. 18. Contours of velocity magnitude and streamlines of fluid flow as calculated by ANSYS FLUENT for (a) 280 A 65 kHz, (b) 280 A, 90 kHz and (c) 535 A, 65 kHz.

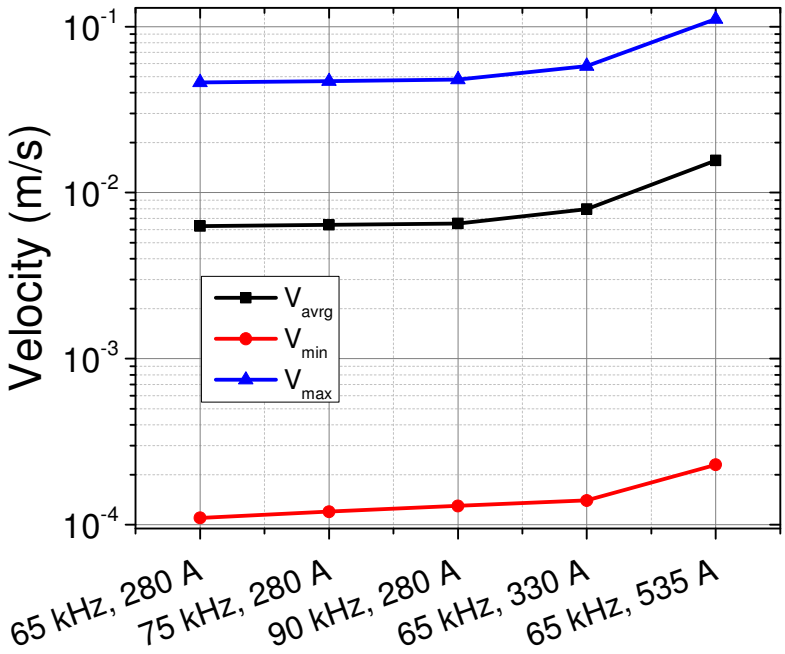

Fig. 19. Comparison of faceted minimum, maximum and average fluid velocities for various parameters.

The calculated flow pattern could explain the observed particle distribution in the experiments. In the experiments, particles were trapped at the wall due to electromagnetic forces, others settled due to the combined effect of gravity, drag and magnetic forces and yet others carried by the flow were deposited at the top central region. It can be seen from the flow pattern that, the top central region has the least flow and therefore offers the most stable place for inclusions circulating within the fluid flow. These particles that circulate in the flow near the central region may agglomerate due to local attractive forces, enhanced by collision *via* fluid or convective transport to become larger and more stable to settle through the fluid. It should also be noted that, along the height of the molten silicon the flow is non-uniform and therefore particles at different locations along the height will settle at different rates, which explains the observed experimental results of apparent different settling velocities of particles through the central part of the melt. Therefore, in a fluid with a more uniform and strong flowing field, all particles could be settled. This idea was verified by using a graphite sheath around the crucible with the aim of shielding the strongest part of the magnetic field and inducing a more uniform field within the melt to cause a more uniform flow for settling particle. The result of this study

is reported in the next chapter, which showed a good agreement with the idea. Interestingly, magnetic field calculations showed a much stronger induced field for this case, leading to stronger fluid flow and hence effective settling of particles.

3.3. Effect of Separation Time

As expressed by Eq.(5), increasing the separation time should significantly improve the separation process. The results shown in Fig. 20 indicate an improved separation for longer separation times. However, due to the settling effect on the particles by the various forces, particles congregated close to the top of the sample by convective forces and settled through the melt over time, and could lead to clusters of particles being observed within the matrix for incomplete settling. Similar observation of this phenomenon was made for other separation conditions of currents and frequencies (see Fig.21 at 90 kHz for example). It is important to note that during the experiments, separation time started after the melt had been under the magnetic field for a while (i.e. t_o) and therefore the times reported in the figures are the recorded experiment duration, which as explained in the section 2.4 could be adjusted based on an exponential fit (Eq.(6)).

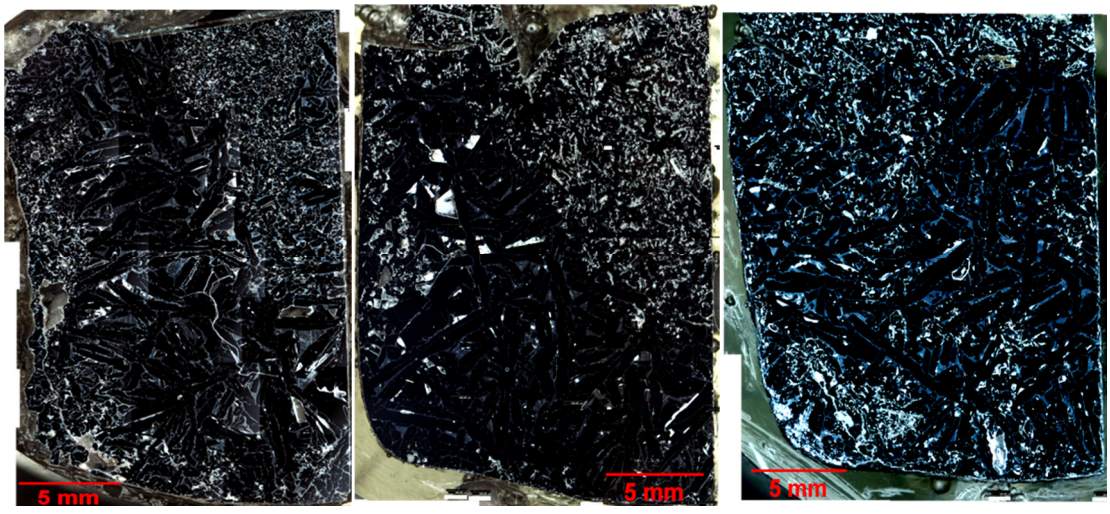

(a) (b) (c)

Fig. 20. Quarter cross-sectional macrographs showing the effect of separation time at coil current I_{rms} = 278 A and frequency f = 65 kHz for (a) 10 s, (b) 60 s, and (c) 120 s.

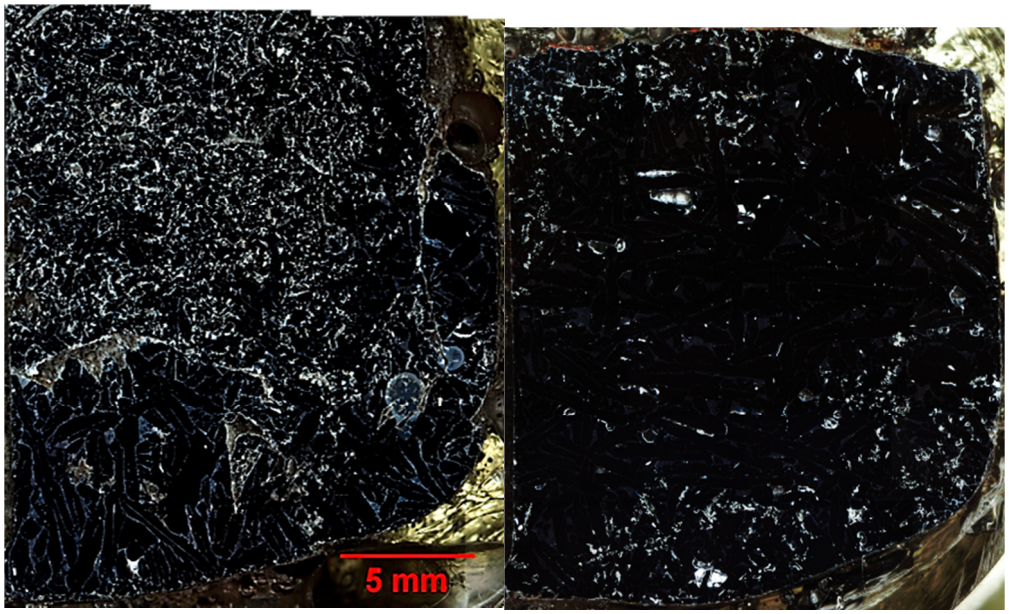

Fig. 21. Quarter cross-sectional macrographs showing the effect of separation time at coil current I_{rms} = 278 A and frequency f = 90 kHz for (a) 10 s, and (b) 60 s.

3.4. Effect of Coil Current, I_{rms}

Increasing the coil current increases the strength of the magnetic field and increases the separation efficiency of the process. A stronger magnetic field produces stronger forces and stronger fluid flow (as seen in section 3.2) which leads to better separation. However, due to the effect of joule heating associated with AC magnetic fields, higher currents result in more power loss to joule heating and unwanted temperature rises which may render the process inefficient. Makarav *et al*. [24] analyzed conventional methods of electromagnetic separation comparing them based on their power efficiencies and concluded that an AC magnetic field in the most power inefficient. Figure 22 compares the effect of coil current on the separation process at a frequency of 65 kHz and separation time of 10 s. Significant improvements in the separation were observed when the coil current was increased from 278 A to 330 A and to 533 A. At higher currents there appears to be a deeper penetration of the settling forces, which draws the particles from the top central part and cements them at the bottom, resulting in a larger area of clean metal as shown in Fig. 22(c). It can also be observed that particles close to the topmost part of the sample appear to be settling, an indication of a downward force acting on them.

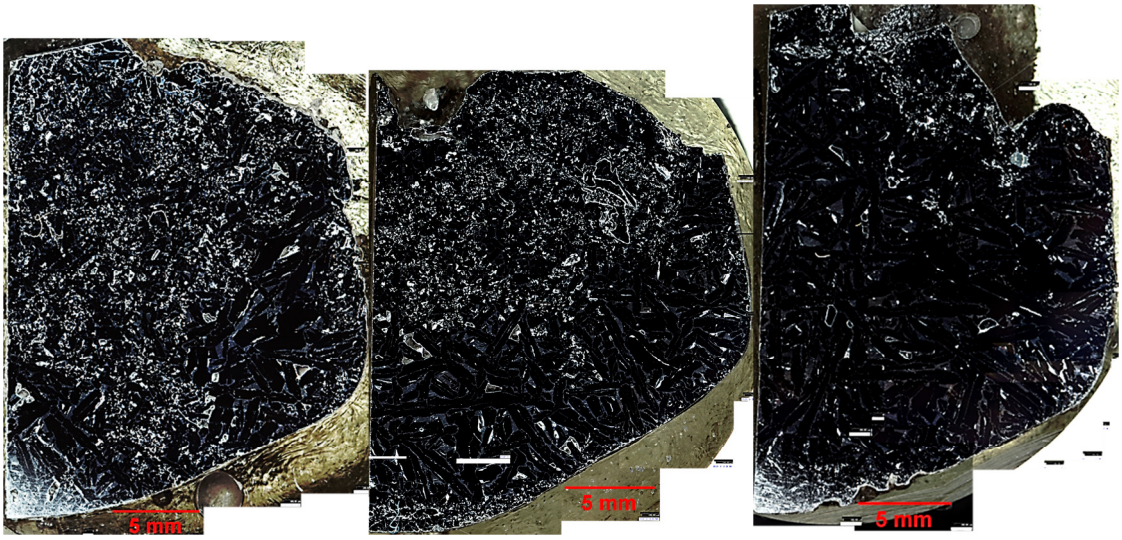

(a) (b) (c)

Fig. 22. Quarter cross-sectional macrographs comparing the effect of coil current (a) 278 A, (b) 330 A, (c) 533 A.

Figure 23 compares the separation efficiency for various coil currents and the changes with time. The experimental data in the curves for I_{rms} = 278 A, and 330 A are exponential fits (see Eq. (5)) while the data for I_{rms} = 533 A was predicted based on extrapolation of the values of λ for I_{rms} = 278 A, and 330 A (see section 2.4 for method). The points for 10 s, and 25 s on line I_{rms} = 278 A are from trial experiments using the *in-situ* dispersion method described in the experimental section.

3.5. Effect of frequency

As seen in the fluid flow pattern, increasing the frequency enhances the fluid velocity, which is expected to improve the separation of particles especially due to particle settling, while the separation due to particle attachment to the side wall is limited as a result of skin depth effect. Figures 24 and 25 compare the separation for 65 kHz, 75 kHz and 90 kHz at a coil current of 278 A for 45 s separation time. It can be seen that increasing the frequency significantly improved the separation by enhancing particle settling. Higher frequencies appear to have concentrated the settling force close to the top region to push the particles toward the bottom of the molten silicon.

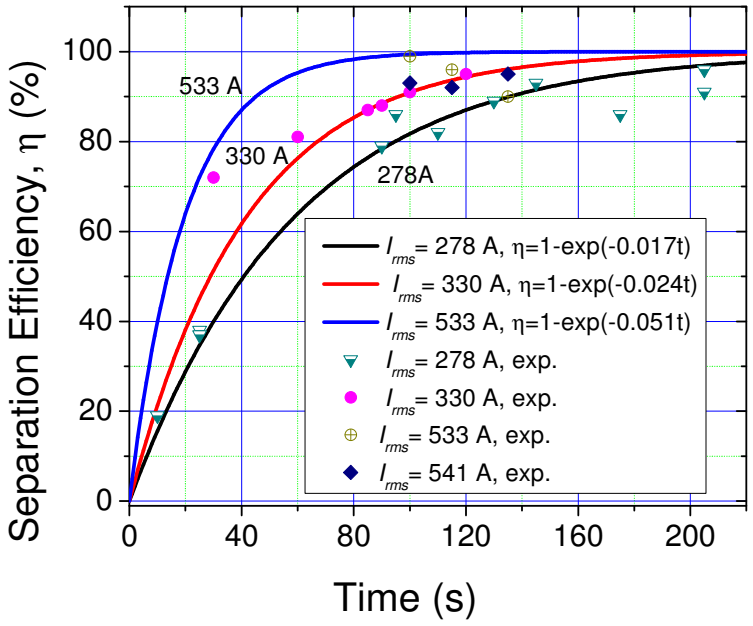

Fig. 23. The dependence of the separation efficiency on coil current and time at 65 kHz based on the corrected time for individual experiments.

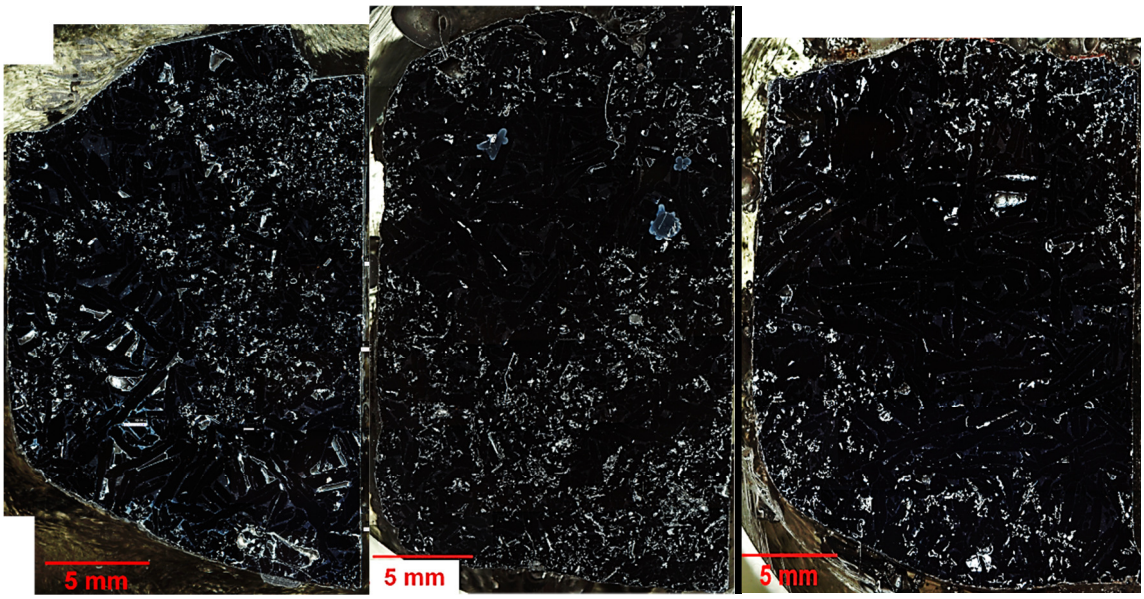

(a) (b) (c)

Fig. 24. Quarter cross-sectional macrographs showing the dependence of separation efficiency on frequency at 278 A and separation time of 45 s for (a) 65 kHz, (b) 75 kHz and (c) 90 kHz.

Unlike the separation at 65 kHz, the clean matrix close to the side wall (left side) of the sample from top to the bottom was not observed for 75 kHz and 90 kHz samples. Rather bulk settling of particles was observed and the rate of settling is highest for 90 kHz. It is worth mentioning that, the method to calculate the separation efficiency described in section 2.4 could overestimate the separation for intermediate and even high frequencies due to the assumption that particles close to the bottom and side walls are deemed to have been effectively separated. However, for such frequencies particles appear to be settling in the central part of the matrix which makes the calculation method less accurate. Therefore the curve for 75 kHz reported in Fig. 25 is an extrapolation based on those for 65 and 90 kHz.

Based on a preliminary study of this process prior to the current study, the result of which is reported elsewhere [19], the effect of frequency on the separation process was found to be related to the coil current. As shown in Fig. 26, at low coil currents, higher frequency resulted in higher separation efficiencies, the difference of which is less pronounced at higher currents. At higher coil currents, the efficiency of the separation process depends more on the current than on the frequency.

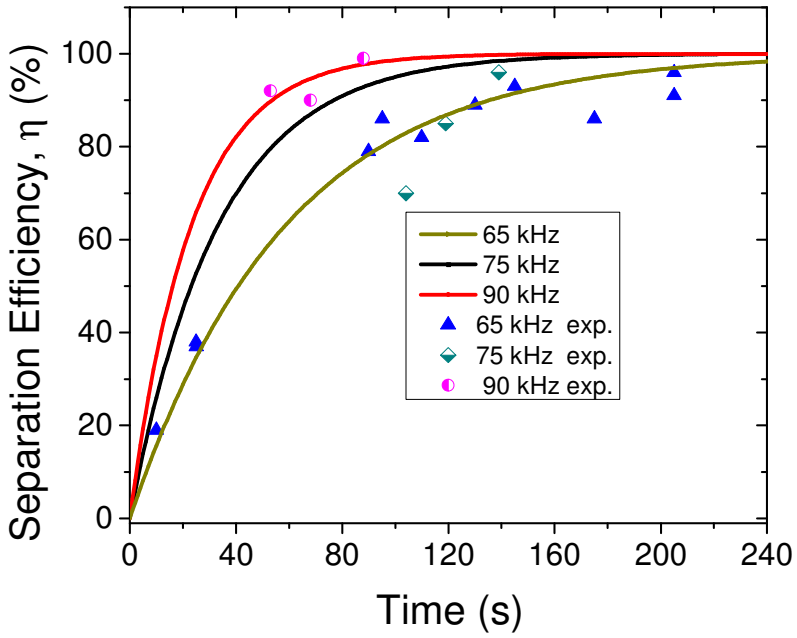

Fig. 25. The dependence of the separation efficiency on the frequency and separation time at a coil current of 278 A.

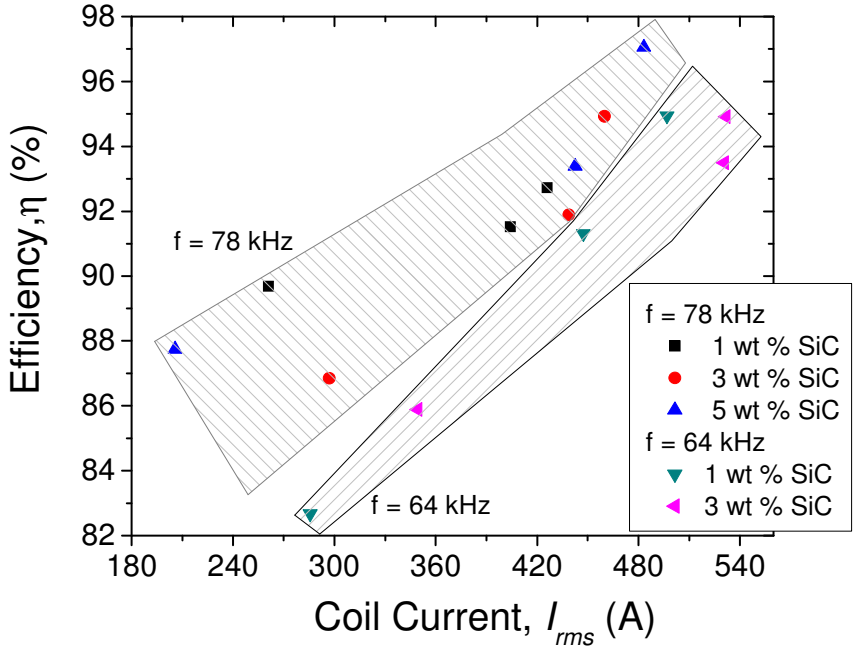

Fig. 26. Recorded separation efficiencies plotted against coil current for various frequencies and particle concentrations.

3.6. Separation in larger volume melt

Results from the particle separation process based on *in-situ* particle dispersion after melting (see Exp. CB 1 – 3 in Table 1) are reported in Fig. 27 and Fig. 28 in which the dashed line marks the clean matrix from the particle matrix regions. Due to much faster rates of solidification in these *in-situ* particle dispersion experiments compared to the stir-solidification method employed in Si (Al) – SiC composite parametric studies, more aluminum was retained in the melt resulting in more bright phases observed**.** The separation in these experiments appeared better than the separation in the smaller volume since the particles congregated at the top are not in an apparent motion to the bottom. This is probably due to a change in the flow pattern for these experiments due to larger volume.

This result is supported by some literature reports. Shu *et al* [25] evaluated the effect of an induced secondary melt flow by an alternating current electromagnetic field on particle separation from an aluminum melt and concluded that the separation efficiency of the process improves significantly.

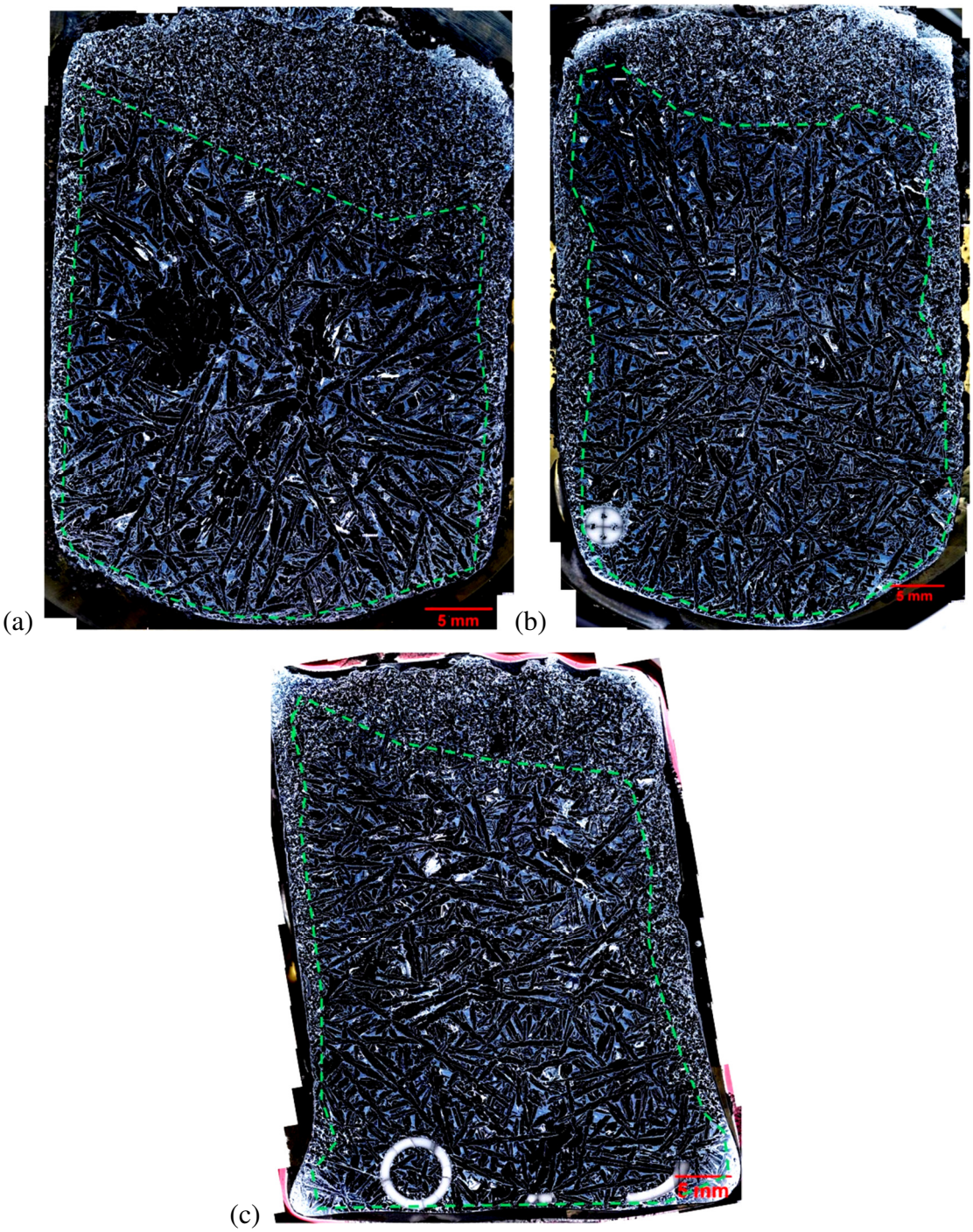

Fig. 27. Optical macrographs of larger size samples separated at a frequency of 65 kHz, coil current of 350 A for respective separation times of 30 s (a), 60 s (b) and 90 s (c). The dashed lines separate the clean region from the particle region and the round bright features are pieces of broken Al_2O_3 stirrer rods.

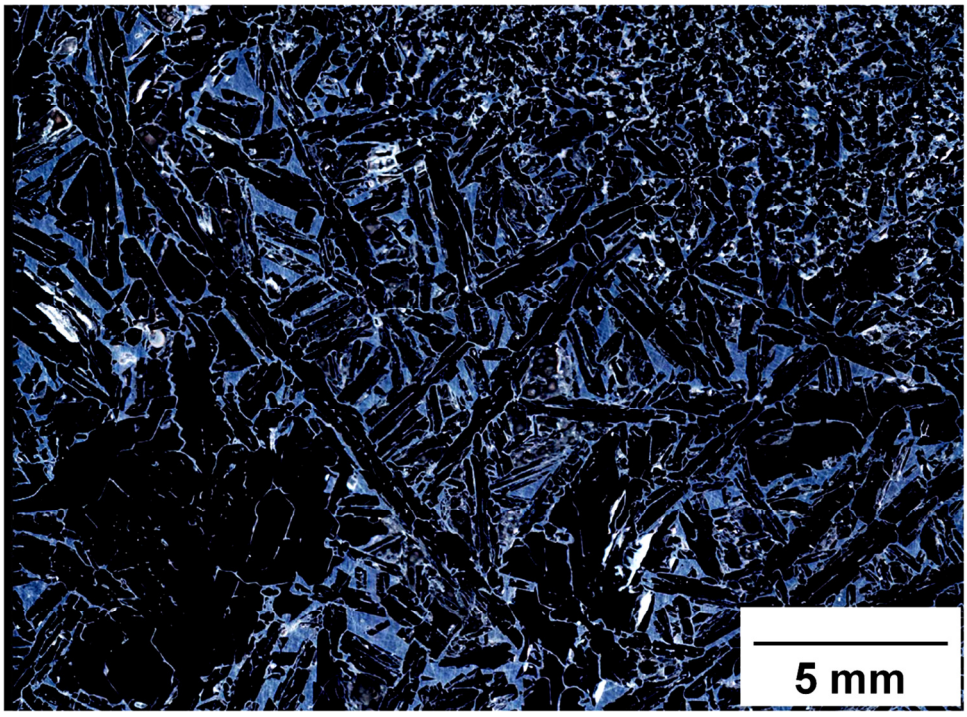

Fig. 28. Enlarged view of the matrix of the samples shown in Fig. 22 showing the clean and the particle containing matrix (top – right corner).

They reported that larger volume melts at high frequencies can generate stronger secondary fluid flow and better separation efficiency, supporting the results from the current study. Bruckner and Schwerdtfeger [26] introduced a semi-empirical relationship for calculating the maximum velocity of the induced secondary flow for rotating magnetic fields, which suggested that the flow velocity could be improved with higher frequency, a stronger magnetic field and larger volume melts.

4. Conclusions

This study investigated the effect of an electromagnetic field on the removal of nonmetallic inclusions from silicon. The effects of particle size, separation time, frequency and coil current on the separation process were evaluated. Inclusion separation efficiencies of over 95 % were recorded. The separation efficiency increased significantly with increases in the frequency, separation time and coil current. Higher frequency induced stronger fluid flow and higher coil currents resulted in stronger magnetic fields

and induced fluid flow for enhanced particle separation. Longer separation times led to enhanced settling of the particles present at the top

Particles were separated from the matrix of the material and were trapped at the top, bottom and side walls of the crucible. Three mechanisms accounted for the separation process:

- Induced secondary fluid flow carried particles from the bulk of the melt, circulated them until particles are acted upon by either other physical forces (leading to trapping at the side wall or settling to the bottom) or they end up at the top central part of the molten silicon;
- Large inclusions were separated first to the side and bottom walls while small inclusions agglomerated and deposited at these sites due to the influence of the electromagnetic force on particles and settling force.
- The contribution from the EM Archimedes force was to trap particles in the vicinity of the side wall of the crucible;
- Magnetic field and fluid flow simulation results showed uneven distribution of the magnetic field in the molten silicon and the fluid had a circulatory flow pattern with the strongest flow at the bottom of the crucible, allowing particles in this region to settle fastest. Convection and magnetization forces enhanced the effect of gravity forces to settle and cement particles to the bottom of the sample.

References

[1] D. Sarti, R. Einhaus, Silicon feedstock for the multi-crystalline photovoltaic industry, Solar Energy Materials and Solar Cells, 72 (2002) 27-40.

[2] N.B. Mason, Industry Developments that Sustain the Growth of Crystalline Silicon PV Output, in: Proceedings of the Photovoltaic Science, Applications & Technology Conference, Durham UK, 2007, pp. 43-46.

[3] A. Lotnyk, O. Breitenstein, H. Blumtritt, A TEM study of SiC particles and filaments precipitated in multicrystalline Si for solar cells, Solar Energy Materials & Solar Cells, 92 (2008) 1236-1240.

[4] L. Zhang, E. Øvrelid, S. Senanu, B. Agyei-Tuffour, A.N. Femi, Nonmetallic Inclusions in Solar Cell Silicon: Focusing on Recycling of Scraps, in: Rewas2008: 2008 Global Symposium on Recycling, Waste Treatment and Clean Technology, TMS, Warrendale, PA, USA, CANCUN, MEXICO, 2008, pp. 1011-1026.

[5] O.S. Fishman, Solar Silicon Part II Advanced Materials & Processes, 166 (2008) 33-34.

[6] O.S. Fishman, Solar silicon Part I, Advanced materials & processes, (2008) 39-40.

[7] G. Lavorel, M. LeBars, Sedimentation of particles in a vigorously convecting fluid, PHYSICAL REVIEW E, 80 (2009) 046324-046321-046324-046328.

[8] L. Zhang, A. Ciftja, Recycling of solar cell silicon scraps through filtration, Part I: Experimental investigation, Solar Energy Materials and Solar Cells, 92 (2008) 1450-1461.

[9] A. Kolin, An electromagnetokinetic phenomenon involving migration of neutral particles, Science, 117 (1953) 134-137.

[10] D. Leenov, A. Kolin, Theory of electromagnetophoresis. I. Magnetohydrodynamic forces experienced by spherical and symmetrically oriented cylindrical particles, Journal of Chemical Physics, 22 (1954) 683-688.

[11] Y. Tanimoto, Y. Kakuda, Influence of strong magnetic field on the sedimentation of red blood cells Journal of Physics: Conference Series, 156 (2009).

[12] J.Y. Hwang, M. Takayasu, F.J. Friedlaender, G. Kullerud, Application of magnetic susceptibility gradients to magnetic separation, J. Appl. Phys., 55 (1984) 2592-2594.

[13] M. Motokawa, Physics in high magnetic fields, Rep. Prog. Phys., 67 (2004) 1995-2052.

[14] Z. Sun, M. Guo, J. Vleugels, O. van-der-Biest, B. Blanpain, STRONG MAGNETIC FIELD INDUCED SEGREGATION AND SELF-ASSEMBLY OF MICROMETER SIZED NON-MAGNETIC PARTICLES, Progress In Electromagnetics Research B, 23 (2010) 199-214.

[15] K. Takahashi, S. Taniguchi, Electromagnetic separation of nonmetallic inclusion from liquid metal by imposition of high frequency magnetic field, ISIJ International, 43 (2003) 820-827.

[16] F. Yamao, K. Sassa, K. Iwai, S. Asai, Separation of inclusions in liquid metal using fixed alternating magnetic field, Tetsu-to-Hagane, 83 (1997) 30-35.

[17] A. Dong, L. Zhang, L.N.W. Damoah, Benefi cial and Technological Analysis for the Recycling of Solar Grade Silicon Wastes, JOM, 63 (2011) 23-27.

[18] A. Dong, L. Damoah, L. Zhang, Removal of Inclusions from Solar Grade Silicon Using Electromagnetic Field, in: Supplemental Proceedings: Volume I: Materials Processing and Energy Materials, TMS 2011, 2011, p.669-676, pp. 669-676.

[19] L.N.W. Damoah, L. Zhang, High Frequency EM purification of Silicon, in: L. Zhang, A. Allanore, C. Wang (Eds.) EPD Congress 2012, TMS (The Minerals, Metals & Materials Society) 2012 Annual Meeting, Orlando, FL, 2012, pp. 501-508.

[20] K. TAKAHASHI, S. TANIGUCHI, Electromagnetic Separation of Nonmetallic Inclusion from Liquid Metal by Imposition of High Frequency Magnetic Field, ISIJ International, 43 (2003) 820-827.

[21] L.-P. Wang, M.R. Maxey, Settling velocity and concentration distribution of heavy particles in homogeneous isotropic turbulence, J. Fluid Mech., 256 (1993) 27-68.

[22] J. Ruiz, D. Macias, F. Peters, Turbulence increases the average settling velocity of phytoplanton cells, PNAS, 101 (2004) 17720-17724.

[23] A. Aliseda, A. Cartellier, F. Hainaux, J.C. Lasheras, Effect of preferential concentration on the settling velocity of heavy particles in homogeneous isotropic turbulence, J. Fluid Mech., 468 (2002) 77-105.

[24] S. Makarov, R. Ludeig, D. Apelian, Electromagnetic Separation Techniques in Metal Casting. I. Conventional methods, IEEE Transactions on Magnetics, 36 (2000) 2015-2021.

[25] D. Shu, B. Sun, K. Li, J. Wang, Y. Zhou, Effects of secondary flow on the electromagnetic separation of inclusions from aluminum melt in a square channel by a solenoid, ISIJ Inter., 42 (2002) 1241-1250.

[26] F.U. Bruckner, K. Scwerdtfeger, Single Crystal Growth with the Czochralski Method involving Rotational Electromagnetic Stirring of the Melt, J. Crystal Growth, 139 (1994) 351-356.

II. SETTLING OF INCLUSIONS IN SILICON UNDER ELECTROMAGNETIC FIELD

Lucas Nana Wiredu Damoah, Lifeng Zhang, Kent D. Peaslee

Department of Materials Science & Engineering
Missouri University of Science and Technology (Missouri S&T)
223 McNutt Hall, Rolla, MO 65409-0340, USA
Email: zhanglife@mst.edu

This manuscript has been prepared for submission to Solar Energy Materials and Solar Cells

Abstract

Several methods to recycle the top-cut silicon scrap generated during directional solidification of solar silicon are currently being researched. One of these is settling under a gravitation field. However, natural settling of inclusions by gravitational forces is a slow process and not attractive to industry. This study investigates the settling of micrometer size inclusions (≤ 10 μm) from silicon under a high frequency electromagnetic field. The results show enhanced settling of SiC particles to the bottom of the sample within one minute under the electromagnetic field. This is in contrast to the settling by gravity in a high temperature furnace without an electromagnetic field in which almost all of the particles remained dispersed within the sample after more than nine hours. The proposed mechanisms responsible for the improved settling under the electromagnetic field are largely due to electromagnetic stirring and to a less extent the effect of the magnetization forces resulting from difference in magnetic susceptibility between the liquid metal and particles under a gradient magnetic field. Increases in the separation time, coil current, and frequency of the field improved the separation results significantly. Longer separation time allowed particles close to the top to be carried by fluid flow and held at the bottom by settling forces. Higher coil current generated a stronger magnetic field leading to a stronger fluid flow, while higher frequency gave rise to a better distribution of flow velocity leading to an improved settling.

1. Introduction

The photovoltaic (PV) industry depends on silicon based materials either as single-crystalline silicon, multi-crystalline silicon (MC-Si), or amorphous silicon [1] for over 90 % of its market share.[2] MC-Si produced by directional solidification of molten solar grade silicon melt dominates the silicon PV market. During the directional solidification process, SiC and Si_3N_4 particles within the melt are pushed by the solidification front to the top part of the ingot which solidifies last. Therefore the top of the ingot is cut generating what is known as top-cut solar silicon scrap. The Si_3N_4 particles are mainly from the coating material on the inner surface of the silica crucible and from air absorption during the solidification process. The SiC particles mainly stem from the carbon reduction process in the primary production of silicon [3]. Due to the growth of the PV industry as a result of global demand for clean, reliable, and affordable

energy [4], there is a need to develop new methods to compliment exiting ones to recycle SoG-Si wastes (e.g. top-cuts) for sustainability.

Settling of inclusions in silicon has been investigated as one of the methods to purify silicon.[5] However, settling of particles based on natural densities could take too long to accomplish and therefore not industrially attractive. It is well known that particles settle in highly convective fluids although there are limits to the level of convection [6] due to the likelihood of turbulent diffusion of particles hindering effective settling of particles. The application of an AC electromagnetic field to a molten metal system may induce fluid flow, enhancing convection and resulting in the ability to improve the settling rates of particles. Hori [7] concluded in his study that by the application of an electromagnetic field to a mixed phase fluid even particles of density less than the fluid can be settled and particles of density greater than the fluid could float or rise to the top. Tanimoto and Kakuda have utilized magnetization forces resulting from an electromagnetic field gradient and based on the magnetic susceptibility difference between suspended particles and the fluid were able to settle red blood cells in a solution [8]. Hwang *et al.* [9] used the difference in magnetic susceptibilities to separate particles from magnetic colloidal fluid. Jin et al. [10] have studied the effect of a high gradient magnetic field on the migratory behavior of primary silicon crystals in hypereutectic Al-Si alloy. They found that under the field, the silicon grains migrated toward one end of the specimen and the thickness of the segregated silicon layer increased with increasing magnetic flux density. They also found that below a magnetic field of 2.3 T, the movement of the silicon grains was not noticeable and showed that static fields played a role in impeding the movement of the silicon crystals.

The advent of superconductors has made the attainment of strong magnetic fields easier [11] and has promoted the study of many interesting phenomena related to materials processing. Some of these are magnetic orientation [12], magneto-hydrodynamics [13], magneto-thermodynamics [14], magnetic effect on chemical reactions [15], crystallization and refining of metals [16]. Sun et al. [16] investigated the effect of a strong magnetic field on the interaction between particles, induced segregation [17], and particle assemblage . They reported enhanced migration of micro size particles from the melt under the influence of a strong gradient magnetic field. They explained that

the particle segregation was the result of inter-particle interaction and migration due to magnetization under the strong magnetic field.

These studies indicate the potential to use electromagnetic fields to separate inclusions from metals either by floating or settling. In this study, the feasibility of using a high frequency AC electromagnetic field to settle suspended inclusions in top-cut silicon is explored and the effect of parameters such as separation time, coil current and the frequency on the separation process studied on a Si–SiC composite material. A graphite susceptor and graphite crucible or sheath around a quartz crucible are arranged within the induction coils, while inducing fluid flow within the silicon melt to enhance settling of the nonmetallic particles.

2. Materials and Experimental Procedure

2.1. Top-cut SoG-Si scrap

Directional solidification is employed during the production of MC-Si for solar cells. In the process, the molten silicon is solidified from the bottom of the furnace. As a result, dispersed inclusions are pushed toward the top surface by the solidification front. Therefore, the top-part of the solidified silicon ingot contains detrimental particles and elemental impurities, and is cut-off to generate the top-cut solar silicon scrap. The inclusions are mainly SiC and Si_3N_4 particles with respective lumpy and rod-like characteristic morphologies as shown in Figure 1. The Si_3N_4 inclusions on the topmost surface appeared with hexagonal cross-sections and are needlelike, several mm long and approximately 20 μm in diameter. SiC particles are lumpy and as large as several hundred micrometers. Inside the silicon, the Si_3N_4 inclusions are usually shorter than 500μm with an average diameter of ~20μm, and the SiC inclusions are smaller than 200μm. The quantity, size and morphology of inclusions changed with depth beneath the top surface. Inclusion clusters with complex morphologies were observed, and these clusters contained both SiC and Si_3N_4 particles beneath the top-surface.

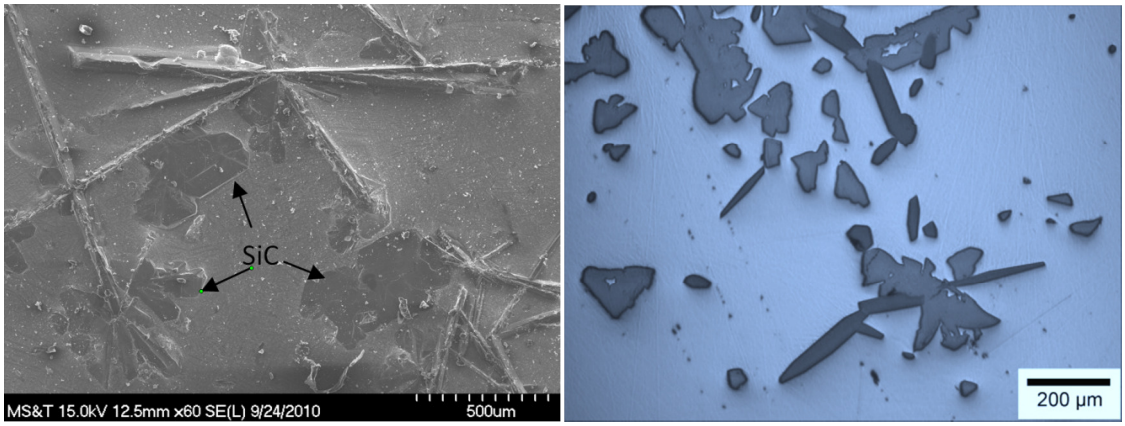

Fig. 1. Optical micrographs of inclusions in a top-cut SoG-Si scrap on the surface (left) and at a depth of 1mm beneath the top surface showing lumpy SiC and rod-like Si_3N_4 particles.

2.2. Si(Al) – SiC Composite

The top-cut SoG-Si scrap have particles concentrated on one of the sides. This makes studies involving particle distribution after the separation process difficult. Therefore, a composite material of silicon containing about 1–2 Wt% aluminum and 3 % SiC particles was prepared by a "stir-solidification" process. In this process, metallurgical grade silicon was melted with electronic grade Al–37 % SiC composite material at 1500^{o}C in an induction furnace. The furnace was turn off after melting and the molten material was stirred continuously with a mullite rod until it solidified. Figure 2 summarizes this process with micrographs of the metallurgical grade silicon, Al–37 % SiC composite and the resulting Si (Al)–3 % SiC composite.

2.3. Equipment and Experimental Set-up

The experimental equipment is made of a water cooled copper induction coil of 7 turns, 196 mm high and 150 mm in diameter. The copper tubing has a 14 mm by 14 mm square cross-section and 12 mm adjacent turn spacing. The coil was powered by a 100 kW generator with a capacitor bank and the capability to change frequency within the range 50-200 kHz by changing the capacitance within the circuit. The power supply is also equipped with LCD touch screen panel where power input can be made and current, voltage, frequency and power information were recorded during the experiment. The set-

up included a graphite susceptor and crucible system as shown in Fig.3. The graphite susceptor, sheath and crucible system all contributed to generating non-uniform magnetic field distribution within the melt due to the high frequency nature of the induced magnetic field.

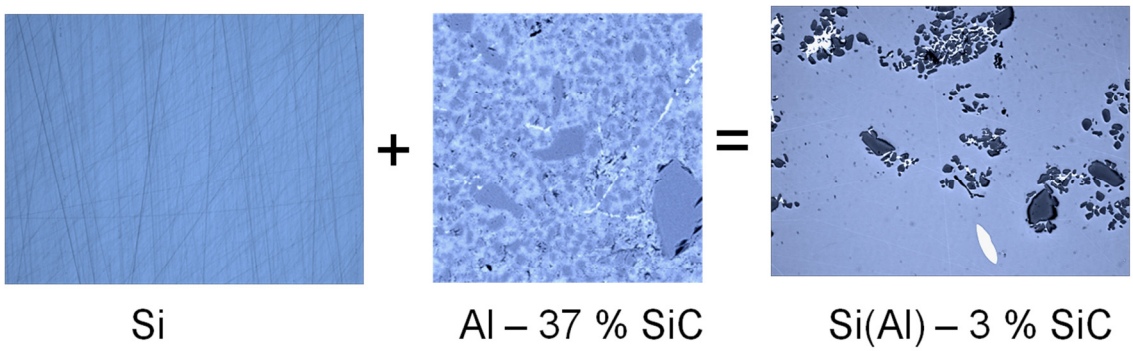

Fig. 2. Si (Al) – 3 % SiC composite material made from metallurgical silicon and Al – 37 % SiC composite through stir solidification.

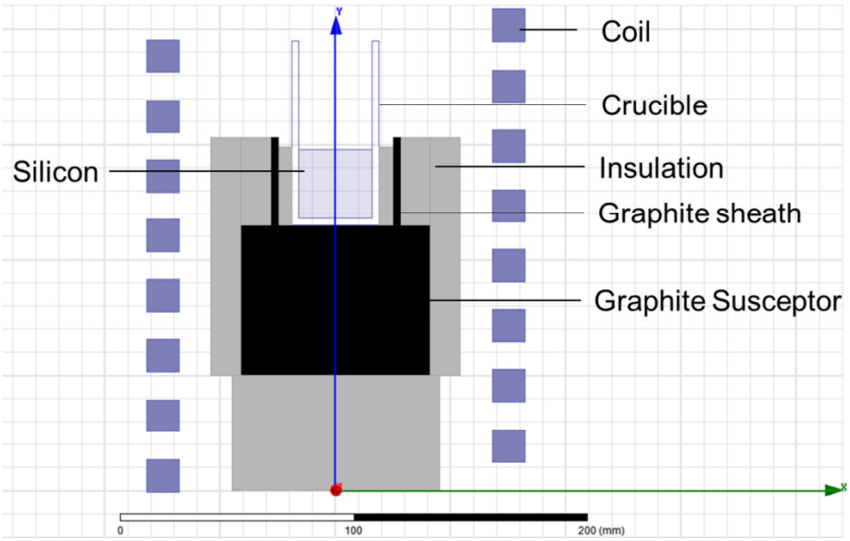

Fig. 3. Scaled schematic of the experimental set-up used for the electromagnetic settling experiments.

2.4. Experimental Procedure for Particle Settling in Top-cut SoG-Si Scrap

To investigate the distribution of particles in the top-cut silicon scrap under natural settling, 50 g of top-cut scrap was prepared and heated in an Al_2O_3 crucible in a

high temperature furnace without an electromagnetic field. The sample was heated at a rate of 4 ^{o}C/min to 1600^{o}C and held for two hours and then cooled at 4 ^{o}C/min to room temperature. Two other experiments were carried out on top-cut scrap under magnetic field. Table 1 gives information about experiments carried out in this study. About 50 g of top-cut scrap was prepared and melted in a graphite crucible with 40 mm inner diameter under electromagnetic field (Si-SD-2 and Si-SD-3). After melting and the molten silicon was at a temperature of approximately 1500^{o}C, the power supply was turned off and the separation parameters were set, then the power supply was turned back on. The molten silicon was allowed to stay under the EM field for 2 minutes in the separation process, after which the power supply was turned off and the sample allowed to cool down to room temperature. The solidified materials were carefully sectioned vertically and samples were prepared and studied with optical and scanning electron microscopes.

Table 1 Experimental scheme used for the EM sedimentation experiments

Exp. #	Coil Current, I_{rms} (A)	Frequency (kHz)	Temperature (^{o}C)
Si-SD–0	No	No	1600 for 3 hours
Si-SD–1	180	76	1500
Si-SD–2	180	64	1500

2.5. Experimental Procedure for Settling of Inclusions in Si(Al) – SiC Composite

The Si(Al) – SiC composite material prepared by the stir-solidification process was cut into pieces each of about 60 g in mass for this study. Particle size distribution in the silicon composite material is shown in Fig. 4. The average particle size was 10 μm with many particles as small as 1 μm. To study the effect of gravity sedimentation on particles in this material, a sample was melted to 1600 ^{o}C at a heating rate of 4 ^{o}C/min without electromagnetic field, and held for 9 hours before cooling down at the same rate to room temperature in an experiment numbered SD-0. In some electromagnetic separation experiments, quartz or alumina crucible with a graphite sheath was used in

place of graphite crucible in this steady to avoid molten silicon-crucible reactions. Table 2 summarizes the experimental plan used in this study.

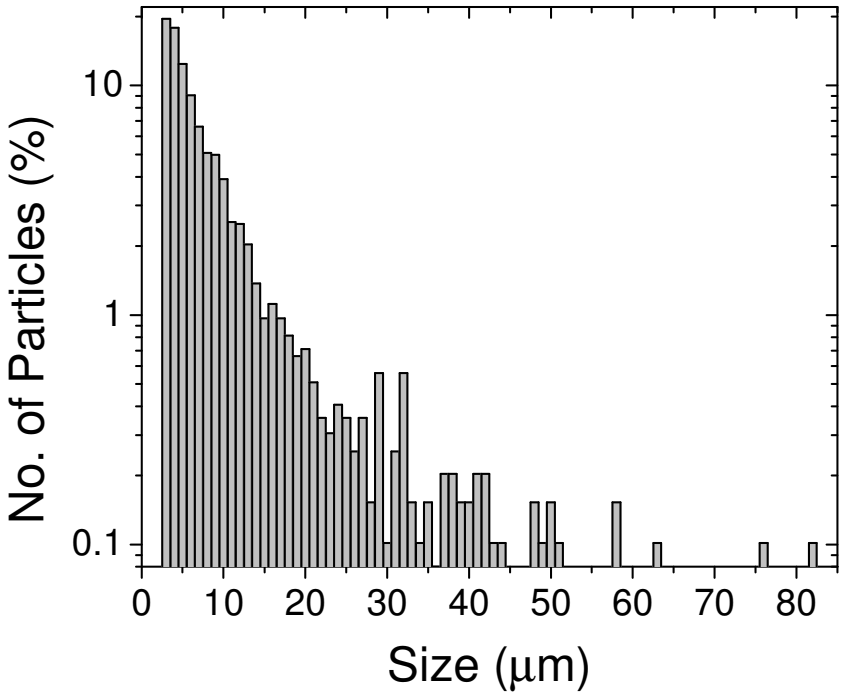

Fig. 4. Particle size distribution of inclusions in the Si (Al) – 3% SiC composite material.

Table 2 Summary of the experimental plan used in this study.

Exp. #	Crucible Material	Coil Current, I_{rms} (A)	Frequency (kHz)	Separation time (s)
SD 1	30 mm diameter graphite crucible	270	65	10
SD 2				30
SD 3				60
SD 4				90
SD 5	32 mm diameter SiO_2 crucible	486	65	50
SD 6		397		
SD 7		305		
SD 8		268		
SD 9			75	
SD 10			90	
SD 11	30 mm diameter Al_2O_3 crucible	370	65	10
SD 12				30
SD 13				70

During the experiment the composite material was placed in the crucible set in place within the coil. The power supply was turned on to melt the material. When complete melting occurred, the separation conditions were set and separation allowed for a set period of time. The equipment was turned off and the sample cooled to ambient temperature. All the samples were melted for a period of 15 minutes using a coil current of 230A before particle separation. The sample was then sectioned vertically to form four quarter sections. A quarter vertical cross-sectional sample was polished for each experiment and analyzed by means of optical macro- and micro-scopes and SEM/EDX.

2.6. Modeling of Magnetic Field and Fluid Flow

To understand the particle separation mechanism, magnetic field and fluid flow simulations were undertaken. The magnetic field in the experimental set-up was modeled in the finite element magnetic field simulation software ANSOFT Maxwell, and the MagnetoHydroDynamics (MHD) was calculated *via* ANSYS FLUENT utilizing the magnetic field data from the ANSOFT Maxwell calculations.

2.6.1. Modeling of Magnetic Field

A 3D model of the experimental set-up was created to scale in ANSOFT Maxwell and the eddy current solver was used to simulate the electromagnetic field which is described by Maxwell's equations (Eq. (1)):

$$\begin{cases} \nabla \cdot B = 0 \\ \nabla \times E = -\dfrac{\partial B}{\partial t} \\ \nabla \cdot D = q \\ \nabla \times H = j + \dfrac{\partial j}{\partial t} \end{cases} \tag{1}$$

where B (Tesla) and E (V/m) are the magnetic and electric fields respectively, and H and D are the induction fields for the magnetic and electric fields respectively. q (C/m^3) is the electric charge density, and j (A/m^2) is the electric current density vector. The skin-depth based approach was adopted to mesh the model shown in Fig. 5 and the insulation boundary condition was employed in the calculation. This boundary condition assumes

there is a perfectly insulating sheet between electrical conductors and that the current cannot pass across it, and the magnetic field is tangential to the boundary.

2.6.2. MHD Modeling with ANSYS FLUENT

A 2D model of the experimental case was created and meshed in ANSYS Gambit for a 32 mm in diameter by 30 mm high cylindrical crucible. The mesh was made of 3840 quadrilaterateral cells of 0.5 mm × 0.5 mm and 3965 nodes. Figure 6 shows the structure of the mesh.

Ohm's law and Maxwell's equations present the coupling between the electromagnetic and fluid velocity field. Eq.(2) defines Ohm's law for an electrically conductive molten metal with a velocity field U.

$$j = \sigma\left(E + U \times B\right) \tag{2}$$

The magnetic induction equation can be derived from Eqs. (1) and (2) for a conductive medium as:

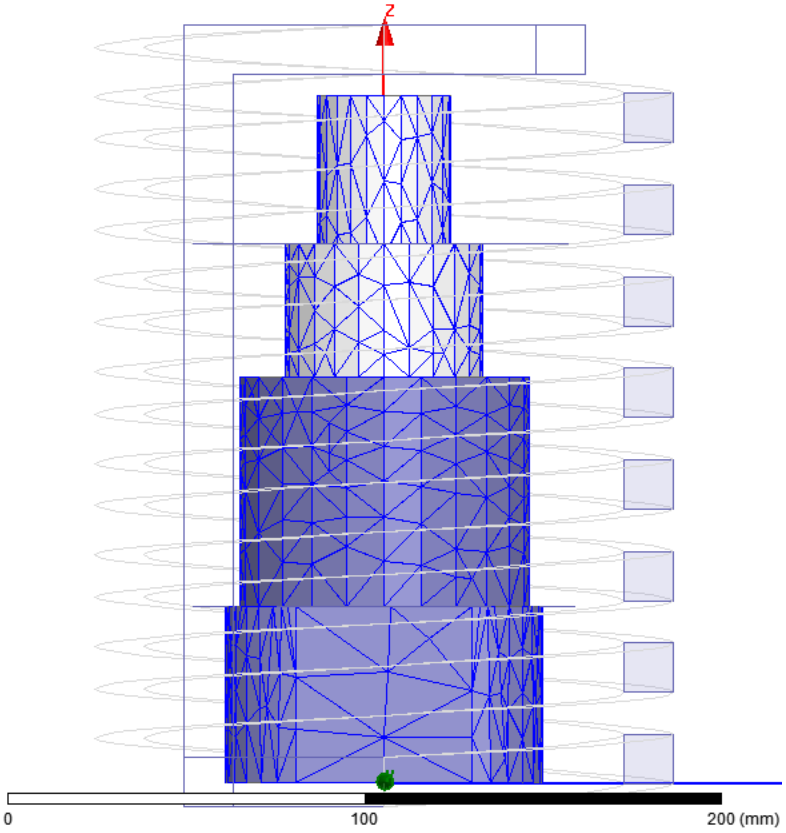

Fig. 5. View of the skin-depth based mesh of the 3D geometry of solids within the coil.

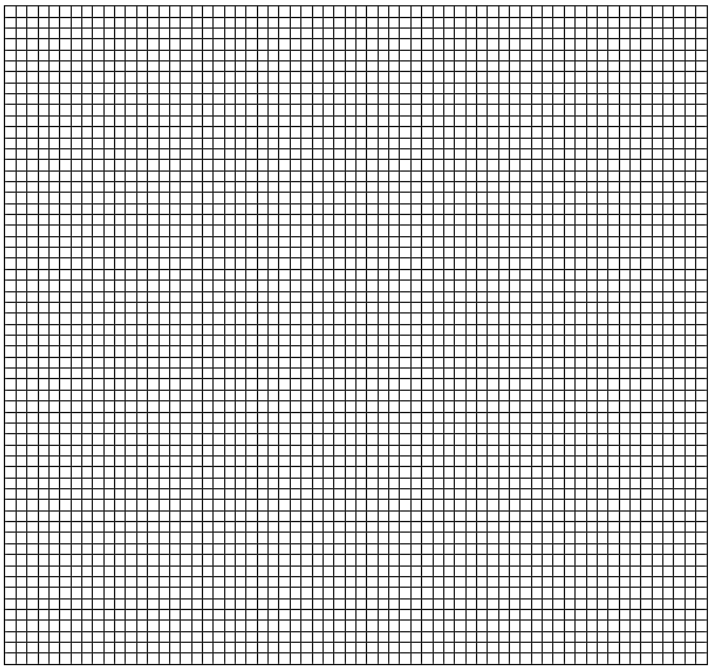

Fig. 6. 2D Mesh of the model solved in ANSYS Fluent.

$$\frac{\partial b}{\partial t}+\left(U\cdot\nabla\right)b=\frac{1}{\mu\sigma}\nabla^2 b+\left(\left(B_o+b\right)\cdot\nabla\right)U-\left(U\cdot\nabla\right)B_o \tag{3}$$

where B_o and b are the externally imposed and induced magnetic fields, respectively, and μ and σ are the magnetic permeability and electrical conductivity of the molten metal respectively.

The current density based on Ampere's law is given by:

$$j=\frac{1}{\mu}\nabla\times\left(B_o+b\right) \tag{4}$$

The boundary condition for the induced field was set as electrically insulating which means $j = 0$ and the tangential components of the magnetic field are zero.

2D transient turbulent fluid flow and heat transfer for the model was calculated by solving the continuity equation, two Navier-Stokes momentum equations, the two equations for turbulent energy and its dissipation rate and the general energy equation. Due to the effect of the electromagnetic fields, additional source terms are introduced to the fluid momentum equation (i.e. Lorentz force (N/m^3) given by Eq.(5)) and energy equation (i.e. Joule heating rate given (W/m^3) by Eq. (6)).

$$F = j \times B \tag{5}$$

$$Q = \frac{1}{\sigma} j \cdot j \tag{6}$$

The no-slip and stationary wall boundary conditions were employed for the momentum equations. The temperature boundary conditions used are 1823.15 K for the side wall, 1973.15 K for the bottom wall and a backflow temperature of 1773.15 K same as the temperature of molten silicon. The wall thickness was 0.003 m for both the side and bottom walls. Table 3 presents data for materials properties used in the calculations. For the initial conditions, the velocity and turbulent parameters were all set to zero. The solution was obtained by iterating at a time step-size of 1.0×10^{-5} s to cater for the possible high frequency errors.

Table 3 Data of materials properties used in the calculations.

Property	Silicon	SiO_2 crucible	Graphite
Density, ρ (kg/m^3)	2570	2210	/
Viscosity, η (kg/m-s)	0.000543	/	/
Thermal conductivity, k (W/m-K)	58	2.01	/
Specific heat capacity, C_p (j/kg-K)	900	733	/
Electrical conductivity, σ (S/m)	1400000	0	1200000
Magnetic permeability, μ (H/m)	1.26×10^{-6}	1.26×10^{-6}	1.26×10^{-6}

3. Results and Discussion

3.1. Settling of Particles in Top-cut SoG Silicon

Combined optical images of the vertical cross-section of the sample from experiment Si-SD-0 conducted without the influence of electromagnetic field is showed in Fig. 7. The distribution of inclusions within the sample after the experiment is observed. It can be clearly seen that after over 3 hours of settling (including the ramping and periods above the 1414 ^{o}C which is the melting point of silicon) almost all the

inclusions stayed close to the top of the sample, an indication of how slow the settling process by only gravity effects could be. The densities of molten silicon, SiC and Si_3N_4 inclusions are shown in Table 4 which indicates appreciable difference between the particles and the molten silicon. Based on data of viscosity of silicon presented by Sato *et al.* [18] the terminal velocities of SiC and Si_3N_4 could be predicted for various particle sizes as shown in Fig. 8. The terminal velocities become significant for particle sizes >20μm (i.e. 270 μm/s for SiC and 370 μm/s for Si_3N_4). By implication, all particles >20μm should settle to the bottom of 30 mm high molten silicon within 2 hours. However, this was not the case observed in the experiment even for particles as large as 100 μm and larger. A probable reason is that the actual viscous forces are higher than that presented in the literature [18].

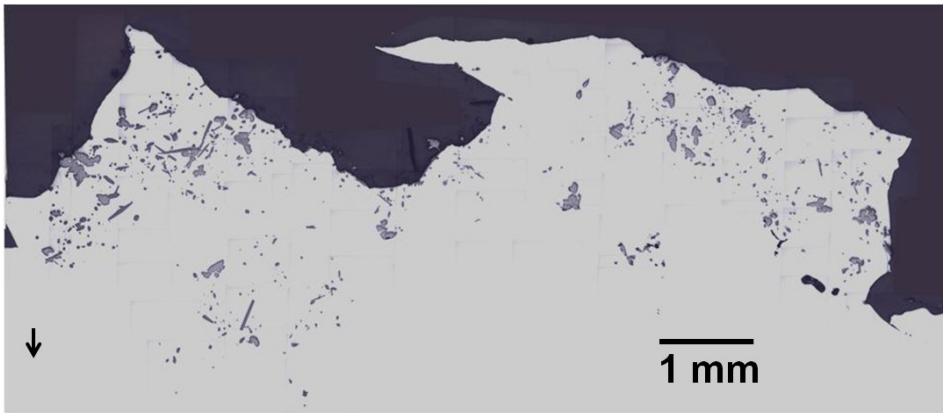

Fig. 7. Collection of optical micrographs showing the distribution of inclusions in a top-cut SoG-Si scrap melted at 1600°C at a heating rate of 4 °C/min and held for two hours before cooling at 4 °C/min to room temperature in a high temperature furnace without EM field. Almost all the particles stayed at the top part of the sample. The arrow shows the direction of gravity.

Table 4 Comparison of densities of molten silicon and inclusions.

Material	Density, g/cm^3	Magnetic Susceptibility, χ ($\times 10^{-5}$)
Molten silicon	2.57	-0.37
SiC	3.21	-1.29
Si_3N_4	3.44	/

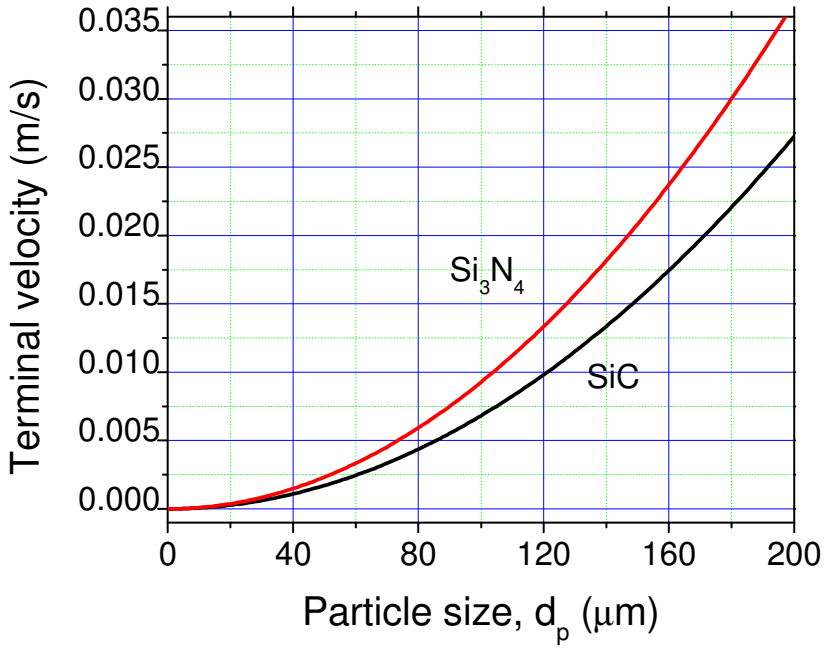

Fig. 8. Terminal velocity of Si_3N_4 and SiC particles in silicon at 1600°C.

When an electromagnetic field was imposed the distribution of inclusions had a different pattern. Figure 9 shows the distribution of inclusions close to the bottom of the sample from experiment Si-SD–1. As is evident, the particles settled to the bottom of the sample. Similar results were obtained in the case of experiment Si-SD–2, indicating repeatability. The distribution of particles along the direction of gravity from the top to the bottom of the two experimental samples is shown in Figure 10 which demonstrates that the particles moved to the bottom of the sample under the electromagnetic field. A continuous phase of SiC particles was also observed at the walls of the crucible and at the bottom as a result of interaction between the graphite crucible material and the molten silicon, as shown in Figure 11. On top of the samples, a continuous phase of SiO_2 was observed indicating silicon oxidation at the top surface. Figure 12 presents further details about the inclusion distribution in the samples from experiment Si-SD–2 showing part of the top and the bottom sections of the sample.

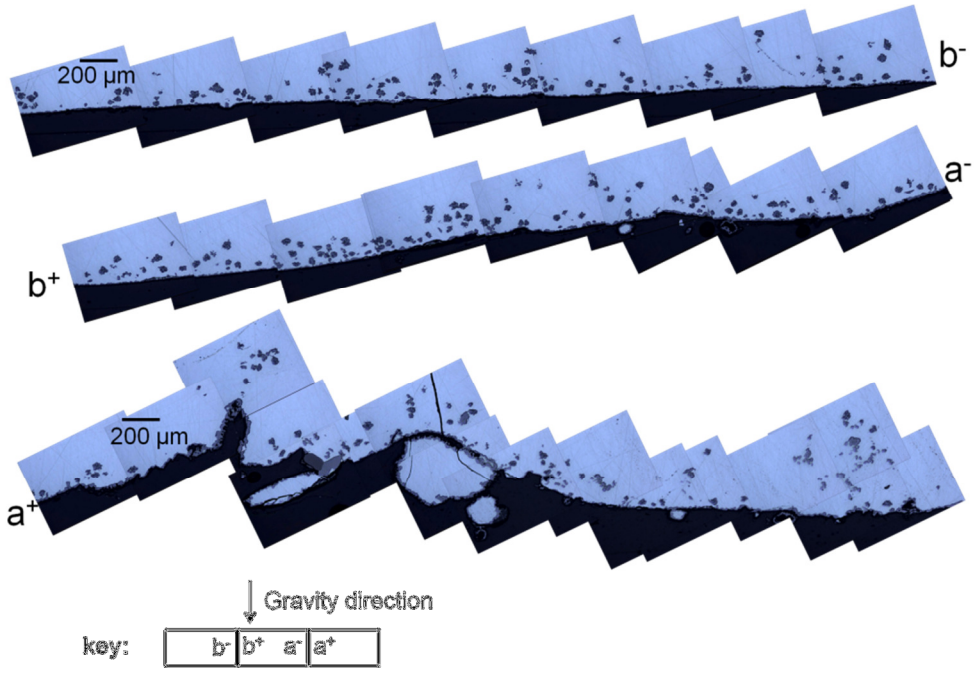

Fig. 9. Optical micrographs of the bottom of the sample after the EM settling experiment Si-SD–1 showing that inclusions settled to the bottom of the crucible and were well distributed along the diameter. The characteristic rod-like Si_3N_4 morphologies were not observed after the experiment.

3.1.1. Status of Si_3N_4 particles in top-cut scrap after EM experiments

The characteristic Si_3N_4 rod-like morphologies observed in Figs. 5 and 6 were not evident in the inclusion distribution micrographs of the treated samples. Optical micrographs and SEM/EDX analysis have both proven unsuccessful in detecting the Si_3N_4 particles in the samples. Several possibilities could explain this observation:

- Decomposition of Si_3N_4 due to contact with air or water molecules to gaseous Si-O-H species and N_2 or NO_x gas species.
- Thermal decomposition of Si_3N_4 resulting from local heating under such a high voltage field (the coil voltage was 300 – 500 V).
- Reaction of Si_3N_4 with oxygen to form silicon oxynitride glassy phases in the top slag layer. SEM/EDX studies of the top layer detected no nitrogen. There is also the question of why would the SiC particles settle to the bottom while Si_3N_4 particles rise to the top?

- Recrystallization of Si_3N_4 in the melt. The solubility of nitrogen in the melt is appreciably low to allow for Si_3N_4 to recrystallize.

Further investigation is required to establish the actual reason responsible for the non-detection of Si_3N_4 particles in the samples after the EM settling experiments.

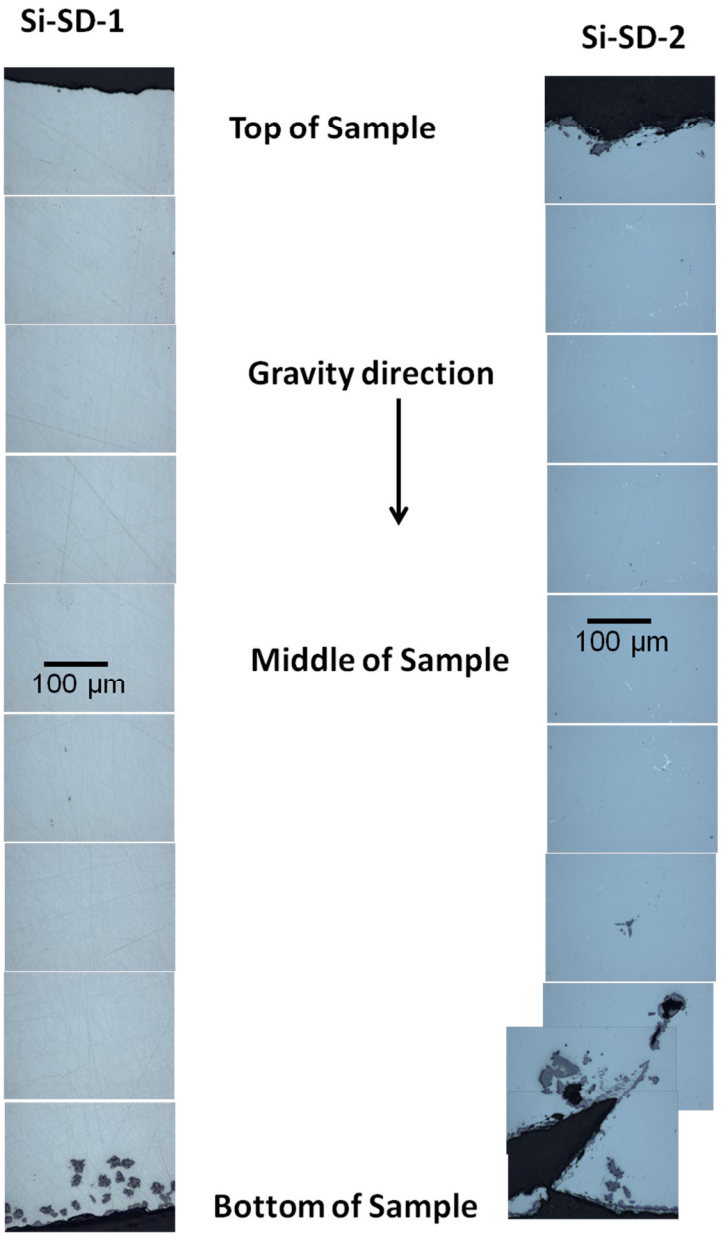

Fig. 10. Optical micrographs from top to bottom of the samples after the EM settling experiments Si-SD–1 and Si-SD–2 showing a cleaner inner silicon matrix and settled particles at the bottom of the samples. The apparent particle seen at the top of the sample in Si-SD–2 is a continuous SiO_2 slag layer indicating oxidation.

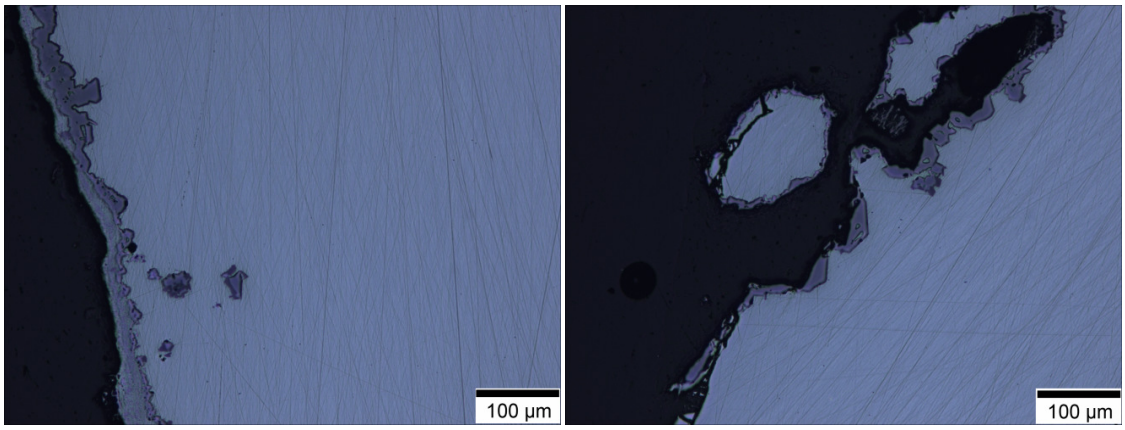

Fig. 11. Optical micrographs showing a continuous SiC phase generated as a result of the interaction between the graphite crucible and molten silicon at the walls of the crucible. These photos indicate significant interaction between the molten silicon and carbon to generate inclusions.

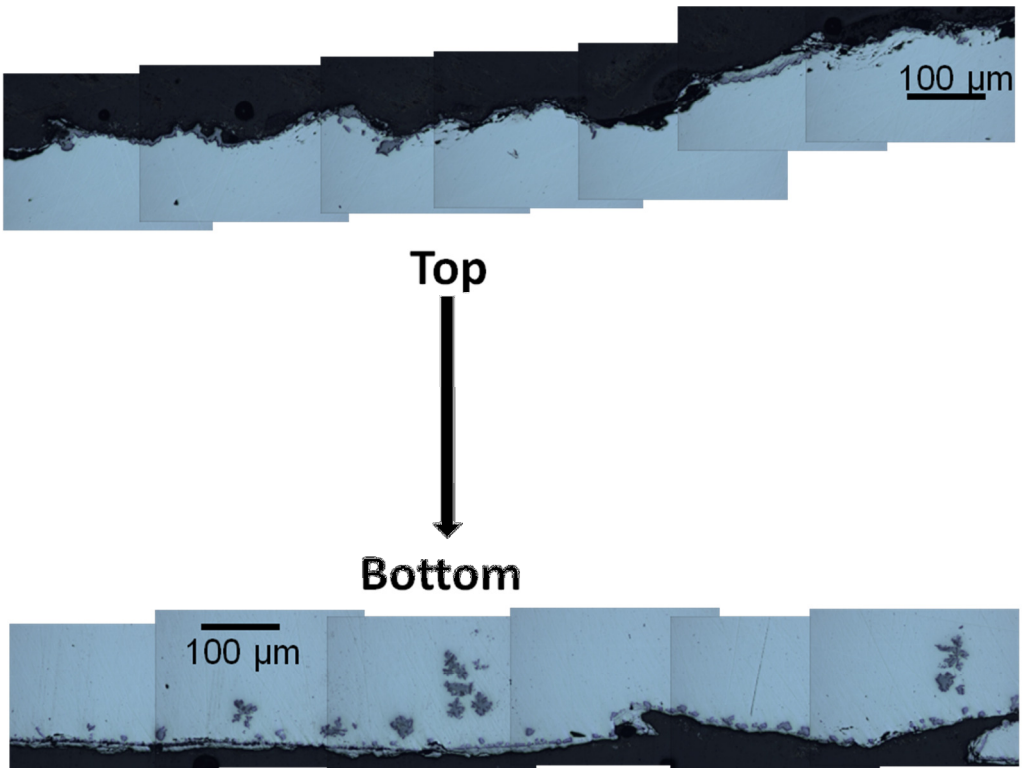

Fig. 12. Part of the top and bottom views of the sample from experiment Si-SD–2 showing settled particles at the bottom, a continuous slag layer on top and a continuous SiC reaction layer at the graphite-molten silicon interface.

3.2. Settling of Particles in Si (Al) – SiC Composite Material

Results from experiment SD-0 showed that even after over 9 hours of settling, particles remained mainly within the matrix rather than settling to the bottom as shown in Fig. 13. The bright dotted phases in the macrograph are the particles, and the dark phase is the primary silicon phase.

Figure 14 shows a quarter vertical cross-sectional macrograph and micrographs showing the microstructures of the sample at the top, middle and bottom. Separation between the SiC particles and the matrix is seen in the figure. Few particles were observed within the top 400 µm but unlike the dense particulate layer at the bottom, the particles at the top were sparsely dispersed. The density of the separated particle layer at the bottom suggests the presence of a strong effective downward force that acted on the particles during the separation process. It can be noted from the figure that particles of all size ranges settled in the process, which is contrary to the results of previous researchers [19-20] that indicate higher efficiencies for particles larger than 100 µm. Makarav *et al*. [21] imposed a helical super conducting coil to separate nonmetallic inclusions from aluminum by sedimentation but achieved little success. They proposed the reason for the poor experimental results compared to the theoretical analysis was the presence of flow inhomogeneity and turbulence in the experiments.

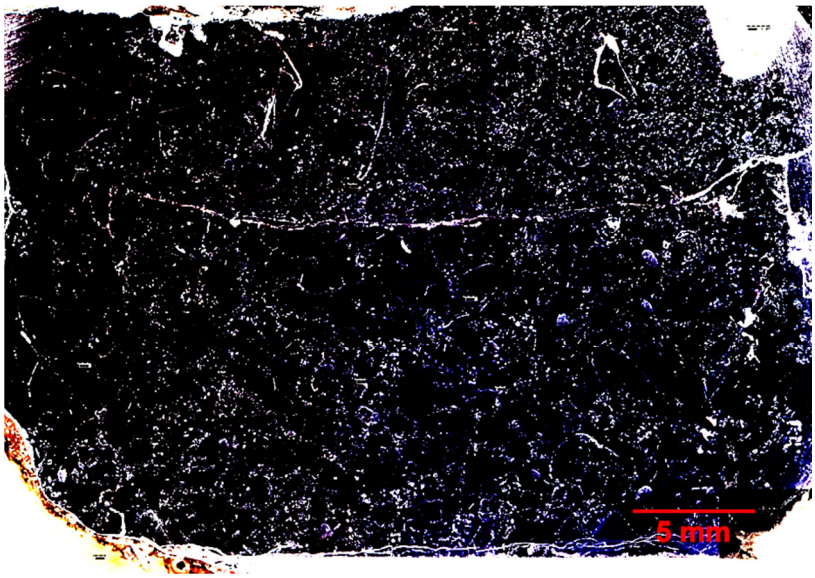

Fig. 13. Distribution of particles across a vertical cross-section sample after gravity sedimentation at 1600 ^{o}C for 9 hours.

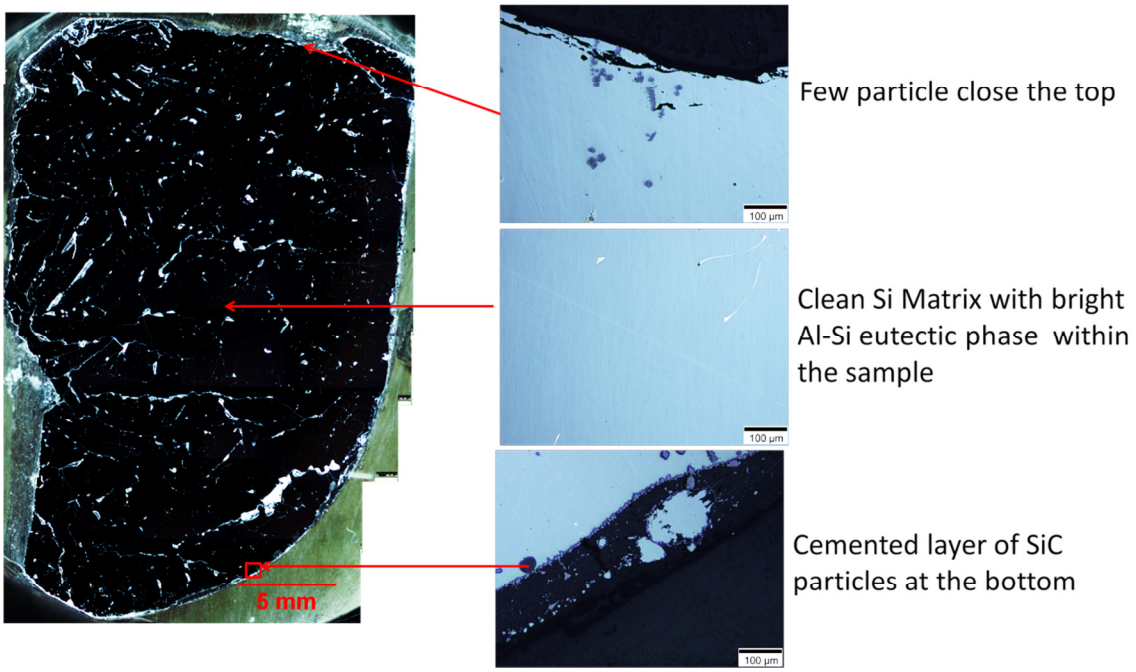

Fig. 14. Optical macro- and micro-graphs of a quarter vertical cross-sectional view of the sample from the settling experiments using 486 A coil current, at 65 kHz and separated for 50 s.

3.2.1. Quantification of settling results

Results from the settling experiments were quantified by two methods: (i) separation efficiency and (ii) particle distribution (or particle concentration) within the matrix.

(i) Separation efficiency

The separation efficiency (η) was defined as the ratio of the clean volume to the total volume of sample which is the ratio of the clean height (h) to the total height (H) of sample for a uniform cross-section as illustrated in Fig. 15.

$$\eta = \frac{h}{H} \times 100\% \tag{7}$$

(ii) Particle concentration

Particle concentration was measured for various positions along the height of the sample. This was done using the particle analysis tool in image processing software *imageJ* to

calculate the area fraction of particles at a position. During the analysis, color threshold was defined for the particles as illustrated in Fig. 16 for an optical micrograph of that area. By this method the profile of area fraction of particles along the height of the sample could be made in a plot of particle concentration *versus* position along the height.

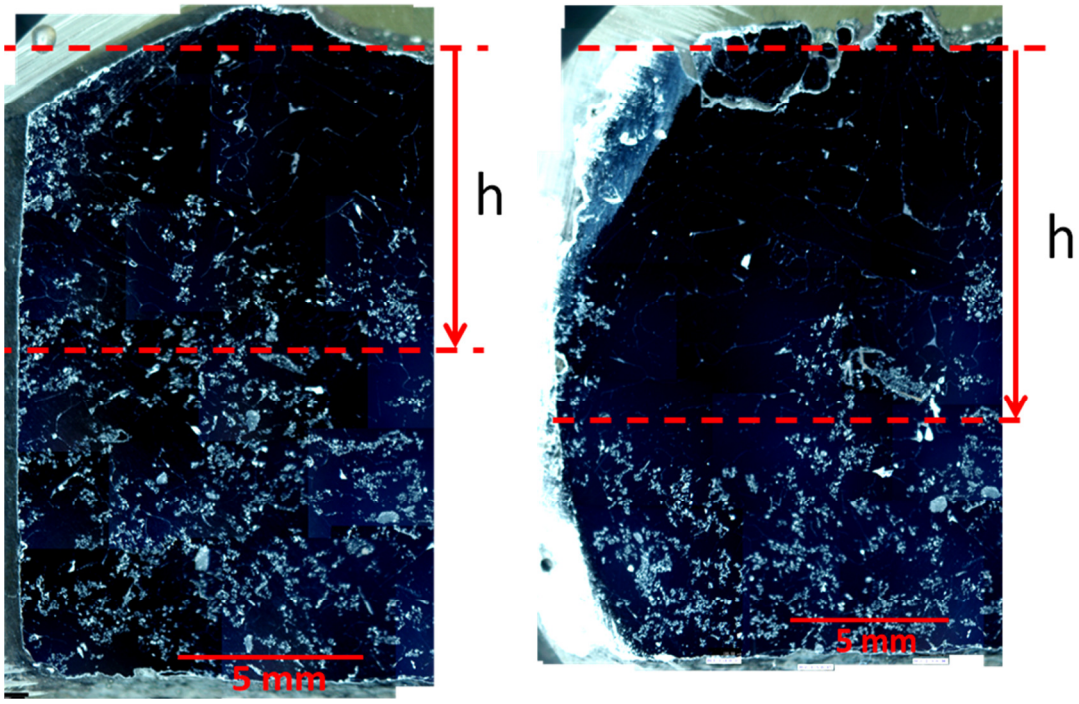

Fig. 15. Optical Macrographs of vertical cross-sections of samples showing the effect of time on the separation process for 10 s (left) and 30 s (right) as repective examples of 45 % and 60 % separation in graphite crucible at I_{rms} = 270 A and f = 65 kHz.

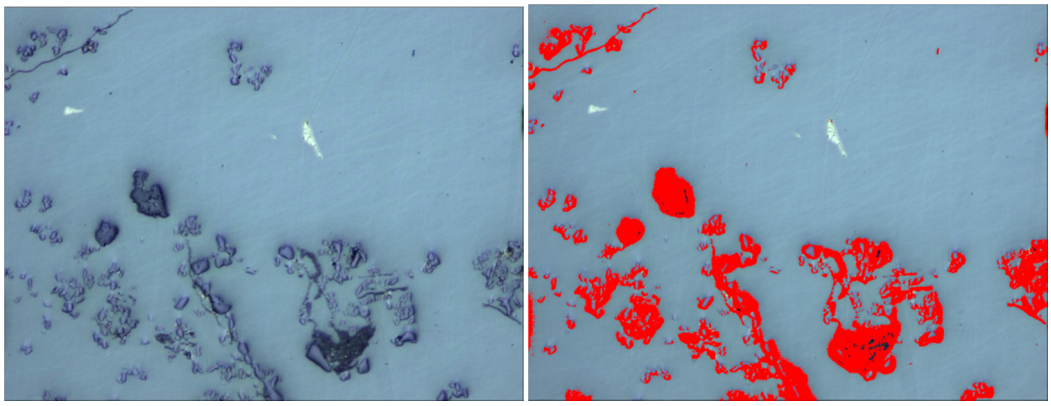

Fig. 16. Area fraction determination using particle analysis tool in image processing software *imageJ*.

3.2.2. Effect of Separation Time

As shown in Fig. 17 longer separation times resulted in higher separation efficiencies. Time is required for the transport of particles within the molten silicon to the bottom. Therefore, for improved separation results, more time is required at the effective current and frequency. Clear differences existed between separation in graphite crucibles and separation in alumina or silica crucibles. Even at lower current, better separation was recorded for the graphite crucible than for alumina crucible.

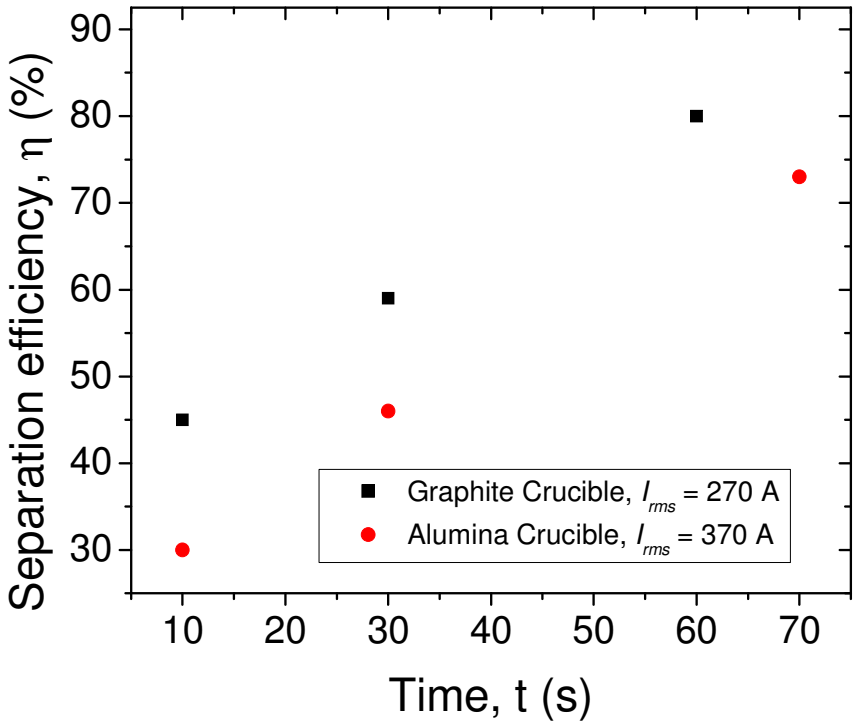

Fig. 17. Dependence of the separation efficiency with time for experiments in graphite and alumina crucibles at 65 kHz.

The reason why separation in a graphite crucible requires less current than in the alumina or quartz crucible is not readily understood. This is probably the effect of direct contact between the molten silicon and graphite crucible enhancing induced current flow and thus stronger induced magnetic field into the molten silicon.

3.2.3. Effect of Coil Current, I_{rms} and Frequency

The current flowing through the coil determines the imposed magnetic field strength. Therefore, higher currents cause stronger magnetic fields and stronger induced fluid flow, hence better separation. Though the limit to the current is not known at the moment, it is believed that too high of a current could produce fluid flow too strong to result in a back diffusion of already settled particles and hence poor separation results. Frequency is a measure of how much the field changes within one second. The higher the frequency, the faster the magnetic field changes and the more unstable the molten silicon becomes. Therefore, higher frequency increases the velocity of the fluid flow.

Figures 18 and 19 compare the particle separation results obtained for different currents and frequencies in a quartz crucible, which demonstrate that increasing current and frequency leads to better separation. However, increases in current have a more significant effect on the separation than increases in frequency. This is seen in the pictures of particles distribution of the samples for various currents and frequencies shown in Figs. 20 – 22. The plots of particle distribution along the height of the sample show that close to the top of the samples there are some particles within about 1mm, which reduces to no particles and the particle concentration begins to increase at some point along the height of the samples until the maximum particle content is obtained at the bottom. Comparing microstructure of the relevant sections shown in Figs. 14 and 21 demonstrates that higher current induces stronger forces acting on the particles during the separation process. While the bottom layer of the sample separated at 486 A coil current shown in Fig. 14 appeared very compact, there appeared a relatively thinner compact particle layer with a thick less compacted particle layer on top of it near the bottom of the sample separated at 397 A (see Fig. 21). In addition, more particles remained close to the top for the lower than for the high current separated sample. In Figs. 22, it is seen that increasing the frequency from 65 kHz to 90 kHz at a coil current of 268 A in 50s resulted in much improved particle settling.

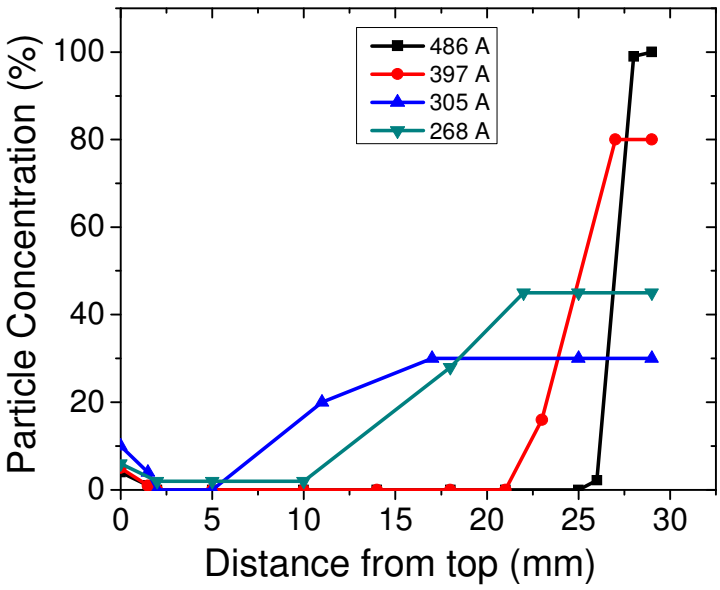

Fig. 18. Distribution of particles (area percent) from top – bottom of the sample comparing separation at the different coil currents.

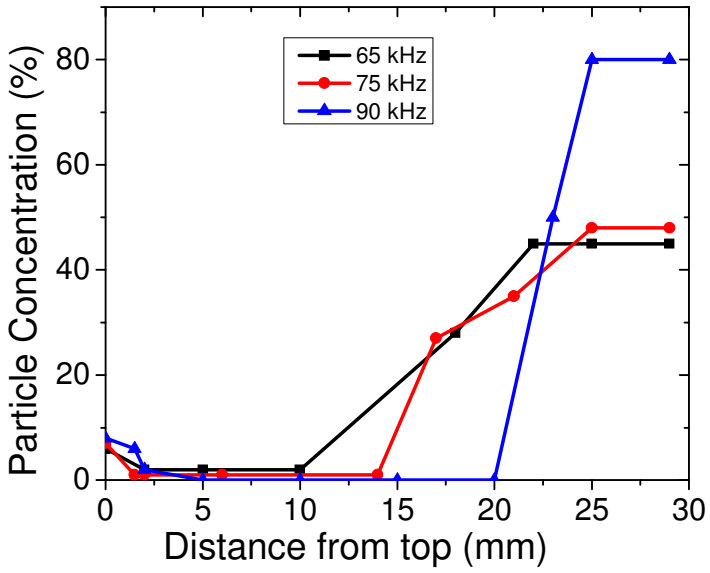

Fig. 19. Distribution of particles (area percent) from top – bottom of the sample comparing separation at the different frequencies.

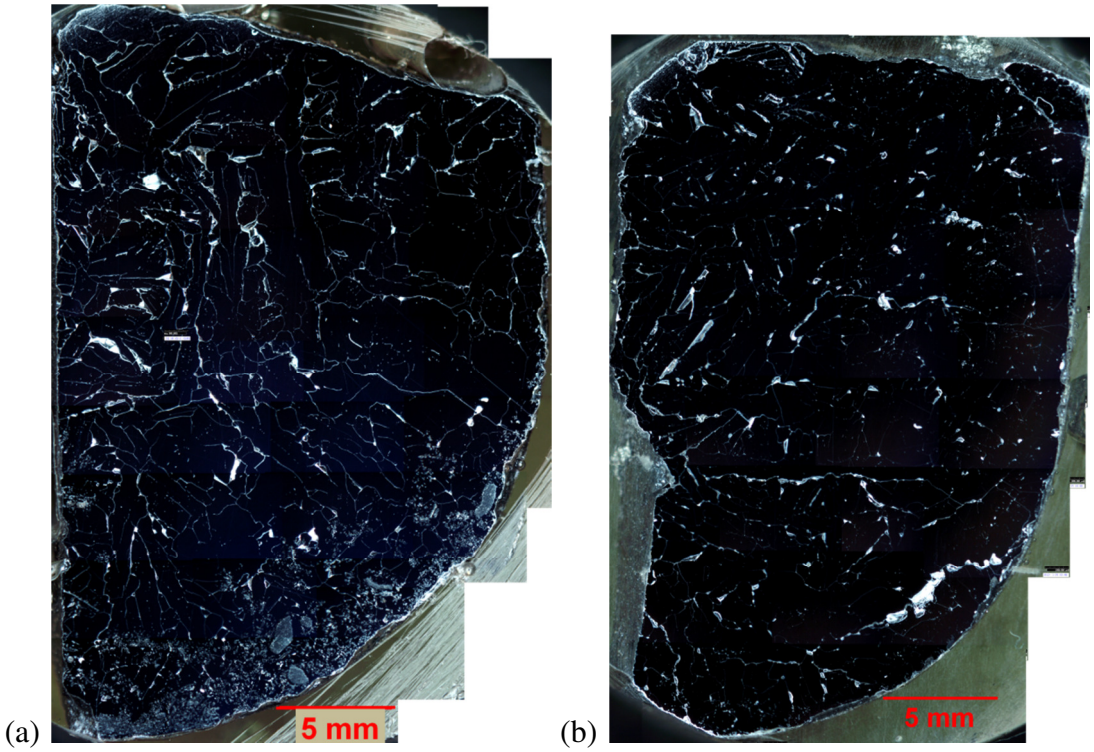

Fig. 20. Macrographs of quarter vertical cross-section of Si (Al) -3 % SiC after settling for 50 s under EM of f = 65 kHz and (a) I_{rms} = 397 A and (b) I_{rms} = 486 A.

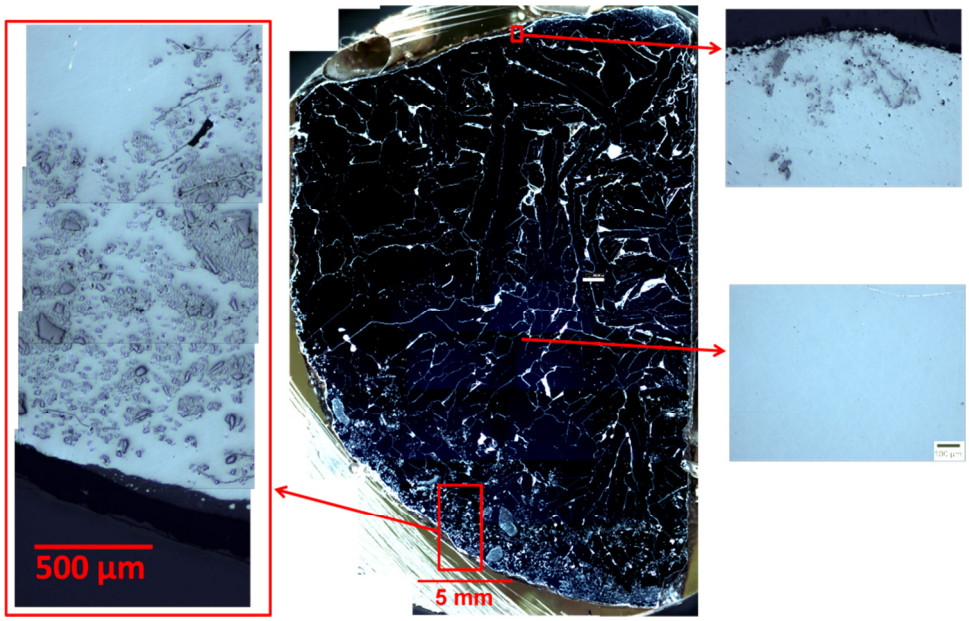

Fig. 21. Optical macro- and micro-graphs of a quarter vertical cross-sectional view of the sample from the settling experiments using 397 A coil current, at 65 kHz and separated from 50 s.

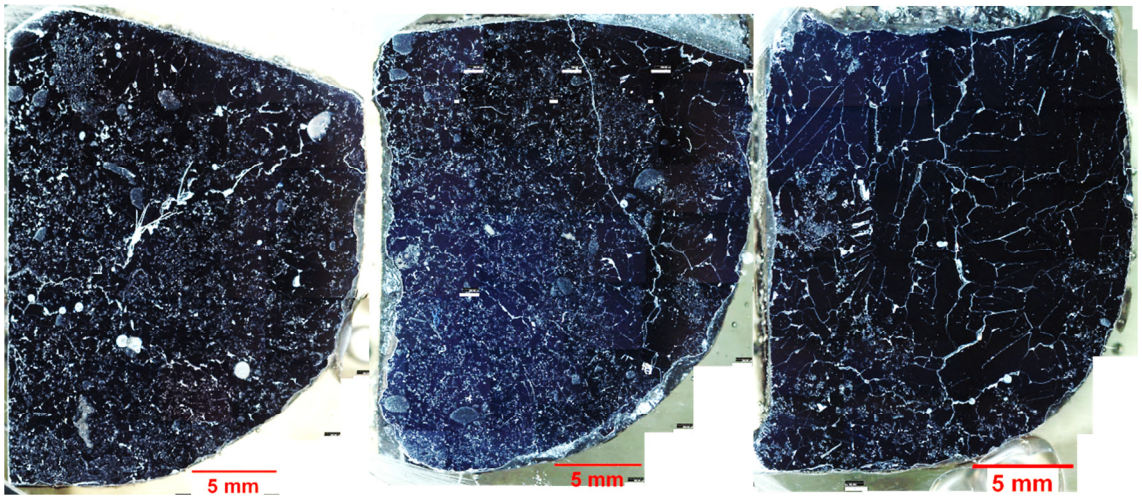

(a) (b) (c)

Fig. 22. Macrographs of quarter vertical cross-section of Si (Al) -3 % SiC after settling for 50 s under EM of I_{rms} = 268 A and (a) f = 65 kHz (b) f = 75 kHz (c) f = 90 kHz.

3.3. Settling Mechanism

3.3.1. Magnetic Field

Results from the magnetic field simulation in ANSOFT Maxwell are shown in Fig. 23 comparing the magnetic field vectors of the calculated domain and contours within the graphite sheath, susceptor, crucible and silicon. The figure compared the magnetic field vectors and contours for different frequencies and currents. Changing the frequency from 65 kHz to 90 kHz did increase the intensity of the magnetic field slightly. However, a change in the current from 270 A to 486 A produced a significant increase in the magnetic field strength. The magnetic field is concentrated on the side surface of the conductors due to skin effect. It then decreases in strength towards the center of the conductor, which coupled with a concentration of magnetic field at the top surface of silicon because of the open space results in magnetic field gradients within the silicon. Therefore, for particles suspended within the molten silicon, due to the difference in magnetic susceptibility, and the length scales of the interface between particles and the molten silicon, this could induce magnetization forces to help separate the particles from the melt in addition to gravity forces.

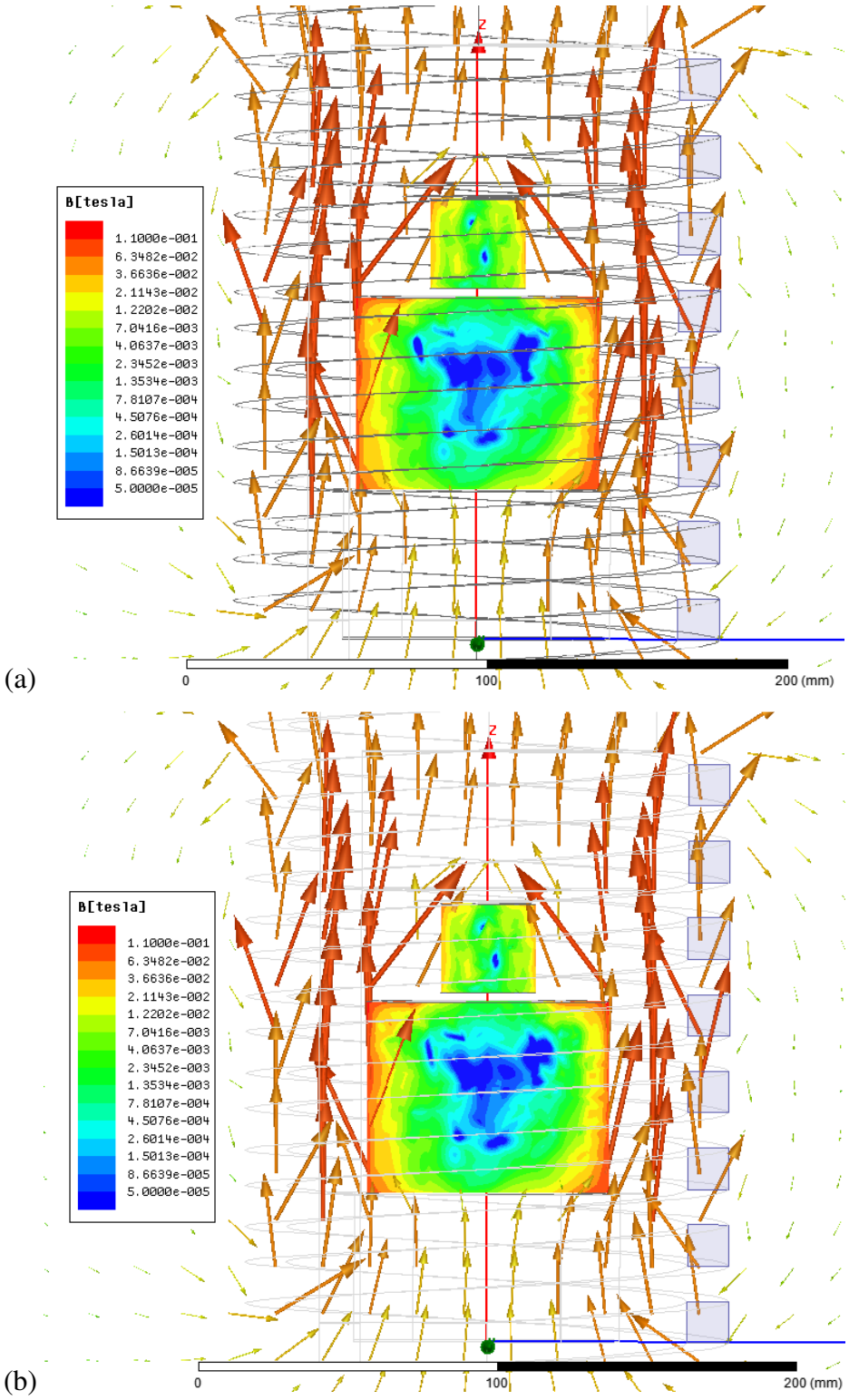

Fig. 23. Magnetic field vectors within the set-up and B contours within the crucible, sheath, susceptor and silicon for (a) 270 A, 65 kHz, (b) 270 A, 90 kHz and (c) 486 A, 65 kHz.

(c)

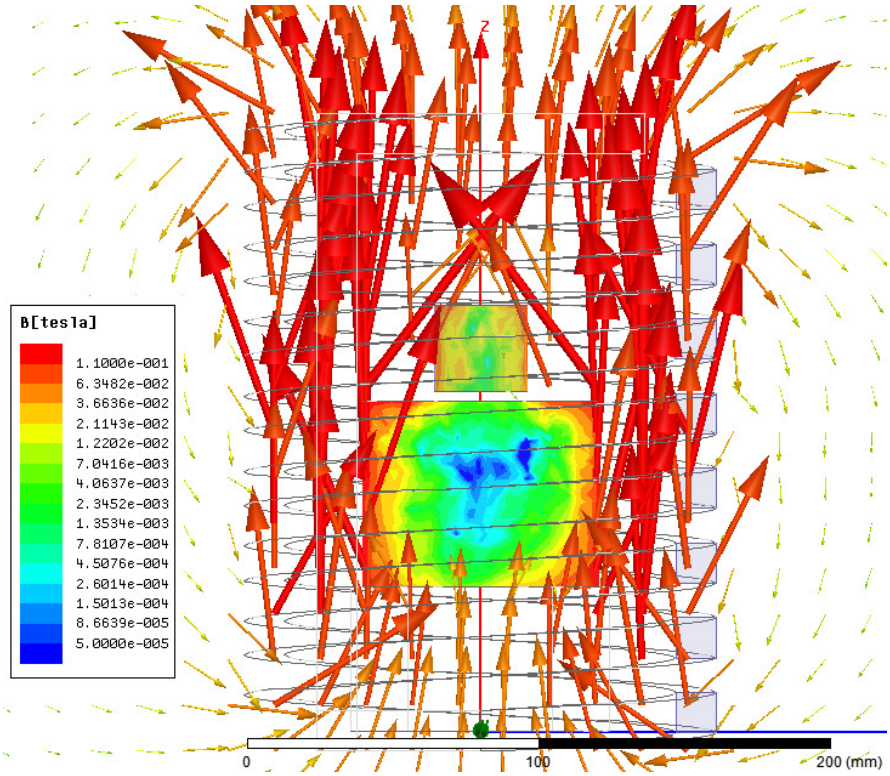

Fig. 23. Magnetic field vectors within the set-up and B contours within the crucible, sheath, susceptor and silicon for (a) 270 A, 65 kHz, (b) 270 A, 90 kHz and (c) 486 A, 65 kHz. (cont.)

3.3.2. Forces acting on a particle

Three important forces potentially act on a suspended particle within the melt: gravity force (F_g), viscous drag force (F_d) and the magnetization (F_B) due to gradient magnetic field and difference in magnetic susceptibility between the melt and particle. The respective mathematical expression for these forces are given by Eqs.(8) – (10).

$$F_g = V\left(\rho_p - \rho_m\right) g \tag{8}$$

$$F_d = \frac{1}{2}\rho_m v_p C_D A \tag{9}$$

$$F_B = V\left(\chi_m - \chi_p\right)\frac{1}{\mu_o} B \frac{\partial B}{\partial z} \tag{10}$$

Particle settling under the electromagnetic field conditions could be attributed to contributions from induced fluid flow and magnetization force.

3.3.3. Induced fluid flow

The dynamics of turbulent flows containing dense particles has gained interest among researchers in diverse fields. Wang and Maxey [22] found from their numerical simulation in a uniform turbulent flow with one-way particle coupling that the settling velocity of the particles was larger than the corresponding Stoke's velocity. Ruiz *et al.* [23] showed with experimental results that phytoplankton (microscopic plants in the ocean) settling velocity increases when turbulence intensifies from the low to the higher values recorded in the upper mixed layers of lakes and oceans. Aliseda *et al*. [24] found in their experimental study that settling velocities of heavier particles in homogeneous turbulent flow were much larger than in a quiescent fluid. They reported that the enhancement of settling velocity was dependent on particle volume fraction and that particle concentration field exhibited large inhomogeneity. Particles interacted with the underlying turbulence and concentrated preferentially in certain flow regions, leading to particle clustering and increase in characteristic size.

Strong flow is induced as a result of the Lorentz force acting on the molten silicon, a consequence of the applied and induced electromagnetic fields. A higher rate of convection implies a higher Reynolds number, hence lower resistance to particle motion within the fluid. The settling velocity (v_p) of particles in a convective fluid could be described by Eq.(11).

$$v_p = \sqrt{\frac{4d_p g}{3C_D}\left(\frac{\rho_p - \rho_m}{\rho_m}\right)}; \quad C_D \approx \frac{24}{\mathrm{Re}}\left(1 + 0.15\,\mathrm{Re}^{0.687}\right) \tag{11}$$

Figures 24 shows that as the temperature of molten silicon increases its viscosity decreases. This leads to minimal fluid resistance on the particle. Figure 25 shows the effect of the Reynolds number on the settling velocity of a 10 μm particle. As can be observed, increasing the Reynolds number significantly increases the particle settling velocity.

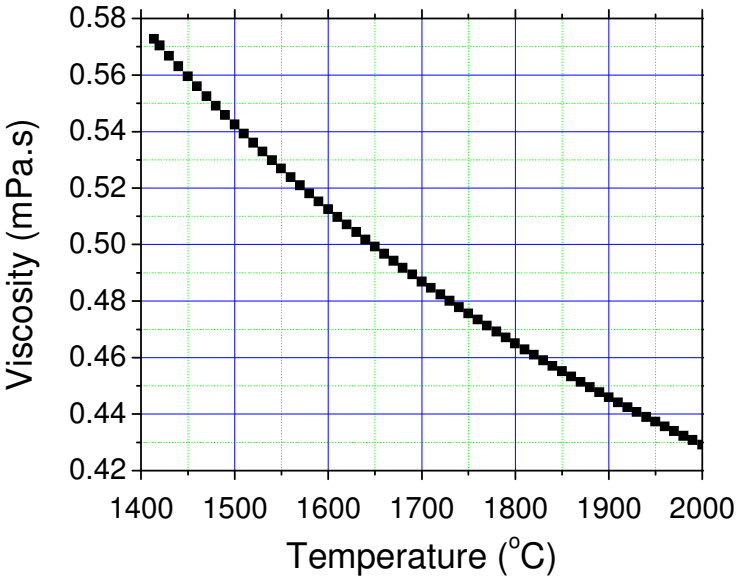

Fig. 24. Effect of temperature on the viscosity of silicon based on the results of Sato *et al.*[18].

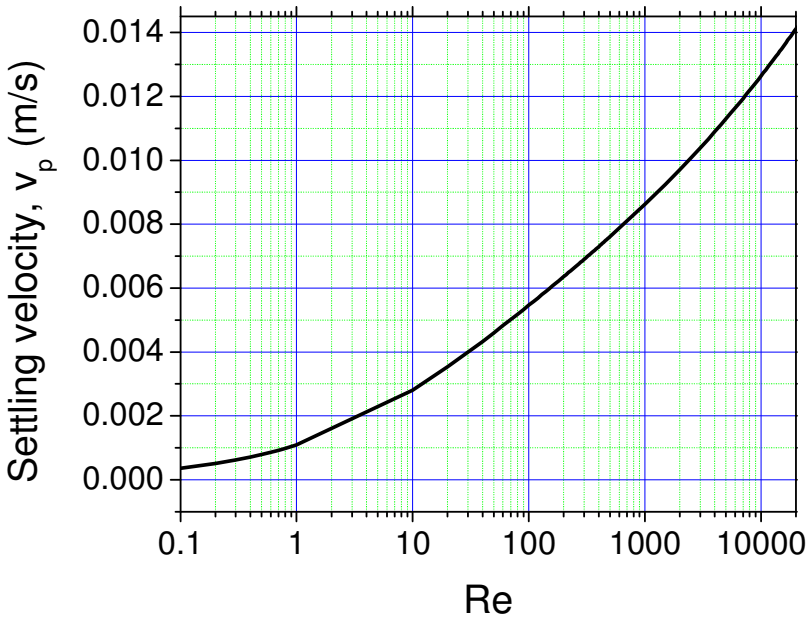

Fig. 25. Effect of Reynolds number on settling velocity of a 10 µm particle.

Figure 26 compares the calculated flow pattern in a vertical plane through the molten silicon. As can be observed from the flow streamlines, several circulatory flow loops developed upon the application of electromagnetic field and the strongest flow is observed closest to the bottom of the crucible. This flow pattern serves to enhance the

settling process as inclusions are transported by the flow and deposited and held at the bottom by settling forces. The contours of fluid velocity indicate that the current has a stronger effect on the fluid flow than the frequency, which is consistent with the magnetic field results. This is demonstrated by the velocities of fluid flow reported in Fig. 27. These velocity values could help explain the experimental results discussed above. It is important to note that, high frequencies distributed the fluid velocity better than low frequencies and thus result in higher effective fluid velocity though they may have comparable mean velocities. This explains why the experimental separation result is better for higher frequencies.

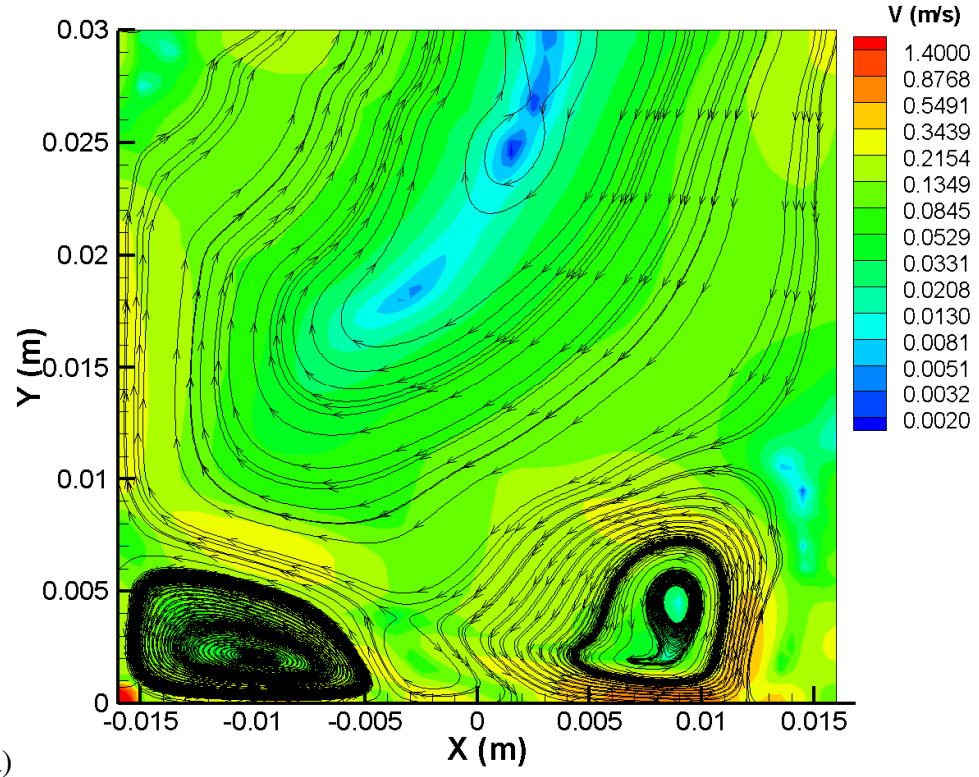

(a)

Fig. 26. Velocity contours and streamlines of induced fluid flow in the crucible calculated by ANSYS FLUENT (a) 270 A, 65 kHz, (b) 270 A, 90 kHz and (c) 486 A, 65 kHz.

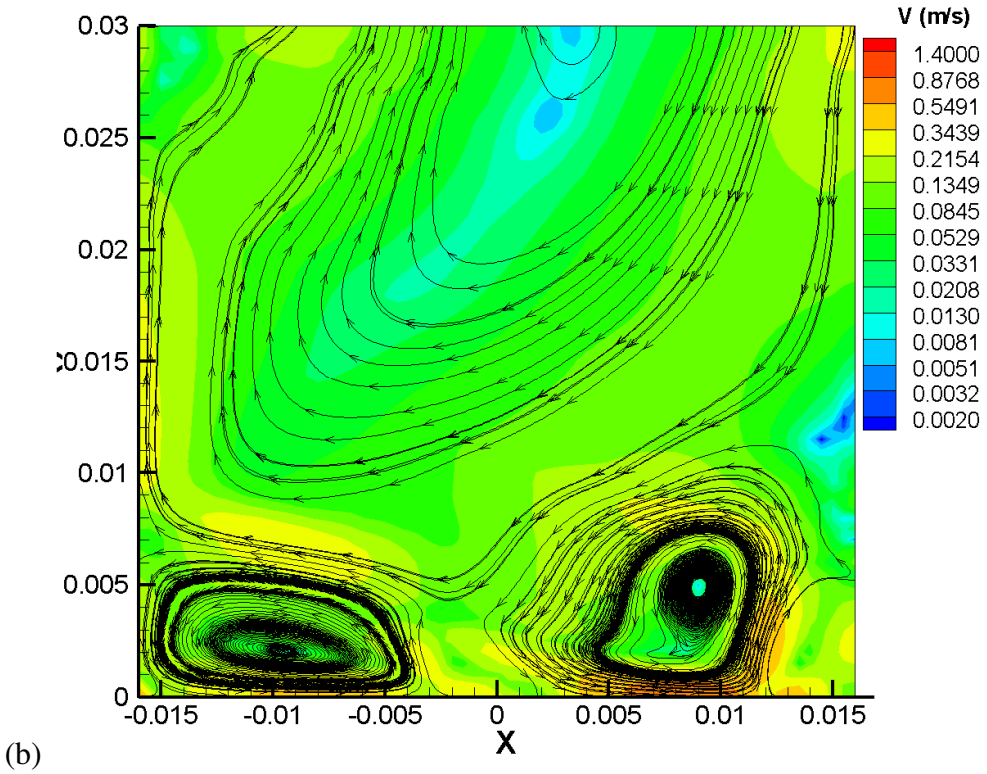

(b)

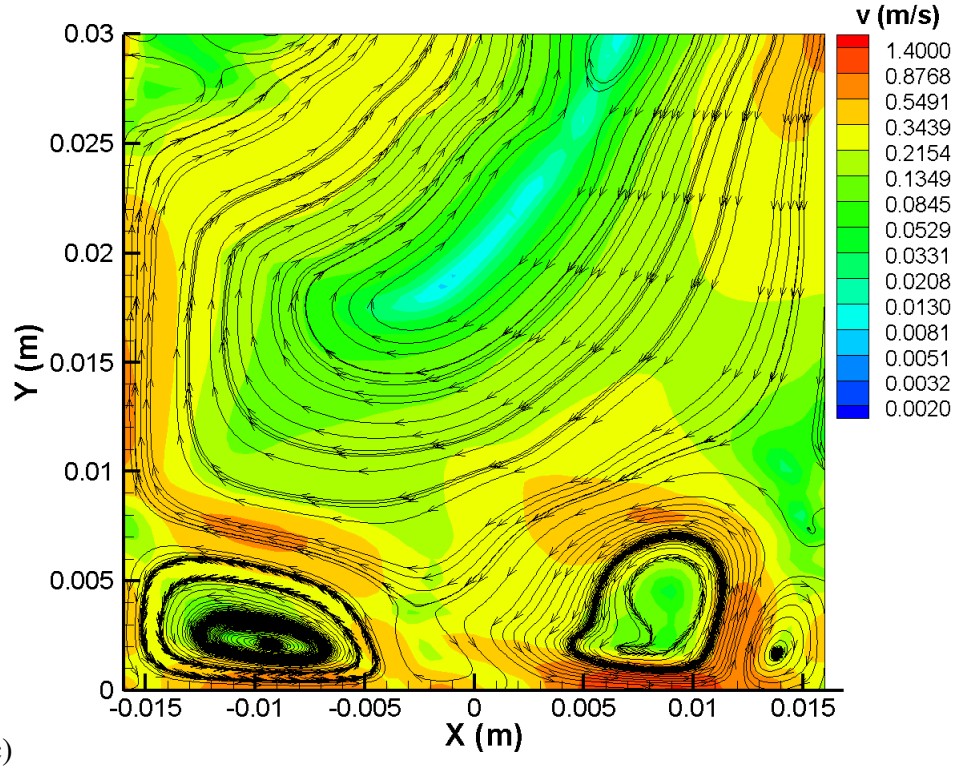

(c)

Fig. 26. Velocity contours and streamlines of induced fluid flow in the crucible calculated by ANSYS FLUENT (a) 270 A, 65 kHz, (b) 270 A, 90 kHz and (c) 486 A, 65 kHz. (cont.)

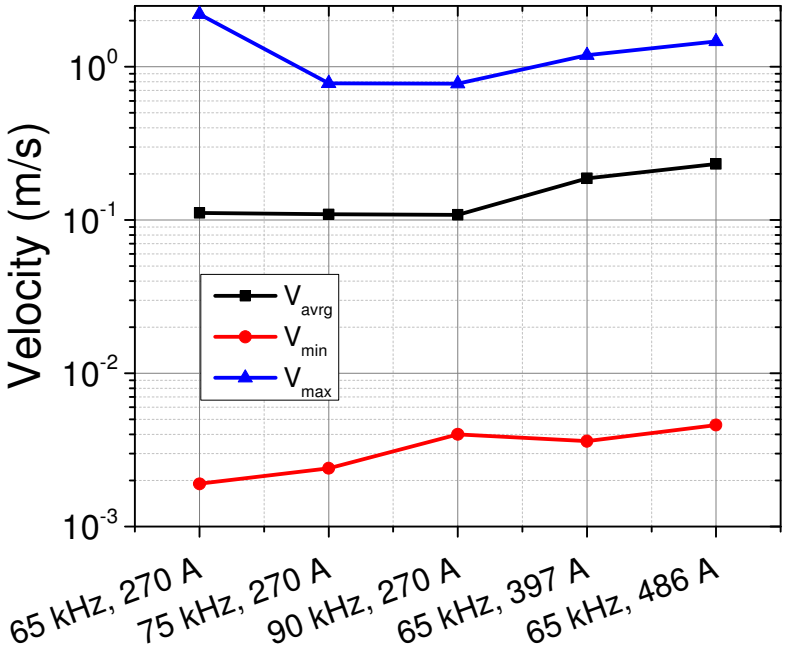

Fig. 27. Comparison of faceted minimum, maximum and average velocities for various parameters.

3.3.4. Magnetization force due to magnetic field gradients

The magnetization force [25] could be used to separate phases based on the magnetic susceptibility difference under a gradient magnetic field.[8, 16] Due to the uneven distribution of magnetic field within the molten silicon, as shown in Fig. 23, the contribution of magnetization force to the separation process is important. The steady-state settling velocity (v_p) of particles under gradient magnetic field may be derived from a combination of gravity, drag and magnetization forces as:

$$v_p = \sqrt{\frac{4d_p}{3C_D\rho_m}\left[\left(\rho_p-\rho_m\right)g+\left(\chi_m-\chi_p\right)\frac{1}{\mu_o}B\frac{\partial B}{\partial z}\right]} \qquad (12)$$

Equation (12) provides many possibilities to electromagnetic removal of particle. Currently, due to the availability of superconductive magnetic materials, strong magnetic field gradients could be used to float or settle particles as desired in a fluid. Figure 28

shows the effect of Reynolds number and gradient magnetic field on the settling velocity of 10 µm SiC particles in molten silicon at 1500 ^{o}C.

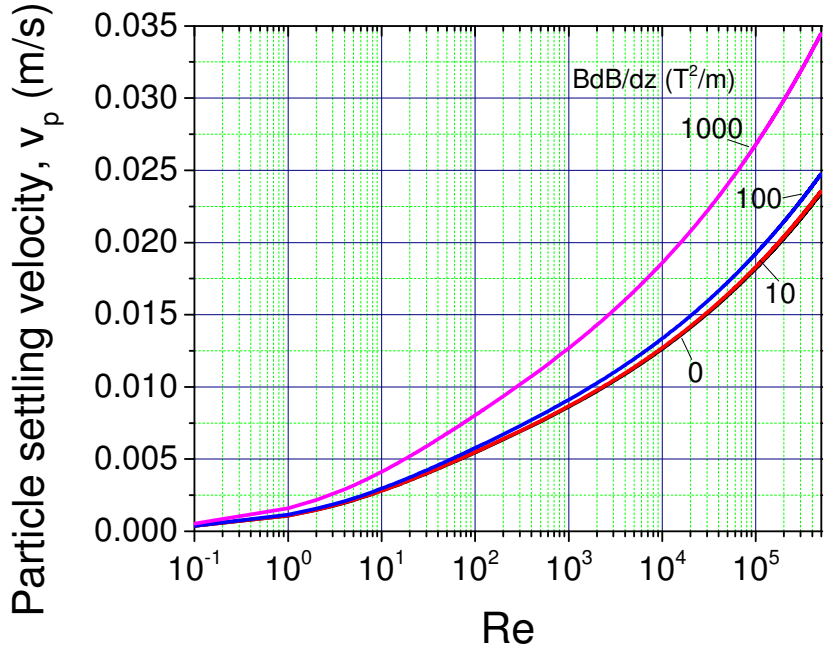

Fig. 28. The effect of gradient magnetic field and Reynolds number on the settling velocity of a 10 µm SiC particle in molten silicon.

The effectiveness of the magnetization force in settling particles is seen in strong gradient magnetic fields. For a 10 µm particle, this force is negligible in convective silicon for gradient fields below 10 T^2/m. In a well convective fluid and under a weak magnetic field gradient as is the case in this study, the contribution of the magnetization force can be considered negligible compared to the convective forces. Though the magnetic field gradient observed in the set-ups do not appear strong enough, considering the local gradient due to the length scale of a particle-molten silicon interface, stronger magnetization forces could be induced to enhance the particle separation process.

4. Conclusions

The feasibility of using a high frequency AC electromagnetic field to settle suspended inclusions in top-cut silicon scrap was investigated. It was found that SiC particles settled to the bottom of the sample within a time of two minutes under the

electromagnetic field. This was contrary to the result of settling by gravity without electromagnetic field for over three hours in which almost all the particles remained in the top-half of the sample. The proposed mechanisms responsible for the improved settling under an electromagnetic field are electromagnetic stirring coupled with gravity forces and the effect of the magnetization forces due to the difference in magnetic susceptibility between the melt and particles under a gradient electromagnetic field.

A parametric study on the settling process was completed using Si (Al) – 3 % SiC composite material. It was found that increasing the separation time, coil current, and frequency improved the separation results significantly. Longer separation time allowed particles to be transported by convective and settling forces from the molten metal stream to the bottom. Calculated magnetic field by ANSOFT Maxwell and fluid flow by ANSYS FLUENT showed that higher coil currents gave stronger magnetic fields and stronger molten metal flow while higher frequency resulted in a better distributed flow velocity leading to improved settling rates.

References

[1] A. Lotnyk, O. Breitenstein, H. Blumtritt, A TEM study of SiC particles and filaments precipitated in multicrystalline Si for solar cells, Solar Energy Materials & Solar Cells, 92 (2008) 1236-1240.

[2] N.B. Mason, Industry Developments that Sustain the Growth of Crystalline Silicon PV Output, in: Proceedings of the Photovoltaic Science, Applications & Technology Conference, Durham UK, 2007, pp. 43-46.

[3] L. Zhang, E. Øvrelid, S. Senanu, B. Agyei-Tuffour, A.N. Femi, Nonmetallic Inclusions in Solar Cell Silicon: Focusing on Recycling of Scraps, in: Rewas2008: 2008 Global Symposium on Recycling, Waste Treatment and Clean Technology, TMS, Warrendale, PA, USA, CANCUN, MEXICO, 2008, pp. 1011-1026.

[4] D. Sarti, R. Einhaus, Silicon feedstock for the multi-crystalline photovoltaic industry, Solar Energy Materials and Solar Cells, 72 (2002) 27-40.

[5] A. Ciftja, E. Ovrelid, M. Tangstad, T. Engh, Settling of Particles in Molten Silicon Before Directional Casting of a Solar Grade Silicon Ingot, in: The TMS 2009 Annual

Meeting Supplemental Proceedings, Volume 2: Materials Characterization, Computation and Modeling, 2009, pp. 261-268.

[6] G. Lavorel, M. LeBars, Sedimentation of particles in a vigorously convecting fluid, PHYSICAL REVIEW E, 80 (2009) 046324-046321-046324-046328.

[7] M. Hori, Application of Electromagnetic Force in Mixed-phase Fluid, in, Japan Atomic Energy Research Institute, JAERI 1055, 1964.

[8] Y. Tanimoto, Y. Kakuda, Influence of strong magnetic field on the sedimentation of red blood cells Journal of Physics: Conference Series, 156 (2009).

[9] J.Y. Hwang, M. Takayasu, F.J. Friedlaender, G. Kullerud, Application of magnetic susceptibility gradients to magnetic separation, J. Appl. Phys., 55 (1984) 2592-2594.

[10] F. Jin, Z. Ren, W. Ren, K. Deng, Y. Zhong, J. Yu, Effect of a high-gradient magnetic field on the migratory behavior of primary crystal silicon in hypereutectic Al-Si alloy, Science and Technology of Advanced Materials, 9 (2008) 1-6.

[11] M. Motokawa, Physics in high magnetic fields, Rep. Prog. Phys., 67 (2004) 1995-2052.

[12] C.M. Hangarter, Y. Rheem, B. Yoo, E. Yang, N.V. Myung, Hierarchical magnetic assembly of nanowires, Nanotechnology, 18 (2007) 205-305.

[13] J.R. Reitz, F.J. Milford, Foundations of Electromagnetic Theory, Addison-Wesley Publishing Company, London, England, 1962.

[14] Z. Ren, X. Li, Y. Sun, Y. Gao, K. Deng, Y. Zhong, Infuence of high magnetic feld on peritectic transformation during solidification of Bi-Mn alloy, Calphad, 30 (2006) 277-285.

[15] F. Larachi, M.C. Munteanu, Magnetic emulation of microgravity for earth-bound multiphase catalytic reactor studies Potentialities and limitations, AIChE J., 55 (2009) 1200-1216.

[16] Z. Sun, M. Guo, J. Vleugels, O. van-der-Biest, B. Blanpain, STRONG MAGNETIC FIELD INDUCED SEGREGATION AND SELF-ASSEMBLY OF MICROMETER

SIZED NON-MAGNETIC PARTICLES, Progress In Electromagnetics Research B, 23 (2010) 199-214.

[17] Z. Sun, M. Guo, F. Verhaeghe, J. Vleugels, O. Van-der-Biest, B. Blanpain, MAGNETIC INTERACTION BETWEEN TWO NON-MAGNETIC PARTICLES MIGRATING IN A CONDUCTIVE FLUID INDUCED BY A STRONG MAGNETIC FIELD I AN ANALYTICAL APPROACH, Progress In Electromagnetics Research, PIER, 103 (2010) 1-16.

[18] Y. Sato, Y. Kameda, T. Nagasawa, T. Sakamoto, S. Moriguchi, T. Yamamura, Y. Waseda, Viscosity of molten silicon and the factors affectingmeasurement, Journal of Crystal Growth 249 (2003) 404–415.

[19] S. Makarov, R. Ludeig, D. Apelian, Electromagnetic Separation Techniques in Metal Casting. I. Conventional methods, IEEE Transactions on Magnetics, 36 (2000) 2015-2021.

[20] A.D. Patel, N. El-Kaddah, Kinetics of inclusions removal from molten aluminum under an applied alternating magnetic field, Light Metals, (1997) 1013-1018.

[21] S. Makarov, R. Ludeig, D. Apelian, Electromagnetic Separation Techniques in Metal Casting. II. Separation with superconducting coils, IEEE Transactions on Magnetics, 37 (2001) 1024-1031.

[22] L.-P. Wang, M.R. Maxey, Settling velocity and concentration distribution of heavy particles in homogeneous isotropic turbulence, J. Fluid Mech., 256 (1993) 27-68.

[23] J. Ruiz, D. Macias, F. Peters, Turbulence increases the average settling velocity of phytoplanton cells, PNAS, 101 (2004) 17720-17724.

[24] A. Aliseda, A. Cartellier, F. Hainaux, J.C. Lasheras, Effect of preferential concentration on the settling velocity of heavy particles in homogeneous isotropic turbulence, J. Fluid Mech., 468 (2002) 77-105.

[25] S. Asai, Recent Development and Prospect of Electromagnetic Processing of Materials, Science and Technology of Advanced Materials, 1 (2000) 191-200.

III. HIGH FREQUENCY ELECTROMAGNETIC SEPARATION OF INCLUSIONS FROM ALUMINUM

Lucas Nana Wiredu Damoah, Lifeng Zhang

Department of Materials Science & Engineering
Missouri University of Science and Technology (Missouri S&T)
223 McNutt Hall, Rolla, MO 65409-0340, USA
Email: zhanglife@mst.edu

This paper is the extended version of one published in the 2012 TMS Proceedings on Light Metals

Abstract

Removal of inclusions from aluminum is a critical step during the production of high quality aluminum alloys. An electromagnetic (EM) purification method for the removal of inclusions has been proposed to complement existing methods. Many researchers have devoted considerable effort to studying the electromagnetic inclusion removal process and have widely published that a high frequency electromagnetic field is limited in the depth of penetration into the molten metal and therefore it is an ineffective method of particle separation. The contribution of the high circulatory fluid flow associated with such high frequencies has also been reported to be negative. The effect of wall temperature on the electromagnetic inclusion removal process has also not been clearly established. This study shows that fluid flow contributes immensely to particle removal in the presence of low wall temperatures during high frequency (63 – 128 kHz) EM purification of aluminum, overcoming the skin depth effect in small and large crucibles. Under such conditions, particles of all sizes are separated across the diameter of the crucible. Higher separation time, coil current and frequency enhance the separation process.

Introduction

The detrimental effects of nonmetallic inclusions on the chemical, mechanical and processing properties, as well as the demand for high quality aluminum and its alloys have motivated many researchers to devote considerable efforts to finding cost effective and clean methods to rid the metal of inclusions. Several methods including flotation, sedimentation, centrifugal separation, filtration, and electromagnetic separation have been proposed.[1-5] Among these methods, filtration requires the least capital investment,[1] but has the limitation of low removal efficiency for inclusions smaller than 10 μm and the disadvantage of filter clogging at high inclusion concentrations. Since the work of Leenov and Kolin [6-7] who first proposed the principle underlining electromagnetic separation, many researchers have devoted considerable effort to studying this method relative to the removal of inclusions from metals. Electromagnetic separation is one method with the potential to remove much smaller particles [8-10] and also has no inclusion concentration dependence [11-12]. Alternating current (AC)

electromagnetic separation is the easiest for industrial implementation with continuous separation among the available options for this technology. However, the skin depth effect of high frequency electromagnetic systems imposes a limitation on this potential inclusion removal technology as has been reported [2]. Associated with the electromagnetic system is strong induced fluid velocity in the molten metal which results in electromagnetic stirring. The effect of electromagnetic stirring during the application of AC magnetic fields for inclusion removal has been reported to be negative due to the strong fluid velocity induced close to the wall where particles are trapped, resulting in the re-entrainment of these trapped particles into the melt.[11] However, there are some positive effects of the induced fluid flow by the electromagnetic field, since it can carry inclusions from the melt to the vicinity of the wall of the crucible where the electromagnetic Archimedes force is effective at trapping the inclusions. Shu *et al.* [13] indicated in their study that induced secondary flow may enhance separation efficiency, with high frequency resulting in stronger secondary flow, although their study was theoretical. This positive effect has yet to be realized with experimental results. Additionally, the effect of the wall temperature on the electromagnetic process has also not been clearly determined although a previous study [11] considered the effect of cooling of the crucible wall during EM separation.

This study investigates the process of high frequency electromagnetic separation of inclusions from molten aluminum in relatively small and large crucibles with cooling aimed at understanding the conditions for separating particles from aluminum with high frequency magnetic fields.

Materials and Experiments

An aluminum-SiC particulate composite (~15 wt% of particles) was procured and used in this study. The particles were of size range of 1 – 30 μm within the matrix of aluminum as illustrated in Fig. 1. Over 60 % of particles had sizes less than 3 μm. The SEM/EDX study of this material showed traces of oxygen and aluminum in the particles clusters (dark phases) suggesting the presence of Al_2O_3, Al_3C_4 and SiO_2 particles in the material in addition to the SiC particles. Figure 2 shows a typical EDX spectrum of particulate clusters observed in the material. In Fig. 1 the bright phases are Al-Fe

intermetallic compounds containing Si and traces of Mn and Mg. The average area fraction of particles was determined as ~29 % with the help of image analysis software, *ImageJ*.

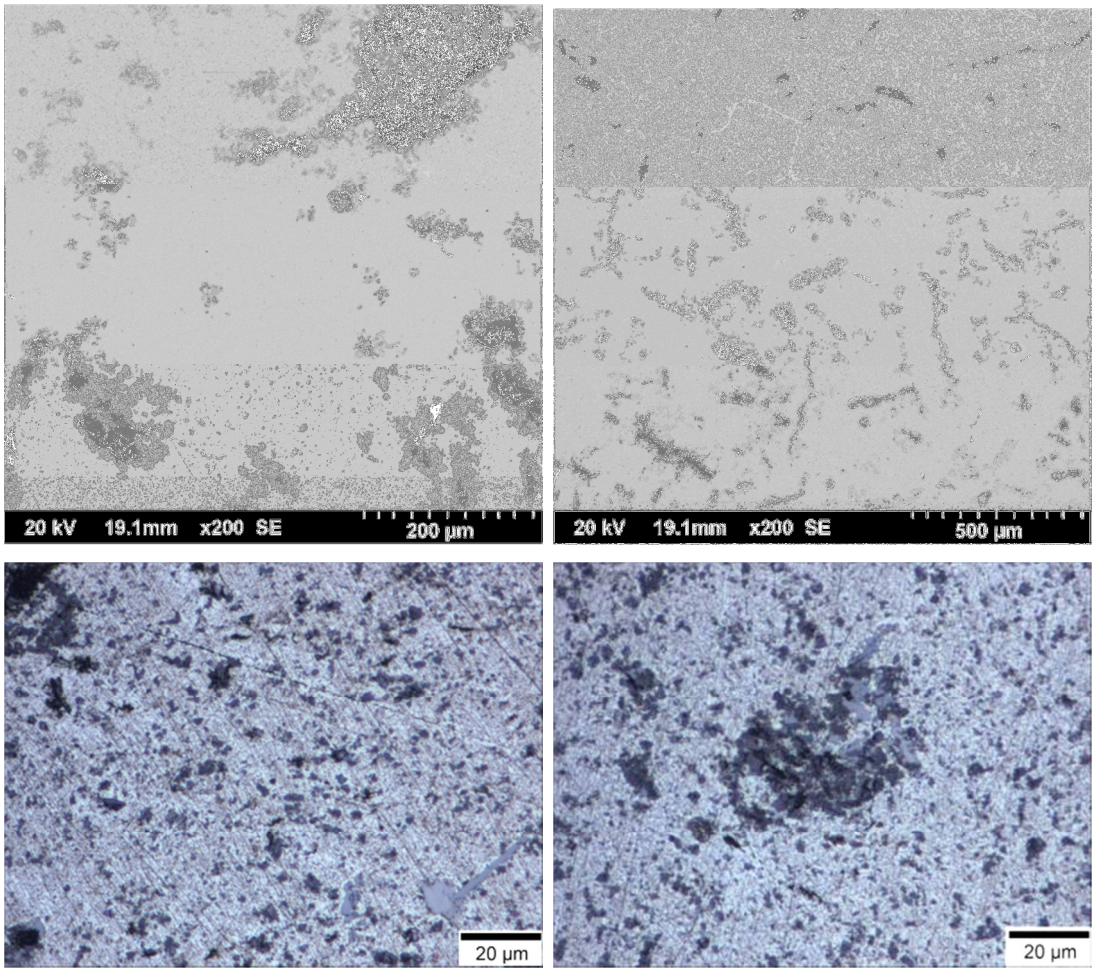

Figure 1. Microstructure of the as procured Al – SiC composite material showing clusters of particles of sizes ranging 1 – 30 µm acquired with SEM (top) and optical microscope (bottom).

Figure 3 shows the schematic of the experimental set-up used in this study. The set-up includes an induction coil powered by a 100 kW capacity power supply with a frequency range of 50 - 200 kHz, the crucible containing the aluminum-SiC particulate composite, and a cooling coil made from Teflon or copper tubing. The Teflon cooling

coil was used to directly spray water on the crucible during separation. In the case of copper coil cooling, a water cooled copper tube was wound tightly around the crucible.

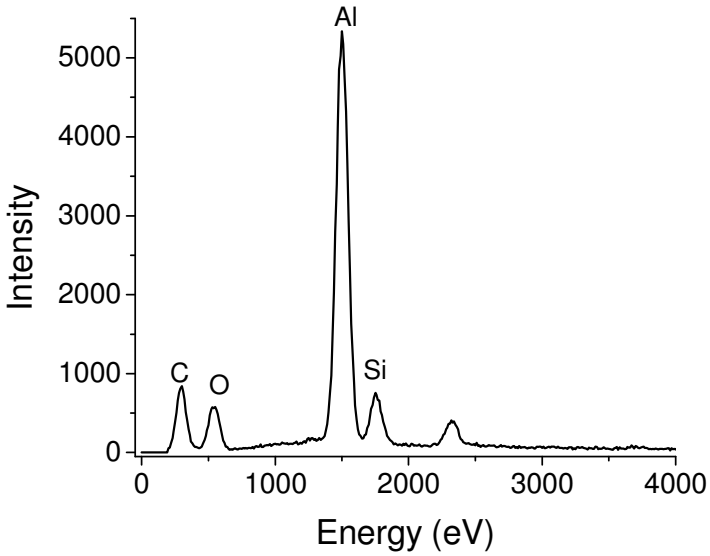

Figure 2. Typical EDX results of the particle clusters in the composite sample.

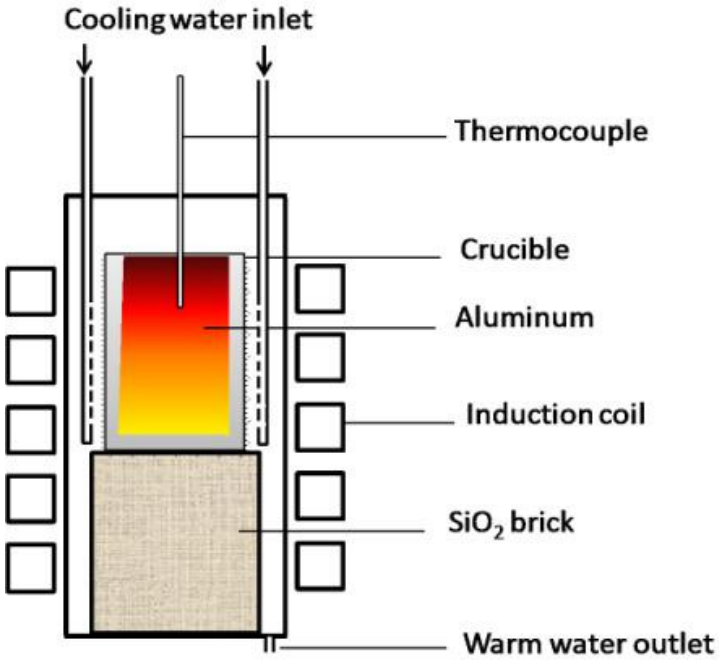

Figure 3. Experimental set-up for EM separation of inclusions from aluminum with water cooling.

In other experimental cases, a fan or compressed air cooling was used instead of water cooling, in which case an anemometer was employed to measure the air velocity around the crucible. The purpose for cooling was to understand the effect that the wall temperature has on the EM separation process, since it affects the viscosity distribution within the molten metal in the vicinity of the crucible wall. Table I gives details about the experimental plan and the parameters used in this study. The experiments were designed to investigate the effect of temperature, size of the crucible and fluid flow on the high frequency EM separation process.

Table I Experimental materials and condition.

Exp. #	Crucible material (diameter)	Cooling Conditions	Temperature outside crucible (^{o}C)	Parameters		
				f (kHz)	i_{rms} (A)	t (s)
Al-EM–1	Al_2O_3 (15 mm)	Not cooled	680			
Al-EM–2	Al_2O_3 (15 mm)	Water cooled	300	63	280	15
Al-EM–3	SiO_2 (40 mm)	Half water cooled	300 – 680			
Al-EM–4	SiO_2 (40 mm)	Cu coil cooled	630			
Al-EM–5	Al_2O_3 (15 mm)	Air cooled (3 m/s)	-	63	280	120
Al-EM–6	Al_2O_3 (15 mm)	Air cooled (1 m/s)	-	128	480	2*

* Accidental separation time due to crucible fracture from thermal shock

During the experiments, a designed amount of composite material was placed in the crucible and the power supply turned on. After melting was complete the temperature was allowed to rise to about 850 ^{o}C. The separation parameters were set at this stage, with simultaneous cooling (for the cases where cooling is required) and the experiment monitored for the desired time. In the cases involving direct water cooling the separation time could not go beyond 15 s because the metal solidified during separation. In the experiment at a frequency of 128 kHz (see Table I) the desired separation time could not

be reached because the temperature of the melt rose too fast causing the crucible to fracture due to thermal shock within 2 s. The outside crucible wall temperature was estimated based on measurements with a thermocouple at the time the power supply and cooling water were turned off. Samples were cut and polished to study the particle distribution under the macro- and microscope.

Results and Discussions

Particle separation from experiments

The originally dispersed particles were expected to be trapped at the wall of the crucible during the experiment due to induced pressure gradients in the melt under the magnetic field. However the results from the experiment which involve no cooling (Al-EM–1) showed no clear separation of particles (see Fig. 4) rather, clusters of the relatively larger particles were observed close to the wall of the crucible and other parts of the sample. This suggests some sort of forces acted on the particles but was not enough to keep them at the wall of the crucible to give the desired separation.

Figure 5 shows the separation results obtained from experiment Al-EM–2 in which the wall of the 15 mm Al_2O_3 crucible was cooled to approximate 300 ^oC during the separation period. A particle accumulated layer of thickness averaging about 2 mm and made up of 53% particles was observed all around the sample. Beyond the particle layer and into the sample, the matrix of the metal was much cleaner with small particles observed in certain areas. Figure 6 gives a more complete view of the sample, showing the cross-section and the separated layer using both a picture of the polished cross-section and an almost complete assembly of optical images of the layer (about 220 pictures of the layer put together). Optical micrographs within the central part of the image are a collection of representative pictures of the central region, typical of the view of this part of the sample away from the particle layer. A separation efficiency of 84 % was calculated for this experiment by measuring the thickness of separated layers and computing the volume of separated particles relative to the initial volume of particles. In the particle layer many areas of porosity can also be observed indicating water entered the crucible through cracks in the wall.

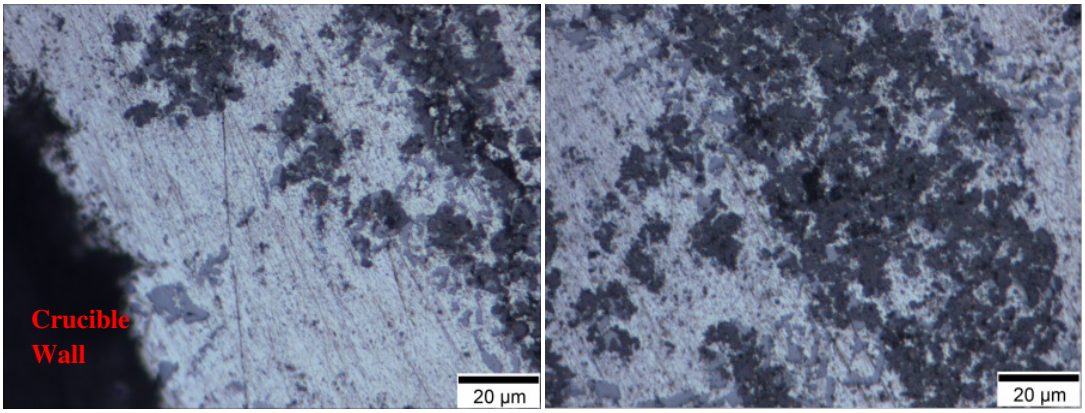

Figure 4. Accumulation of larger particles in the vicinity of the crucible wall where fluid viscosity is not high enough to trap them due to the high wall temperature observed from experiment Al-EM–1 – no clear separation of particles.

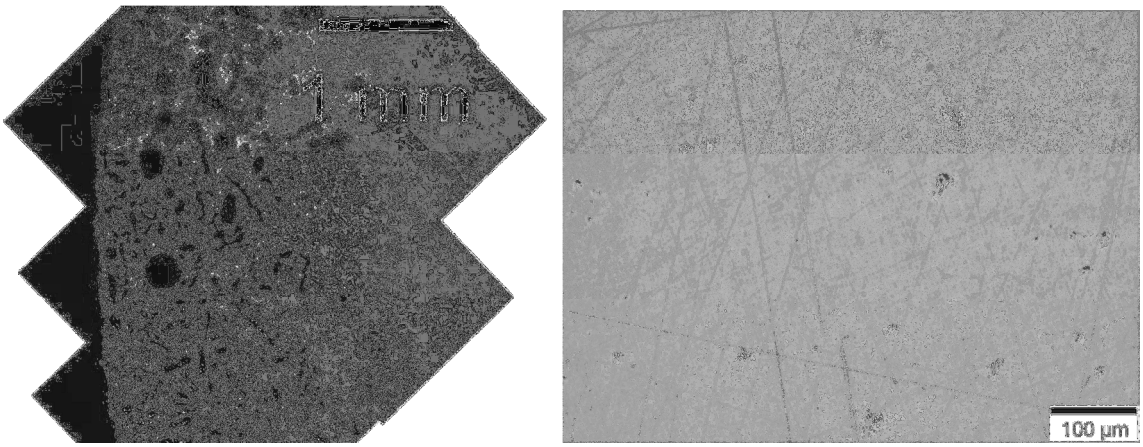

Figure 5. Thick accumulation of particles at the wall of the crucible (left) and a cleaner aluminum matrix close to the center of the crucible observed from Exp. Al-EM–2.

To minimize the severity of the cooling process and to reduce the amount of porosity in the particle layer, air cooling was introduced. In experiment Al-EM–5 two cooling fans were employed to create air flow at an average velocity of 3 m/s around the crucible during the separation process at a frequency of 63 kHz, coil current 280 A (same as Al-EM–2) and a time of 120 s. The result from this experiment is compared with the result of experiment Al-EM–2. Figure 7 shows optical macrographs of a horizontal cross-section through the samples.

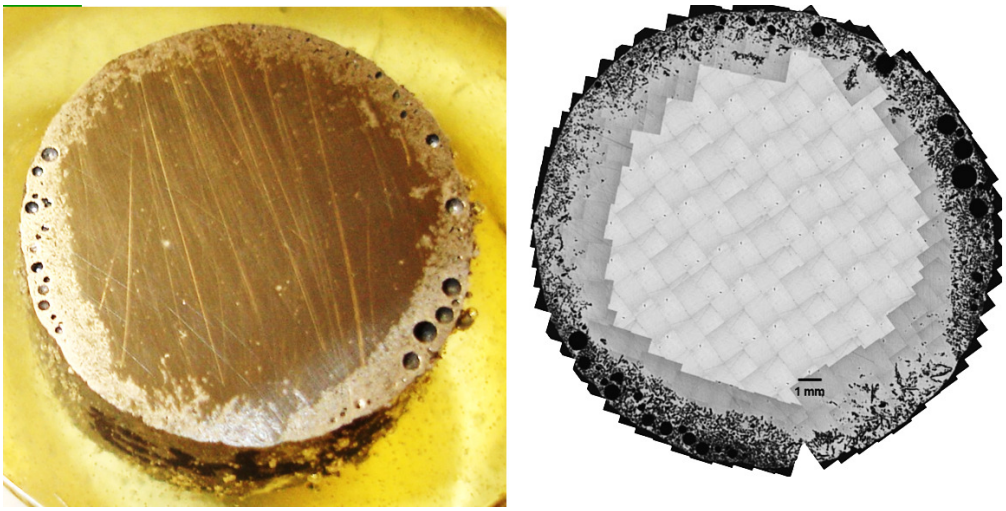

Figure 6. Complete view of the cross-section of the sample from Exp. Al-EM–2 showing a thick accumulation of particles at the wall of the crucible and a cleaner aluminum matrix close to the center of the crucible. A separation efficiency of 84% was recorded.

An oxide skin was trapped from a part of the wall into the melt of the air-cooled sample, which led to the accumulation of particles around both sides of the skin. Otherwise, it can be noted that the air-cooled experiment gave similar results to the water-cooled experiment. This suggests that the strength of the coolant could be reduced from that of water- to air- cooling, which is easily achievable in an industrial process. It is important to note that the separation times of the experiments were different. While the water-cooled experiment could not run for more than 15 s without total solidification of the melt, the air-cooled experiment ran for 2 minutes without the melt solidifying, indicating that the heat losses are much lower with the air-cooled process.

Closer observation of the matrices of the two samples shows that the air cooled sample had a cleaner matrix than the water cooled. This can be attributed to the separation times involved in the two experiments. Longer separation time favors better separation, hence the improved result.

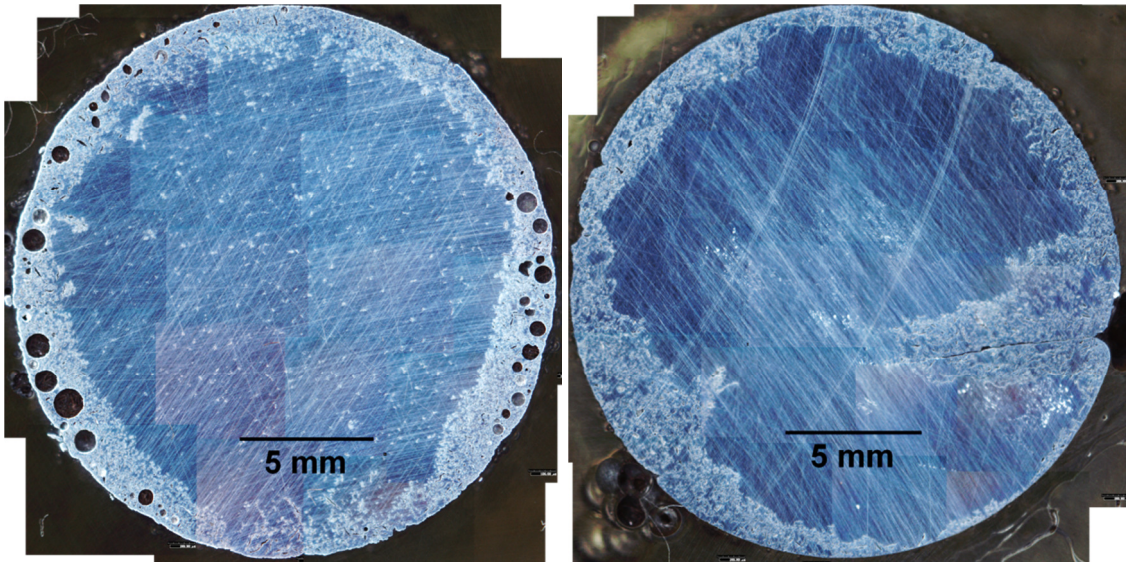

(a) (b)

Figure 7. Optical macrographs of a horizontal cross-section of the samples from (a) Exp. Al-EM–2 (water cooled) and (b) Exp. Al-EM–5 (Air cooled).

In experiment Al-EM–3, a 40 mm diameter SiO_2 crucible was used and the bottom half cooled (see Table I). This experiment was designed with the aim of understanding further the important role of temperature in the separation process. The outside temperature of the cooled crucible ranged approximately 300 - 680^{o}C. Figure 8 is a scanned image, and Fig. 9 shows part of the polished vertical cross-section of the sample from experiment Al-EM–3. These figures show that the cooled part had particles separated from the inner matrix to the wall of the crucible whereas the top part of the sample which was not cooled had particles dispersed throughout the matrix. This result supports the premise that lower crucible wall temperature than the melting point of the metal will enhance the electromagnetic separation process. However, other results from experimental trials show that, this observation might not be entirely due to temperature effects but the nature and strength of fluid flow along the height of the crucible.

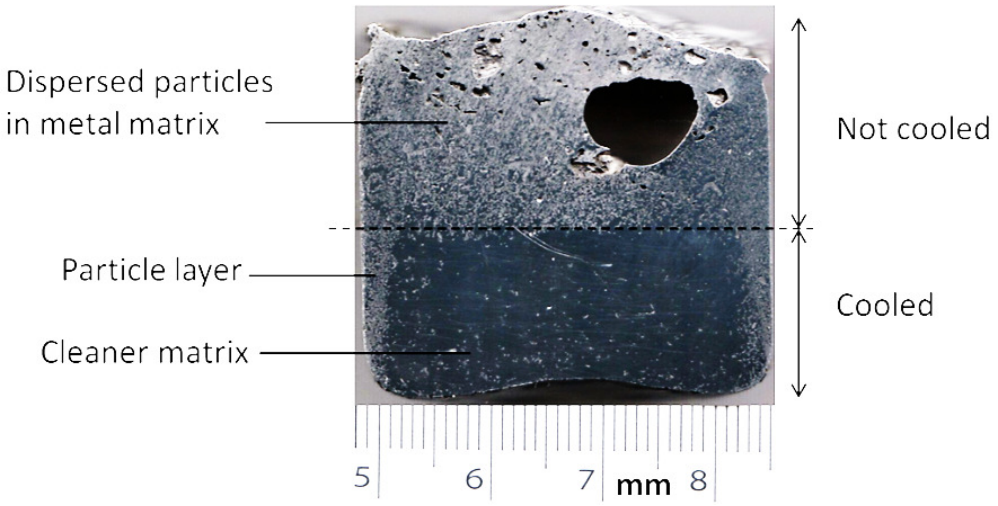

Figure 8. Scanned vertical cross-sectional image close to the center of the crucible from experiment Al-EM–3 (40mm SiO_2 crucible), which was water cooled on the bottom half showing a cleaner matrix and separated particle layer in the bottom half and well distributed particles in the matrix of aluminum in the upper half.

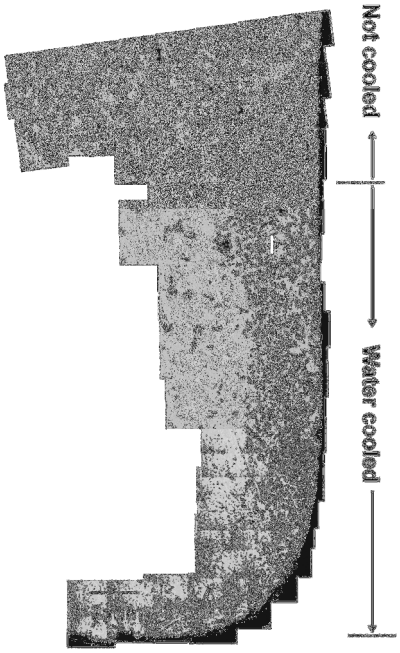

Figure 9. Optical micrographic view of part of the side wall along the vertical cross-section from experiment Al-EM–3 (40mm SiO_2 crucible), which was water cooled at the bottom half of the crucible showing a cleaner matrix and a separated particle layer where cooled and a well distributed particle in the matrix of aluminum in the upper half.

A comparison of the separated regions from experiments Al-EM–2 and Al-EM–3 fail to show a clear difference because a uniform separation is observed throughout the matrix of the sample along the diameter. The much discussed limitation by skin depth effect [14-16] on the separation process was not observed. The skin depth is the depth to which the Lorentz force penetrates into the melt. For molten aluminum under a frequency of 65 kHz, the skin depth can be calculated as ~1 mm from the wall of the crucible into the liquid metal, which means separation should be limited to this distance. However, the separation permeated throughout the diameter of the crucible. Therefore, there must be another mechanism different from the effect of the electromagnetic Archimedes force by which particles are transported from the liquid metal and are trapped to the wall. This is the influence of the induced secondary flow of the molten metal.

Flow pattern and Separation Mechanism

The induced fluid flow is demonstrated by the results from experiment Al-EM–4 shown in Fig. 10. In experiment Al-EM–4, copper coil cooling was employed in which water- cooled copper tubing was wound around the crucible to provide some shielding effect of the primary magnetic field of the induction coil in order to allow for the induced flow pattern to be observed. The sweeping effect of fluid flow on particles and a print of the circulatory flow pattern can be observed close to the bottom of the crucible. The optical micrograph in Fig. 10(b) shows a section of the metal at the bottom in the vicinity of the wall. It can be concluded from this figure that particles within the bulk of the melt are carried by the induced flow to the vicinity of the wall of the crucible where the electromagnetic Archimedes force is effective and if the metal adjacent to the crucible wall is viscous enough, the particles are trapped. Thus, high frequency electromagnetic separation relies on Lorentz and viscous forces to be effective.

The induced flow pattern was also observed for the sample from Exp. Al-EM–6, in which the separation was done for 2 s at a frequency of 128 kHz, coil current of 480 A, and the wall of the crucible cooled with compressed air with average air circulation velocity of ~1 m/s. This was done with nozzles outside of the induction coil and blowing air through the gaps in the coil, preventing the nozzle from heating up and also interfering

with the induced magnetic field as would have been the case if it was inside the induction coil.

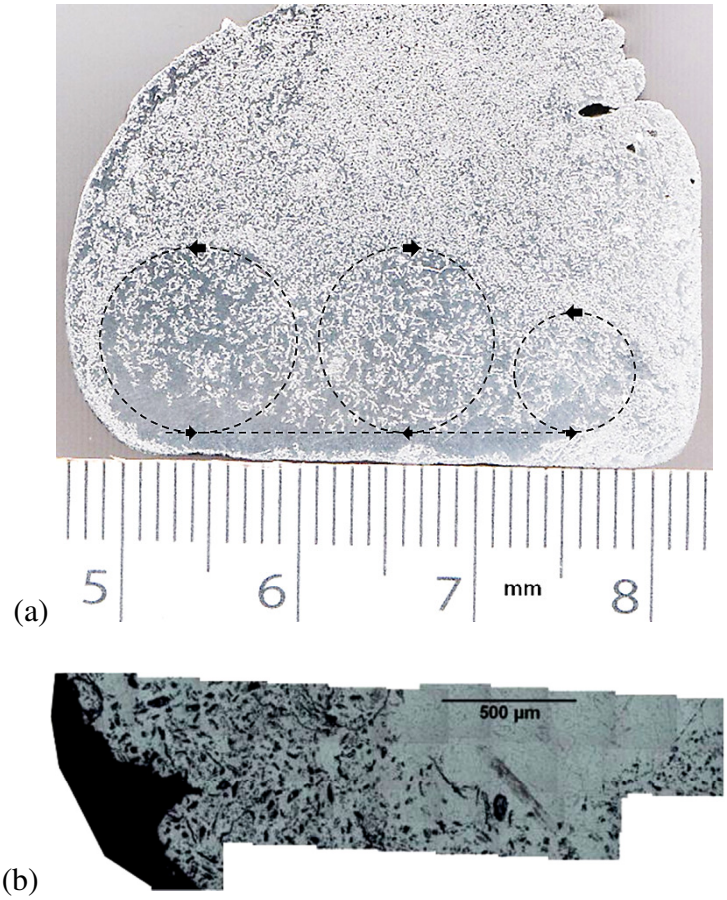

(a)

(b)

Figure 10. Particle distribution in the metal after experiment Al-EM–4 showing the path of fluid motion during the experiment; (a) scanned vertical cross-sectional image of the sample and (b) the microstructure of part of the separated layer revealed by the flow pattern.

Figure 11 shows the vertical cross-section of the air-cooled sample close to the bottom compared with that from experiment Al-EM–4. The path of fluid flow is clearly seen in the samples, which shows strong fluid flow close to the bottom of the crucible. For the copper coil-cooled sample there appears to be several flow loops close to the bottom. In the case of air cooled sample, the flow appears to have developed vertically through the middle part of the bottom.

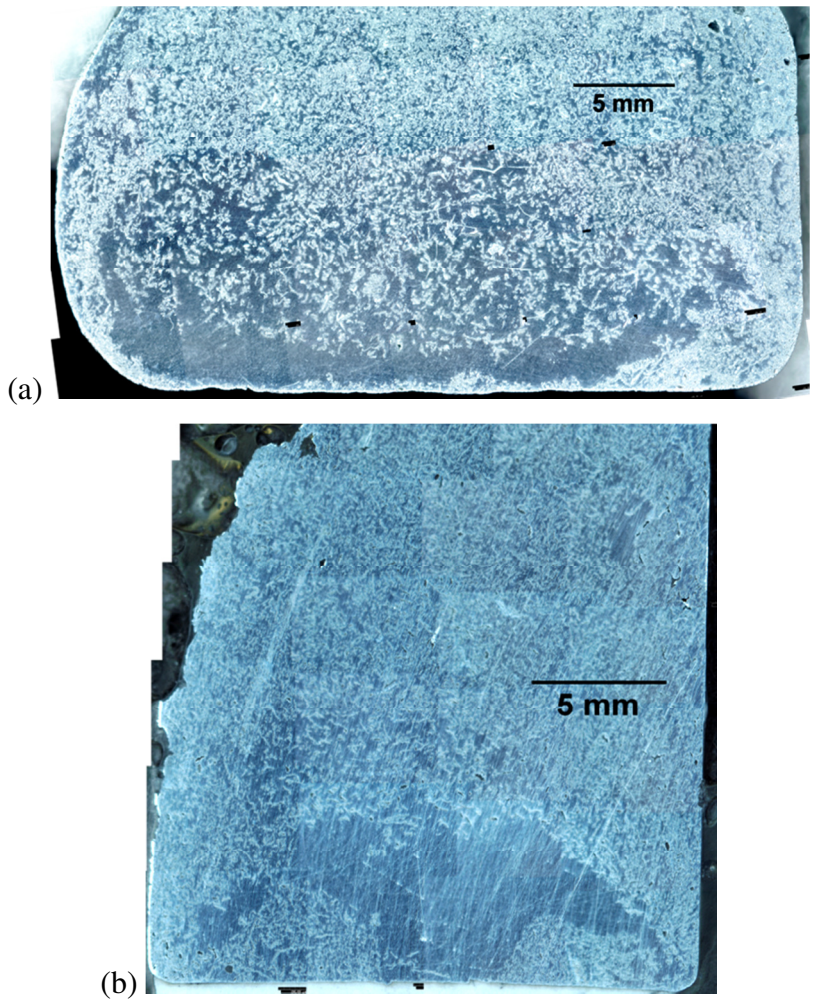

Figure 11. Particle distributions showing the fluid flow paths for (a) copper coil cooled and (b) air cooled melt.

There is a fundamental difference between the two configurations besides the cooling effects, which is the nature of the induced magnetic field. While the copper cooling coil provides some shielding effect and a possible secondary magnetic field due to mutual induction with the primary inductor, the air-cooled sample depended directly on the primary field induced. The magnetic field was modeled for both configurations in the finite element application, ANSOFT Maxwell via the 3D eddy current solver and the insulating boundary condition available in the software. Figure 12 shows the magnetic field vectors and contours within the aluminum for the two set-ups and as can be clearly seen the magnetic field in aluminum is stronger in the air-cooled case than the copper coil-cooled case. This probably explains the difference in the observed flow pattern.

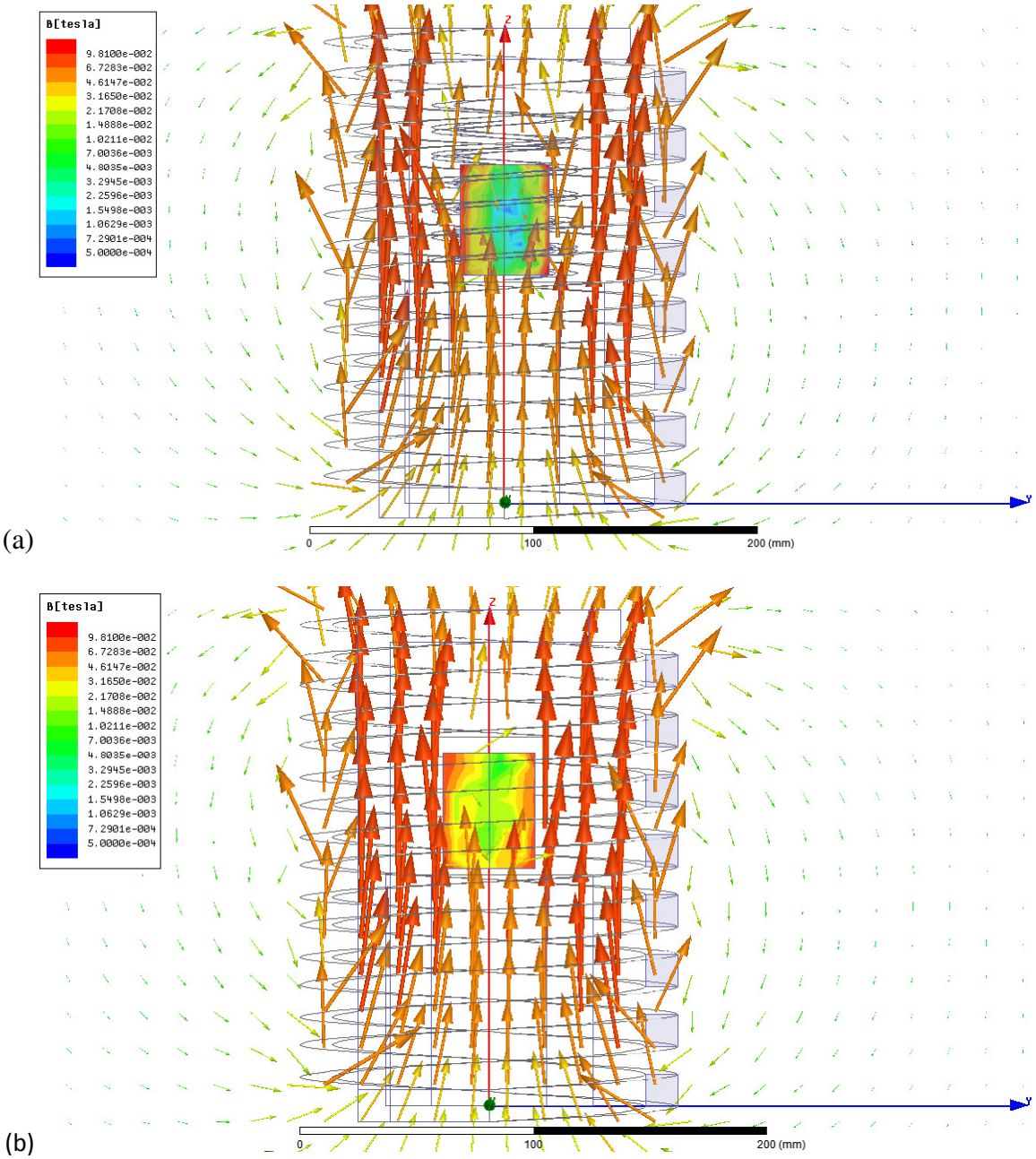

Figure 12. Magnetic field vectors and contours of magnetic field within aluminum for the experimental set-up involving (a) copper coil cooling (280A and 63 kHz) and (b) air cooling (280A and 128 kHz).

A 2D turbulent magnetohydrodynamics (MHD) model was solved via ANSYS Fluent, based on the prediction of magnetic field distribution in the aluminum by ANSOFT Maxwell software for a crucible of 40 mm diameter and 50 mm high molten

aluminum. The calculation was made for a current of 280 A and frequencies of 63 kHz and 128 kHz respectively for the copper coil- and air-cooled cases. Results of the model are showed in Fig. 13. The flow streams within molten aluminum in both experimental configurations show strong fluid flow near the bottom of the crucible and in the copper coil-cooled case the development of flow loops close to the bottom. The calculations indicate moderate agreement with the experimental results, especially for the copper coil-cooled case. It must be noted that, the model was solved for a lower current (280 A instead of 480 A) and a larger crucible (ID=40 mm) in the air-cooled case compared to the actual experiment (ID=15 mm).

In principle, increasing the current will increase the magnetic field strength thus increasing the strength of the induced fluid flow, which has the tendency to increase the separation efficiency. However, there is a limit to the magnitude of fluid velocity due to possibility of washing already separated particles by turbulent flow.

Temperature and Viscosity Distribution

As an example calculation, a general solidification model (see Eq. (1)) may be solved analytically considering the Al_2O_3 crucible to predict the temperature distribution within the metal for various outside crucible wall temperatures after a time of 10s separation time. For the development of the model refer to reference [17].

$$T = T_m + \frac{1}{erf\left(\phi\sqrt{\frac{\alpha_s}{\alpha_l}}\right)-1}\left[T_\infty erf\left(\phi\sqrt{\frac{\alpha_s}{\alpha_l}}\right) - T_m + (T_m - T_\infty)\, erf\left(\phi\frac{x}{2\sqrt{\alpha_l t}}\right)\right] \qquad (1)$$

$$\phi = f\left(T_o, T_\infty\right)$$

where T_o, T_m, and T_∞ are temperature of the outside crucible wall, melting point of metal and the molten metal respectively, α is the thermal diffusivity, subscripts “s” and “l” stand for solid and liquid metals respectively, and x is the distance from the crucible wall. Table II gives the material properties used in the calculations.

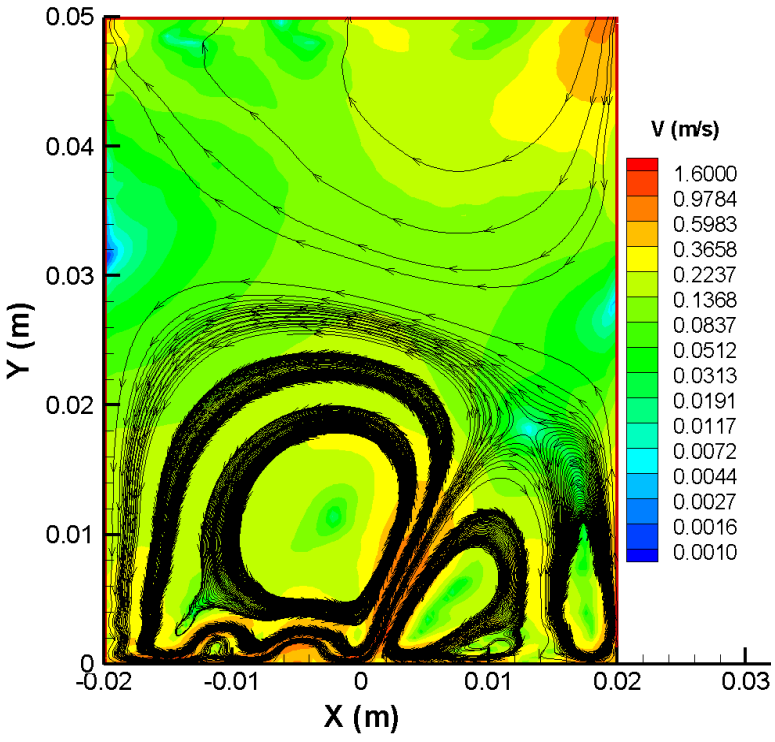

(a)

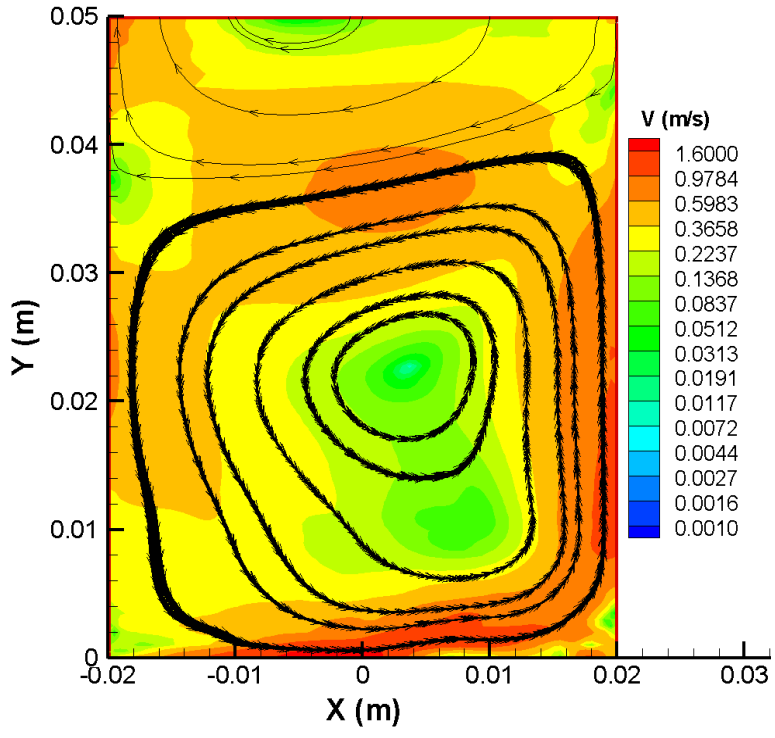

(b)

Figure 13. Calculated fluid contours and streamlines for the experimental set-up (a) with copper coil cooling and (b) without copper coil cooling.

Table II Material properties for the crucible and aluminum.

Property	Al_2O_3 Crucible	Solid Al	Liquid Al
Thermal Conductivity (kW/mK)	0.023	0.211	0.091
Density (Kg/m^3)	3950	2555	2368
Specific heat (kJ/kgK)	1.90	1.19	1.09
Latent heat of fusion (kJ/kg)	-	398	-

It is seen that the thermal conditions on the outside of the crucible have serious implications on the conditions inside the crucible, which may lead to cooling of the metal below its melting temperature of 933 K (660 ^{o}C). Beyond the frozen layer the temperature increases steadily toward the center of the crucible until the stream temperature is reached. For a 15 mm Al_2O_3 crucible maintaining the outside wall temperature at ~300 ^{o}C leads to complete freezing after 15 s in the experiments, which is explained by the calculations. Changes in the metal temperature affect the viscosity of the melt significantly as seen in the viscosity distribution Figure 14.

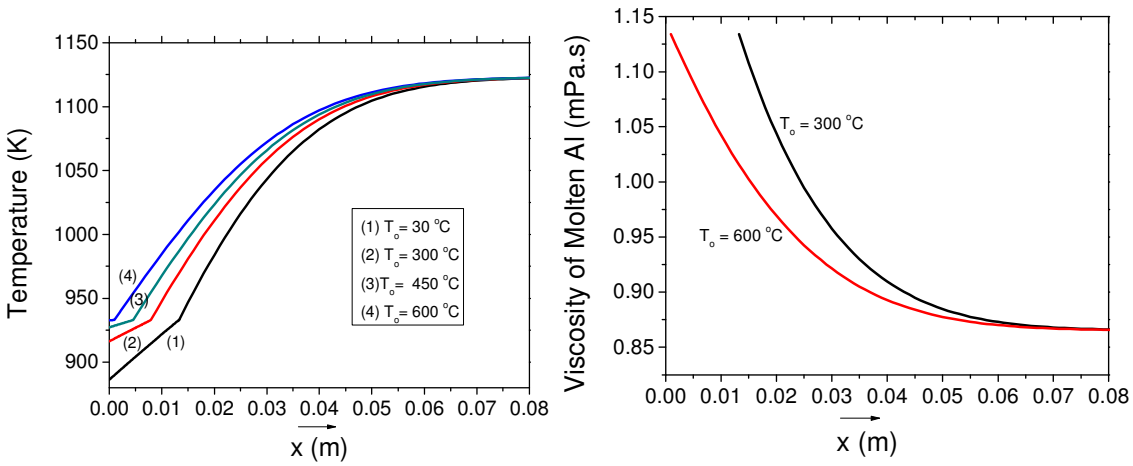

Figure 14. Temperature and viscosity distribution within the metal for various outside wall temperatures, T_o of Al_2O_3 crucible after a time of 10 s. The viscosity distribution is after the results in the literature [18].

Therefore designing the system to keep the surface temperature of the crucible wall around the melting temperature of the molten metal may generate a favorable viscosity which keeps the particles trapped at the wall of the crucible while preventing freezing of the molten metal during the electromagnetic purification process. This result may be useful for future industrial designs of an electromagnetic separation unit for removing nonmetallic particles from molten metals

Summary

The conditions and mechanism for high frequency electromagnetic separation of inclusions from aluminum was investigated on an Al –SiC particulate composite with particles sizes ranging 1 – 30 μm. Experiments using small and large crucibles were carried out with and without cooling. It was found that without cooling particles could not be separated to the wall of the crucible due to the sweeping effect of induced circulatory flow on the particles. With cooling, a more viscous fluid is generated close to the wall of the crucible, which helped to trap particles as they are transported by fluid flow to the vicinity of the wall where the electromagnetic force acting on particles is effective. Freezing of the metal may occur close to the wall if the temperature of the wall is not well controlled during cooling. It is recommended for the inner wall surface temperature to be controlled to be about the melting point of the metal to help develop the requisite viscosity to trap particles at the wall. Therefore air cooling may be more useful than water cooling. The separation was not limited by the size of the crucible as long as there was sufficient fluid flow throughout the melt. Increasing separation time, coil current and frequency increases the strength of induced fluid flow thereby enhancing the separation process. Particles of all size were effectively separated.

References

1. Damoah, L.N.W. and L. Zhang, *Removal of inclusions from aluminum through filtration.* Metallurgical and Materials Transactions B, 2010. **41B**: p. 886-907.

2. Makarov, S., R. Ludwig and D. Apelian, *Electromagnetic Separation Techniques in Metal Casting. I. Conventional Methods.* IEEE TRANSACTIONS ON MAGNETICS, 2000. **36**(4): p. 2015-2021.

3. Zhang, L., A. Ciftja and L. Damoah. *Removal of non-metallic inclusions from molten aluminum*. in *Proceedings of EMC*. 2007.

4. Fernandes, M., J.C. Pires, N. Cheung and A. Garcia, *Investigation of the chemical composition of nonmetallic inclusions utilizing ternary phase diagrams.* Mater. Char., 2003. **49**: p. 437-443.

5. Zhou, M., D. Shu, K. Li, W. Zhang, B. Sun, J. Wang and H. Ni, *Performance improvement of industrial pure aluminum treated by stirring molten fluxes.* Mater. Sci. Eng. A, 2003. **347**: p. 280-290.

6. Kolin, A., *An Electromagnetokinetic Phenomenon Involving Migration of Neutral Particles* Science, 1953. **117**: p. 134-137.

7. Leenov, D. and A. Kolin, *Theory of Electromagnetophoresis. I. Magnetohydrodynamic Forces Experienced by Spherical and Symmetrically Oriented Cylindrical Particles.* J. Chem. Phys, 1954. **22** (4): p. 683-688.

8. SHU, D., B.D. SUN, J. WANG, T.X. LI and Y.H. ZHOU, *Study of Electromagnetic Separation of Nonmetallic Inclusions from Aluminum Melt.* METALLURGICAL AND MATERIALS TRANSACTIONS A, 1999. **30A**: p. 2979-2988.

9. Sun, Z., M. Guo, J. Vleugels, O.V.D. Biest and B. Blanpain, *NUMERICAL CALCULATIONS ON INCLUSION RE-MOVAL FROM LIQUID METALS UNDER STRONG MAGNETIC FIELDS.* Progress In Electromagnetics Research, PIER, 2009. **98**: p. 359-373.

10. Kim, J.-H., J.-P. Park and E.-P. Yoon, *A Study on Elimination of Alumina Particles in Molten Aluminum using Direct Electromagnetic Force.* Metals and Materials, 1999. **5**(4): p. 339-343.

11. TAKAHASHI, K. and S. TANIGUCHI, *Electromagnetic Separation of Nonmetallic Inclusion from Liquid Metal by Imposition of High Frequency Magnetic Field.* ISIJ International, 2003. **43** (6): p. 820-827.

12. S.Taniguchi, N.Yoshikawa and K.Takahashi, *APPLICATION OF EPM TO THE SEPARATION OF INCLUSION PARTICLES FROM LIQUID METAL*, in *The 15th Riga and 6th PAMIRConference on Fundamental and Applied MHD (Invited Lectures)*. 2005: Rigas Jurmala, Latvia. p. 55-63.

13. Shu, D., B. Sun, K. Li, J. Wang and Y. Zhou, *Effects of secondary flow on the electromagnetic separation of inclusions from aluminum melt in a square channel by a solenoid.* ISIJ Inter., 2002. **42**(11): p. 1241-1250.

14. Shoji TANIGUCHI, J.K.B., *Theoretical Study on the separation of inclusion particles by pinch force from liquid steel flowing in a circular pipe.* Tetsu-to-Hagane, 1994. **80**(1): p. 24-29.

15. Yamao, F., K. Sassa, K. Iwai and S. Asai, *Separation of inclusions in liquid metal using fixed alternating magnetic field.* Tetsu-to-Hagane, 1997. **83**(1): p. 30-35.

16. Shu, D., B.D. Sun, J. Wang, T.X. Li and Y.H. Zhou, *Study of electromagnetic separation of nonmetallic inclusions from aluminum melt.* Metall. Mater. Trans. A, 1999. **30A**(11): p. 2979-2988.

17. Dantzig, J.A. and C.L. Tuckler, *Modeling in Materials Processing*. 2001, New York: Cambridge University Press.

18. Cherne(III), F.J. and P.A. Deymier, *Calcultation of the transport properties of liquid aluminum with equilibrium and non-equilibrium molecular dynamics.* Scripta Materialia, 2001. **45**: p. 985-991.

IV. REMOVAL OF INCLUSIONS FROM ALUMINUM THROUGH FILTRATION

Lucas Nana Wiredu Damoah, Lifeng Zhang

Department of Material Science and Engineering
Missouri University of Science and Technology (Missouri S&T)
223 McNutt Hall,
Rolla, MO 65409-0330, USA
Email: zhanglife@mst.edu

This paper was published in Metallurgical and Materials transactions B with two schematics included and edited for this dissertation

Filtration experiments were carried out using both AlF_3 slurry coated and uncoated Al_2O_3 ceramic foam filters to study the removal of both nonmetallic inclusions and impurity elements. The results showed that the 30 ppi ceramic foam filter removed up to 85% of the inclusions from aluminum. Several digital images of two and three dimensional morphologies of both nonmetallic and intermetallic inclusions have also been presented. Two contributing mechanisms for the removal of nonmetallic inclusions in the deep bed filtration mode are proposed: (1) collision with walls and interception effect, and (2) the formation of both intermetallic and nonmetallic inclusion bridges during filtration. Fluid dynamic modeling of inclusion attachment to the filter walls showed that most inclusions, especially those with larger sizes, are entrapped at the upper part of the filter while smaller inclusions dispersed well throughout the filter. Calculated inclusion removal fractions for the 30 ppi filter showed that almost all > 125 μm inclusions are removed and inclusions ~ 5 μm in size are removed up to 85 %. The interfacial energy between two collided same-size inclusions was calculated, indicating that strong clustering of inclusions may result within the filter window. Magnesium impurities were removed up to 86 % by the AlF_3 slurry coated filter. The filter acted in active filtration mode, in addition to the contribution by air oxidation of dissolved [Mg], which was calculated to be 13 %. The total mass transfer coefficient of dissolved [Mg] to the reaction interface was calculated to be 1.15×10^{-6} m/s.

I. INTRODUCTION

ALUMINUM cleanliness has been in the limelight during the last three decades and still remains a concern in the aluminum casting industry. In general, cleaning aluminum and its alloys refers to minimizing contaminants such as dissolved gasses (especially hydrogen), non-metallic inclusions (such as oxides, carbides, nitrides), a variety of intermetallic compounds, and alkali and alkaline-earth elements such as sodium, lithium and calcium. These contaminants enter the molten aluminum through the ore and raw materials used in the extractive metallurgical processes, from refractory materials and the atmosphere during production of aluminum and even through the refining processes. The common types of inclusions in aluminum have been reported to be: oxides, nitrides, carbides, fluorides and borides.[1]

Extensive research has resulted in a significant improvement in our present understanding of the various aspects of these contaminants, and in many foundries, melt-cleaning practices have been established and are routinely used. However with the ever-increasing demand for improved metal properties, the requirements for molten metal cleanliness have become extremely stringent. Various methods such as sedimentation, flow transport, bubble flotation, filtration, and electromagnetic force are being used for the removal of inclusions from molten aluminum. Investments in filtration systems are relatively cheap and hence every effort at making them even more efficient must be explored.

AlF_3 is used to purify the molten aluminum by removing dissolved impurities such as Na and Ca through powder fluxing [2-3] and granular bed filtration [4]. It was reported that ~98% Na and Ca were removed from aluminum through AlF_3 granular bed filtration[4-5]. The use and the evaluation of the efficiency of ceramic foam filters in the removal of non-metallic inclusions from molten aluminum have been widely studied in the literature [6-14]. Reports from these studies indicated that ceramic foam filters (CFFs) are capable of achieving high aluminum filtration efficiencies and the formation of bridge-like structures of inclusions at the top area of the filter contributes to the high efficiencies. It is well known that CFFs also remove inclusions smaller than the pore size of the filter in a deep bed filtration mode. However there is inadequate information to explain the removal mechanism of smaller particles within the filters. Furthermore, using the existing Al_2O_3 CFFs coated with AlF_3 to purify molten aluminum has the potential to remove both dissolved impurities and non-metallic inclusions simultaneously.

The current study observed the morphologies of inclusions commonly found in aluminum in both two and three dimensions and experimentally investigated on a laboratory scale the removal of nonmetallic inclusions and, the removal of unwanted impurity elements from the molten aluminum by the use of regular uncoated Al_2O_3 CFF, and Al_2O_3 CFFs coated with AlF_3. Fluid dynamic calculations and other theoretical modeling were used to explain the underlying inclusion removal mechanism.

II. MATERIALS AND EXPERIMENTAL METHODS

The experiment was in two parts. The first part studied the morphology of inclusions, both metallic and nonmetallic, in aluminum as all the information published centered on two dimensional inclusion morphology. This was followed by filtration experiments using 30 ppi ceramic foam filter. Four aluminum samples were observed for the morphology of the inclusions present. Table I gives a description of these samples. The samples were ground with different grades of SiC grinding paper and finally polished with diamond paste on a 1µm polishing cloth. Samples S3 and S4 underwent partial acid extraction using 35 % HCl solution. The purpose was to dissolve the surface of the metal to reveal the three dimensional morphology of inclusions. Trial etching was done for 100 s and it was observed after that time that certain inclusions, especially intermetallic inclusions were partly dissolved by the acid. Figure 1 shows the microstructure of the alloy sample S3 after 100 s etching time. Therefore, several etching trials were run to determine the optimum etching time for the samples for which approximately all inclusions were stable enough for their morphologies to be examined. Etching was done for 40 seconds for samples S3 and 30 seconds for sample S4. After etching the samples were immediately washed and dried.

Table I. Experimental Samples Used in Inclusions Observation

Sample number	Description	Partial acid extraction (time)
S1	Filtered Al/SiC composite alloy	No
S2	Ceramic foam filter material used for filtration of sample S1 containing solidified aluminum	No
S3	Aluminum alloy (Al-95.4%, Mg-4.5%, others -0.1%)	Yes (40 s)
S4	PoDFA filter sample used for filtration of sample S3	Yes (30 s)

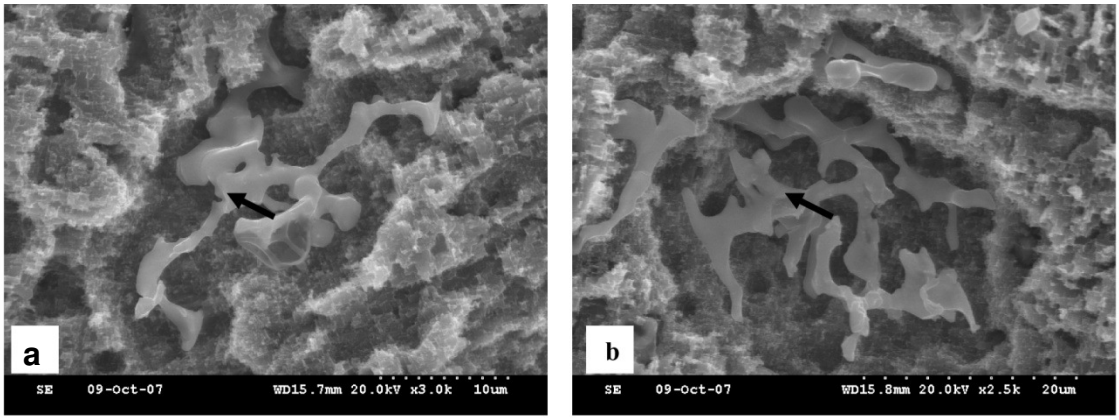

Fig. 1—Microstructure of HCl etched Al-Mg alloy revealing dissolves matrix and partly dissolved Fe-rich intermetallic phase after 100 seconds etching time. (a) Dissolved aluminum matrix with Fe-rich intermetallic (composition: 23.28 wt% O, 48.61 wt% Al, 4.92 wt% Mn and 23.19 wt% Fe), (b) complex network of Fe-rich intermetallic with composition 29.49 wt% O, 1.55 wt% Mg, 50.64 wt% Al, 3.26 wt% Mn and 15.06 wt% Fe.

The schematic experimental set up, graphite crucible, and experimental scheme used for molten aluminum filtration are shown in Figure 2 and Table II. The experimental furnace used was an induction furnace. In the experimental set-up the crucible, fitted with the filter was placed in the induction coils of the furnace and a graphite tray positioned at the bottom of the furnace, directly under the molten metal outlet of the crucible to collect the filtered metal. The vacuum in the induction furnace was not used. Aluminum scrap cut into lumps of dimension 20 mm × 40 mm were charged into the crucible. The crucible with aluminum scrap was heated to an aim temperature of 950°C in the induction furnace. Additional aluminum scrap was charged into the crucible until an appreciable molten metal volume was reached. The scrap used in the filtration experiments were of two forms: Alloy-1 (Al ~ 99.56 wt%, Si ~ 0.10 wt%, Mg ~0.01 wt%, Fe – 0.275 wt%, others < 0.05 wt%) and Alloy-2 (Al ~ 98.25 wt%, Si ~ 1 wt%, Mg ~0.45 wt%, Fe – 0.20 wt%, others < 0.1 wt%). Alloy-1 contained few SiC particles while alloy-2 contained many dispersed SiC particles. The composition of the alloys were determined by glow discharge mass spectrometry (GDMS), which was set not to determined carbon because it was not an alloying element but present as SiC. The filtered

molten metal was collected in the alumina coated graphite tray placed at the bottom of the furnace. Furnace heating was discontinued at about 950 °C during filtration to solidify some metal within the filter to allow for studies of the filtration mechanism and the inclusion distribution within the filter.

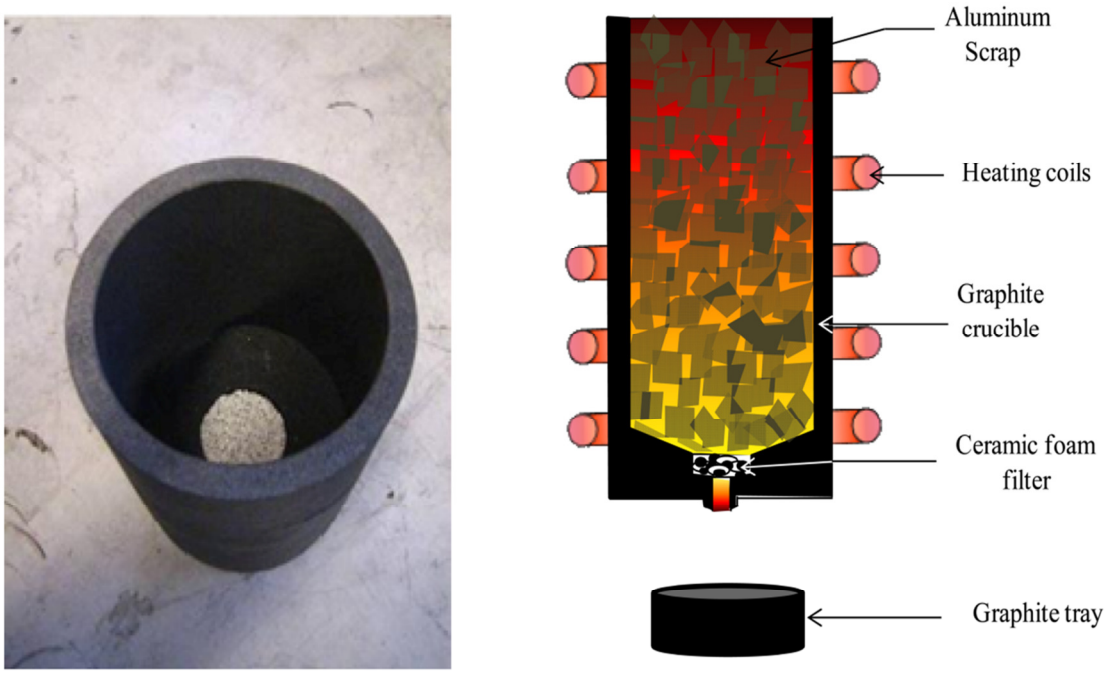

Fig. 2—Filtration crucible fitted with filter at the bottom and schematic filtration experimental set-up.

The filtration time was measured by timing the interval between the first drop and the last drop of molten metal into the graphite tray. The last drop was simply determined by removing the graphite tray. The filtered metal in the graphite tray was weighed to estimate the mass flow rate. We appreciate the limitation of this method to give the exact flow rate; however, it presents a fair idea of the relative flow rates in the filtration experiments. Two types of ceramic foam filters were used, regular Al_2O_3 ceramic foam filter and AlF_3-slurry coated Al_2O_3 filter, both of which were phosphate bonded. Figure 3 shows the two filters used in the experiments. The slurry coated CFF had less porosity than the uncoated Al_2O_3 CFF because the AlF_3 slurry used for coating closed some pores in the filter.

Table II. Filtration Experiments Parameters

Experiments #	E1	E2	E3
Aluminum sample	Alloy-1	Alloy-1	Alloy-2
Filter	Uncoated	Slurry coated	Slurry coated
Molten metal mass (g)	2350	2431	2780
Maximum temperature/ ^{o}C	1010	970	900
Mass filtered (g)	1932	1780	1581
Filtration time (s)	602	361	705
Average mass flow rate (kg/s)	3.21×10^{-3}	4.93×10^{-3}	2.24×10^{-3}

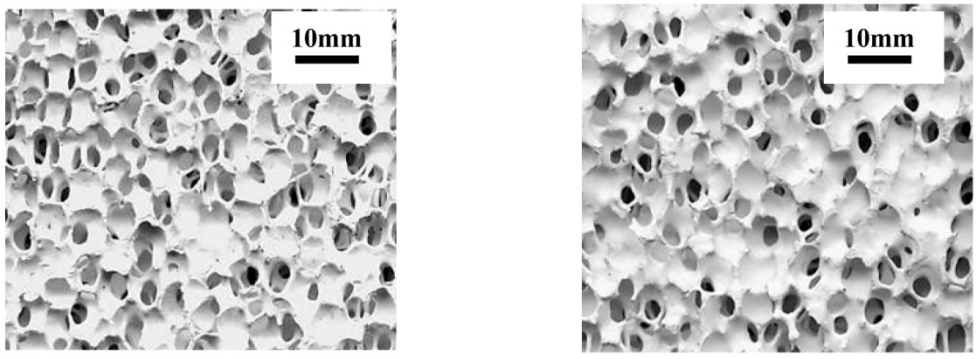

Fig. 3—30 ppi uncoated Al_2O_3 CFF (a) and AlF_3 slurry coated CFF (b).

Metal and filter samples from the experiments were taken for light microscopy inclusion observation, SEM with EDX capability to identify, count and determine elemental composition of nonmetallic inclusions, and electron probe micro-analyzer (EPMA) to make X-ray maps of elemental compositions in inclusions and aluminum. GDMS was used to analyze the concentration of impurity elements. Several samples

were taken before filtration from the unmelted scrap after they had been cut for the experiments for analysis. To study the mechanisms for the removal of inclusions, filter samples were carefully prepared and the distribution of inclusions within the filters from the molten aluminum entrance point to the exit was studied.

An important consideration for designing molten metal filtration using a CFF is the pressure drop across the filter–molten metal interface, which may drive or oppose the flow of molten metal through the filter. The expected pressure drop, *capillary pressure* Δp, across the filter may be given by the Young – Laplace equation,

$$\Delta p = -\frac{4\sigma\cos\theta}{d} \qquad [1]$$

where σ is the surface tension of molten aluminum, d is the mean pore size of the respective filter (whether coated or uncoated) and θ is the wetting angle. For non-wetting solids, such as alumina in molten aluminum [15], the wetting angle is $\theta=150^{o}$, therefore $\Delta p>0$. Thus, a positive external pressure is needed to initiate the flow of molten metal. Conversely, for wettable solids the wetting angle is $\theta<90^{o}$, leading to $\Delta p<0$ and a resultant spontaneous flow of molten metal through the filter. However, in real solids with interconnected networks of irregular pores of different sizes such as the CFF, geometrical corrections are needed to account for pore shape [16], and the expression for the capillary pressure becomes

$$\Delta p = -\frac{(1-\varepsilon)\rho A\sigma\cos\theta}{\varepsilon} \qquad [2]$$

where ε is porosity, ρ is the solid's density and A is the specific area of the solid (i.e. surface area per unit mass, m^2/kg). Assuming a maximum nonwetting angle for alumina in the molten aluminum, i.e. $\theta=180^{o}$, $\cos\theta=-1$ and the Young – Laplace equation becomes

$$\Delta p = \frac{\rho A\sigma(1-\varepsilon)}{\varepsilon} = \frac{S\sigma(1-\varepsilon)}{\varepsilon} \qquad [3]$$

which gives the minimum external pressure to be applied to allow molten aluminum flow through alumina CFF. S is the surface area per unit volume of solids (m^2/m^3). The pressure p within molten metal with density ρ_m and metallostatic height h is given by

$$p = \rho_m g h \quad [4]$$

The molten metal pressure given by Eq.[4] should be greater than the pressure drop Δp to ensure the molten aluminum flows through the filter, thus

$$h \geq \frac{(1-\varepsilon) S \sigma \cos\theta}{\varepsilon \rho_m g} = \frac{\Delta p}{\rho_m g} \quad [5]$$

For many applications in the aluminum industry, the metallostatic head is limited to 0.1 m or 0.2 m in order to force the molten metal through the filter [17]. Setting ρ_m to be 2400 kg/m^3, σ to be 1.01 N/m [15] and using data for CFFs of various pore sizes (Table III) [18], values for h can be calculated. Figure 4 shows the calculated pressure drop across the filter, and the corresponding metallostatic head h, to overcome for various Al_2O_3 CFF pore sizes. The results show that the metallostatic head of molten metal increases as the specific surface of the filter increases. The calculated h values indicate that in order to have molten metal flow through a 30 ppi Al_2O_3 CFF the height of molten metal on top of the filter should be greater than 209 mm.

Table III. Data for Various CFF Pore Sizes Adopted from Reference [18]

Pore size (ppi)	Porosity, ε	Surface area per unit volume, S (m^2/m^3)
10	0.878	1.71×10^4
30	0.874	3.37×10^4
45	0.802	2.78×10^4
60	0.857	6.84×10^4

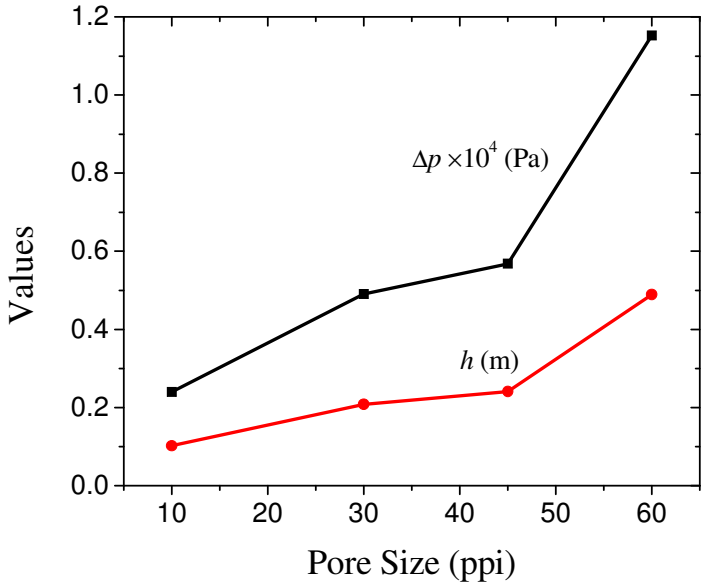

Fig. 4—Pressure drop across filter, Δp and corresponding metallostatic height, h of various pore sizes of Al_2O_3 CFFs.

III. INCLUSIONS IN ALUMINUM

Figure 5 (a) and (b) show respectively two and three dimensional lumps of aluminum oxide inclusions observed in sample S3. The 3D morphological view reveals faceted polygonal lumps of Al_2O_3 inclusion. Dark films of Al_2O_3 inclusions were also observed in the samples with thickness $\leq 2\mu m$, similar to the results of Simensen and Berg [1] and Liu and Samuel [19].

Aluminum carbide, Al_4C_3 inclusions, are commonly found in aluminum coming from the electrolysis process and are present in commercially pure aluminum ingot used to produce aluminum alloys [1, 20]. The carbides are hexagonal or grey discs and are normally found as clusters isolated or together with oxides and boride particles [1]. Measurements by Simensen and Berg [1] showed that aluminum from the electrolysis cells contains 10 to 35 ppm Al_4C_3 and commercial aluminum contains 2 to 12 ppm Al_4C_3. They also reported that the main source of carbide formation is the reaction between the

melt and the cathode or anode in the cell. Addition Al_4C_3 inclusions may form from stirring and/or degassing of the molten metal using a graphite impeller for a fairly lengthy period of time at high temperatures [20]. They may also result from a reaction between molten aluminum and the unprotected surface of silicon carbide crucibles with deteriorated surface coating according to Eq. [6] [21-22]. Figure 5 (c) and (d) show Al_4C_3 particles in both two and three dimensional views embedded in aluminum. It has been reported that Al_4C_3 particles precipitate as black needles.[20] Figure 5(c) shows black needles of Al_4C_3, which is in good agreement with the results reported by Liu and Samuel. The 3D morphological results show that Al_4C_3 inclusions may also appear as bright, irregular or faceted lumps and cluster of lumps. Figure 5(d) shows hexagonal gray discs of Al_4C_3 inclusion similar to reported results [1].

MgO is a common oxide inclusion found in most Al – Mg alloys. They are usually present in the matrix as dispersed clusters, as shown Figure 5(e) and (f). They are formed by a reaction of dissolved magnesium in aluminum with air in the furnace or ladle during foundry melting and refining processes. MgO and $MgAl_2O_4$ particles are described in the literature [1] as black or brown, thick films or elongated lumps consisting of loosely adherent particles. Figure 5(f) shows a 3D view of large a MgO cluster morphology observed in sample S4. Its composition was determined to be 58 wt% Mg and 42wt% O.

Silicon carbide inclusions may be termed exogenous since they are not generated through any molten metal chemical reaction but originate from physical interaction between the liquid metal and crucible or furnace wall, which causes wear and/or corrosion of the wall. Due to the superior properties of carefully dispersed SiC particles in aluminum, the potential of Al – SiC metal matrix composites is being tapped in many applications today. However, SiC particles are usually attacked by molten aluminum in a reaction to produce Al_4C_3, (Eq. [6]), if their surfaces are not well protected. Figure 5(g) shows a 3D lump of SiC observed in aluminum. There were several clusters, platelets and lumps of varying sizes observed in this study, especially in sample S2.

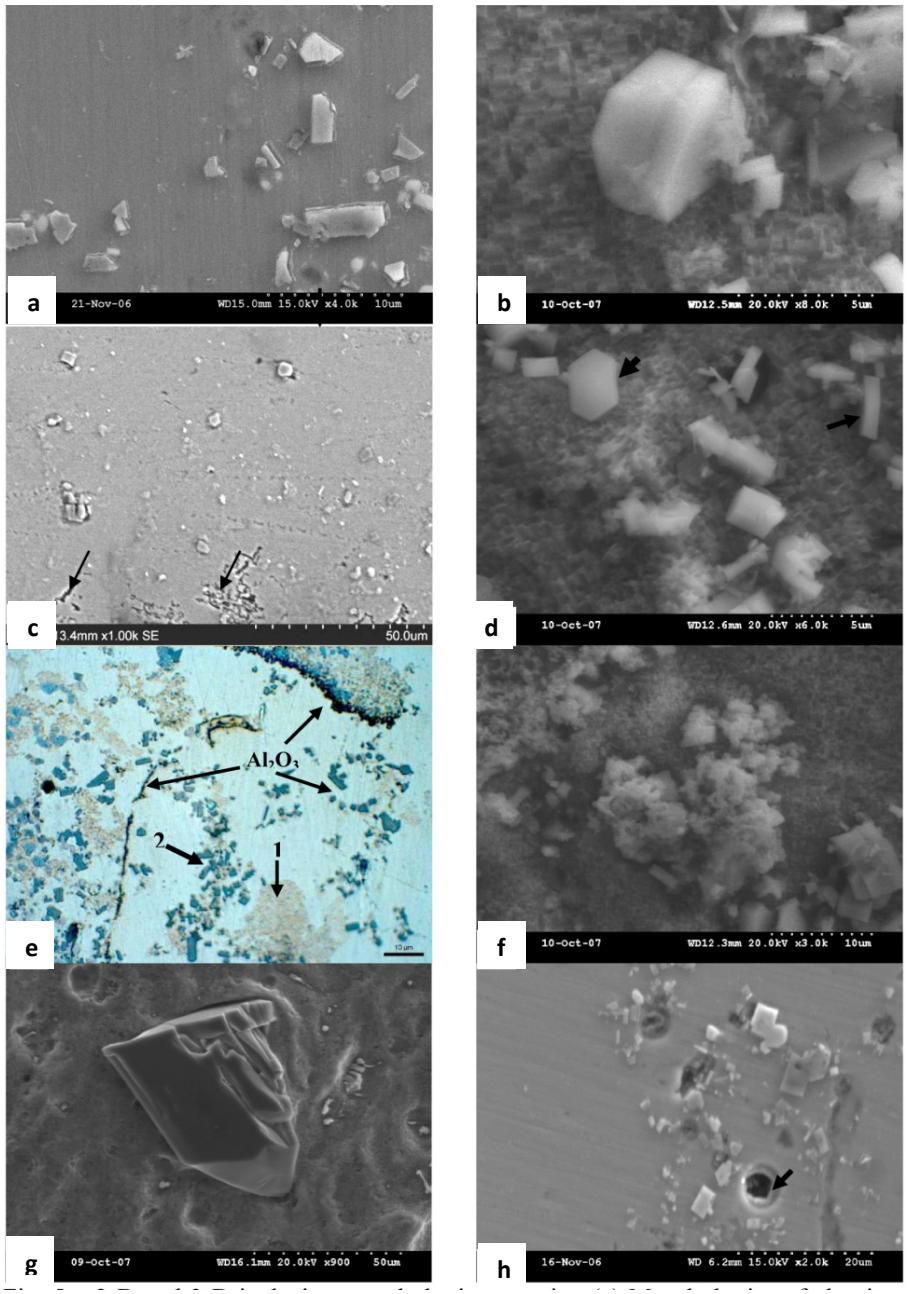

Fig. 5—2D and 3D inclusion morphologies showing (a) Morphologies of aluminum oxide inclusions observed showing inclusion clusters in un-etched sample S2, (b) three dimensional morphology of faceted lump of Al_2O_3 observed in sample acid etched sample S3 (c) Morphologies of aluminum carbide inclusions, (d) dark pins of Al_4C_3 in un-etched sample S2 hexagonal platelet of Al_4C_3 particle similar to the results of Simensen and Berg [3] (e) optical micrograph showing brown dispersed clusters (labeled 1) and cuboids (labeled 2) of MgO in un-etched sample S4 (f) dispersed MgO clusters in three dimensional view with composition: Mg – 58 and O – 42 wt %, etched sample S4, (g) and (h) 2D view of graphite particle showing a ring as a result of Al – C interactions.

Graphite particles are introduced into aluminum during the electrolysis as particles fall off either the anode or the cathode. Simensen and Berg [1] have shown from microstructural analysis that the metal occasionally contains carbon particles and grey graphite. They reported the presence of Al_4O_4C inclusions and a few small TiC particles. Results of this study shown in Figure 5(h) indicate the presence of large carbon particles in the microstructure of the metal. These carbon particles may react with molten aluminum to precipitate Al_4C_3 particles which are detrimental to the mechanical properties and machining of aluminum.

Several morphologies of Al_2SiO_5 inclusions were observed in aluminum in both two and three dimensions. Al_2SiO_5 particles are mainly irregularly shaped lumps (as shown in Figure 6(a)), large rods and clusters with a glassy appearance. They also appeared as films, which were associated with Fe-rich intermetallic phases as shown in Figure 6(b). Our two dimensional observation of this phenomenon showed a broken interface between the Al_2SiO_5 and Fe-rich intermetallic phases. This is in agreement with the result presented by Miller *et al* [23], who studied the role of oxides in the formation of a primary Fe-rich intermetallic phase by a deliberate addition of oxide particles to the molten metal. The iron-rich intermetallic phase was associated with oxides in the final microstructure, and crack-like defects were often observed in the β-Fe plates.

Diverse morphologies of $MgAl_2O_4$ spinel were identified in samples S3 and S4, one of which is showed in Figure 6(c) and (d). $MgAl_2O_4$ appeared mainly as “spongy” lumps, clustered films and large flakes. The lumps were sometimes associated with lumps of Al_2SiO_5.

Other oxide inclusions such us zirconia and SiO_2 were observed in association with each other.

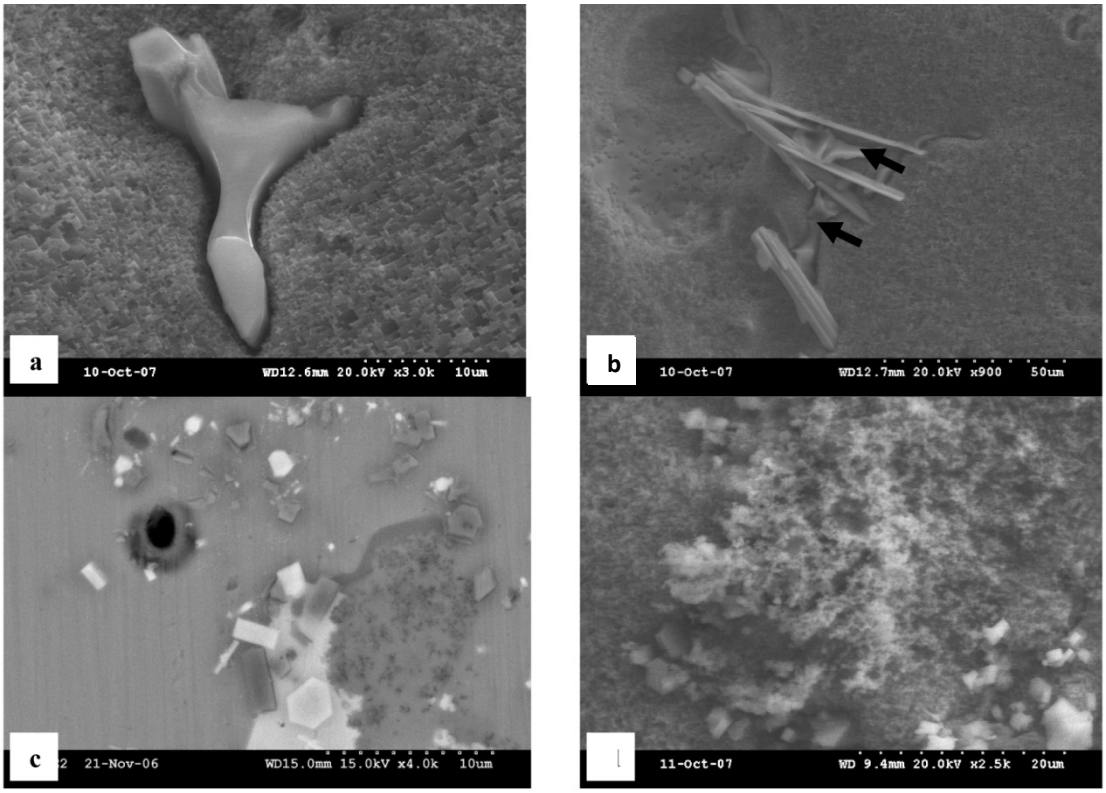

Fig. 6—Morphologies of double oxides (a) 3D morphology of Al_2SiO_5, (b) Al_2SiO_5 films holding rod-like and flaky Fe-rich intermetallic phases together, (c) Films of $MgAl_2O_4$ (spinel), also showing light colored Ti-Al-V faceted, and hexagonal particles and (d) Large clusters of $MgAl_2O_4$ films.

IV. REMOVAL OF NONMETALLIC INCLUSIONS

A. Evaluation of inclusions removal

Figure 7(a) shows that the microstructure of Alloy-1 before melting and filtration, contained many inclusions, which were identified by EDX as Al_2O_3, SiC and Al_4C_3 inclusions. However, after filtration using both uncoated CFF (Figure 7(b)) and AlF_3 slurry coated CFF, (Figure 7(c)) there were no visible non-metallic inclusions with particle size $\geq$ 3µm, an indication of the effectiveness of the CFF filtration process. Several clusters of fine precipitates of light colored features, identified to be Fe-rich intermetallics, were observed within the microstructure both before and after the filtration process. Iron (Fe) has unlimited solubility in molten aluminum but in solid aluminum is soluble only up to 0.04 wt%. This explains why the Fe-rich precipitates are present in the

metal both before and after filtration. The Fe-rich intermetallics observed are secondary precipitates with low melting temperatures according to their composition (92.62 atom% Al and 7.38 atom% Fe) and the Al-Fe phase diagram [24]. Their melting point is ~ 637°C, which is lower than the filtration temperature of 900°C. Pontevichi *et al*, [25] observed four main types of Fe-rich intermetallics to be in equilibrium with the molten aluminum at 727°C. These were described as the θ-, α-, γ- and δ-Fe phases, which may be removed through filtration during industrial processing of molten aluminum. Figure 8 presents more results from the study of the morphologies of the Fe-rich intermetallics in both two and three dimensions, which show in general, that their sizes are ≥ 5 μm. In Figure 8 it is clear from the 3D morphologies of the Fe-rich intermetallics that, when present in aluminum, they are likely to affect the mechanical properties by acting as points of stress concentration under load. Therefore, every effort at removing iron, as an impurity element, from aluminum must be pursued.

Similar results were recorded for the filtration of the Alloy-2 using the AlF_3 slurry coated CFF shown in Figure 9(a)-(d). Figure 9(a) shows many Al_2O_3 and SiC particles contained in the microstructure of Alloy-2 before filtration. After filtration with the AlF_3 coated alumina CFF, Figure 9(b) and (c) show a cleaner aluminum matrix. However, flakes of AlSi and Fe-rich intermetallic precipitates were observed as shown in Figure 9(b) and (c), and several Al_4C_3 particles were also observed in the metal after filtration (Figure 9(d)), which were not made in the metal before filtration. This observation may be attributed to the interaction between molten aluminum and SiC, as in Eq.[6] [21-22].

$$4[Al] + 3SiC \rightarrow 3Si + Al_4C_3 \qquad [6]$$

This reaction might have resulted in the local [Si] concentration increases leading to the precipitation of the AlSi upon cooling. The many Al_4C_3 particles observed in Figure 9(d) suggests that great caution should be exhibited during processing of Al – SiC composites because Eq.[6] has the tendency to derail the entire inclusion removal process and may also change the composition of the metal.

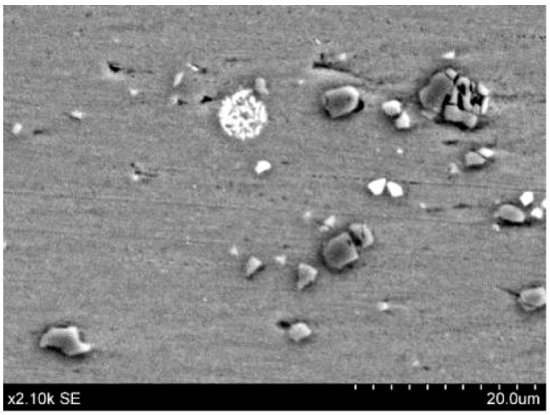

(a)

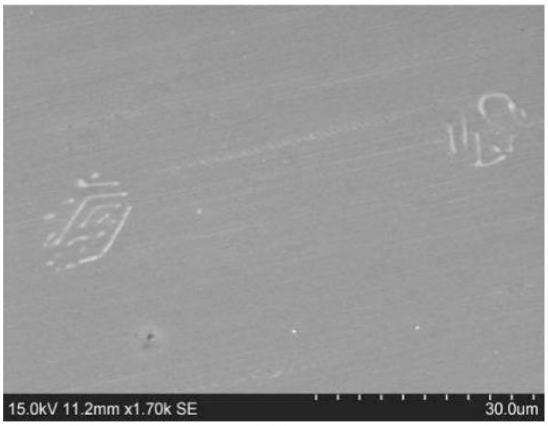

(b)

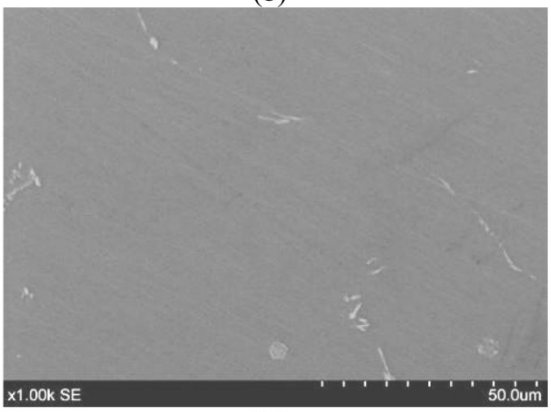

(c)

Fig. 7—Contribution of filtration to inclusion removal from molten aluminum: (a) cluster of Al_2O_3, SiC and Al_4C_3 inclusions in aluminum matrix before filtration; (b) cleaned aluminum matrix after filtration (experiment E1); (c) cleaned aluminum matrix after filtration (experiment E2), showing clusters of precipitated Fe-rich intermetallics.

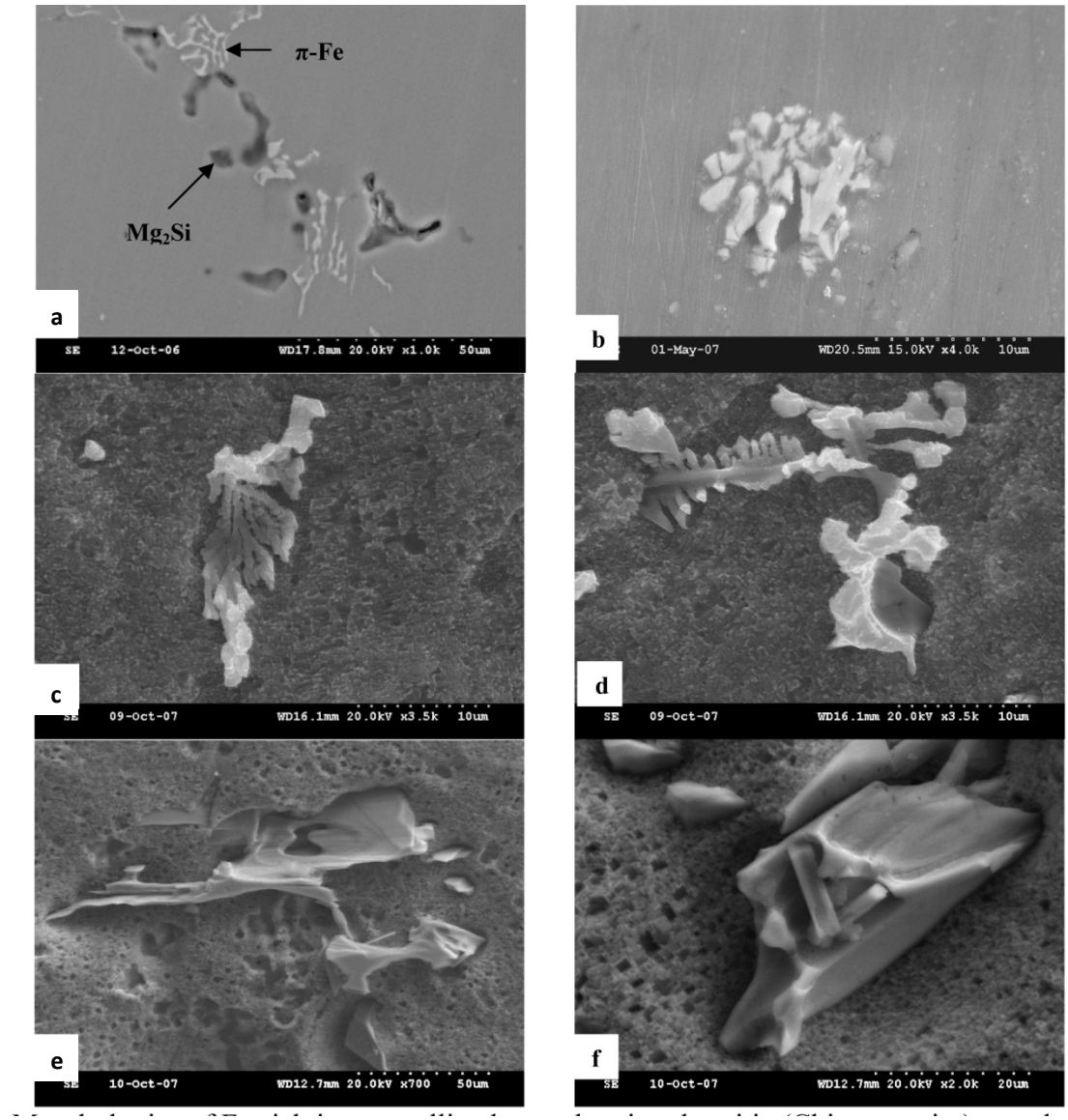

Fig. 8—Morphologies of Fe-rich intermetallic phases showing (a) dentritic (Chinese script) morphologies of β-$Al(FeMn)_3Si$ and π- $Al_8FeMg_3Si_6$ with intermetallics two dimensional morphologies of scripts (bright) and Mg_2Si (dark), (b) "circular" 2D cluster of α-Fe rich intermetallic phase in sample S1 (c) dentritic α-$Al(FeMn)_3Si$, (d) large dendrite of Al(FeMn)Si(Mg) with "dried leaves" appearance, (e) flakes of $Al_6(FeMn)$, and (f) lump of $Al_6(FeMn)$. The 2D un-etched observation (a) and (b) hides greater detail about the Fe-rich phases while etching reveals their actual morphologies.

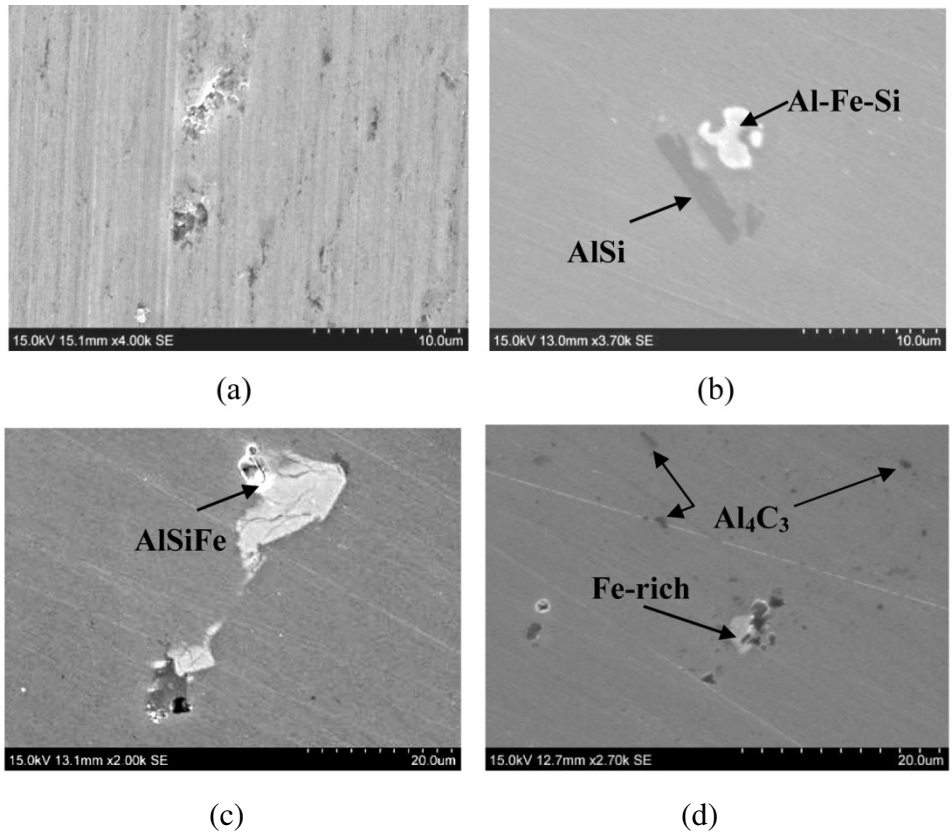

Fig. 9—Contribution of filtration to inclusion removal from molten aluminum: (a) cluster of Al_2O_3 and SiC inclusions in the matrix of Alloy-2 before filtration (experiment E3); (b) and (c) cleaned aluminum matrix after slurry coated filtration, showing flakes of precipitated Al-Fe-Si (white) and AlSi (dark lakes) phases; (d) Al_4C_3 inclusions resulting from the reaction shown in Eq.[6].

Evidence of this reaction was not clearly seen in the matrix of Alloy-1 after filtration (experiment E2) although several Al_4C_3 particles were observed as shown in Figure 10. Alloy-1 contained some Al_4C_3 particles before filtration (see Figure 7(a)). It is therefore difficult to tell the exact source of Al_4C_3 in the metal after filtration. Flakes of AlSi were not observed with alloy-1 after experiment E2 as was the case for experiment E3. This is attributed to the relatively lower [Si] content in Alloy- 1 (~ 0.10 wt% Si) than in alloy- 2 (~1.0 wt% Si). Again alloy-2 had many more SiC particles than alloy-1.

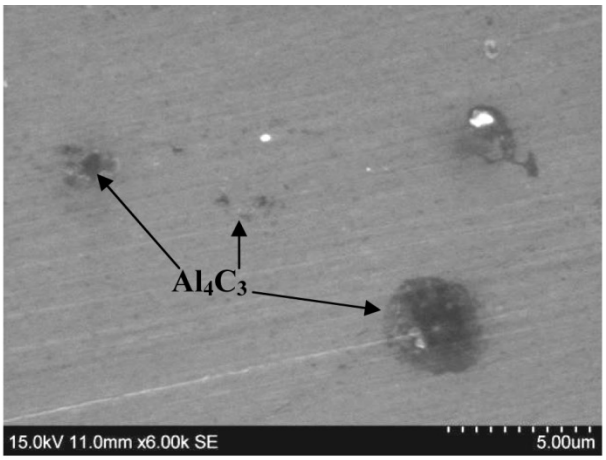

Fig. 10—Al_4C_3 particles, resulting from Eq.[6], in aluminum matrix after slurry coated filtration of Alloy-1 (experiment E2).

Another phenomenon that was observed in the filtration process is the re-oxidation of aluminum after filtration due to entrapped air. Figure 11(a) and (b) show the results of this phenomenon after experiments, E2 and E3 respectively. Al_2O_3 particles were produced, which further aided the nucleation of the Fe-rich intermetallics and the AlSi phases in the case of experiment E3 during solidification and cooling. Although Al_2O_3 particles were present in the alloys before filtration, the broken appearance of the Al_2O_3 particles (blow holes) in Figure 11(a) and (b) is the source of our suspicion that they resulted from re-oxidation. The difference between Figure 11(a) and (b) is the presence of precipitated AlSi and Fe-rich intermetallics in Figure 11(b) but not in (a). This is perhaps due to the effects of Eq.[6], which leads to increased [Si] concentration beyond the solubility limits at various points in the molten metal, hence the precipitation of AlSi phase upon solidification of alloy- 2, in experiment E3 and not in alloy- 1, experiment E2.

SEM studies conducted on used filter samples revealed that many inclusions were trapped within the windows of the filter during the filtration process as shown in Figure 12(a) and (b). X-ray maps of elements in the trapped inclusions within the filter windows were made by electron probe micro-analysis (EPMA) and are shown in Figure 12(c) and (d). The maps indicate that many Al_2O_3, SiC, and Al_4C_3 inclusions were trapped in the windows of the filter material during filtration. The large number of inclusions observed

within the filter window is evident to the high filtration efficiencies recorded. Trapped inclusions observed within the filter windows had particle size ranging from 1 – 30 µm. Figure 13 shows more evidence of trapped smaller inclusions within the filter.

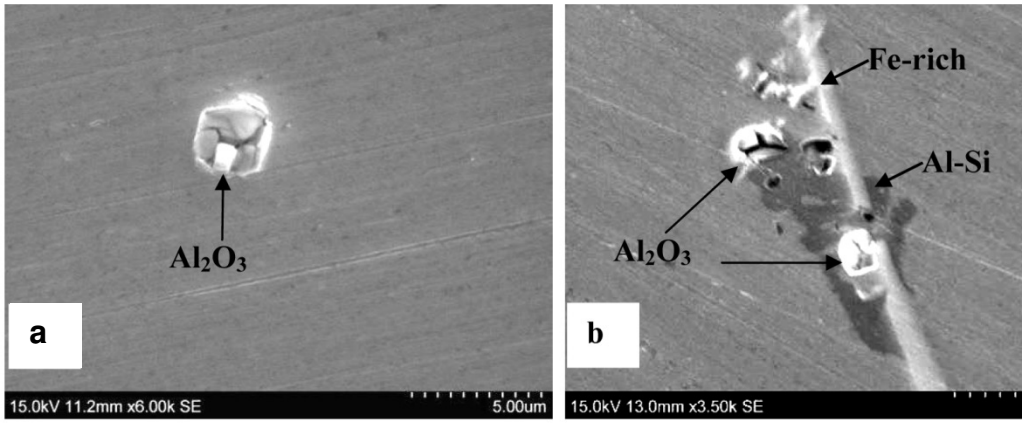

Fig. 11—Al_2O_3 particles resulting from reoxidation of filtered aluminum during experiments: (a) Experiment E2; (b) Experiment E3. The Al_2O_3 particles appear broken and porous, indicating they resulted from entrapped air molecules during solidification of the filtered metal.

The filtration efficiencies of the various experiments were estimated by measuring the average number of particles per mm^2 of aluminum matrix before and after the filtration process using SEM detection of nonmetallic particles of sizes ≥ 1µm, as presented in Table IV. The filtration efficiency, *E* was thus calculated using Eq.[7].

$$E = \frac{N_i - N_o}{N_i} \times 100\% \qquad [7]$$

where N_i and N_o are the average number of inclusions measured per square millimeter of aluminum matrix before and after filtration respectively. Filtration efficiencies of 84.4, 81.3 and 85.2 % were recorded for experiments E1, E2, and E3 respectively.

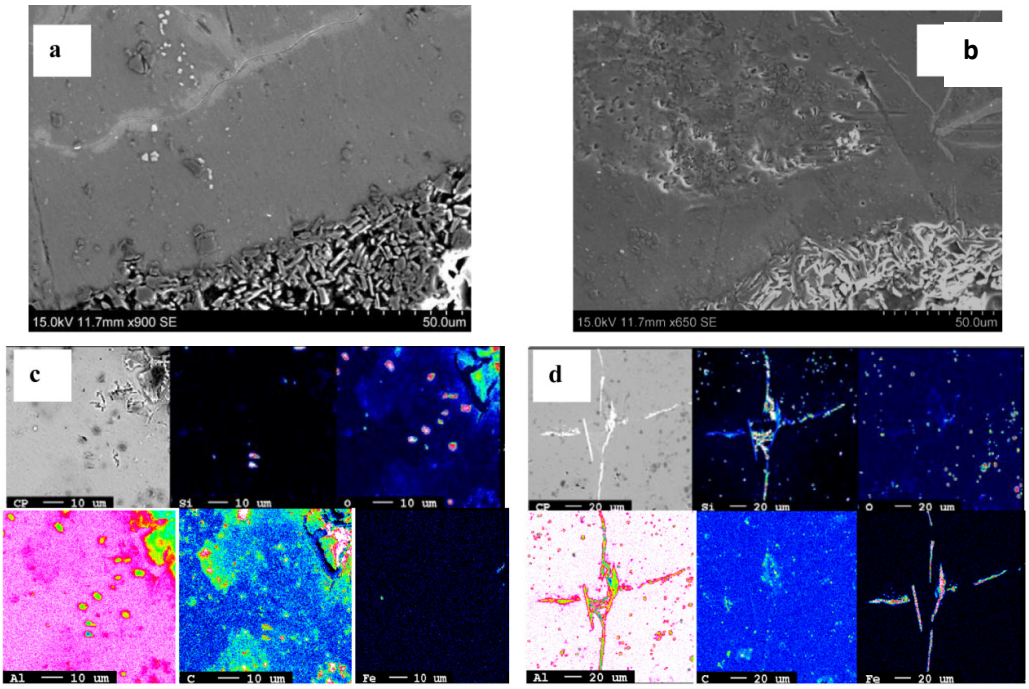

Fig. 12—Evidence of inclusions trapped within filter windows (SEM observation (a) and (b)) and EPMA map of elements present within filter window within metal matrix: (c) experiment E1; (d) experiment E3.

Table IV. Removal of Inclusions by CFF from Molten Aluminum

Experiment	Number of particles before, N_i (mm^{-2})	Number of particles after, N_o (mm^{-2})	Flow rate (kg/s)	Filtration efficiency, E (%)
E1	9860	1420	3.21×10^{-3}	84.4
E2	9860	1839	4.93×10^{-3}	81.3
E3	5200	770	2.24×10^{-3}	85.2

These high filtration efficiency values are reflected in the clean microstructure of the various alloys after filtration, as shown in Figures 7 and 9. We want to indicate at this point that the average number of particles after filtration included Al_4C_3 inclusions and "reoxidation" particles that resulted in the metal through reactions during or after the filtration process. The effect of molten metal flow rate on the filtration efficiency is

clearly seen in the calculated values. Experiments E2 had the highest estimated flow rate of 4.93×10^{-3} kg/s, followed by E1 with 3.21×10^{-3} kg/s and the E3 with a flow rate of 2.24×10^{-3} kg/s. The filtration efficiency increased with decreasing molten metal flow rate through the filter.

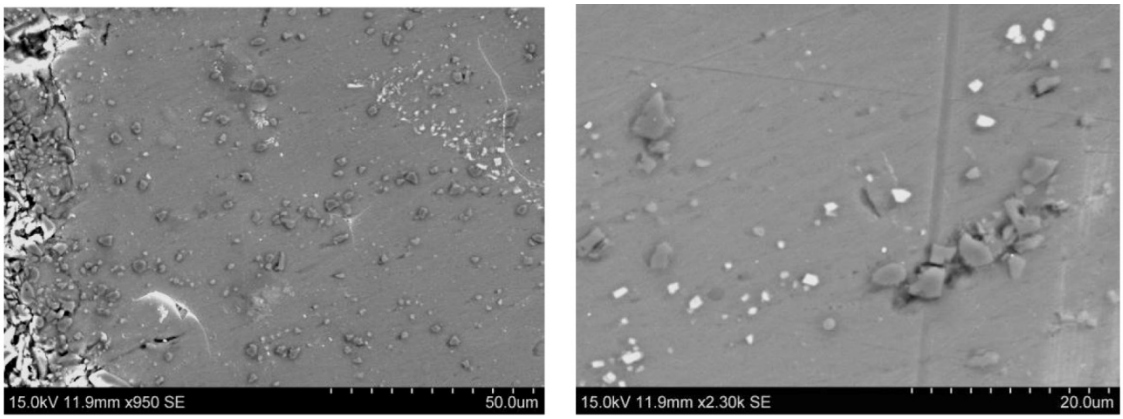

Fig. 13—Inclusions with varying size distribution trapped within filter windows after filtration (experiment E1).

B. Filtration Mechanisms

Filtration efficiency of a filter material may be influenced by several parameters which may be classified as the *filter parameters*: geometrical dimension, size of structural units, their distribution and arrangement in the filter, porosity and chemistry; *inclusion parameters*: nature, size and number; and *fluid and process parameters*: alloy, use of grain refining rod, filtration speed and upstream treatment. These parameters contribute through a number of mechanisms to determine the filtration efficiency of the filter material in a filtration process. Mechanisms that contribute to the removal of inclusions are sieving, cake mode filtration and deep bed filtration [26-27]. If the size of inclusions is larger comparable to the filter pore, size cake mode filtration will occur in which case the particles remain trapped on top of the filter material and successive inclusions approaching the filter are trapped by the preceding ones. If the inclusions are smaller than the filter pore size, the foam filter functions as a deep bed filter. Three mechanisms contribute jointly or individually to bring about effective deep bed filtration.

1. *Collision with walls and Interception Effect*

Since the pore size of the 30 ppi CFF is very large, deep bed filtration in which inclusions attach to the filter wall is a major mechanism for inclusion removal. Inclusion capture in deep bed filtration is the result of two sequential events: transport of the particles from the bulk melt to inner parts of the filter pores, and attachment of the particles to the pore walls. The first step is controlled by different mechanisms such as collision with walls, interception (fluid transport), sedimentation (gravity), diffusion (or Brownian motion) for very small inclusions, turbulent fluctuation, and hydrodynamic effects. The pore size affects filtration efficiency very much. More inclusions will be removed with smaller pore filters. However, small pores are easily blocked by the inclusions. Thus, the size of the filter pore should be optimized for any filtration process. Figure 14 shows that many inclusions are captured by the corner space of the filter. Close to the corner, the turbulent energy dissipation is low and therefore particles diffuse preferentially from the bulk of the molten metal to the corner where they are captured. The schematics shown in Fig.14 illustrate this mechanism.

Three-dimensional turbulent fluid flow in a number of filter channels are calculated by solving the continuity equation, three Navier-Stokes momentum equations, the two equations for turbulent energy and its dissipation rate (two-equation turbulent model).[28]

Inclusion motion in the filter channel and entrapment to the filter walls were also simulated by solving the motion equation of particles considering the fluid drag force, gravitational force and virtual mass force[28-29], as shown in Eq.[8]

$$\frac{du_{pi}}{dt} = \frac{18\mu}{\rho_P d_P^2}\frac{C_D \mathrm{Re}_P}{24}\left(u_i - u_{pi}\right) + \frac{\rho_P - \rho}{\rho} g_i + \frac{1}{2}\frac{\rho}{\rho_P}\frac{d}{d_t}\left(u_i - u_{pi}\right) + \frac{\rho}{\rho_P} u_i \frac{\partial u_i}{\partial x_i} \qquad [8]$$

where u_{Pi} is particle velocity at direction i (m/s); t is time (s); C_D is dimensionless drag coefficient; Re_P is particle Reynolds number; d_P is particle diameter (m); ρ_P is inclusion density (kg/cm^3). The drag force coefficient is given by:

$$C_D = \frac{24}{\mathrm{Re}_P}\left(1 + 0.186\,\mathrm{Re}_P^{0.6529}\right) \qquad [9]$$

The first term in Eq.[9] is the drag force per unit particle mass, the second term is the gravitational force, the third term is the "virtual mass" force accelerating the fluid surrounding the particle, and the fourth term is the force stemming from the pressure gradient in the fluid.

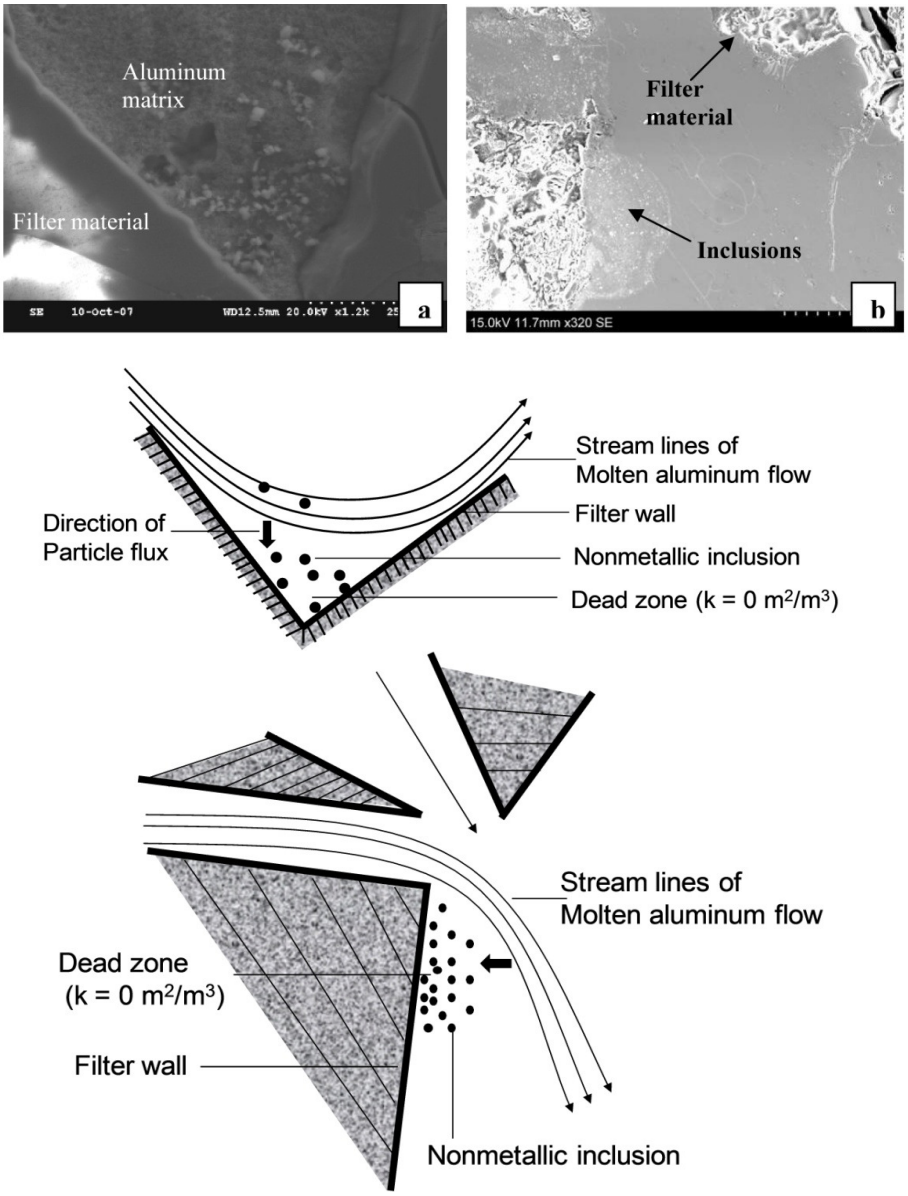

Fig. 14—Inclusion removal through interception effect during filtration (a) Capturing inclusions at the corner of the filter, (b) Inclusions trapped in metal close to filter wall (experiment E3) with schematic illustrations of the particle capture mechanisms.

To incorporate the "stochastic" effect of turbulent fluctuations on the particle motion, the "random walk" model [28-29] is used. In this model, particle velocity fluctuations are based on a Gaussian-distributed random number chosen according to the local turbulence kinetic energy. The random number is changed, thus producing a new instantaneous velocity fluctuation, at a frequency equal to the characteristic lifetime of the eddy. The instantaneous fluid velocity is then given by:

$$u = \overline{u} + u' \quad [10]$$

$$u' = \xi\sqrt{\overline{u'^2}} = \xi\sqrt{2k/3} \quad [11]$$

where $\overline{u}$ is mean fluid phase velocity (m/s); u' is random velocity fluctuation (m/s); ξ random number; k is local level of turbulent kinetic energy (m^2/s^2).

In the simulation, as a boundary condition for inclusions, it was simply assumed that once the inclusions collide with the wall, they will be captured by the wall. The velocity at the inlet of pores depends on the molten aluminum flow rate used in the experiments.

Figure 15 shows the fluid flow velocity distribution, inclusion trajectory and the capturing locations of inclusions onto the wall of the 30ppi filter. Most of the inclusions, especially the larger ones, are entrapped at the upper part of the filter, which matches very well with the experimental observation, as shown in Figure 16. The attachment locations of the large inclusions are more likely around the intersection between pores, and small inclusions disperse well on the whole wall of a pore due to the fact that for small inclusions the effect of turbulent fluctuation is more dominant than their inertial effect. The calculated inclusion removal fraction is shown in Figure 17, indicating that small pore-sized filters can remove more inclusions and larger inclusions can be removed more effectively than smaller inclusions. For the filtration using 30ppi filters, almost all >125μm inclusions are removed, and even very small inclusions such as 5 μm can also be over 85% removed. The experimental observation showed that smaller inclusions were dispersed in the filter. Suspension of many smaller particles within the windows of the filter indicates the presence of other mechanisms for inclusion removal within the filter besides particle attachment to the filter wall.

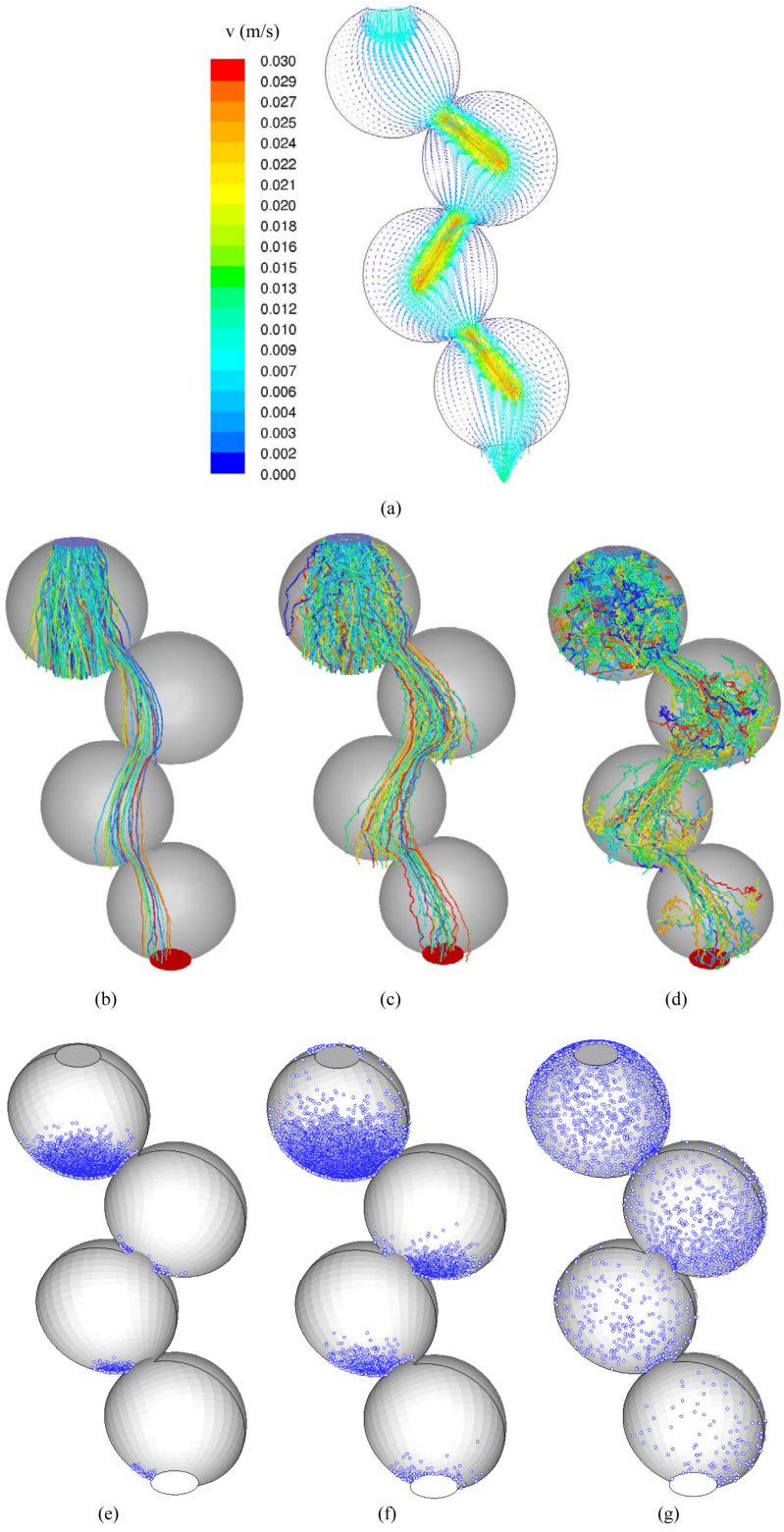

Fig. 15—Calculated fluid flow velocity (m/s) (a) and trajectories of 100 µm (b), 50 µm (c), 10 µm (d) inclusions and their attachment locations at filter walls (e, f, g for 100 µm, 50µm, 10 µm inclusions respectively).

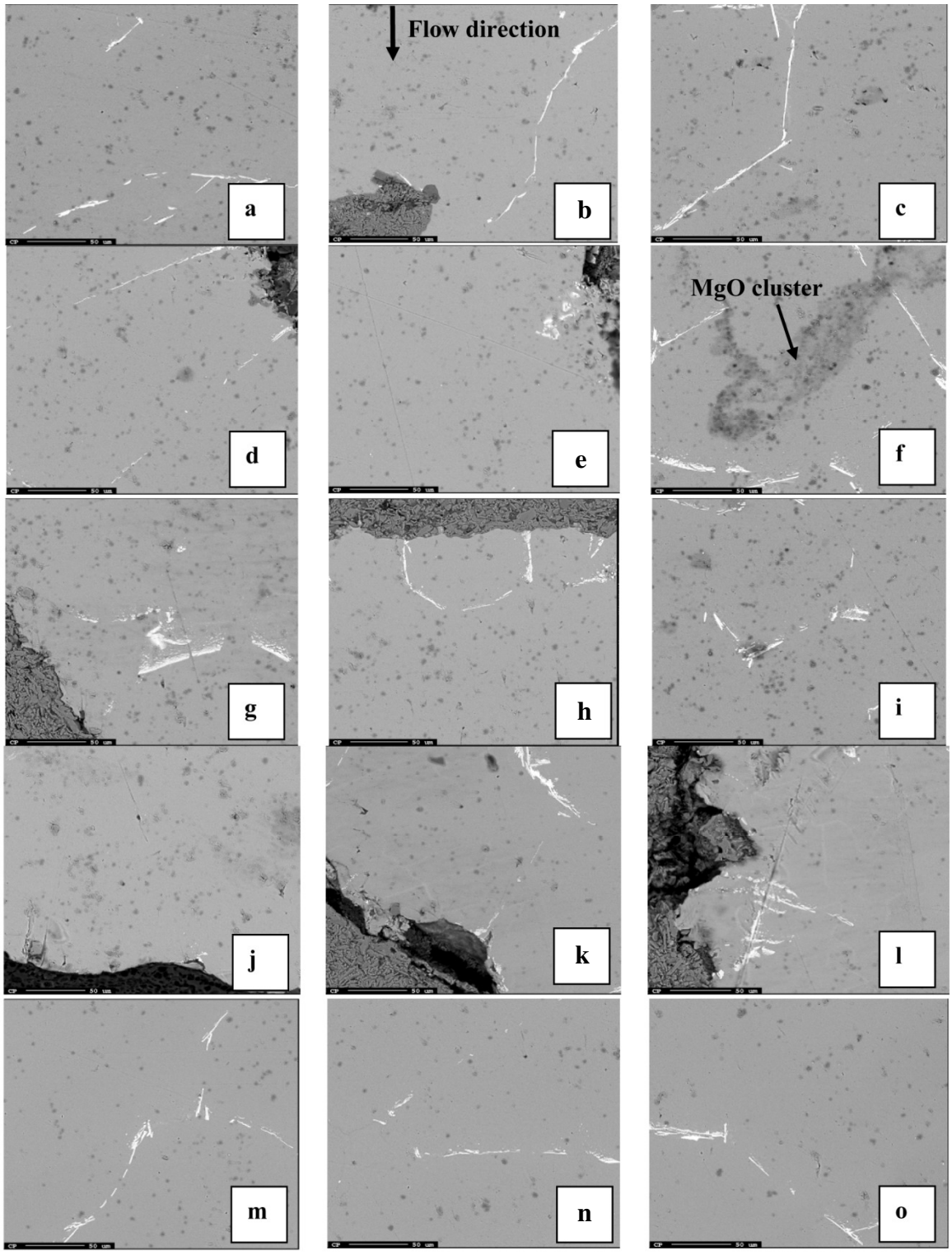

Fig. 16—Distribution of inclusions within the filter from the top of filter (molten aluminum entry), (a) to bottom of filter (molten aluminum exit), (x) (Experiment E3).

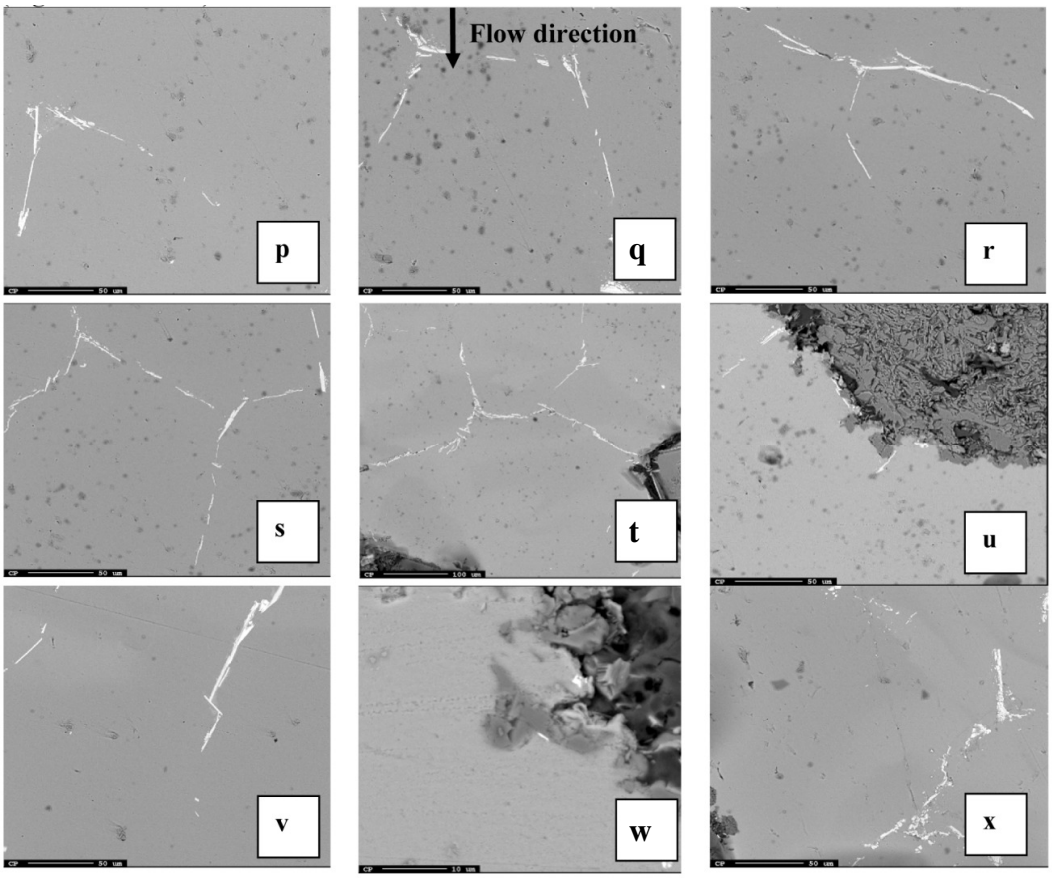

Fig. 16—Distribution of inclusions within the filter from the top of filter (molten aluminum entry), (a) to bottom of filter (molten aluminum exit), (x) (Experiment E3). (conti.)

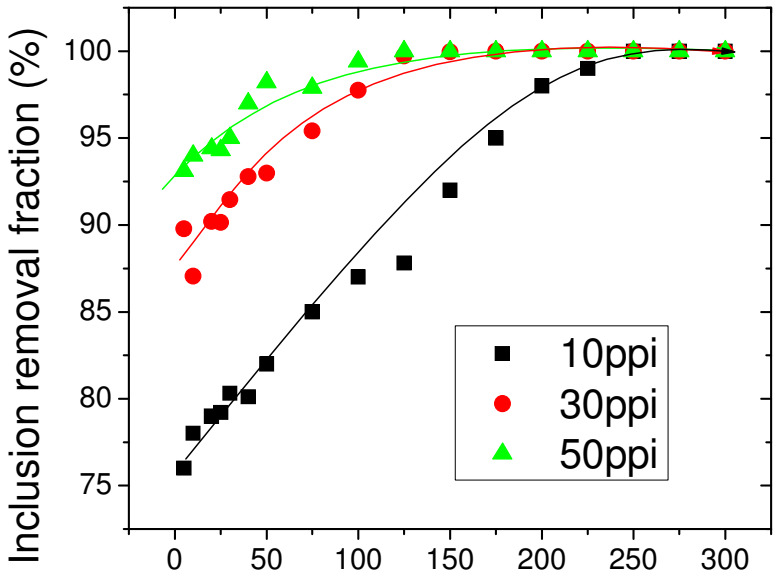

Fig. 17—Calculated inclusion removal fraction through 3-D fluid flow simulation.

One of the issues of small pore-sized filters is their life because they may be quickly blocked since lots of inclusions are captured at the top holes. Another issue is the need to overcome the high pressure drop across the filter, as discussed later in the section VI. New filter designs should be developed for future filtration due to these issues.

2. *Effect of Inclusion Bridges on Filtration*

Inclusions first approach filter walls, attach to the wall, and grow into a large network of inclusions (bridge), which intercept moving particles that come its way. The attraction of inclusions toward each other may lead to the formation of a "mushy zone" of inclusions within the filter, which act as nucleation sites for forced or premature precipitation of Fe-rich phases even at a higher temperature, as shown in Figures 18 and 19. Precipitated Fe-rich phases reinforce particles in the "mushy zone" to form bridges of inclusions. These bridges trap more inclusions that come their way, thus sieving the molten metal in the process. In this case, small channels between the inclusion bridge and the filter wall may become way of escape for smaller sized inclusions.

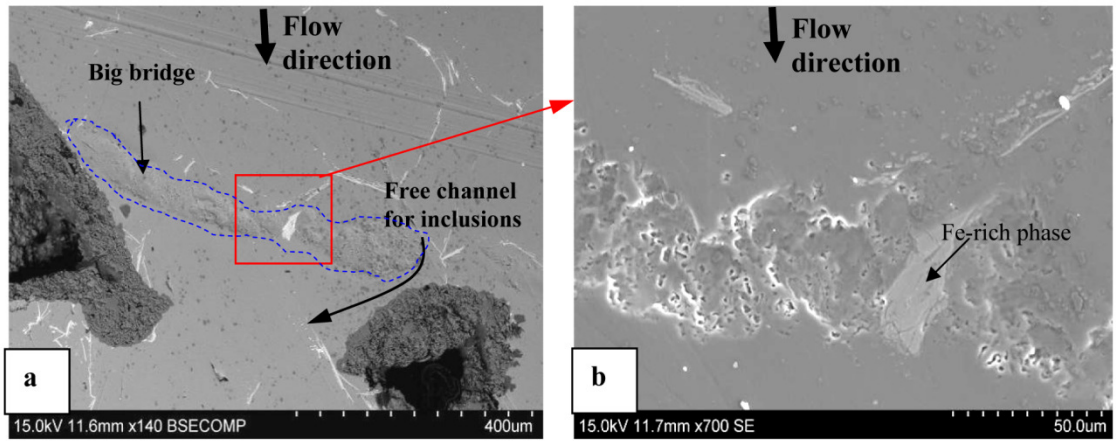

Fig. 18—Inclusion ("mushy zone") bridge within filter window showing inclusions trapped on to the bridge (experiment E3). (b) is a closer look at the inclusions bridge showed in (a). Many particles are seen trapped on to the bridge, while just under the bridge the particle are not observed.

3. *Interfacial Energy between Two Collided Inclusions*

Interfacial forces at the three interfaces between molten metal and filter material, metal and inclusions, and inclusions and filter play an important role in an efficient filtration process. As an example, two spherical solid particles with size of 5μm collide with each other. After reaching steady touching state, there will be a vacuum film generated between the two particles, as shown in Figure 20.

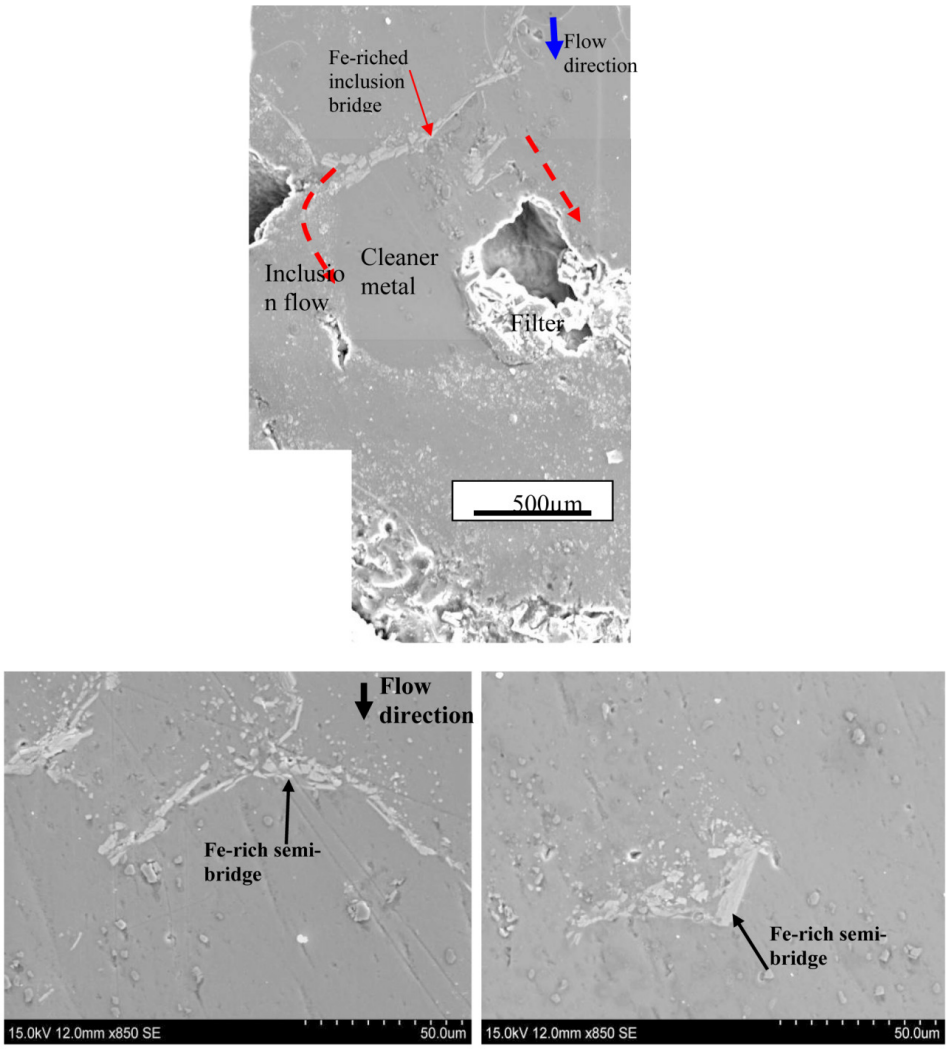

Fig. 19—Fe-rich inclusion bridges collecting more inclusions during use (experiment E3). Molten aluminum flowing beneath each bridge (or semi-bridge) shows a cleaner metal stream and on top of the bridges are trapped inclusions. Some particles escape through smaller channels where, it is assumed the attractive forces is weak.

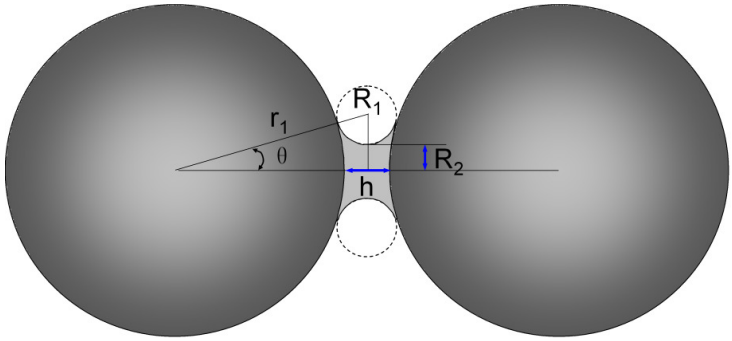

Fig. 20—Schematic collision between two particles in liquid: r_1 is particle radius, R_2 is neck radius and h is distance between the two attaching particles.

The energy of two separate particles before touching is given as

$$E_o = 2\sigma_{LS}(S_1 + S_2) \quad [12]$$

The energy under steady collision is

$$E = 2\sigma_{LS}S_2 + 2\sigma_S S_1 + \sigma_L S_3 \quad [13]$$

where S_1 is the particle contact area with the liquid, and S_2 is the particle contact area with a vacuum, and S_3 is vacuum contact area with the liquid. σ_{LS} is the surface energy between liquid and solid, σ_L is the surface energy between liquid and vacuum, and σ_S is the surface energy between solid and vacuum. Table V gives the surface tensions of certain inclusions in aluminum.

The calculated surface energy as function of neck radius R_2 and distance h is shown in Figure 21. For a given distance h, the collision between two particles needs an initiated energy E_a, and then they can finally steadily stay together with the energy of E_s.

The fluid flow energy acting on a particle with size d_p can be expressed by

$$E_F = 2k\rho_L \times 1/6\pi d_p^{\ 3} \quad [14]$$

where k is the turbulent energy in m^2/s^3, is typically 10^{-1}-10^{-4} m^2/s^3 for metallurgical systems [28-29]. Thus E_F is ~ $(10^{-1}$-$10^{-4})\times10^{-12}$ J for metallurgical systems.

Table V. Interfacial Properties in Liquid Aluminum – Inclusion Systems at 850 ^{o}C

Particle	Contact angle, θ (degrees)	σ_S (N/m)	Surface tension of molten aluminum, σ_L (N/m)*	σ_{LS} (N/m)
Al_2O_3	152 [15]	0.935	1.01 .[15]	1.906 [15] **
SiC	134 [30]	1.84 [30]	1.01 .[15]	2.42 [30]
Graphite, C	152 [30]	1.02 [30]	1.01 .[15]	1.76 [30]
SiO_2	98 [31]		1.01 .[15]	

* σ_L is the surface tension of liquid aluminum at 900 ^{o}C;

** the interfacial tension between the molten aluminum and alumina is at 900 ^{o}C.

Comparing the energy shown in Figure 21 to the energy calculated by Eq.[14] the following conclusions can be reached:

- Steady attachment occurs if the distance between the two 5 μm inclusions is <5-200nm;
- Fluid flow energy cannot break 5μm alumina aggregates if distance is <1μm, because energy E_s is ~3 orders larger than the fluid flow energy;
- Once particles steadily attach, the surface energy E_s is far larger than the van de Waals energy if the distance is less than 1000 nm;
- Particles cannot rely on van der Waals energy to stay together because it is far smaller than the fluid flow energy.

For particle – particle attachments, it has been reported in the literature on clustering and agglomeration leading to subsequent removal of oxide inclusions from liquid steel that the attractive forces acting between solid Al_2O_3 inclusions are of the order 10^{-16} N, and operate at the distance of 50 μm [32].

This result suggests how strong forces of attraction between inclusions in molten metals are. The energy due to surface tension is higher for two attaching 10 μm inclusions than for two attaching 5 μm inclusions as shown in Figure 21. Furthermore, the binding energy of two attaching 10 μm inclusions is operational between the particles

up to 3.2 µm separation while that holding two 5 µm inclusions together operates up to a distance of 1.5 µm. However, with temperature increase of molten aluminum beyond 900°C the interfacial energy becomes smaller (see Figure 22) [15],and therefore, surface tension cannot hold the inclusions together.

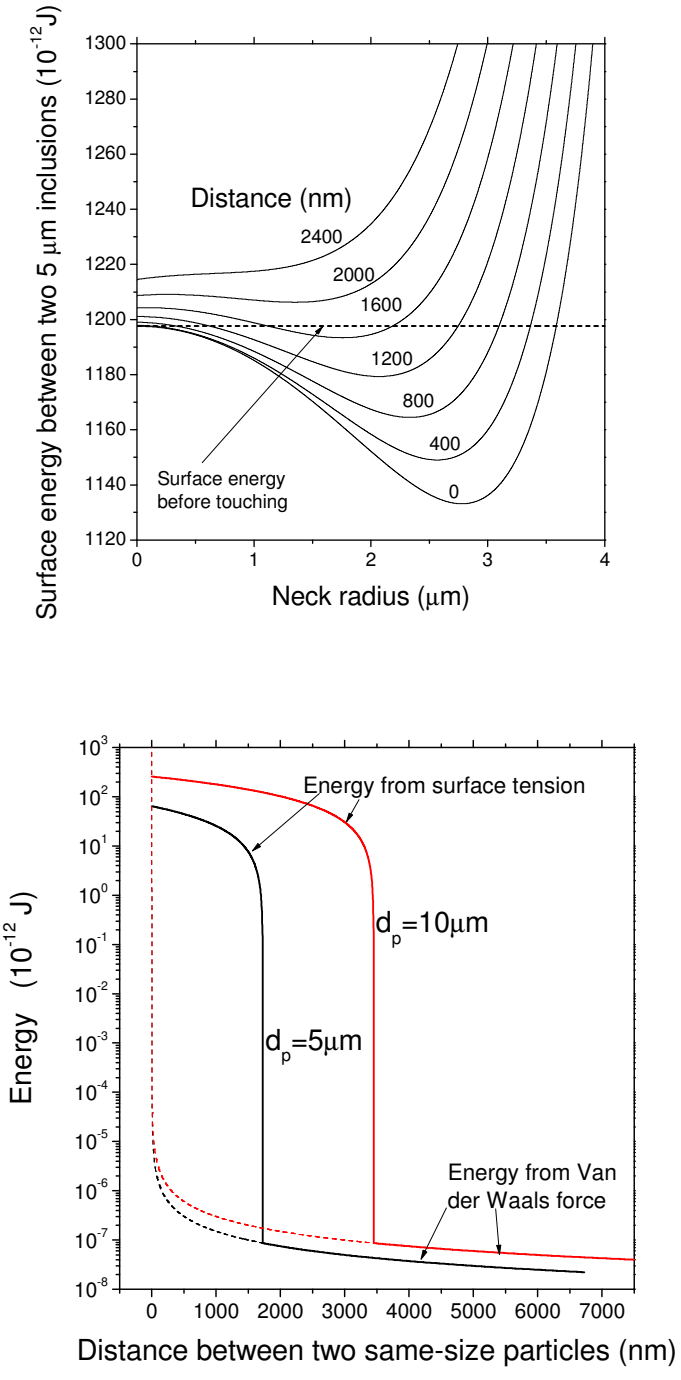

Fig. 21—Energy between two 5 µm, and 10 µm collided particles.

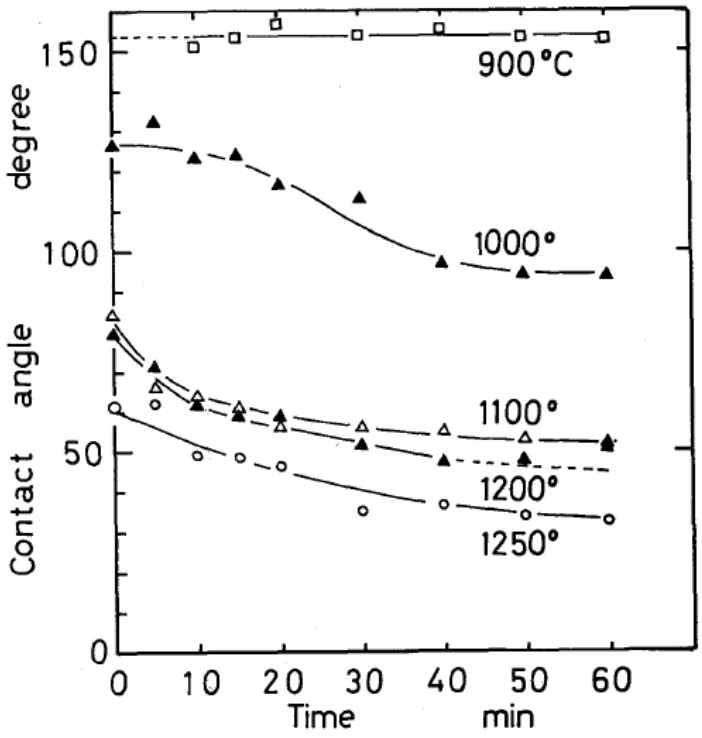

Fig. 22—Time dependence of contact angle for pure aluminum on alumina at temperature 900 ^{o}C to 1250 ^{o}C.[15]

V. REMOVAL OF IMPURITY ELEMENTS

Glow discharge mass spectrometry (GDMS) was used to study the impurity elements removal capabilities of the two filters. The initial Mg levels were 90 ppm in Alloy-1 and 4500 ppm in Alloy-2. However, the initial levels of Ca and Na elements within the aluminum alloys used were too low to allow for appreciable reaction. Table VI gives a summary of the GDMS results. In experiment E1, no reactive AlF_3 layer was used, thus the removal of the [Mg] can only be by evaporation followed by air oxidation, Eq.[15], and accounts for ~13% removal.

$$2[Mg] + O_2 = 2(MgO) \qquad [15]$$

$$\Delta G^{o}_{\mathrm{Re}action}(T) = -1219140 + 233.04(T)\ kJ/mol \quad [33]$$
$$\Delta G^{o}_{\mathrm{Re}action}(900\,^{o}C) = -945.7\ kJ/mol \qquad [16]$$

Table VI. Elemental Composition Before and After Filtration GDMS (in Ppm)

		Mg	Ca	Na
Alloy-1, uncoated	Before	90	0.30	1
filter, E1	After	78	0.35	1.5
	Efficiency%	13.3%	/	/
Alloy-1, coated filter,	Before	90	0.30	1
E2	After	13	0.80	1
	Efficiency%	86.7%	/	/
Alloy-2, Coated filter,	Before	4500	2	0.25
E3	After	1600	2	0.25
	Efficiency%	63.5%	/	/

Eq.[15] represents a spontaneous reaction between dissolved [Mg] in the molten metal and entrapped O_2 molecules. This phenomenon may explain the observation of MgO inclusions trapped in the filter as shown in Figure 16(f). We did not observe MgO inclusions in the alloy before filtration (before melting) and also after filtration. As stated earlier in the section on the experimental procedure, the alloys were analyzed before melting in the filtration experiments to determine the kind of inclusions present. It is our belief that due to the high vapor pressure of magnesium at 900^{o}C, oxidation might be occurring at the surface of the molten metal [33], followed by entrainment into the molten metal due to the higher density. This might have led to the entrapment of MgO particles in the filter window (Figure 16(f)).

The coated filter removed 63-87% Mg through Eq.[17].

$$3[Mg] + 2(AlF_3) = 3MgF_2 + 2[Al] \qquad [17]$$

Figure 23 clearly shows Mg removal to the whole depth of the filter materials and carbide inclusions attachment on the filter surface. In the current study, [Ca] and [Na] could not be removed further due to their low initial concentrations. However, the results of Gorner *et al,* [34] showed [Na] removal efficiency of up to 98 % and 78 % efficiency for the removal [Ca] for active granular bed filters coated with aluminum fluoride.

Assuming first – order reaction rate with respect to *M*, assuming pure AlF_3 and only one dissolved impurity element, the removal efficiency of dissolved impurity, *E*, may be given by Eq.[18] [35].

$$E = 1 - \exp(-ct)$$
$$c = \frac{hS(1-\varepsilon)}{\varepsilon} \qquad [18]$$

where *t* is the residence time of molten aluminum within the filter, *h* is the total mass transfer coefficient of the dissolved impurity element, *S* is the surface area per unit volume of the filter material and ε is the porosity of the filter. The mass transfer coefficient for calcium is taken as 4.15×10^{-5} m/s [4], data for *S* and ε for various CFFs was presented in Table III[18]. Figure 24 shows the calculated removal efficiencies for dissolved [Ca] by AlF_3 coated CFFs. It indicates that, if no other elements are present in the molten aluminum, within 30 s residence time of the molten aluminum in the filter, 99.8 % of [Ca] could be removed by the 30 ppi filter.

The major difference in the characteristic of the various filter grades is their contact surface, *S*. Increasing the contact surface will therefore reduce considerably the contact time required to achieve higher removal efficiencies, as is evident in Figure 24. However, chemical equilibrium, the activity of AlF_3 in the filter (assuming impure), and the presence of other impurities in real systems will affect the reaction kinetics and mass transfer and hence could increase the time required to achieve higher removal efficiencies. The contributions from these factors can be seen in the calculated removal efficiency for dissolved [Mg], as shown in Figure 25. Using the data presented in Tables III and VI on dissolved [Mg] removal, removal efficiency of 86.7 % in 361 s, and Eq.[18], the total mass transfer coefficient of dissolved [Mg] in molten aluminum towards the walls of the filter was calculated to be 1.15×10^{-6} m/s. A removal efficiency of 90.4 % within 7 min. (420 s) could be achieved by a 30 ppi AlF_3 coated CFF. The standard Gibbs energy of formation of CaF_2 and MgF_2 are approximately -1080 and -950 kJ/mol respectively [36], which indicates that thermodynamically dissolved [Ca] will react preferentially with AlF_3 before [Mg]. Comparing Figures 24 and 25, it can be seen that the removal efficiencies of [Ca] by the coated filter is much higher than that of the [Mg] for the same residence time within the various filters.

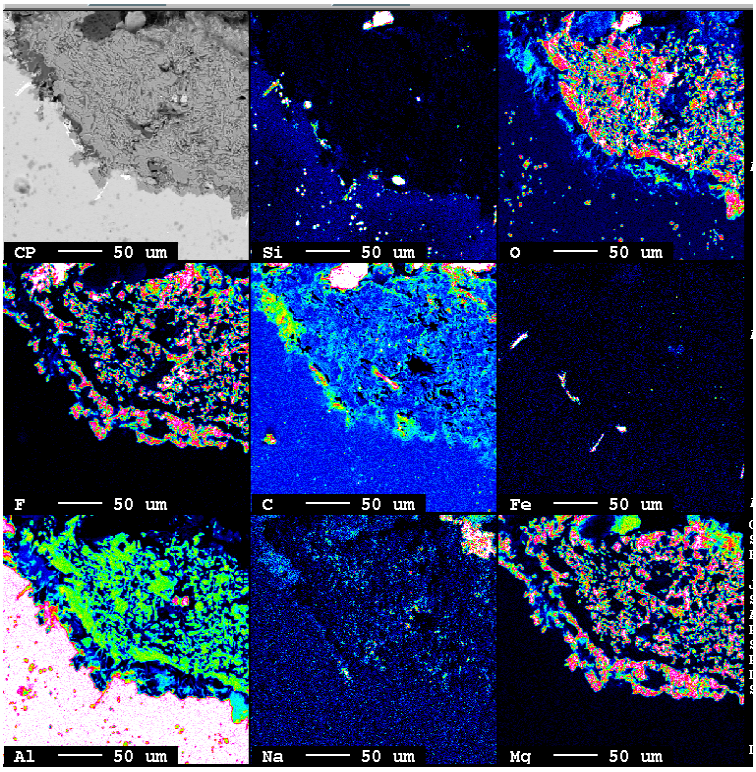

Fig. 23—EPMA map of elements present within filter window with metal matrix in between (AlF_3 slurry coated filtration of alloy 2 – E3).

These results indicate that for longer residence times (more than 60 s) of molten metal within a coated filter, the equilibrium state of reaction with dissolved [Ca] (and [Na]) and AlF_3 will be reached, thus [Mg] will be removed. This may result in challenges when purifying Al-Mg alloys because magnesium, in this case, is an expensive addition.

VI. NEW DESIGNS OF FILTRATION

It is obvious from the filtration results of this work that certain particles found their way back into the metal even though filtration efficiencies higher that 80 % were obtained. During industrial aluminum filtration processes in which greater volumes of the molten metal are processed, filter clogging and inclusion re-entrainment into the molten metal due to overloading hampers the attainment of the high filtration efficiencies recorded in the present work. In CFFs which react with impurity elements within the molten metal, the residence time and contact area with the presence of trapped inclusions might not be enough to harness the full potential of such filters. We therefore propose the

following three methods for future filtration research and subsequent industrial applications.

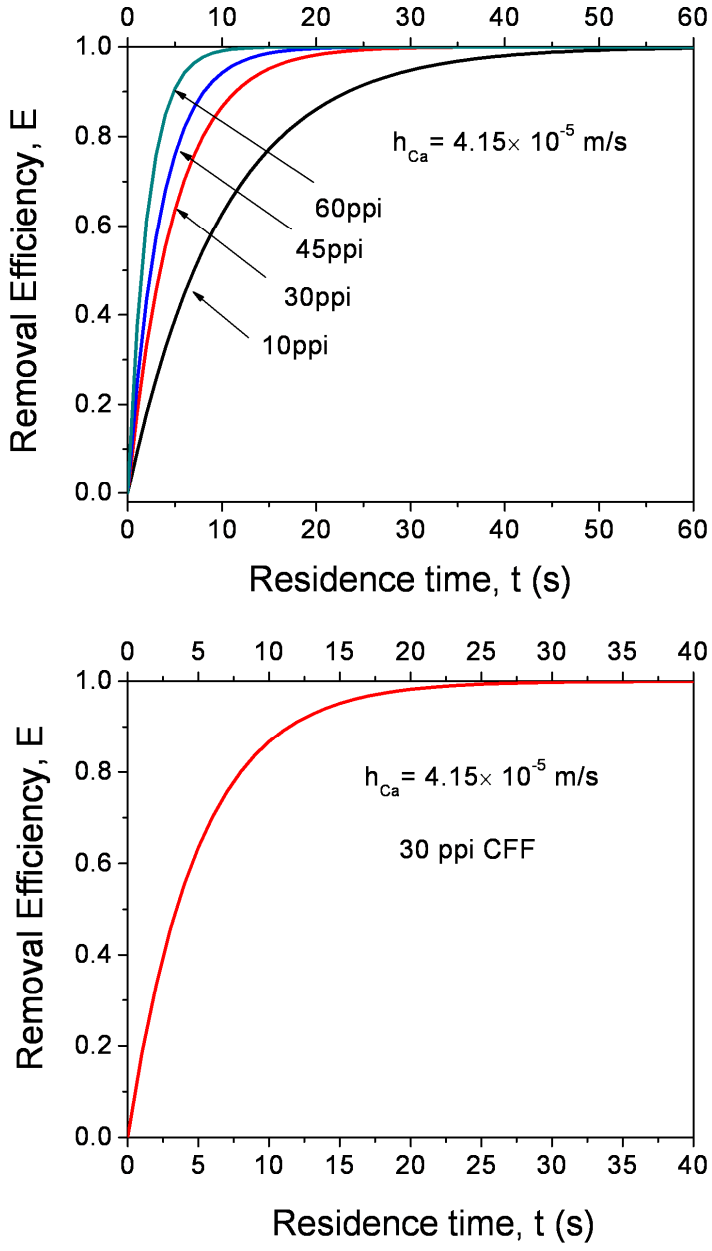

Fig. 24—Removal efficiency of [*Ca*] by coated filter plotted against residence time of molten aluminum in filter.

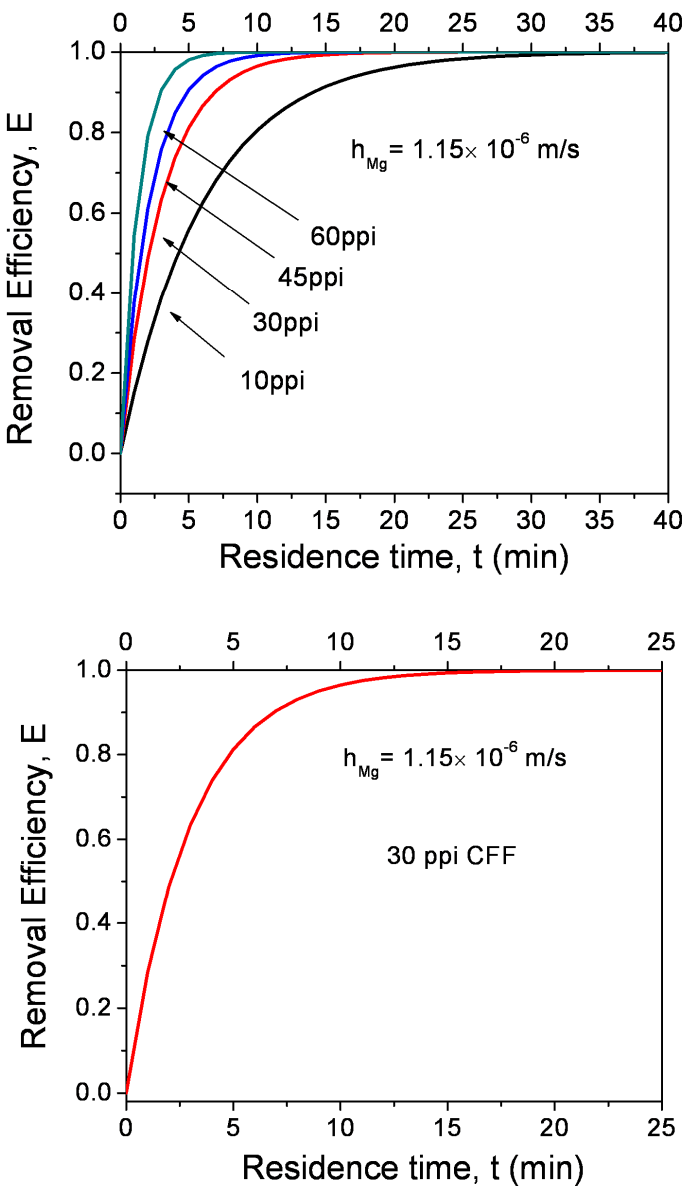

Fig. 25—Removal efficiency of [*Mg*] by coated filter plotted against residence time of molten aluminum for various pore sizes.

A. Multi-pore filtration

This method implies the use of a CFF with two or more pore sizes or gradually decreasing in pore diameter as the molten metal flows across the depth of the filter. Figure 26(a) shows a schematic representation of the filter which includes three zones with CFF pore sizes of 10 ppi (coarse zone), 30 ppi (middle zone) and 45 ppi, representing the "fine zone". Larger particles within the molten metal are expected to be

removed within the coarse zone while median-sized particles are removed by the 30 ppi filter. The 45 ppi filter is expected to trap particles finer than could be trapped by the 30 ppi CFF. Therefore, this method is expected to improve upon the filtration efficiencies of > 80 % recorded by the 30 ppi filter in the present study.

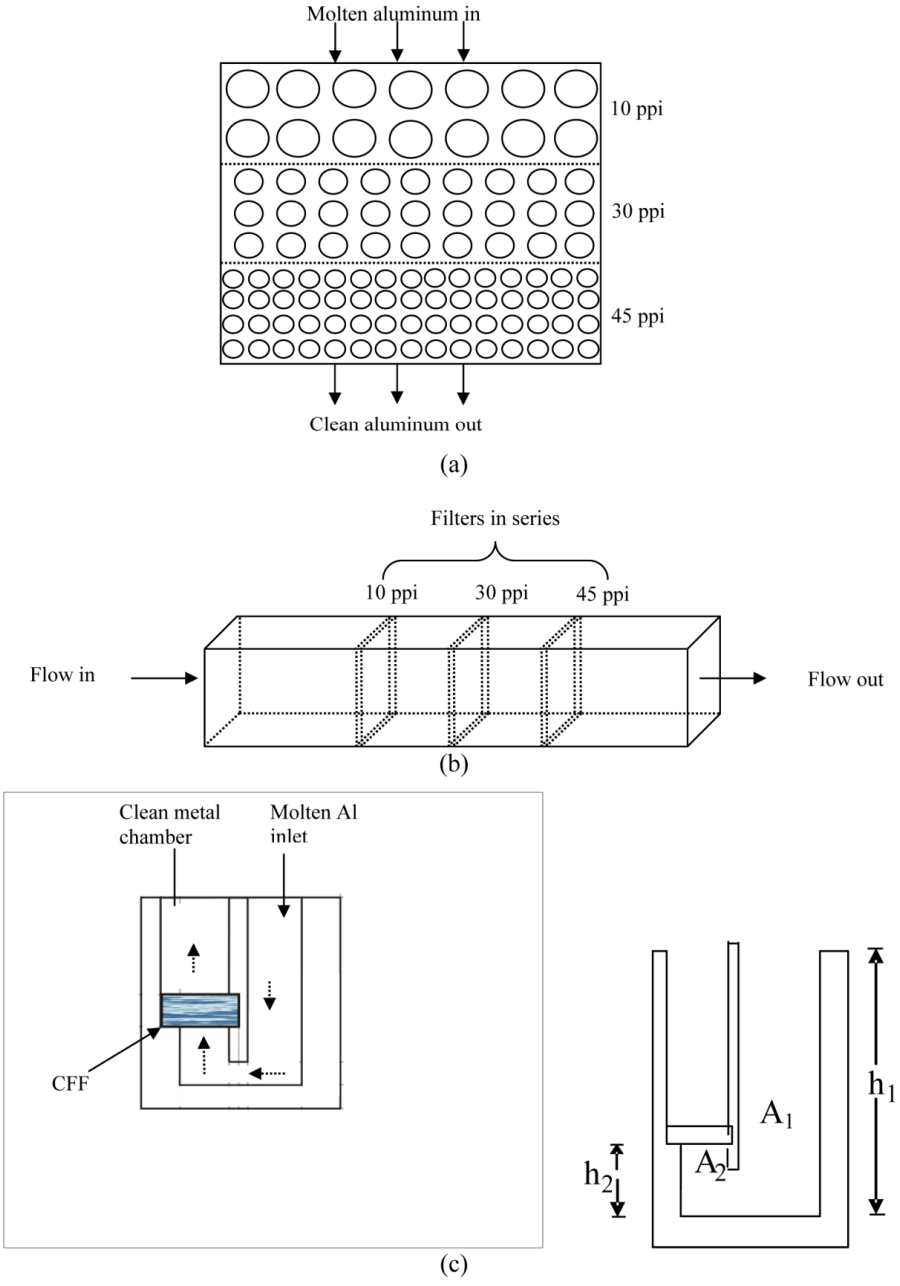

Fig. 26—Future filtration design concepts (a) Multi-pore filtration, (b) multi stage filtration, and (c) reverse filtration.

B. Multi – stage filtration

This method proposes a three-stage filtration system having filters arranged in series. For example, 10 ppi, 30 ppi, 45 ppi CFFs could be arranged in series in the launder or a special filtration cell. Figure 26(b) shows a schematic example of the set-up. This method, by our estimation, would not require complicated designs, and can easily be integrated into the current industrial launder system. Multi-stage filtration has previously been proposed which included gas purging across the filter outlet was described by the inventors [37]. Per the current proposition, we expect that particles < 1 μm will be removed in the three stage filtration system with filters arrange in series as indicated the Figure 26(b).

C. Reverse filtration

This method is currently under study in our laboratory. It employs a set-up similar to the schematic example shown in Figure 26(c). The filtration system is designed to be a part of an aluminum scrap melting furnace for aluminum recycling. Here, the molten aluminum by design will flow from the bottom-up of the melting furnace through the filter. The idea here is to allow very large particles that may clog the filter to settle down to the bottom of the furnace and smaller ones to be trapped by the filter. It is also expected to give the required residence time needed for reactions to take place within CFFs that have been coated to remove dissolved impurity elements by reacting with them during the filtration process. The design of the filtration system for the reverse filtration must take the metallostatic pressure head into consideration. According to Figure 26(c), Eq.[4] may therefore be modified as follows:

$$p = \rho_m g \left(h_1 - h_2 \right) \quad [19]$$

$$A_1 \geq A_2 \quad [20]$$

where A_1 and A_2 are the respective cross-sectional areas of the two sections as indicated in the Figure , and $h_1 – h_2$ is the driving force for molten metal flow through the filter. The condition for molten metal to flow through the filter can be set by Eq.[21].

$$(h_1 - h_2) > \frac{\Delta p}{\rho_m g} \quad [21]$$

One anticipated challenge to this method is how to remove the clustered particles from the bottom of the furnace.

VII. CONCLUSIONS

Ceramic foam filtration of molten aluminum using Al_2O_3 filters coated with AlF_3 has been proposed due to the prospects of removing both dissolved impurity elements and inclusions. The current work studied the filtration of aluminum using regular uncoated 30 ppi CFF and AlF_3 slurry coated CFF. Three dimensional inclusion morphologies in aluminum were also studied. The following conclusions are drawn from the study.

- Three dimensional observations of inclusions reveal more details about their morphology, which can contribute to the understanding of how they influence properties of the metal better than can be obtained from two dimensional inclusions studies.

- Ceramic foam filtration of molten aluminum using 30 ppi Al_2O_3 filters was found to be an effective method of removing inclusions from aluminum. Both coated and uncoated CFF gave very good filtration results. Filtration efficiencies of > 81% were recorded for the 30 ppi CFF.

- Larger inclusions were observed to attach to the upper most part of the filter, while the small inclusions were removed throughout the thickness of the CFF.

- Two main mechanisms contributed to the removal of inclusions within the CFF during the filtration process. These are (1) collision with walls and interception effect and (2) the formation of both intermetallic and nonmetallic inclusion bridges during filtration.

- Fluid dynamic modeling of inclusion attachment to the filter walls showed that most inclusions, especially larger sized, are entrapped at the upper part of the filter while smaller inclusions dispersed well throughout the filter.

- Calculated inclusion removal fractions for the 30 ppi filter showed that almost all > 125 µm inclusions are removed and inclusions ~ 5 µm in size are removed up to 85 %.

- The interfacial energy between two collided inclusions was calculated, indicating that very strong attractive forces hold the particles together within the filter. This explains why many small particles could be trapped within the filter although they did not attach to the walls. These forces are effective in molten aluminum at temperatures lower than 900^{o}C.

- The AlF_3 coating could remove dissolved Mg up to 87%, including ~13% contribution from evaporation and oxidation. The total mass transfer coefficient of dissolved [Mg] was calculated to be 1.15×10^{-4} m/s. Sodium and Ca removal by the filter were insignificant due to initial low levels. However, theoretical calculation showed that dissolved [Ca] in molten aluminum can be removed up to 99% by the coated filter in 30 s.

- Multi-pore filtration, multi-stage filtration and reverse filtration are three proposed systems for future molten aluminum filtration research and industrial application.

ACKNOWLEDGEMENTS

This research is supported by a grant from the University of Missouri Research Board, the Material Research Center (MRC) and Intelligent Systems Center (ISC) at Missouri University of Science and Technology (Missouri S&T).

REFERENCES

1. Simensen, C.J. and C. Berg, *Survey of Inclusions in Aluminum.* Aluminium, 1980. **Vol. 56**(5): p. 335-340.

2. Valdes, A.F., M.A. Hinojosa-SanMiguel, A.H. Castillejos-Escobar, E. Macias-Avila and F.A. Acosta-Gonzalez. *A comparative study on the efficiencies of Na2SiF6 and AlF3 for demagging molten aluminium by submerged powder injection*. in *TMS Annual Meeting-Light metals*. 1997: TMS, Warrendale, PA, USA.

3. Gariepy, B. and G. Dube. *TAC: new process for molten aluminium refining*. in *TMS Annual Meeting-Light metals*. 1986: TMS, Warrendale, PA, USA.

4. Gorner, H., T.A. Engh, M. Syvertsen and L. Zhang, *Removal of Na and Ca from Aluminum Scrap through Filtration.* Mater. Sci. Forum, 2007. **Vol. 546-549**: p. 801-807.

5. Harald, G., S. Martin, O. Eivind and T. Engh. *AlF3 as an aluminium filter medium*. in *TMS Annual Meeting-Light metals*. 2005: TMS, Warrendale, PA, USA.

6. Simensen, C.J. and C. Berg, *Analysis of Oxides in Aluminium by means of Melt Filtration.* Zeitschrift fuer Metallkunde, 1985. **Vol. 76**: p. 409-414.

7. Apelian, D. and K.K. Choi, *Metal Refining by Filtration.* Foundry Process-Their Chemistry and Physics, S. Katz and C.F. Landefeld, eds., Plenum Press, (New York-London), 1988: p. 467-494.

8. Ciftja, A., L. Zhang, A. Kvithyld and T.A. Engh, *Purification of Solar Cell Silicon Materials Through Filtration.* Rare Metals, 2006. **Vol. 25**: p. 180-185.

9. Lae, E., H. Duval, C. Riviere, P.L. Brun and J.-B. Guillot, *Experimental and numerical study of ceramic foam filtration.* Light Metals (TMS), 2006: p. 753-758.

10. Keegan, N.J., W. Schneider, H.P. Krug and V. Dopp, *Evaluation of the efficiency of ceramic foam and bonded particle cartridge filtration systems.* Light Metals (TMS), 1997: p. 973-982.

11. Keegen, N.J., W. Schneider and H.P. Krug, *Evaluation of the efficiency of fine pore ceramic foam filters.* Light Metals (TMS), 1999: p. 1031-1041.

12. Towsey, N., *The Influence of Grain Refiners on the Efficiency of Ceramic Foam Filters.* Light Metals (TMS), 2001: p. 973-977.

13. Towsey, N., W. Schneider and H.-P. Krug, *The Effect of Rod Grain Refiners with differing Ti/B ratio on Ceramic Foam Filtration.* Light Metals (TMS), 2002: p. 931-935.

14. Towsey, N., W. Schneider and H.-P. Krug, *A Comprehensive Study of Ceramic Foam Filtration.* 7th Austral. Asian Pacific Conference on Aluminium Cast House Technologies (TMS), 2001: p. 125-137.

15. Nasaaki, N., Y. Hirono and I. Okamoto, *Wetting of Alumina by molten Aluminum and Aluminum-Copper Alloys.* Transactions of JWRI, 1984. **13**(2): p. 29-34.

16. Asthana, R., A. Kumar and N. Dahotre, *Materials Science in Manufacturing*. 1996: Elseviser Inc. 273-275.

17. Engh, T.A., *Principle of Metal Refining*. 1992: Oxford University Press. 61.

18. Richardson, J.T., Y. Peng and D. Rumue, *Properties of ceramic foam catalyst supports: pressure drop.* Applied Catalysis A: General, 2000. **204**: p. 19-32.

19. Liu, L. and F.H. Samuel, *Assessment of melt cleanliness in A356.2 aluminium casting alloy using the porous disc filtration apparatus technique: Part II Inclusions analysis.* Journal of Materials Science, 1997. **32** p. 5927-5944.

20. Liu, L. and F.H. Samuel, *Assessment of melt cleanliness in A356.2 aluminium casting alloy using the porous disc filtration apparatus technique: Part I Inclusions measurements.* Journal of Materials Science, 1997. **32** p. 5901-5925.

21. Lloyed, D.J., *The solidification microstructure of particulate reinforced aluminium/SiC composites.* Comp. Sci. Technol., 1989. **35** p. 159–179.

22. Lloyed, D.J., H. Lagace, A. Mcleod and P.L. Morris, *Microstructural aspects of aluminium silicon-carbide particulate composites produced by a casting method.* Mater. Sci. Eng. A, 1989. **107** p. 73–80.

23. Miller, D.N., L. LU and A.K. Dahle, *The Role of Oxides in the Formation of Primary Iron Intermetallics in an Al-11.6Si-0.37Mg Alloy.* Metallurgical and Materials Transactions B, 2006. **37B**: p. 873-878

24. Z.K. Liu and Y.A. Chang, *Thermodynamic Assessment of the Al-Fe-Si System.* Metall. Mater. Trans. A, 1999. **30A**: p. 1081-1095.

25. Pontevichi, S., F. Bosselet, F. Barbeau, M. Peronnet and J.C. Viala, *Solid-liquid phase equilibria in the Al-Fe-Si system at 727 ^{o}C.* Journal of Phase Equilibria and Diffusion, 2004. **Vol. 21**(6): p. 528-537.

26. Olson-III, R.A. and L.C.B. Martins, *Cellular Ceramics in Metal Filtration.* Advanced Engineering Materials, 2005. **Vol. 7**(4): p. 187-192.

27. Zhang, L., A. Ciftja and L.N.W. Damoah, *Removal of Non-metallic Inclusions from Molten aluminum.* Proceedings of the European Metallurgical Conference, EMC 2007, June 11-14, Dusseldorf, Germany, 2007. **Vol. 3**: p. 1413-1428.

28. Zhang, L., *Fluid Flow, Heat Transfer and Inclusion Motion in a Four-Strand Billet Continuous Casting Tundish.* Steel Research International, 2005. **76**(11): p. 784-796.

29. Zhang, L., J. Aoki and B.G. Thomas, *Inclusion removal by bubble flotation in a continuous casting mold.* Metal. & Material Trans. B., 2006. **37B**(3): p. 361-379.

30. Stefanescu, D.M., A. Monitra, A.S. Kascar and B.K. Dhindaw, *The influence of buoyant forces and volume fraction of particles on the particle pushing/entrapment transition during directional solidification of Al/SiC and Al/graphite composites.* Metall. Mater. Trans. A, 1990. **21A**: p. 231-239.

31. Laurent, V., D. Chatain and N. Eustathopoulos, Mater. Sci. Eng, 1991. **A135**: p. 89.

32. Yin, H., H. Shibata, T.Emi and M. Suzuki, *Characteristics of Agglomeration of Various Inclusion Particles on Molten Steel Surface.* ISIJ International, 1997. **Vol. 37**(No. 10): p. 946-955.

33. Ng, D.H.L., Q. Zhao, C. Qin, M.-W. Ho and Y. Hong, *Formation of aluminum/alumina ceramic matrix composites by oxidizing an Al-Si-Mg alloy.* Journal of European Ceramic Society, 2001. **21**: p. 1049-1053.

34. Gorner, H., T.A. Engh and M. Syvertsen, *Kinetics of an AlF_3 Aluminium Filter*. Light Metals 2006, (TMS), 2006: p. 756-770.

35. Damoah, L.N.W. and L. Zhang, *Reactive Filter for Removal of dissolved alkali metals from Aluminum* (To be Submitted to) Metallurgical and Materials Transactions B, 2008.

36. Utigard, T.A., *Properties of Fluxes used in Molten Aluminum Refining*. Proceedings of the International Symposium on Extraction, Refining and Fabrication of Light Metals, (Ottawa, Canada; CIM), 1991: p. 353-365.

37. Eckert, E.C., C.J. Cox, T.R. Hornack, R.E. Miller, J.A. Kaems, D. Apelian, E.L. George and R. Mutharasan, *Multistage rigid media filter for molten metal*, in *Bulletin 1996/45*, E.P. Office, Editor. 1996, EP 0 490 371 B1. Aluminum Company of America.

V. ALF_3 REACTIVE AL_2O_3 FOAM FILTER FOR THE REMOVAL OF DISSOLVED IMPURITIES FROM MOLTEN ALUMINUM: PRELIMINARY RESULTS

Lucas Nana Wiredu Damoah, Lifeng Zhang

Department of Material Sciences and Engineering
Missouri University of Science and Technology (Missouri S&T)
223 McNutt Hall,
Rolla, MO 65409-0330, USA
Email: zhanglife@mst.edu

Published in Acta Materialia, and edited for this Dissertation

Abstract

Filters coated with AlF_3 are to be used to filter molten aluminum to simultaneously remove nonmetallic inclusions and dissolved alkali and alkaline earth metal impurities. Coating experiments were carried out in which anhydrous HF gas was generated from reactions involving NaF or CaF_2 and concentrated H_2SO_4, and used in a reaction with Al_2O_3 ceramic foam filter to produce a layer of AlF_3 coating on the surface of the Al_2O_3 filter. Samples from these experiments were studied with XRD, SEM and EPMA. Preliminary results of the coating experiments showed that it is possible to coat Al_2O_3 filters with AlF_3 by this method. Increasing the HF gas pressure increased the yield of AlF_3 in the filter. Theoretical evaluation of the removal efficiency of dissolved impurity elements showed that, dissolved calcium in molten aluminum can be removed up to 99.8 % within 30 seconds of contact time with the filter material.

1. Introduction

The expanding use of aluminum alloys for making critical components in castings, extrusions and rolling for the aerospace, automotive and other industries makes concerns with melt quality inevitable. This means that more companies will have to invest heavily in current state of the art cast house technologies. Furthermore, there will be a strong drive from downstream companies for further improvements and new developments in the upstream processes leading to quality products. Two major classes of impurities can be distinguished in molten aluminum as dissolved elements and suspended particles, which may be nonmetallic or intermetallic in character. Sources of these impurities can be traced back to the electrolysis process, melt processing operations, and interactions between the molten metal and refractory materials and also the environment. Essentially, melt quality can be controlled by the removal of alkali and alkaline-earth trace elements, hydrogen and inclusions [1-2]. Various technologies, such as in-line spinning nozzle units, furnace fluxing and packed bed, and rigid media ceramic foam filters are used to control impurity levels. Impurities in the aluminum melt are a major cause of product failure both during processing and use. However, nonmetallic

inclusions may play an important role in facilitating the crystal nucleation process and other primary phases [3], since they are usually present as solid particles in the molten aluminum during solidification. They also help in precipitating platelet Fe-rich intermetallic phases which are a major problem to the mechanical properties of aluminum. Various methods such as filtration, sedimentation and bubble floatation are already being employed to get rid of nonmetallic inclusions from molten aluminum.

Commonly dissolved unwanted impurities usually found in molten aluminum from the electrolysis cell are Na, Li, Ca, Fe, and H_2. Hydrogen is the only known gas with appreciable solubility in molten aluminum. Dissolved alkali and alkaline earth elements originate from the presence of fluoride salts such as NaF, LiF and CaF_2 in the electrolyte used during the Hall-Heroult process. Due to their relatively high vapor pressure, Na and H are regarded as volatile elements. Impurities such as Ca and Li can be removed by adding a variety of chemicals to the melt, and may, therefore, be referred to as reactive elements. Elements such as Fe and Si may be referred to as non-reactive because they are very difficult to remove from aluminum by ordinary fluxing processes. Na and Li can cause edge cracking during hot rolling by forming low melting point phases at the grain boundaries. For most products, Na levels are kept below 10 ppm. Also extrusion defects are linked to higher Na levels. However some researchers see no concern in Na levels significantly in excess of 10 ppm for common alloy extrusions.[4] H_2 causes porosity due to its low solubility in solid aluminum, coming out of solution during solidification. The porosity can cause blisters in extrusions or during hot rolling of sheet metal. Na causes hot shortness in alloys which contain magnesium. Li creates an undesirable black film on foil products. Due to these unwanted properties, both Na and Li must be reduced to very low levels.

Refining of aluminum typically involves fluxing out dissolved alkali impurities using Cl_2 or salts of chlorine or fluorine, argon degassing for H_2 removal and, finally, floatation/settling/filtration operations for the removal of solid inclusions [5]. However, due to their ease of handling and better refining results compared to gases, AlF_3 powder and granular particles are being injected into molten aluminum for the removal of dissolve impurities [6-8]. Optimization of these techniques enhances the removal rates with

respect to H, alkali and alkaline earth metals, and inclusions. Furthermore, the consumption of refining agents, which strongly depends on thermodynamics and kinetics, needs to be optimized. Optimization is important because in addition to the cost of the refining agent and its environmental impact, any excess of it will be involved in reactions with the alloy, which may generate more impurities that would have to be removed later [9].

AlF_3 can be employed for the removal of dissolved alkali and alkaline earth metals from molten aluminum through three main methods: (1) Powder injection,[10] (2) deep bed filtration,[11-12] and (3) ceramic foam filtration.

With respect to option (1) above, AlF_3 is injected into the molten metal in the treatment crucible and the melt stirred simultaneously. Application of AlF_3 in industrial refining of molten aluminum is economically advantageous compared to chlorine gas and chloride salts in spite of its higher market price. However, analyses of these processes, with respect to kinetics have shown that AlF_3 is utilized in an inefficient manner.[13] Furthermore, crucible treatment with AlF_3 results in reaction products that require further processes to be removed and long crucible treatment times are required in order to maximize the efficiency of the fluxing process. The latter usually leads to the oxidation of the metal leading to the formation of more nonmetallic inclusions and increased metal losses.

Contact area per time of molten aluminum exposure to AlF_3 could be considerably increased in the granular bed filter. Such a filter containing AlF_3 as a filter media could actively remove alkali from the melt and at the same time retain the reaction products. Equations [1] – [3] are the reactions involved in the purification process. Some of these products such as NaF or KF act as surfactants, which is suggested to possibly reduce surface tension and enhance alkali removal and/or particle capture.[14]

The following chemical reactions give the mechanism by which AlF_3 removes dissolved alkali and alkaline earth impurities from molten aluminum.

$$[Ca]+\frac{2}{3}AlF_3 = CaF_2 + \frac{2}{3}[Al], \quad \Delta G^o(T) = -230687 + 3.31T \ J/mol \qquad [1]$$

$$[Mg]+\frac{2}{3}AlF_3 = MgF_2 + \frac{2}{3}[Al], \quad \Delta G^o(T) = -116195 - 0.604T \ J/mol \quad [2]$$

$$3[Na]+ AlF_3 = 3NaF + [Al], \quad \Delta G^o(T) = -230086 + 42.37T \ J/mol \quad [3]$$

In the deep bed filtration method the molten metal flows through the packed bed and interacts with the AlF_3 particles according to the above reactions. However, this method is not being applied by the aluminum industry at the moment.

High efficiency of up to 98 % was reported for AlF_3 to remove dissolved impurities such as Na and Ca from aluminum through granular bed filtration.[13-14] The use and the evaluation of the efficiency of ceramic foam filters (CFFs) in the removal of nonmetallic inclusions from molten aluminum through filtration have been widely studied in the literature.[15-19] Therefore, using the existing Al_2O_3 CFF material coated with AlF_3 to filter molten aluminum has the potential to remove dissolved alkali and alkaline earth metal impurities and non-metallic inclusions simultaneously.

There are three main methods by which AlF_3 can be employed in ceramic foam filtration. First, Al_2O_3 CFF can be immersed with AlF_3 slurry and sintered for use as filtration material.[20] There have been several patents about the coating of CFF filters with other materials, [21-23] such as soda silicate [21-22] and silicon carbide [23], which have softening points at the temperature of molten aluminum. The coated filters were supposed to be used for the removal of inclusions and dissolved alkali elements from the molten metal. Second, AlF_3 CFF can be produced for molten aluminum filtration by infiltrating polyurethane foam with AlF_3 slurry followed by firing to the AlF_3 sintering temperature. This may also be done by casting AlF_3 slurry mixed with appropriate sizes and amount of polymeric particles into a box, as shown in Figure 1. The cast product is then pyrolyzed to remove the polymer, followed by sintering to form AlF_3 ceramic foam filter. The third method, which is the subject of the present article, is by reacting Al_2O_3 with HF gas to form AlF_3 on and within the Al_2O_3 CFF.

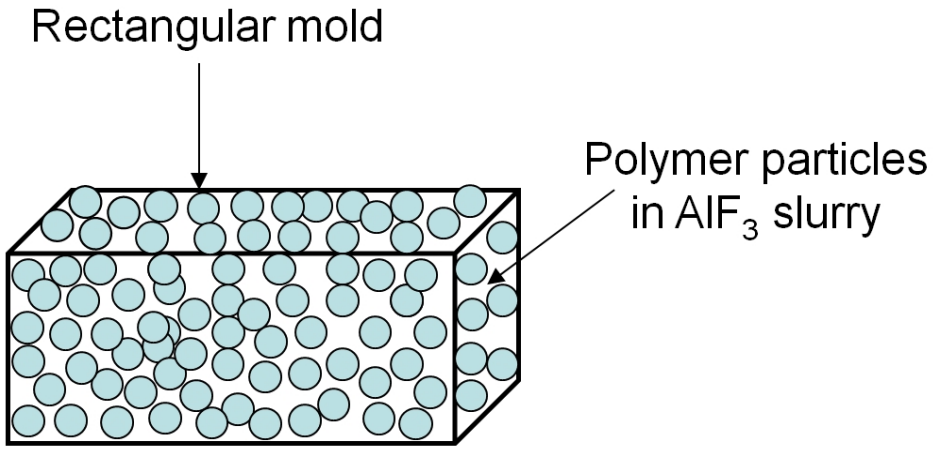

Fig.1. Schematic of AlF_3 CFF slip casting in a rectangular mold. The polymer particles are expelled during a pyrolysis process preceding sintering to allow for porosity development.

There have been several patents on the production of AlF_3 by the reaction between HF gas and solid Al_2O_3,[24-28] some as far back as 1971.[24] In Eisele's patent, it was explained in detail about how to react CaF_2 with H_2SO_4 acid to generate HF gas at ~200^oC, then HF gas reacting with solid alumina to achieve AlF_3.[28] And in Blake's report, it was suggested to use waste HF acid to produce an AlF_3 filter for aluminum purification.[24] However, Al_2O_3 CFFs coated with AlF_3 are not being employed in industrial aluminum purification despite its obvious advantages. This is due to the lack of a clear-cut industrial filter making process to facilitate economic and environmentally friendly Al_2O_3 CFFs coated with AlF_3 for the aluminum industry.

The present article preliminarily explores the coating of alumina CFF with AlF_3 through a method by which Al_2O_3 was reacted with anhydrous hydrofluoric acid (HF) in a high temperature furnace. Samples from the coating experiments were characterized by x-ray diffraction (XRD), scanning electron microscope (SEM) with electron dispersive x-ray (EDX) capabilities, and electron probe microanalysis (EPMA). Theoretical analysis of the removal efficiency of such a filter has also been carried out through mathematical modeling of the refining process and results presented.

2. Experiments

2.1. *Trial Experiments*

A method of coating an Al_2O_3 ceramic foam filter (CFF) with AlF_3 by dipping into a slurry prepared using AlF_3 of 94 % purity followed by sintering has been explored.[20] However, the slurry blocked some of the pores of the original filter. In the current study, the reaction of alumina foam filters with aqueous HF in an attempt to form a layer of AlF_3 on alumina was unsuccessful, as the aqueous HF (48 % and 24 %) dissolved the alumina rapidly.

2.2. *Reacting Al_2O_3 Filter with Anhydrous HF Gas*

The experimental setup consists of three reactors, as shown in Figure 2, with three major reactions occurring – HF gas generation, AlF_3 coating and excess HF gas neutralization reactions. The experimental furnace was water cooled and controlled with a PID temperature controller. The target reaction occurs in the quartz tube furnace, leading to the formation of the AlF_3 coating on the Al_2O_3 filter. The feasibility of generating HF from a reaction between sulfuric acid and NaF has been studied.[29] The following reactions are involved in the respective reactor processes during the experiments.

$$2NaF_{(s)} + H_2SO_{4\,(conc)} = Na_2SO_{4\,(s)} + 2HF_{(g)} \quad [4]$$

$$Al_2O_{3(s)} + 6HF = 2AlF_{3(s)} + 3H_2O_{(g)} \quad [5]$$

$$NaOH_{(aq)} + HF_{(g)} = NaF_{(liq)} + H_2O_{(liq)} \quad [6]$$

Powdered CaF_2 was also used here in place of NaF to react with sulfuric acid to generate HF gas in an experiment according to equation [7]. The use of CaF_2 to produce HF gas is a well-known process. Using CaF_2, and not NaF, prevents the evaporation of sodium into the filter materials during the experiment.

$$CaF_{2\,(solid)} + H_2SO_{4\,(conc)} \rightarrow CaSO_{4\,(solid)} + 2HF_{(gas)} \quad 7]$$

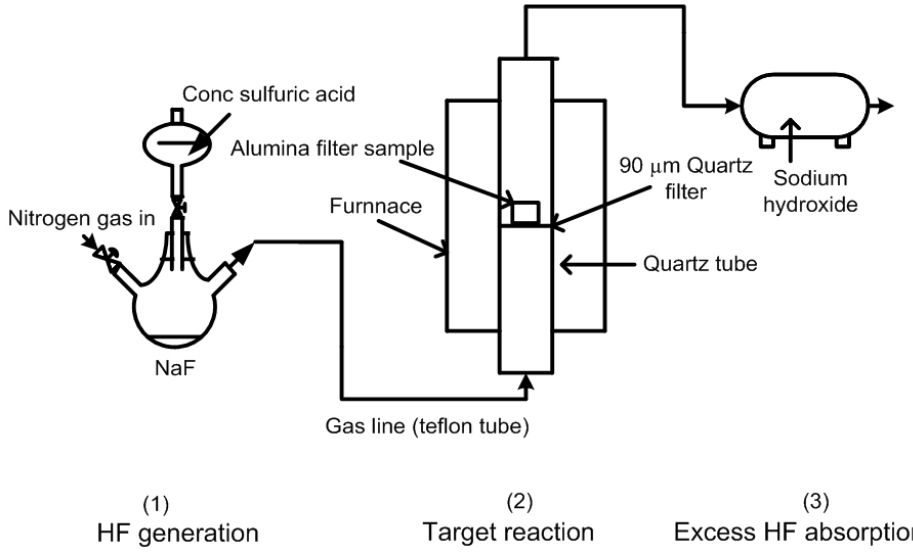

Fig. 2. Schematic diagram of the experiment setup used for HF gas coating process.

Material selection for constructing the experimental setup was an important factor given the severe corrosiveness and poisonous nature of hydrofluoric acid (HF). The reactor vessels were thus selected from quartz material and connected to each other by Teflon tubes. The joints and fittings were adequately sealed with the help of Teflon tape to avoid HF gas leakages. Quartz has an appreciable HF resistance under the prevailing experimental conditions.[30] A quartz filter of 90 μm pore size was fitted within the furnace to be a platform for the filter sample and also maintain a certain HF gas pressure within the reacting filter. The furnace was controlled by heating to 700^{o}C at a rate of 200^{o}C/hr and held at this temperature for a few minutes before cooling at a rate of 200^{o}C/hr.

According to the reaction stoichiometry, a minimum of 1 mole of anhydrous HF is required to produce 28.0 g of AlF_3. This formed the basis for the choice of quantities of the reagents for equation [4], where HF is generated for use in equation [5]. Thus 1 mole of NaF and 0.5 moles sulfuric acid were required to produce 28 g of AlF_3. The strength of the sulfuric acid used was 97%. Five experiments were conducted using NaF_2 and one experiment using CaF_2. Table 1 gives information about the various experiments. The yield of HF gas from equation [4] is below 100% and has been reported not to depend on the strength of the sulfuric acid,[29] as 80% and 96.5% sulfuric acid were found to give

approximately 80% yield. However, excess sulfuric acid above the required stoichiometric amount is reported to decrease the yield of HF and higher temperatures favor HF yield.

The setup was purged with nitrogen gas until the final temperature reached 700^{o}C in the furnace and reactor [1] had attained a preheating temperature of about 120^{o}C. The nitrogen gas purging helps to minimize corrosion in the reactors. The flow of nitrogen gas was discontinued before equation [4] was initiated by opening the valve to let concentrated sulfuric acid into reactor [1]. After a reaction time of five minutes, the nitrogen flow was resumed to force the generated HF gas from reactor vessel (1) to the furnace to initiate equation [5]. This process continued until the furnace cooled down to 25^{o}C. Excess HF gas was absorbed in a 30% (15.75 M) NaOH solution as shown in equation [6]. To ensure that negligible amounts of HF gas were released into the atmosphere, 5.5 liters of NaOH solution (far in excess of required volume) was used to neutralize the excess HF gas.

Table 1
Experimental conditions.

Experiment #	Qty of NaF or CaF_2 (g)	Volume of 97% H_2SO_4 (mL)	Holding Time (min) at 700 ^{o}C
1	40	26	15
2	60	40	25
3	80	60	30
4	80	52	20
5	100	67	15*
6**	100	71.94	30

* holding temperature 650^{o}C

** CaF_2 was used in place of NaF in Eq.[4]

Coated filter samples were cut to approximately 1 mm × 2 mm, embedded in epoxy, ground on various grades of SiC paper and then polished for observation with

SEM and analysis by EPMA. X-ray diffraction samples were ground to fine powders averaging 2 µm in grain size with the help of an alumina mortar and pestle. Due to the high sensitivity of XRD to impurities and contaminants, the alumina mortar and pestle were thoroughly washed with water and rinsed with ethanol and dried before successive samples were prepared in it.

3. Results and Discussions

3.1. *Comparison between Al2O3 Filters Coated with AlF3 Slurry and coating by Reacting with HF Gas*

Figure 3 shows the distribution of pores within the filters coated by AlF_3 slurry and gaseous HF. The slurry coated CFF showed less porosity than the HF gas coated CFF material because the AlF_3 slurry blocked part of the pores. The visual examination indicated the HF gas coated filters had porosity just like the original uncoated Al_2O_3 CFF. When touched, the AlF_3 coating on the filter by the slurry method appeared to fall off, indicating weaker adhesion strength of the AlF_3 coating to the Al_2O_3 base material. Distribution of fluoride within the walls of the slurry coated and the HF gas coated filters have been shown in Figure 4. While fluoride was detected throughout the wall thickness of the base material in the HF gas coated filter, fluoride in the slurry coated filter appeared as an additional layer onto the pores of the filter. This increased the wall thickness of the filter material from the slurry coated process, thus reducing porosity.

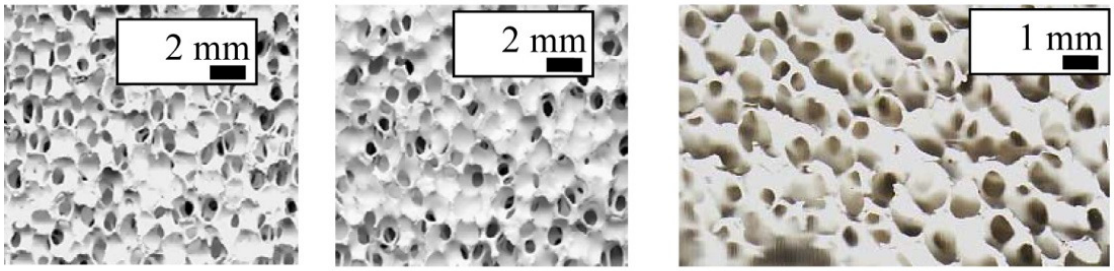

Fig. 3. Images of uncoated Al_2O_3 CFF (a) and AlF_3 slurry coated (b) and HF gas coated (c) CFF as taken with a scanner (30ppi).

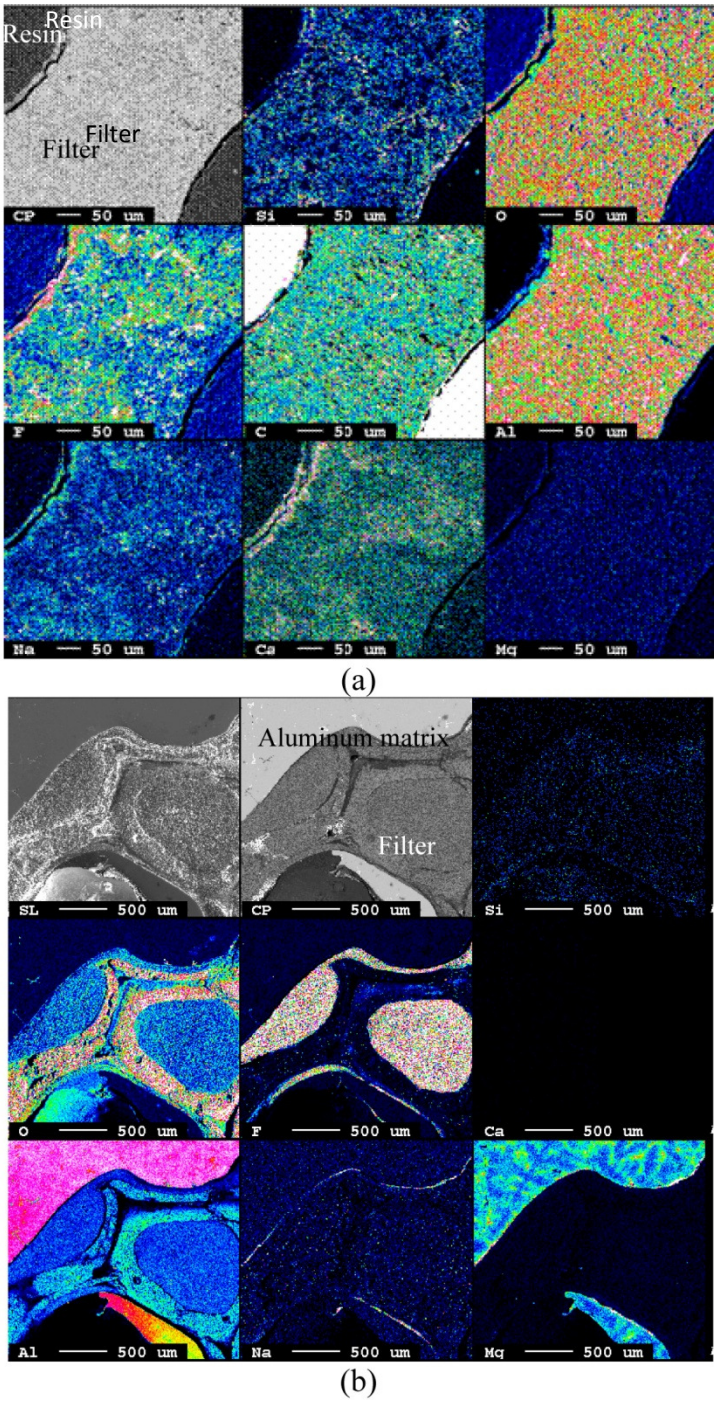

Fig. 4. Comparison between (a) HF gas coated filter and (b) slurry coated filter in the distribution of fluoride in filter walls. Some aluminum was allowed to solidify in the slurry coated filter after a filtration experiment. The filter shows an extra AlF_3 layer, which extends into the pores of the filter thereby reducing porosity.

Figure 5 shows the microstructure of filters. There was not a significant difference in the microstructures of the uncoated filter (Figure 5(a)) and the coated filter by the HF gas process (Figure 5(b)). Figure 5(c) shows the microstructure of the filter immersed in an aqueous HF solution. The wall thickness of the filter decreased to be very thin as a result of dissolution of alumina by the aqueous fluoride solution and no AlF_3 layer remained on the filter. The remaining Al_2O_3 material was very fragile and therefore cannot be used by the metal industry for filtration purposes. Figure 5(d) shows that the wall thickness of the filter coated by the AlF_3 slurry process increased, with an extra layer of fluoride. An important observation is the grain boundary (surface misfit) between the layers of the filter and the AlF_3 coating on the filter walls. This is probably the reason for the weak adhesion of the AlF_3 coating to the base material that we observed. Figure 6 is the EDX results of elemental compositions of the filters from the various HF gas coating experiments.

The first set of columns (experiment number zero) represents the uncoated filter, while the last set (experiment number seven) represents the filter from the aqueous HF experiment. Various elements such as silicon (Si), sodium (Na), and phosphorus (P) were detected alongside oxygen (O), aluminum (Al), and fluorine (F). The uncoated filter contained O, Al and P. Aluminum phosphate is a binder/sintering aid used in the manufacturing of the Al_2O_3 filter. It can be seen that, fluoride was successfully introduced into the filters in all the HF gas coating experiments. Traces of other elements other than fluorine were also detected in the filters from certain experiments. Sodium was detected in the filters from experiments 1, 3, 5 and 6. Silicon was detected after experiments 2, 5 and 6.

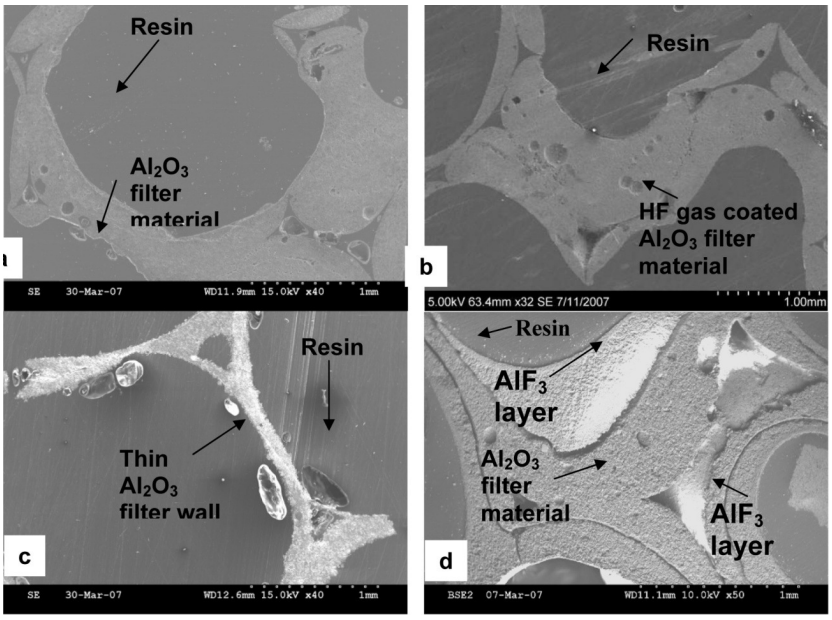

Fig. 5. Microstructure of various filters (a) uncoated filter, (b) HF gas coated, (c) aqueous HF coated and (d) slurry coated filter, with an additional layer (fluoride layer).

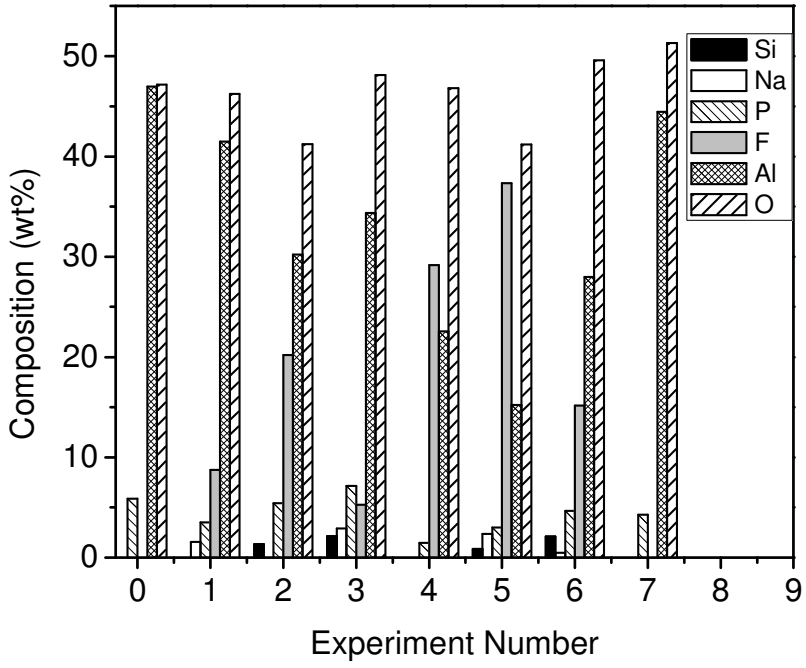

Fig. 6. Compositions of various elements detected in the filters after the various experiments. The columns of experiment number seven represent the filter from the aqueous HF experiment. For the conditions of the different experiments please see Table 1.

According to the EDX results, the filter material coated in experiment 4 did not contain traces of sodium and silicon. The base filter material is phosphate bonded alumina. The relationship between fluoride yield in the filter and the amount of HF gas supplied is shown in Figure 7, where the fractional increase in the quantity of reagents relative to experiment 1 is plotted against the respective fluoride yield in the filter. This indicates that increasing the pressure of HF gas has the tendency to increase the yield of fluoride within the filter.

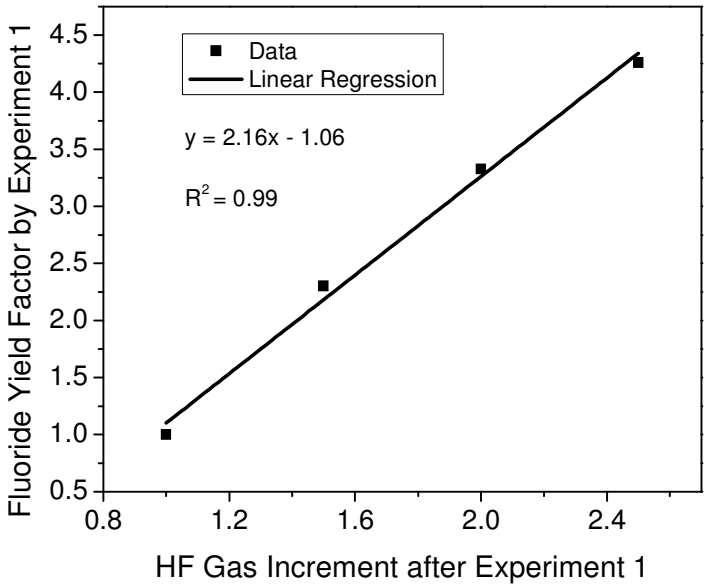

Fig. 7. Dependence of fluoride yield in the filter on the HF gas pressure. This result does not include points from experiments 3 and 6 because they were under different conditions.

The chemical compositions of the filters were confirmed by EPMA as shown in Figures 8 – 11. Figures 10 and 11 are X-ray diffraction spectra of the filters coated by the slurry method and HF gas methods respectively, showing the compounds formed within the filters during the coating process.

3.2. *Evaluation of HF gas coating process*

EDX results of filter walls shown in Figure 6 indicate that the concentration of fluoride within walls of the CFF increased with increasing amounts of HF generated from Eq. [4]. The highest average fluoride concentration within the filter walls was measured

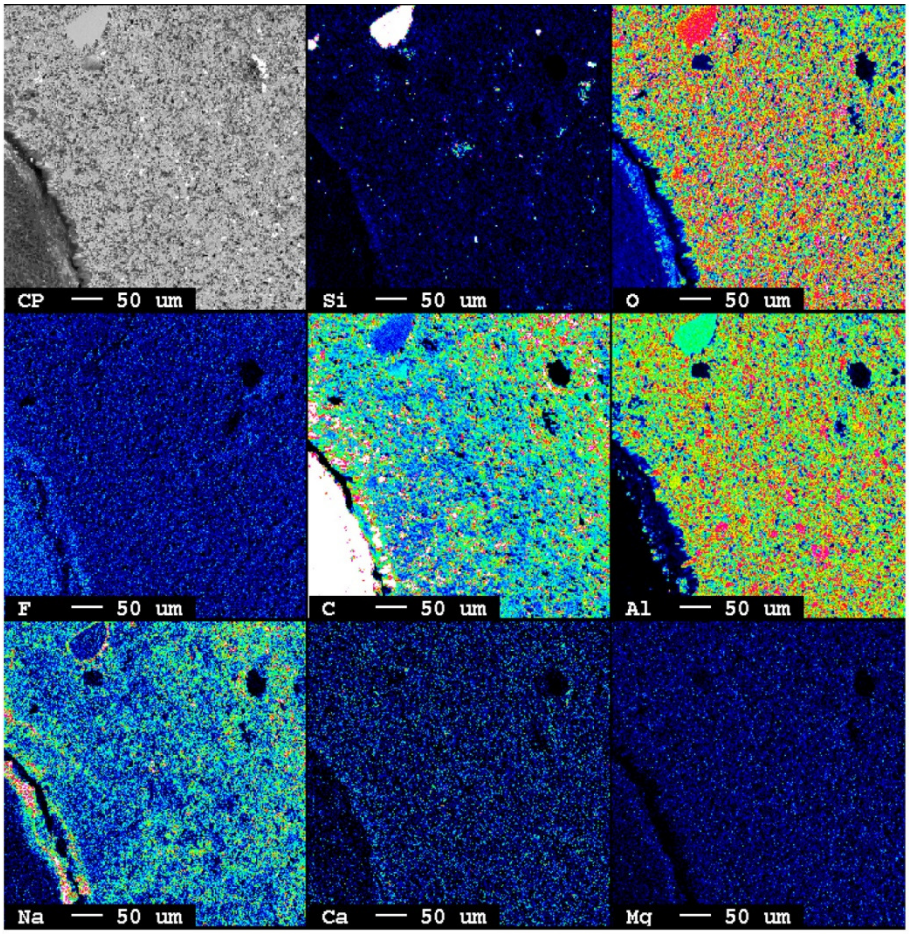

Fig. 8. EPMA mapping of elements in uncoated filter.

for experiment 5 to be 37.35 wt% followed by the results of experiment 4 with 29.17 wt% of fluoride. Experiment 3 gave the least fluoride yield in the filter with a fluoride concentration of 5.28 wt% followed by experiment 1 with 8.77 wt% fluoride. These results were expected because more HF was expected to yield from Eq.[4] as the stoichiometric concentration of NaF and concentrated H_2SO_4 increased. Therefore, fluoride yield from experiment 5 was expected to be highest followed by that from experiments 4, 3, 2 and 1. However, less HF gas yield was recorded for experiment 3 judging from the results of fluoride within the filter material. HF yield from Eq.[4] is reported to reduce dramatically when quantity of H_2SO_4 is in excess of stoichiometric requirements.[29] This probably, is the reason for the low HF gas yield in this experiment leading to the least fluoride yield among the experiments. As shown in Table 1, there was

excess sulfuric acid in experiment 3. The explanation given for the results of experiment 3 is reinforced by the results of experiment 4 which was a great success. It was a repeat of experiment 3 with stoichiometric quantities of NaF and concentrated H_2SO_4.

The concentration difference between the fluoride in the filters from experiments 1 and 2 is over 130 % of the concentration of fluoride in the filter from experiment 1 even though the increase in HF yield reagents (i.e. NaF and concentrated H_2SO_4) from experiment 1 to 2 is only about 50 %. (see Table 1) Thus the fluoride yield in the CFF may be improved by the supply of more HF to the filter. This result was observed throughout the experiments, from experiment 1 to 5, as shown in Figures 6 and 7. Experiment 5 was performed at a temperature of 650^{o}C, the lowest holding temperature among all the experiments. The furnace was allowed to cool down after heating and held at 700^{o}C for 30 minutes followed by a lowering of temperature until a temperature of 650^{o}C was reached before HF gas from Eq. [4] was introduced into the furnace. The holding time of the furnace at 650^{o}C was 15 minutes before the cooling scheduled was resumed, down to a temperature of 25 ^{o}C. Thus the success of experiment 5 is an indication that the process could be performed at a lower temperature than 700^{o}C. The calculated standard molar Gibbs energy of Eq. [5], shown in Eq. [8], indicates that the reaction can occur at temperatures below 820^{o}C. All data for the thermodynamic calculations were taken from reference [31].

$$\Delta G_m^o(T) = -430700 + 394T \qquad [8]$$

The thermodynamics suggest that the reaction possesses greater energy at lower temperatures and that coating results would be better at temperatures far below 25^{o}C. Therefore, the process can be undertaken at room temperature. The temperature of 700^{o}C was arrived at after a review of literature.

Figure 7 shows clearly that the fluoride yield in the filter material increases linearly with increasing the HF gas pressure. It is significant to mention that even though the best fluoride yield was encountered during experiment 5, it also produced the second highest Na concentration in the filter, as detected by EDX, second only to experiment 3 (Figure 6). Figure 8 shows elemental maps of the Al_2O_3 CFF before the coating

experiments. It shows moderate traces of sodium, ~1 wt% within the filter before coating. This could be the result of atmospheric contamination. However, there is no doubt that the coating experiments introduced sodium into the filter as can be seen from Figure 9. The EPMA maps show that the filter with the most Na concentration was from experiment 5, Figure 9(e) while clearly experiment 3 also gave very high traces of Na within the filter.

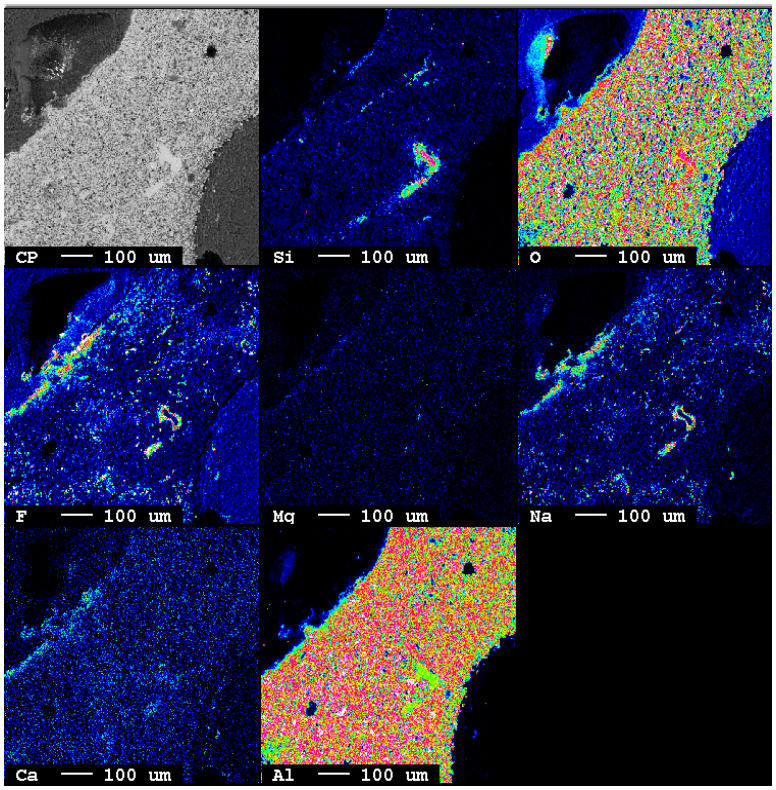

(a)

Fig. 9. Mapping of elements in filter after coating experiment (a) 1, (b) 2, (c) 3, (d) 4, and (e) 5.

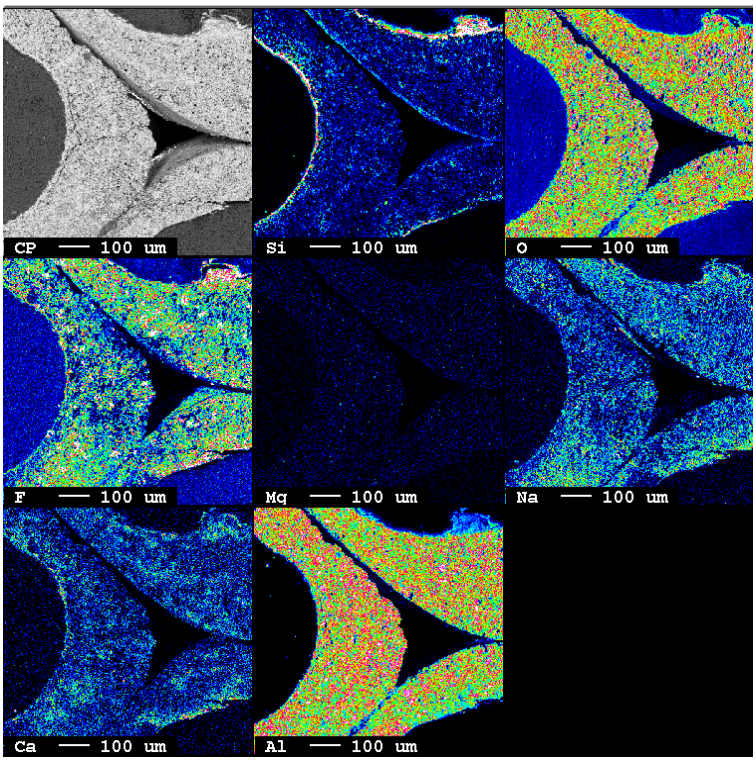

(b)

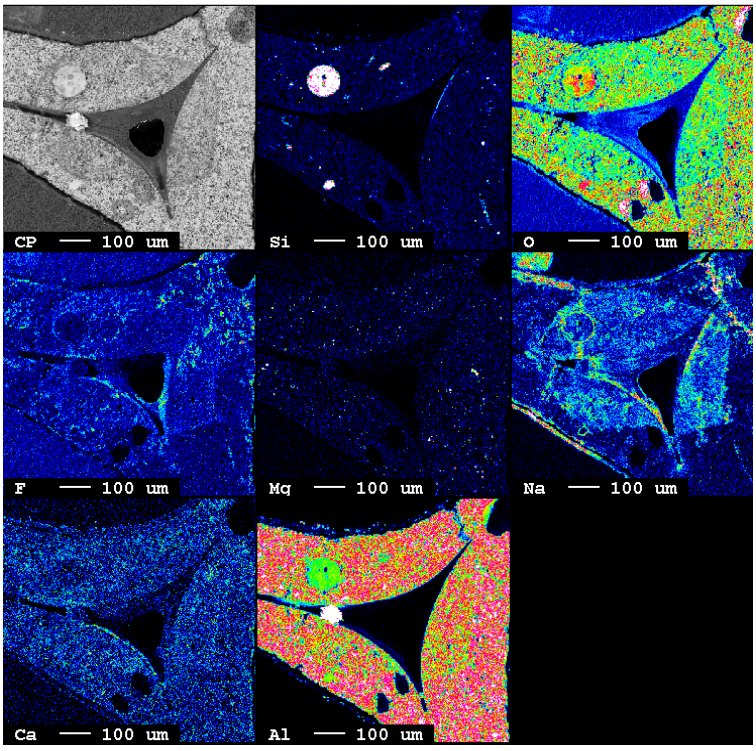

(c)

Fig. 9. Mapping of elements in filter after coating experiment (a) 1, (b) 2, (c) 3, (d) 4, and (e) 5. (cont.)

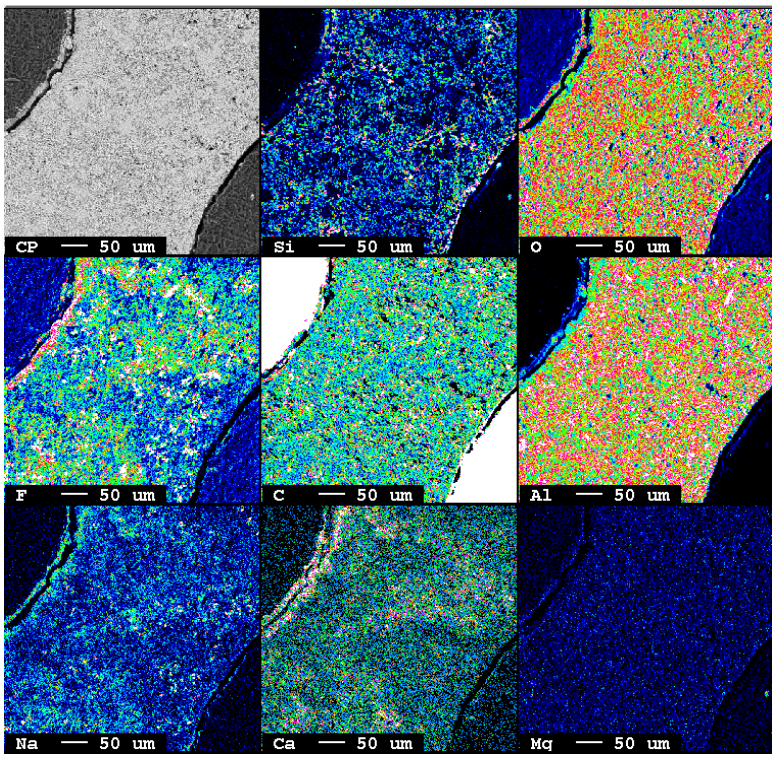

(d)

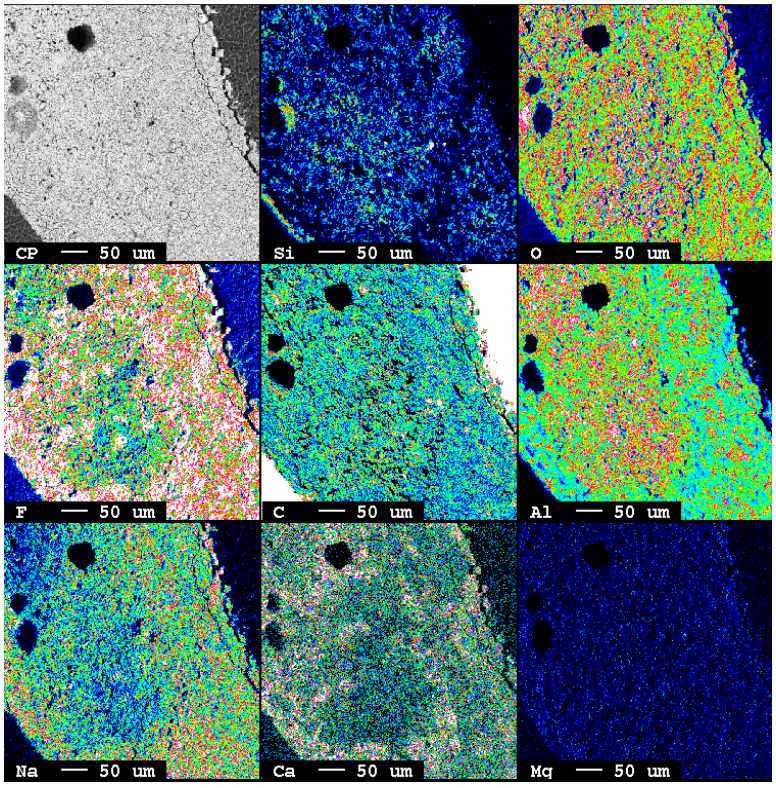

(e)

Fig. 9. Mapping of elements in filter after coating experiment (a) 1, (b) 2, (c) 3, (d) 4, and (e) 5. (cont.)

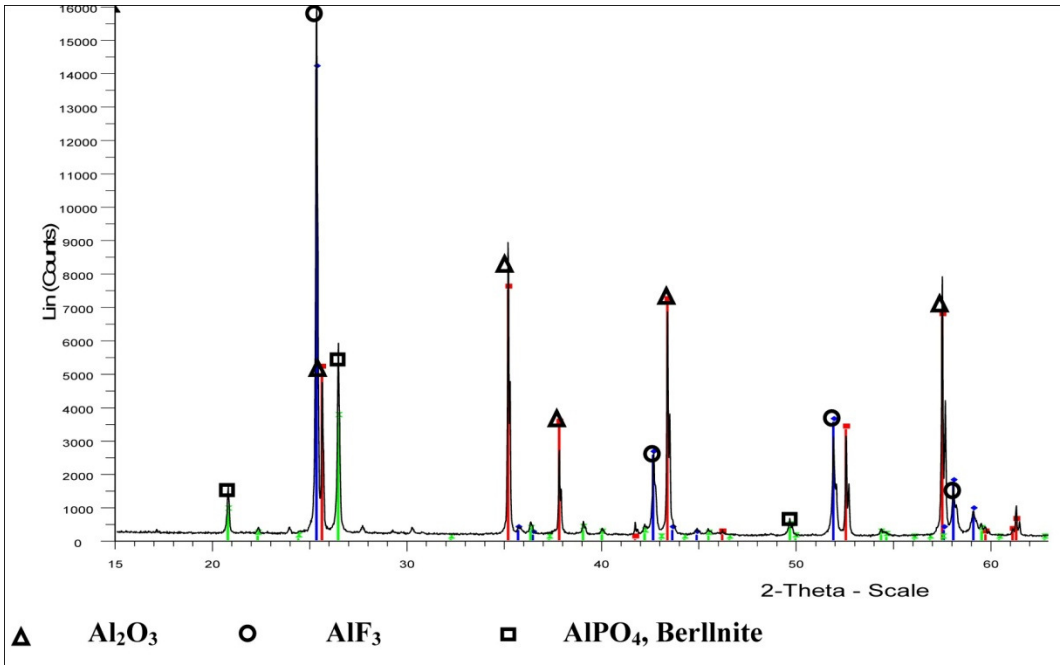

Fig. 10. XRD results of slurry aluminum fluoride coated alumina CFF.

The reason for the highest Na concentration in the filter from experiment 5 is not readily known. However, there is no doubt that the preheating processes might have evaporated some Na into the filter material. Experiment 4, Figure 9(d), appeared to suggest no traces of Na. We therefore, consider this experiment as the most successful in the experiments involving NaF.

Since sodium is not desirable in the filter, its chemical form was investigated by XRD. Figures 10 and 11 show the XRD spectra of these filter materials. The results show that sodium was present in the form of NaF in the filter from experiment 1. Another form, $(Na_2O)_{1.52}Al_2O_3(SiO_2)_{65}\cdot\times H_2O$ (sodium aluminum silicate hydrate) was detected in samples from other experiments. The distribution and the intensities of fluoride within the walls of the filters compared to that of Na as shown in Figure 8 indicate that more fluoride than Na was introduced into the filter. Fluoride in the filters was detected by XRD as AlF_3. A comparison between the filters coated by the slurry method and those by the HF gas method showed that more AlF_3 was detected in the slurry coated filters than in the HF gas coated filters. This is evident from the AlF_3 peaks of Figures 10 and 11. However, the EPMA maps indicate that for HF gas coated filters, not only is there fluoride on the surface of the CFF but it is also within the entire CFF material. Therefore,

under the appropriate HF gas pressure and temperature it is possible to convert the entire thickness of the filter wall into AlF_3 by this method resulting in higher AlF_3 activity within the filter without significantly changing the porosity of the filter.

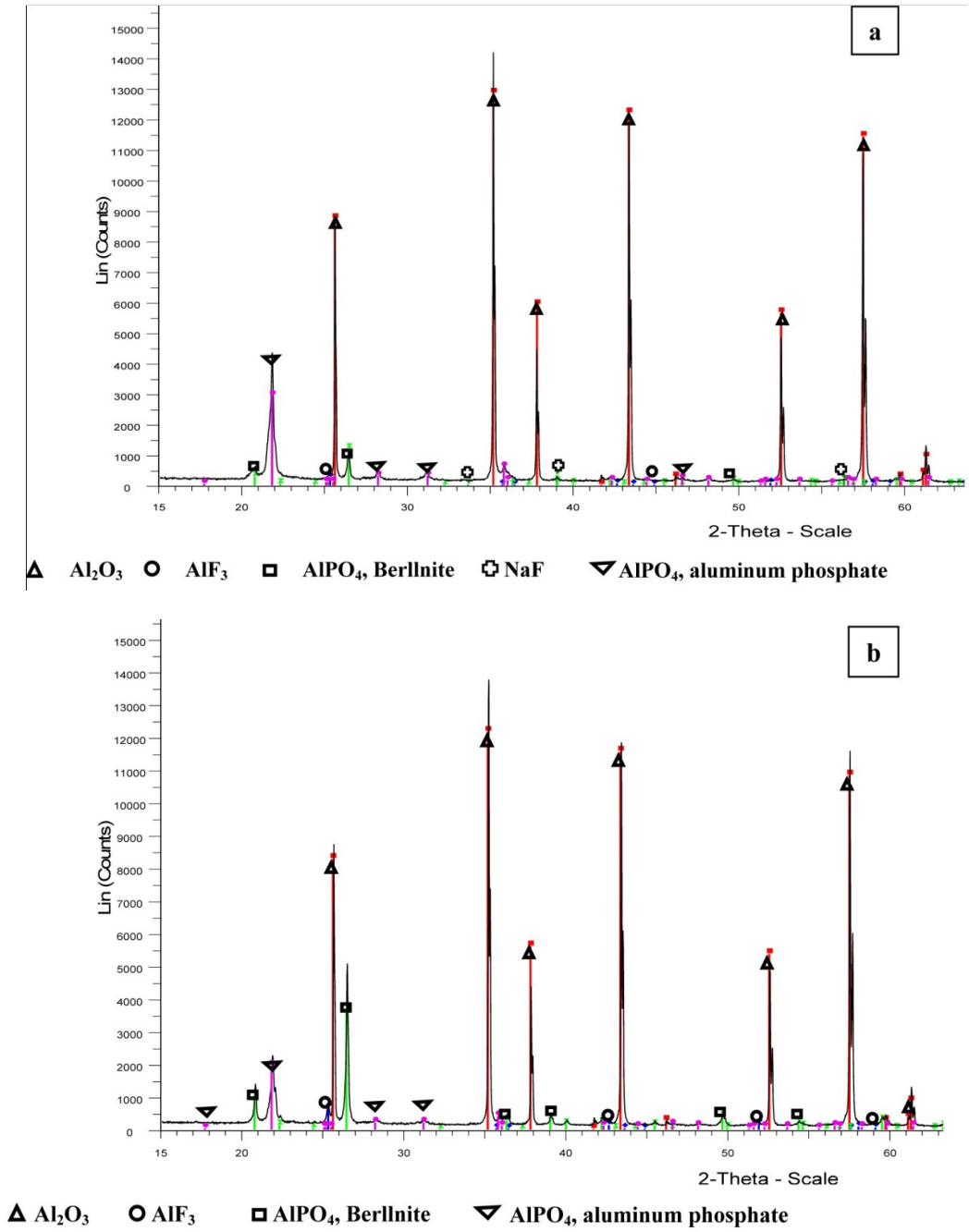

Fig. 11. XRD spectra of AlF_3 coated filter by HF gas method in experiment (a) 1 and (b) 2.

The unfortunate observation of NaF within the sample prompted an experiment using CaF_2 instead of NaF (experiment 6). Eq. [4] was then replaced by Eq. [9] in the process.

$$CaF_2 + H_2SO_4 = 2HF + CaSO_4 \quad [9]$$

$$\Delta G_m^o(T) = 62600 - 228.3T \quad [10]$$

The thermodynamics of this reaction, Eq. [10], indicate that it is a spontaneous reaction at room temperature. There is therefore no need for higher temperature preheating of CaF_2. The results from this experiment are shown in Figure 12. Even though there was a preheating of CaF_2 to 140^{o}C before the reaction, there was no significant detection of Ca made by EPMA. The results show a successful coating process with an even distribution of fluoride within the filter. However, more sodium was detected within the filter material after this experiment. It should be mentioned that the same experimental set-up was used for all six experiments. Therefore, the source of sodium in the filter material of experiment 6 is a result of evaporation and condensation of sodium compounds from within the Teflon tubes and the quartz stage of the filter. To eliminate the fear of introducing Ca into the filter, AlF_3 may be used instead. In that case, reaction (1) will proceed as follows

$$2AlF_3 + 3H_2SO_4 = 6HF + Al_2(SO_4)_3 \quad [11]$$

$$\Delta G_m^o(T) = 381700 - 677.7T \quad [12]$$

The standard molar Gibbs energy of this reaction shows that AlF_3 requires to be preheated to temperatures >260 ^{o}C for the reaction to occur.

The reactor materials also have the ability to reduce the amount of HF available for the reaction with Al_2O_3 CFF. The amount of HF available to react with the CFF is reduced if the reactor materials are not inert to HF attack. Thus corrosion of the reactor material by HF can reduce the extent of reaction with Al_2O_3 CFF to produce AlF_3.

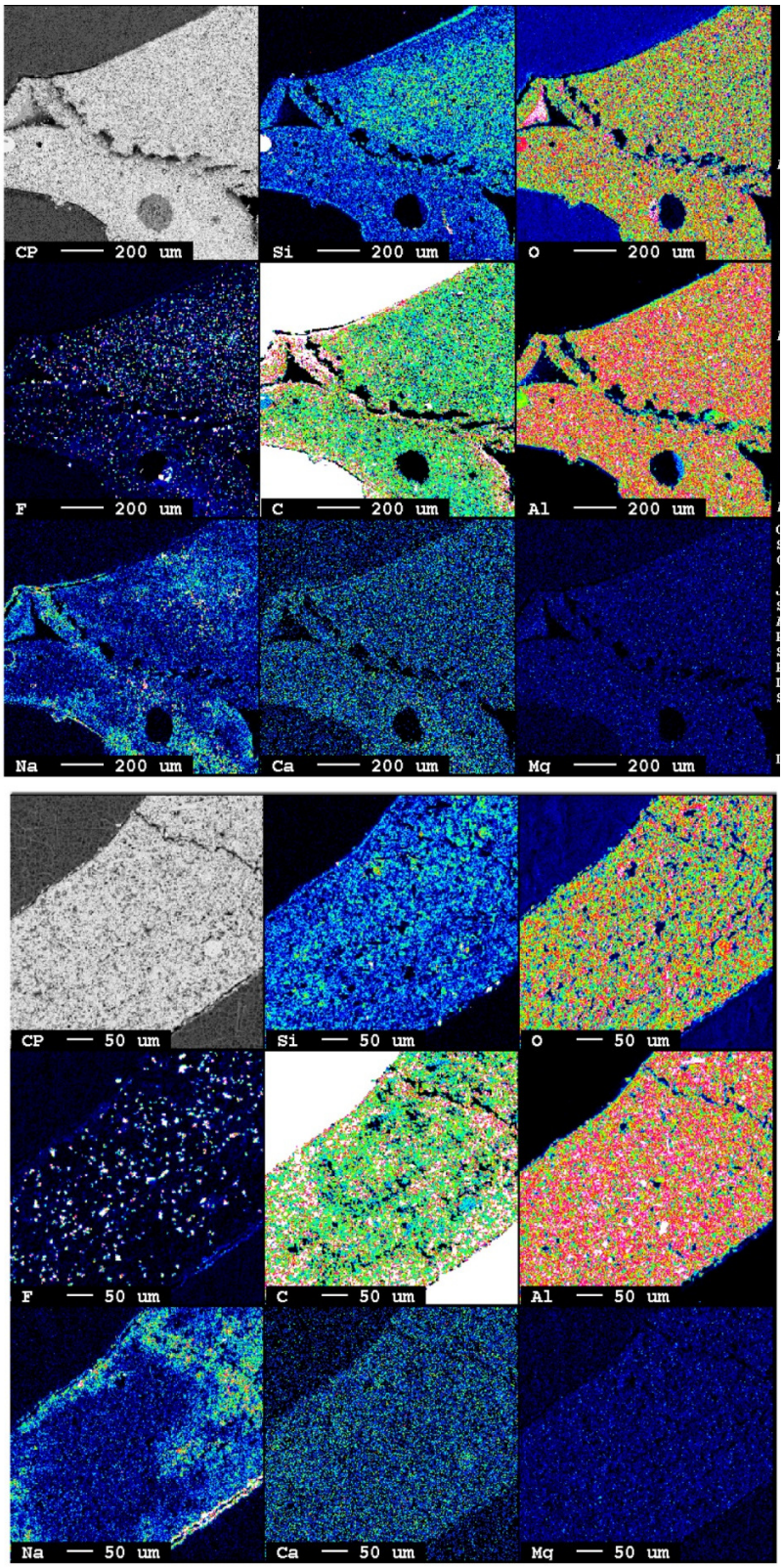

Fig. 12. Elemental maps of HF coated filter from experiment 6.

3.3. *Theoretical analysis of [Ca] and [Mg] removal from molten Al*

The AlF_3 coated CFF holds great prospects for the successful removal of dissolved elemental impurities from molten aluminum simultaneously with the removal of inclusions. Filtration results using AlF_3 slurry coated CFF showed that dissolved magnesium could be removed up to 87% through the following equation[32].

$$[Mg]+\frac{2}{3}AlF_3 = MgF_2 + \frac{2}{3}[Al] \quad [13]$$

In the study, [Ca] and [Na] could not be removed further due to their initial low levels. Dissolved [Na] removal efficiency of up to 98% and 78% efficiency for the removal of [Ca] using active granular bed filters coated with aluminum fluoride have been reported.[13] The removal efficiency of dissolved impurities by the filter may be evaluated by considering the reaction kinetics during the filtration process. If M is the dissolved impurity alkaline earth element, the following reaction would be expected

$$[M]+\frac{2}{3}AlF_3 \rightarrow MF_2 + \frac{2}{3}[Al] \quad [14]$$

Assuming a first order reaction rate with respect to *M*, and assuming pure AlF_3 and only one dissolved impurity element in aluminum, the rate of reaction can be written as

$$R_M = kC_M \quad [15]$$

where *k* is the rate constant and C_M is the concentration of [*M*] at the reaction interface. Figure 13 is a schematic diagram of the reaction interface, showing the concentration profile of [*M*]. The mass flux of [*M*] to the interface between the filter and molten aluminum can be written as follows;

$$J_M = h\left(C_{M,b} - C_M\right) \quad [16]$$

where *h* is the mass transfer coefficient, and $C_{M,b}$ is the concentration of [*M*] in the bulk of the molten metal.

At steady state, the rate of consumption [*M*] by the reaction is required to be equal to the mass flux of [*M*] to the reaction interface. This can be expressed as

$$R_M = J_M \quad [17]$$

leading to equations [18] and [19].

$$C_M = \frac{h}{h+k} C_{M,b} \quad [18]$$

$$R_M = \frac{C_{M,b}}{1/k + 1/h} \quad [19]$$

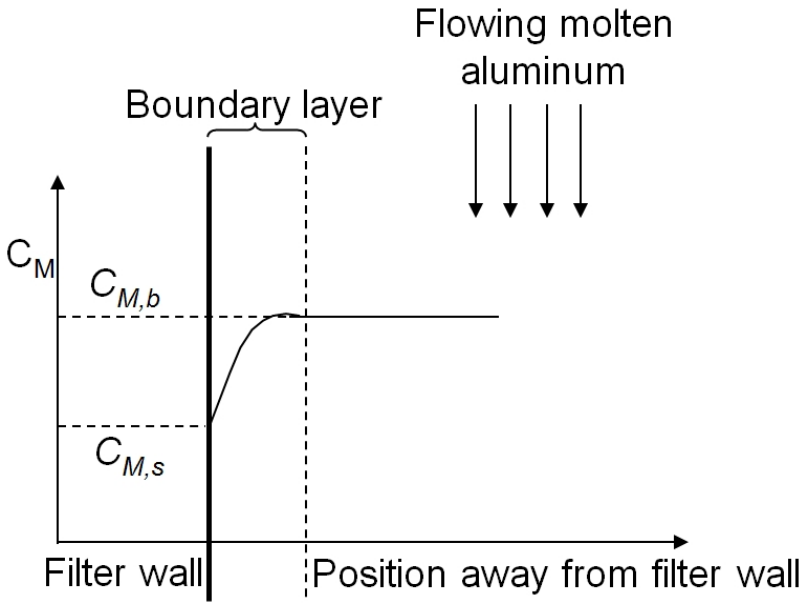

Fig.13. Schematic of the concentration profile of [*M*] at the filter molten aluminum interface.

For the high temperature filtration system, the rate constant, which depends exponentially on the temperature can be conveniently said to be far greater than the mass transfer coefficient (i.e. $k>>h$) [33] and that,

$$R_M = hC_{M,b} \quad [20]$$

Since mass transfer of [*M*] to the reaction interface includes diffusion through the bulk of the molten aluminum and the filter material, *h* would be replaced by the total mass transfer coefficient, h_t, to include the diffusion coefficients. The rate of consumption of [*M*] then depends on the mass transfer coefficient. Since the concentration of [*M*] varies along the depth of the filter, it is important to define the concentration of [*M*] over the depth of the filter. This can be achieved through a molar balance as follows

$$\frac{QC_{M,b}(z) - QC_{M,b}(z+\Delta z)}{\Delta z} = R_M \cdot S_v \cdot A \quad [21]$$

where Q is the volumetric flow rate of molten aluminum [m^3/s], z is the depth of the filter [m], S_v is the surface area per unit volume of AlF_3 active filter material [m^2/m^3] and A is the cross sectional area of the filter [m^2]. Substituting Eq. [20] in [21] and re-arranging leads to Eq. [22].

$$\frac{dC_{M,b}}{C_{M,b}} = -\frac{h_t S_v A}{Q} dz \quad [22]$$

The removal efficiency of dissolved [M] by the coated filter can be defined by Eq. [23].

$$E = \frac{C_{M,bin} - C_{M,bout}}{C_{M,bin}} = 1 - \left(\frac{C_{M,bout}}{C_{M,bin}} \right) \quad [23]$$

The removal efficiency can then be related to the filter properties as show by Eq. [24].

$$\ln(1-E) = -\frac{h_t S_v A z}{Q} \quad [24]$$

$$E = 1 - \exp\left(-\frac{h_t S_v A z}{Q} \right) \quad [25]$$

The cross-sectional area of the filter material A, and the volumetric flow rate of the molten metal, Q, can be related to the bulk volume of the filter, V_b, and porosity of the filter, ε, as follows.

$$A = \frac{V_b}{z}(1-\varepsilon) \quad [26]$$

$$Q = \frac{V_b \cdot \varepsilon}{t} \quad [27]$$

where t is the residence time of molten aluminum within the filter. The dissolved impurity elements removal efficiency can then be written as follows.

$$E = 1 - \exp(-ct) \quad [28]$$

$$c = \frac{h_t S_v (1-\varepsilon)}{\varepsilon} \quad [29]$$

The total mass transfer coefficient for calcium at the molten aluminum filtration temperature is reported to be 4.15×10^{-5} m/s [12] and $1.23 \pm 0.15 \times 10^{-3}$ m/s [13]. Table 2 gives information about the CFFs, compiled based on data from reference [34].

Table 2
Data for various CFF pore sizes adopted from Ref. [34].

Pore size (ppi)	E	S_v (m^2/m^3)
10	0.878	1.71×10^4
30	0.874	3.37×10^4
45	0.802	2.78×10^4
65	0.857	6.84×10^4

Figure 14 shows theoretical calculation of the removal efficiency of calcium by the filter for various parameters. It can be seen that the removal efficiency of the AlF_3 coated CFF depends exponentially on the residence time of the molten metal within the filter, the contact area of the filter by the molten metal and the mass transfer coefficient. Increases in the contact area (increasing ppi of filter) of the filter increased the removal efficiency significantly. Similarly, increases in the mass transfer coefficient reduce the time required to obtain higher removal efficiency. This implies that, dissolved elements with higher mass transfer coefficients in aluminum will be removed first and/or faster than those with relatively smaller mass transfer coefficients. Using 4.15×10^{-5} m/s as the mass transfer coefficient of [Ca] for a 30 ppi coated CFF, it can be seen from Figure 14 that the reaction proceeds at a fast rate within the first 28 s resulting in corresponding [Ca] removal efficiency of 99.65% and then slows down until after 61 s when 100% Ca removal efficiency is recorded. The standard Gibbs energy of formation of CaF_2 and MgF_2 are approximately -1080 and -950 kJ/mol,[35] respectively, indicating that thermodynamically, [Ca] will react preferentially with AlF_3 to [Mg]. Magnesium might be an expensive addition in Al-Mg alloys and therefore, the AlF_3 coated CFF might not be recommended, especially where the dissolved [Ca] content is low in the molten aluminum. The mass transfer coefficient of dissolved [Mg] in aluminum was calculated to be 1.15×10^{-6} m/s.[32] Therefore, both the thermodynamics and kinetics favor removal of dissolved [Ca] from molten aluminum preferentially to [Mg].

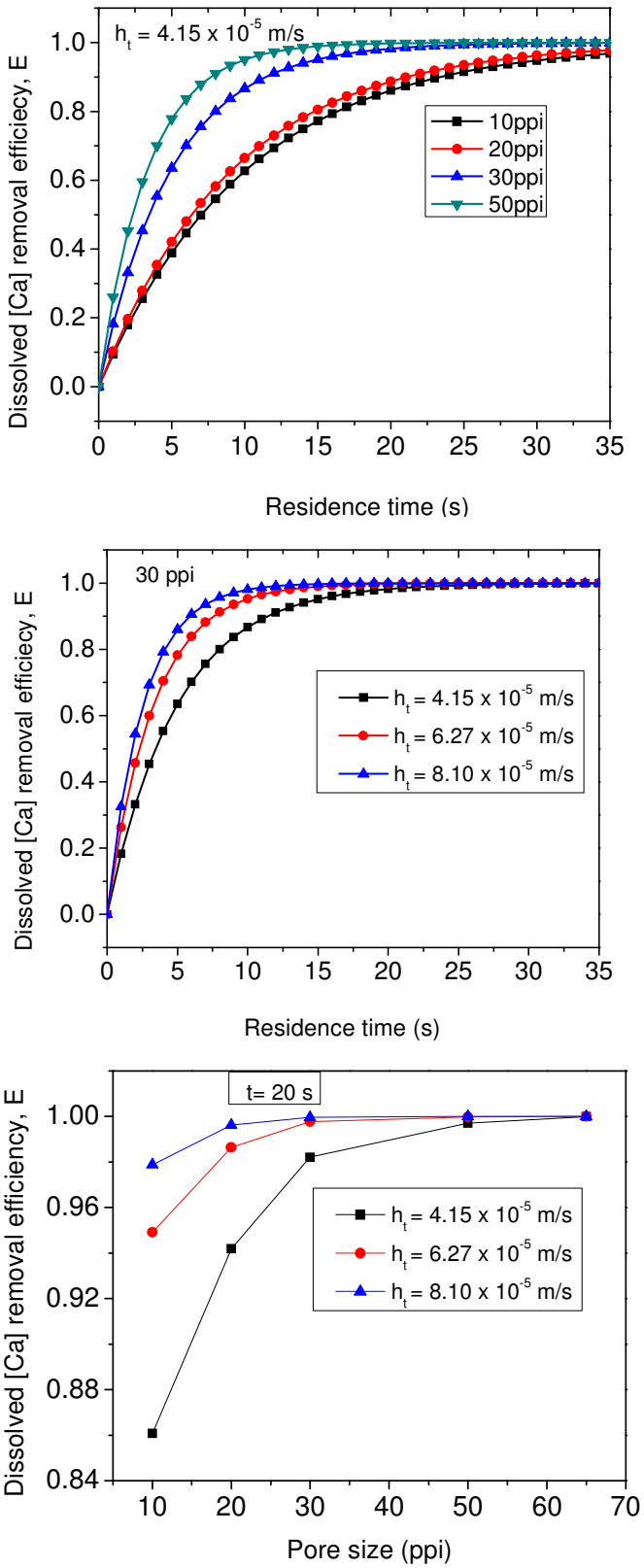

Fig. 14. The effect of various parameters including filter pore size, mass transfer coefficient, and time on removal efficiency of a coated filter for dissolved [*Ca*].

3.4. *Experimental Results of molten aluminum purification with a coated filter*

Aluminum filtration experiments using AlF_3 coated Al_2O_3 CFF by the HF gas method are yet to be conducted. However, to have an idea about the impurity elements removal efficiency of the AlF_3 coated CFF, preliminary filtration experiments were carried out by the authors and published[32] which tested the removal of dissolved magnesium from aluminum using the AlF_3-slurry coated 30ppi Al_2O_3 filter. The results showed that the slurry coated filter could remove dissolved [Mg] up to 87% in the filtration process, without compromising the nonmetallic inclusion removal efficiency of the filter. This result is in agreement with the prediction of the model for [Mg] removal. Figure 15 shows the results from experiments using AlF_3 slurry coated CFF.[20]

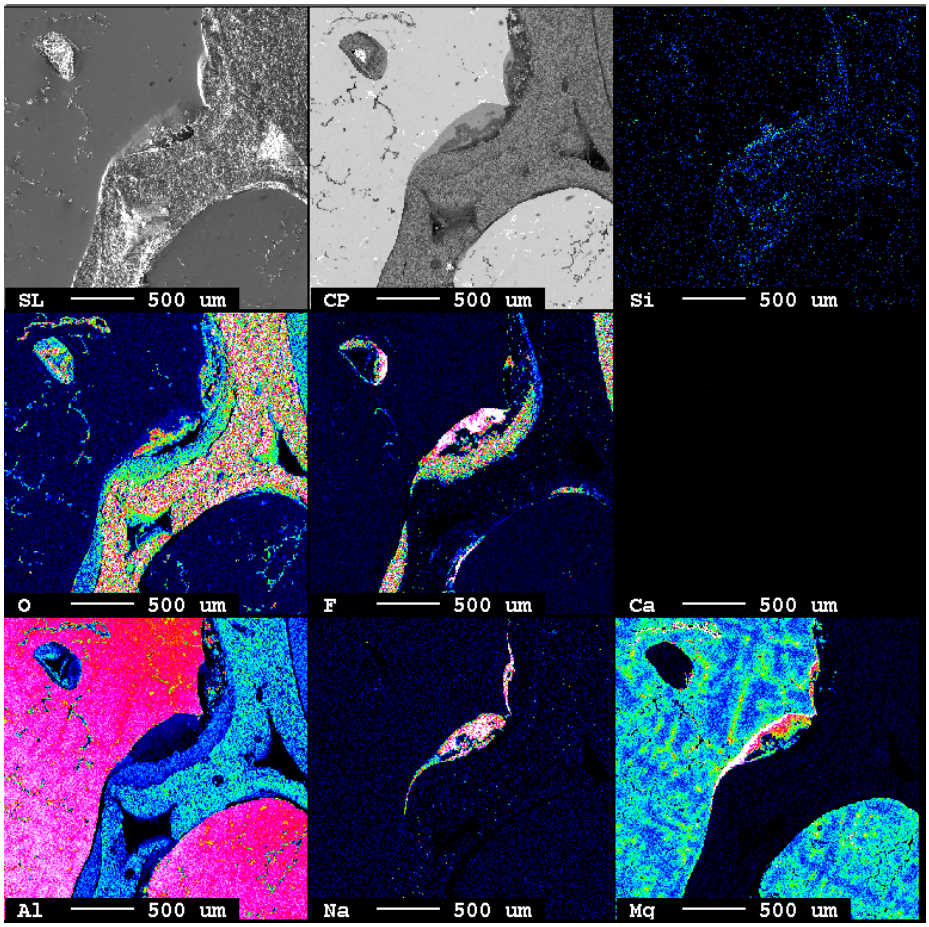

Fig. 15. Filtration results after the use of AlF_3 slurry coated Al_2O_3 CFF. It shows solidified aluminum within the filter and reaction products between the AlF_3 coating and dissolved [Na] and [Mg].[20]

It shows that the AlF_3 coating reacted with dissolved [Na] and [Mg] in the molten aluminum, leading to segregation of sodium and magnesium on the surface of the filter. It is observed that, the filter retains the products of the reactions with the impurity elements. The coating removed sodium from the molten aluminum through Eq. [30].

$$3[Na] + AlF_{3\ (s)} = 3NaF_{(s)} + [Al] \qquad [30]$$

Figure 16 shows filtration results using an AlF_3 granular bed filter, taken from reference [13]. It provides further evidence of the reactions that occur between the surface fluoride on the filter and dissolved [Na] and [Ca].

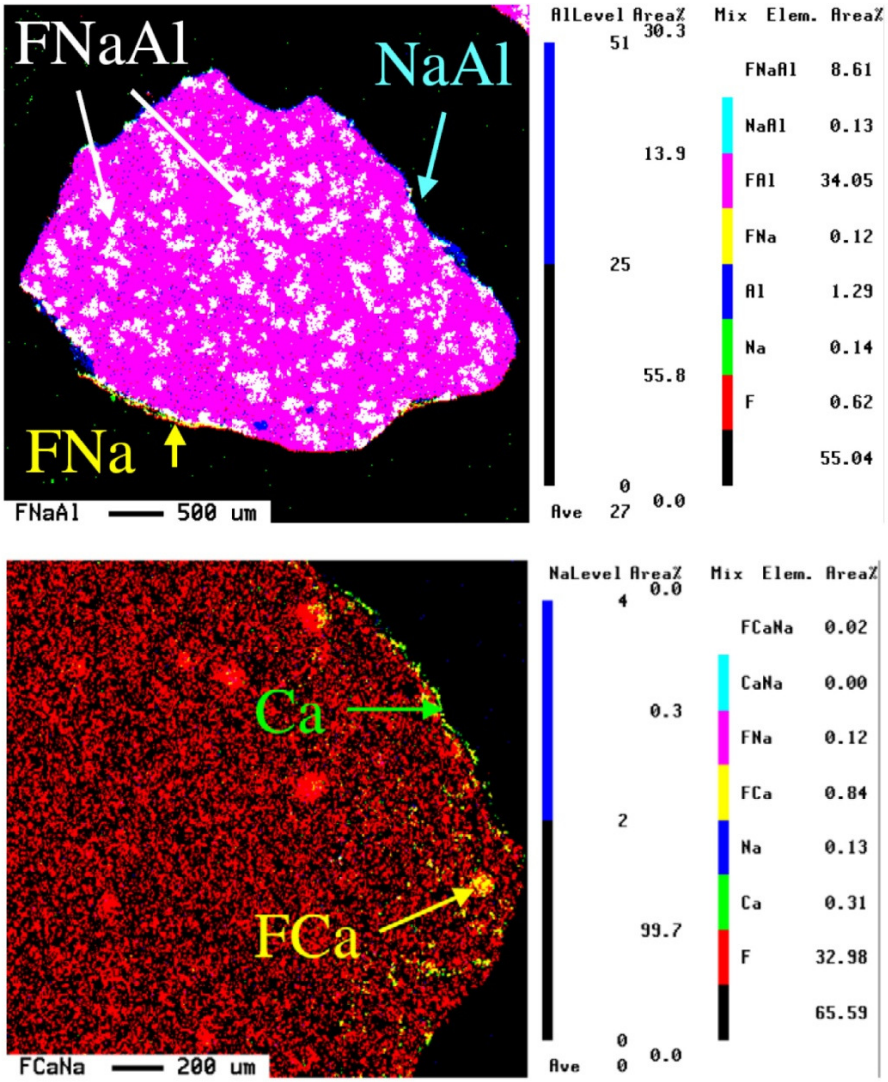

Fig. 16. EPMA maps of elements on granular bed filter after aluminum filtration.[13] It shows reaction products between AlF_3 and dissolved [Na] and [Ca].

These filtration results indicate that both AlF_3 coated Al_2O_3 CFFs and AlF_3 CFFs have the potential to remove dissolved alkali and alkaline earth impurity elements from the molten aluminum while removing inclusions from the metal.

4. Summary

Anhydrous HF gas was generated from a reaction between NaF/CaF_2 and H_2SO_4, which was used to react with an Al_2O_3 ceramic foam filter to produce an AlF_3 coating on the filter surface. The coated filter is expected to be used to filter molten aluminum to remove both nonmetallic inclusions and dissolved alkali and alkaline earth dissolved impurities. Theoretical evaluation of the capability of the coated filter to remove dissolved impurity elements was also undertaken with a case study on dissolved [*Ca*]. The results indicated that

- It is possible to coat an Al_2O_3 filter with AlF_3 by reacting it with anhydrous HF gas without compromising filter porosity. HF gas could be generated from a reaction between NaF, CaF_2 or AlF_3 and H_2SO_4. NaF and CaF_2 can react at room temperature while AlF_3 reacts at temperatures above 290^{o}C.
- Increasing the pressure of HF gas involved in the coating reaction increased the yield of AlF_3 within the filter.
- The AlF_3 coating produced by this method formed part of the original filter wall; therefore the porosity of the filter was retained.
- Na/NaF was introduced in the filter materials due to evaporation and condensation. There was not significant detection of Ca in the filter when CaF_2 was used. The use of AlF_3 is proposed to resolve the possible introduction of Na/Ca impurities into the filter.
- The theoretical calculations showed that the removal efficiency of dissolved elements in aluminum by the AlF_3 coated CFF depends exponentially on the residence time of the molten metal within the filter, the contact area of the filter by the molten metal and the mass transfer coefficient. Increasing the contact area of the filter increases the removal efficiency significantly. Similarly, increases in the mass transfer coefficient reduced the time required to obtain near 100 %

removal efficiency. Calculated examples showed that, it is possible to obtain well above 99 % removal efficiency for dissolved [Ca] impurities by the use of AlF_3 coated CFF for filtration within 30 s of residence time for 10 ppi – 50 ppi filters.

5. Future work

- Coating experiments using AlF_3 and sulfuric acid will be undertaken in addition to the determination of the optimal coating conditions.
- Further studies will be carried out using AlF_3 in place of NaF and CaF_2. Optimum coating conditions will be determined and properties of the coated filters evaluated relative to the coating process parameters.
- The useful life of the AlF_3 coating on the filter will be investigated.
- Active filtration of aluminum will be experimented using AlF_3–coated Al_2O_3 CFF, coated by reacting with anhydrous HF gas to study their efficiency in removing dissolved alkali and alkaline-earth metals.

Acknowledgement

This research is supported by a University of Missouri Research Board Grant, the Laboratory of Green Process Metallurgy and Modeling (GPMM), the Materials Research Center (MRC), and the Intelligent Systems Center (ISC) at Missouri University of Science and Technology (Missouri S&T).

References

[1] Apelian D, Shivkumar S. Molten Metal Filtration - Past, Present and Future Trends. Proceedings of 2nd International Conference on Molten Aluminium Processing , Orlando, Florida November 1989: 6.

[2] Grandfield JF. Melt Quality specifications. Aluminium Melt Treatment and Casting (TMS), Edited by M. Nilmani 1993:80.

[3] Kim JK, Rohatgi PK. Nucleation on Ceramic Particles in Cast Metal-Matrix Composites. Metall. Mater. Trans. A 2000;vol. 31A: 1295.

[4] Eckert CE. Molten Metal Quality Considerations for Aluminum Extrusion Ingot Product. Proceedings of International Aluminium Extrusion Technology Seminar (Aluminium Association Inc, & Aluminium Extruders Council) 1997;vol. 1:477

[5] Guthrie RIL, Nilmani M. Impurity Sources and Control - Generals of Melt Treatment. In: Aluminium Cast House Technology, (TMS), Editored by Nilmani 1993:85.

[6] Beland G, Depuis C, Leroy C. Aluminium Cleanliness Monitoring: Methods and Applications in Process Development and Quality Control. Light Metals (TMS) 1995:p. 1189.

[7] Sibley SR. Granular Fluxes for Aluminium Alloys, Environmental and Technological Advances. Proceedings of the 4 th International Conference on Molten Aluminium Processing 1995:417.

[8] Eckert CE, Miller RE, Apelian D, Mutharasan R. Light Metals (TMS) 1984:1281.

[9] Gorner H, Engh TA, Syvertsen M. AlF3 as an Aluminium Filter Medium. Light Metals (TMS), Edited by H. Kvande 2005:939.

[10] Dube G. Removal of Alkali Metals and Alkaline Earth Metals From Molten Aluminum. US Patent No. 4470846 1984.

[11] Montgrain L. Apparatus and Method for Removal of Alkali and Alkaline Earth Metals from Molten Aluminum. US Patent No. 4277280 1981.

[12] Gorner H, Engh TA, Syvertsen M, Zhang L. Removal of Na and Ca from Aluminum Scrap through Filtration. Mater. Sci. Forum 2007;Vol. 546-549:801.

[13] Gorner H, Engh TA, Syvertsen M. Kinetics of an AlF3 Aluminium Filter. Light Metals 2006, (TMS) 2006:756.

[14] Gorner H, Engh TA, Syvertsen M, Zhang L. Removal of Na and Ca from Aluminum Scrap through Filtration. In: al. YHe, editor. Mater. Sci. Forum, vol. 546-549, Light

Metals, Aerospace Materials and Superconductors. Proceedings of 2006 Beijing International Materials Week, June 25-30, 2006, Beijing, China, 2006. p.801.

[15] Instone S, Badowski M, Schneider W. Development of molten metal filtration technology for aluminium. Light Metals (TMS) 2005:933.

[16] Keegan NJ, Schneider W, Krug HP, Dopp V. Evaluation of the efficiency of ceramic foam and bonded particle cartridge filtration systems. Light Metals (TMS) 1997:973.

[17] Schneider W, krug HP, Keegen NJ. Efficiency and performance of Industrial Filtration Systems. Sixth Australasian Asian Pacific Conference on Aluminium Casthouse Technology 1999:159.

[18] Smith DD, Aubrey LS, Miller WC. LiMCA II evaluation of the performance characteristics of single element and staged ceramic foam filtration. Light Metals (TMS) 1998:893.

[19] Strom A, Black JW, Guthrie RIL, Tian C. Non-ferrous alloy filtration efficiency study of fully sintered reticulated ceramics utilizing LiMCA and LAIS. Light Metals (TMS) 1992:1093.

[20] Gorner H, Zhang L. Active Filtration of an Al-Mg alloy using a Ceramic Foam Filter (CFF) coated with AlF_3 In: Zhang L, editor. Trondheim, Norway, 2006.

[21] Eckert CE. Method and apparatus for treating molten aluminum using improved filter media. USA, 2003.

[22] Nagakura Y, Yokota M, Osumi K. Filter for molten aluminum alloy or molten aluminum. In: Mitsubishi Aluminum Co. LSAC, Ltd.; Sumitomo Light Metal Industries, Ltd.; Nippon Light Metal Company, Ltd.; Kabushiki Kaisha Kobe Seiko Sho; The Furukawa Electric Co., Ltd.; Showa Denko K.K., editor. USA, 2005.

[23] Tungatt PD, Tyler DE, Cheskis HP. Silicon carbide coated porous filters. In: Publication OC, editor. USA, 1988.

[24] Blake HE, Thomas WS, Moser KW, Reuss JL, Dolezal H. Utilization of Waste Fluosilicic Acid (In Two Sections). 1. Laboratory Investigations. 2. Cost Evaluation. Washington, D.C., 1971.

[25] Alfred S, Tschebull W. Lentia Gesellschaft mit beschränkter Haftung. Germany, 1979.

[26] Rinaldi F, Bragante L, Cuzzato P. Process for the preparation of aluminum fluoride. In: S.p.A. A, editor, 2001.

[27] Cuzzato P, Bragante L, Rinaldi F. Process for the preparation of aluminum fluoride. In: S.p.A. SS, editor. EP, 2005.

[28] Eisele DJ. Using an air jacket to capture the heat of reaction for waste heat recycle in the production of aluminum fluoride. In: LLC AWA, editor, 2006.

[29] Sikdar SK, Moore JH. Process for Producing Fluorine Compounds and Armorphous Silica. USA Pat No. 4,308,244

[30] Ballato JM, Laffey SM, Riman RE, Vig JR. Etching Quartz Crystals in Anhydrous HF Gas. In: Proceedings of IEEE International Frequency Control Symposium 1996:102.

[31] Kubaschewski O, Alcock CB, Spencer PJ. Materials Thermochemistry. 6th Ed. Pergamon Press 1993:258.

[32] Damoah LNW, Zhang L. Removal of inclusions from aluminum through filtration. Metallurgical and Materials Transactions B 2010.

[33] Evans JW, Jonghe LCD. The Production of inorganic Materials. Macmillan Publishing Company 1992:96.

[34] Richardson JT, Peng Y, Rumue D. Properties of ceramic foam catalyst supports: pressure drop. Applied Catalysis A: General 2000;204:19.

[35] Utigard TA. Properties of Fluxes used in Molten Aluminum Refining. Proceedings of the International Symposium on Extraction, Refining and Fabrication of Light Metals, (Ottawa, Canada; CIM) 1991:353.

[36] Pisch A, Krautlein C, Le Brun P, Rombach G, De Vries P, Ryckeboer M, Simensen CJ. New Experimental Approach in the Search of Intermetallic Compounds for Fe, Mn and Si Removal in Aluminum Recycling. Light Metals 2005.

VITA

Lucas Nana Wiredu Damoah was born in Wassa Akropong, a town in the Western Region of Ghana. He receive B.S. in Materials Science and Engineering (June 2004) from the Kwame Nkrumah University of Science and Technology in Ghana and proceeded to the Norwegian University of Science and Technology in Trondheim, Norway where he received M.S. in Light Metals Production (July 2007). During his undergraduate education, he worked as an intern engineer at the Western Castings Limited, a foundry in Takoradi, Ghana. Immediately after his undergraduate education, he was appointed a teaching assistant at the Department of Materials Engineering in Kwame, Nkrumah University of Science and Technology, where he spent one year helping undergraduate students through classes in physical metallurgy, powder metallurgy, refractory materials, welding, and foundry technology. His research project tittles were "prediction of fatigue stress of metals under mean stress" and the "purification of aluminum through filtration" during his B.S. and M.S. studies respectively.

Upon graduation with his M.S. degree, he was appointed faculty member at the Department of Materials Science and Engineering, University of Ghana where he spent two and half years teaching several undergraduate classes in Mechanics of materials, materials processing, heat and mass transfer, materials structure and phase equilibria. He spent two months in the summer of 2008 at the Department of Materials Science and Engineering, Missouri University of Science and Technology as a visiting scholar.

Lucas began his PhD studies in the spring of 2010 with a research focus on the purification of metals through filtration and electromagnetic separation. He has presented his work at international conferences and published two manuscripts in highly ranked journals with two more yet to be published. He successfully defended his Doctoral research in spring 2012 and received his PhD degree in December 2012.